

THESIS FOR THE DEGREE OF DOCTOR OF PHILOSOPHY

On Control of Back-to-Back Converters and
Sensorless Induction Machine Drives

ROLF OTTERSTEN



Department of Electric Power Engineering
CHALMERS UNIVERSITY OF TECHNOLOGY
Göteborg, Sweden 2003

On Control of Back-to-Back Converters and
Sensorless Induction Machine Drives
ROLF OTTERSTEN
ISBN 91-7291-296-0

© ROLF OTTERSTEN, 2003.

Doktorsavhandlingar vid Chalmers Tekniska Högskola
Ny serie nr. 1978
ISSN 0346-718X

Technical Report No. 450
School of Electrical Engineering
Chalmers University of Technology
ISSN 1651-498X

Department of Electric Power Engineering
Chalmers University of Technology
SE-412 96 Göteborg
Sweden
Telephone +46 (0)31-772 1000

Chalmers Bibliotek, Reproservice
Göteborg, Sweden 2003

On Control of Back-to-Back Converters and
Sensorless Induction Machine Drives
ROLF OTTERSTEN
Department of Electric Power Engineering
Chalmers University of Technology

Abstract

This thesis focuses on design and analysis of the control system structure for back-to-back converter squirrel-cage induction machine drives. Particularly, sensorless control of induction machines, meaning vector control without a mechanical shaft sensor, and vector control of pulsewidth-modulated (PWM) rectifiers are considered.

The back electromotive force (EMF) is used as the basis for sensorless control in this thesis. A variant of the classical “voltage model” is adopted for sensorless flux estimation. It is shown that the estimator must be redesigned for the purpose of arbitrarily placement of the closed-loop poles. A thorough stability analysis of the redesigned estimator shows that asymptotical stability can be guaranteed at nominal speeds. The stability at very low frequencies is, however, largely affected by the knowledge of the stator resistance. The presence of a singularity for zero stator frequency is found, which makes it impossible to guarantee stable operation at very low frequencies, except for the case of zero external load torque.

The underlying mechanisms behind the two widely acknowledged instability phenomena for sensorless control at low frequencies are revealed. The most critical form of instability is the infamous *flux collapse*: the flux collapses to approximately zero, giving nearly total loss of torque, and uncontrolled rotation in the direction of the external load torque. The less well-known instability phenomenon *frequency lockup* is not as critical: the field orientation deteriorates, such that the torque reduces but not vanish, and the stator frequency and rotor speed lock on to constant values close to zero.

A control system structure is developed for the PWM rectifier. The previously proposed concept of virtual flux is adopted for grid-voltage synchronization, and three different synchronization algorithms are analyzed. The PWM rectifier is also considered for an active filtering application, for which a vector current control system designed for the deadbeat response is designed. An analysis shows that the resulting deadbeat control system is equivalent to previously proposed Smith predictor structures.

Index Terms: Flux estimation, induction motor, sensorless control, back-to-back converter, pulsewidth-modulated rectifier, virtual flux, vector current control, active filtering.

Acknowledgements

This research project was fully funded by the Sydkraft Research Foundation of Sydkraft AB, which is gratefully acknowledged. I particularly thank Bengt Ahlmann at Sydkraft for supporting this project.

I would like to express my deepest gratitude to Prof. Lennart Harnefors for supervising most of the work described in this thesis, for his invaluable technical advice, and for persistently revising the manuscript.

I further would like to thank Dr. Torbjörn Thiringer for his support during my stay at the department, and for providing me with invaluable laboratory assistance.

Dr. Jan Svensson supervised this work during my first two years at the department, and I owe him many thanks for introducing me to the world of electric drives.

Finally, I would like to thank all my colleagues at the department who have assisted me during the work on this thesis, and particularly Ph.D. candidate Andreas Petersson for good companionship.

Contents

Abstract	iii
Acknowledgements	v
Contents	vii
1 Introduction	1
1.1 Back-to-Back Converter	1
1.2 Sensorless Control	2
1.3 Vector Control of PWM Rectifier	3
1.4 Scientific Contributions	4
1.5 Publications	5
2 Induction Machine Dynamics and Vector Control	7
2.1 Induction Machine Model	7
2.1.1 Electrical Subsystem Model	7
2.1.2 Flux EMF and Back EMF	10
2.1.3 Parameter Variations	10
2.1.4 Mechanical Subsystem Model	11
2.2 Time-Scale Separation	11
2.2.1 Component and Polar Representation of Flux Dynamics	12
2.3 Flux Estimation	13
2.3.1 Direct and Indirect Field Orientation	13
2.4 “Current Model”	14
2.4.1 Indirect Field Orientation	15
2.4.2 Parameter Sensitivity	15
2.5 Inherently Sensorless Flux Estimation	16
2.5.1 Speed Estimation	19
2.6 “Voltage Model”	20
2.6.1 Lowpass Integrator	21
2.6.2 Modified Voltage Models	21
2.6.3 Discussion	22
3 Analysis and Development of the SCVM	23
3.1 Indirect Field Orientation	23
3.1.1 Slip Relation in Disguise	24

3.2	Stability Analysis	25
3.2.1	Nonlinear Dynamics Resulting from the SCVM	26
3.2.2	Equilibrium Points	26
3.2.3	Linearization of Closed-Loop System	27
3.2.4	Stability Analysis for EP1 at Nominal Speeds	30
3.2.5	Stability Analysis for EP1 at Low Speeds	32
3.3	Instability Phenomena	36
3.3.1	Instability and Flux Dynamics	37
3.3.2	Flux Collapse	37
3.3.3	Frequency Lockup	41
3.4	Parameter Sensitivity	42
3.4.1	Selection of Model Parameters	43
3.4.2	Lower Limit for Sustained Low-Frequency Operation	44
3.5	Destabilization of Frequency Lockup	46
3.5.1	Destabilization through i_q	46
3.5.2	Destabilization through λ	46
3.6	Implementation Issues	49
3.6.1	Discrete Implementation	49
3.6.2	Summary of Recommended Model Parameters	49
3.6.3	Combined “Current Model” and SCVM	50
3.7	Experimental Results	51
3.7.1	Very Accurately Modeled Stator Resistance	52
3.7.2	Flux Collapse	53
3.7.3	Frequency Lockup	53
3.7.4	Very Slow Speed Ramping	55
3.7.5	Destabilization of Frequency Lockup through λ	55
4	PWM Rectifier Models and Vector Control	59
4.1	PWM Rectifier Models	59
4.1.1	Introducing Grid Flux	60
4.1.2	Synchronous and Stator-Oriented Reference Frames	60
4.1.3	Dynamic Inductor Filter Model	60
4.1.4	Grid Voltage Disturbances	61
4.1.5	Active and Reactive Power	63
4.1.6	DC-Link Model	63
4.2	Grid-Flux Estimation	64
4.2.1	Voltage-Sensorless Flux Estimation	65
4.2.2	VM for Grid-Flux Estimation	66
5	Analysis and Development of Grid Flux Estimators	69
5.1	SCVM	69
5.1.1	Stability Analysis	70
5.2	PLL-Type Estimator	71
5.2.1	Stability Analysis	71
5.2.2	Rejection of Voltage Harmonics	73

5.3	Modified Compensated Voltage Model	74
5.3.1	Stability Analysis	74
5.3.2	Rejection of Voltage Harmonics	75
5.3.3	Modified PLL-Type Estimator	76
5.3.4	Implementation Issues	77
5.4	Simulations	77
5.4.1	Rejection of Voltage Harmonics	78
5.4.2	Response to Phase-Angle Jump	81
5.5	Summary	82
6	Controller Design	83
6.1	Internal Model Control	83
6.1.1	Two-Degrees-of-Freedom IMC	85
6.1.2	Back-Calculation	86
6.2	Grid Current Control	87
6.2.1	Assessment of Disturbance Reduction	89
6.3	DC Voltage Control	90
6.3.1	Feedback Linearization	90
6.3.2	Controller Design	91
6.3.3	Assessment of Disturbance Reduction	92
6.4	Induction Machine Controllers	94
6.5	Simulation of PWM Rectifier	95
6.5.1	Fast DC Voltage Control Loop	96
6.5.2	Slow DC Voltage Control Loop	96
7	Active Power Filtering and Deadbeat Current Control	99
7.1	Active Filtering	99
7.1.1	System Configuration	100
7.1.2	Effect of Delayed Current Response	101
7.1.3	Selective Active Filtering	102
7.1.4	Detection of Current Harmonics	103
7.1.5	Experiments	107
7.1.6	Summary	111
7.2	Deadbeat Control and Saturation Strategies	111
7.2.1	Computational Delay	111
7.2.2	Design of Deadbeat Current Controllers	112
7.2.3	Stability Analysis of the Two-Samples Deadbeat Controller	118
7.2.4	Overmodulation and Saturation	121
7.2.5	Limiting Command Voltage Vector	123
7.2.6	Experimental Results	127
7.2.7	Summary	130
8	Conclusion	133
8.1	Summary	133
8.2	Future Research	134

Contents

A Per-Unit System	135
B Induction Machine Data	139
C Glossary of Symbols, Subscripts, Superscripts and Abbreviations	141
References	145

Chapter 1

Introduction

Variable-speed electric machine drives are nowadays used various kinds of kinds industrial processes, transportation systems, wind turbines and household appliances in the western world. It has been estimated that electric drives consume 50 % of the produced electrical energy in Europe [18]. The vast majority of drives are fairly primitive devices, which hardly require any control at all, or perform well with fairly simple control methods. A very important but fairly small number of electric drives are, on the other hand, used in demanding applications, where precise and fast control of the drive is essential. For such applications, sophisticated and well-performing control design is a key issue.

1.1 Back-to-Back Converter

The back-to-back converter, depicted in Fig. 1.1, consists of two three-phase PWM converters with a common dc-link voltage. For historical reasons, the grid-connected PWM converter is normally referred to as PWM “rectifier,” while the machine-side PWM converter is referred to as PWM “inverter.”

An important property of the back-to-back converter is that it allows for true *four-quadrant* operation, meaning that the direction of the active power flow can be reversed at any instant. Traditionally, four-quadrant operation has mainly been useful for regenerative loads, where it is economically beneficial to feed back the braking power of the ac machine to the utility grid [35]. Recently, the four-quadrant capability of the back-to-back converter has also found use in new applications, of which variable-speed wind turbines that employ the wound-rotor induction generator [3, 98] and HVDC light [80] are perhaps the most well-known.

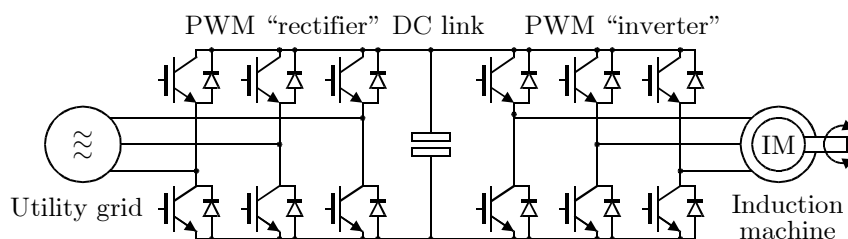


Fig. 1.1. Structure of a back-to-back converter induction machine drive.

In this thesis, control of the back-to-back converter squirrel-cage induction machine drive is studied. Particularly, so-called sensorless vector control of induction machines and vector control of PWM rectifiers are considered. These research topics are partly decoupled from each other, even though some similarities will be shown, so the resulting conclusions hold also for several other drive system structures. For instance, the control system for the PWM rectifier are not dependent on what type of ac motor that is connected to the PWM inverter.

1.2 Sensorless Control

Precise and accurate torque control for the induction machine (IM) can only be accomplished by *vector control*, as invented by Blaschke [15] in the late 1960s. In terms of space vector theory [74], vector control implies that the instantaneous torque is controlled by way of the stator current vector that is orthogonal to the rotor flux vector. Precise knowledge of the rotor flux angle is therefore essential for a vector controlled IM.

IMs do not allow the flux position to be easily measured, so most modern vector controlled IM drives rely on flux estimation. This means that the flux angle is derived from a flux estimator, which is a dynamic model of the IM. Given that the rotor speed of the IM is measured by a mechanical shaft sensor, then flux estimation is a fairly easy task. The famous “current model” (CM), for instance, is stable for all speeds and torques [42, 115]. However, there has for several years now existed a strong development towards sensorless control, which implies vector control of the IM without a mechanical shaft sensor. The driving motivations behind the development in sensorless control are:

- *Lower cost.* For low- and medium-power drives, the cost of the shaft sensor can be comparable to the cost of the IM itself.
- *Reliability.* Shaft sensors—tachometers, encoders, and resolvers are commonly used [35]—are prone to eventually fail, just like any other component of an IM drive. The removal of the shaft sensor results in one less critical component, thus improving the availability of the IM drive.
- *Operating environment.* Shaft sensors are delicate mechanical devices that cannot always be mounted in certain hostile environments, such as chemical plants.

Research in sensorless control has now been carried out for almost two decades, of which some of the most remarkable achievements are referenced in Chapter 2. The topic is therefore in many ways mature, and there are indeed several commercial sensorless IM drives on the market. In Scandinavia, the most well-known commercial implementations are perhaps the DTC family of ABB [111] and NFO Sinus [90]. Although commercial sensorless IM drives are generally well-performing, no strict proof of stability—taken into account inaccurate model parameters—is known to the author. There are also strong indications that particularly low-speed operation is still being problematic, even for commercial sensorless IM drives. A comprehensive survey [12], made two years ago by the drive manufacturer Baldor Electric Co., showed that several commercial sensorless

IM drives could not properly achieve stable low-speed-large-torque operation. Similar findings have also been presented by the academic research community [32, 46, 94, 100]. Recently, some fairly drastic, but apparently required, control algorithms [31, 76] have been proposed in order to secure stable sensorless control at low speeds. Therefore, sensorless control at low speeds and large torques can still be improved. Sensorless operation at nominal speeds, on the other hand, can no longer be considered as a problem.

In this thesis, the flux EMF is used as the basis for sensorless control. The flux EMF is the time derivative of the rotor flux, which is estimated by subtracting the voltage drops across the stator resistance and the total leakage inductance from the stator voltage. A rotor flux estimate can then be found from a flux estimator that integrates the flux EMF. Traditionally, the “voltage model” (VM) [30, 116] is used for this purpose, even though this flux estimator has several drawbacks [22, 47].

1.3 Vector Control of PWM Rectifier

An important reason for choosing a PWM rectifier over a simpler and less expensive rectifier, such as a three-phase diode rectifier [35], is that bidirectional power flow is enabled, as already discussed. In addition, a PWM rectifier offers the following advantages:

- *Good power quality.* Nearly sinusoidal currents can be obtained by using fairly small filters [55]. Moreover, the fully controlled input current of a vector controlled PWM rectifier makes it possible to even improve the local power quality. This can, for instance, be achieved by way of flicker mitigation or active filtering of current harmonics. Such improvement of power quality is today commercially available, the best-known example is perhaps the SVC light [43], albeit using a different converter topology than here studied.
- *Controllable dc-link voltage.* The controllable dc-link voltage improves the immunity of the electric drive towards voltage sags [117]. In addition, some applications increase the dc-link voltage when the loading ac machine operates above base speed [1]. This way, flux weakening for the machine is avoided and the maximum torque is always available.

Vector control of a PWM rectifier requires knowledge of the grid voltage angle, which is in close correspondence to the rotor flux angle of an IM. A virtual grid flux [36, 84, 85] can be introduced, such that the problems of grid-flux and rotor-flux estimation become nearly equivalent.

The vector control system of a PWM rectifier should preferably achieve good rejection of voltage disturbances, which are prone to appear in the utility grid. Otherwise, the grid voltage disturbances easily spread to the PWM rectifier input currents, which then become more distorted [20].

1.4 Scientific Contributions

The following results in Chapter 3 on sensorless control are considered as new, in the opinion of the author:

- A variant of the VM [101], in this thesis referred to as the “statically compensated voltage model” (SCVM), is adopted for sensorless flux estimation. The SCVM is then redesigned, such that arbitrarily placement of the closed-loop poles is made possible.
- The resulting dynamics from the SCVM are thoroughly analyzed. For accurate model parameters, stability is shown at nominal speeds, while stability at low speeds is guaranteed only for small machines. For inaccurate model parameters, the presence of a singularity for zero stator frequency makes it impossible to guarantee stable low-frequency operation for the SCVM, except for the case of zero external load torque or if the stator resistance is perfectly known.
- The underlying mechanisms behind instability for sensorless control are believed to be not well familiar. Based on the thorough stability analysis, these mechanisms are revealed for the SCVM. It is argued that the instability phenomena to a large extent are related to the physics of the IM itself, and can thus occur for any flux-EMF-based flux estimator.
- Recommendable choices for model parameters selections, with respect to overestimation and underestimation, are given for the SCVM. These recommendations cannot avoid instability, but may avoid total failure for a sensorless IM drive.
- Simple parameter selection rules are derived for the SCVM, reducing the amount of trial-and-error work required in the design and tuning of the drive.

Some very thorough research has been carried out on the PWM rectifier, of which some are referenced in Chapters 4–7. Even though not all of the following results cannot be considered as entirely new, some problems for the PWM rectifier are addressed, and several analyses provide interesting observations, believed to be not well-known.

In Chapter 5, three grid-flux estimators are analyzed, of which two estimators are designed in this chapter. The SCVM is found to be applicable not only for flux estimation of synchronous and induction motors [50], but also for vector control of a PWM rectifier.

In Chapter 6, controllers for a PWM rectifier are derived and analyzed. A classical cascaded control system structure is chosen, consisting of an inner vector current control loop and an outer loop for dc voltage control.

In Chapter 7, deadbeat current control for active power filtering at a low switching frequency is studied. The stability and the parameter sensitivity for the two-samples deadbeat controller is assessed, and it is shown that the controller is equivalent to previously proposed Smith predictor control structures.

For all three mentioned chapters regarding the PWM rectifier, simple controller and estimator parameter selection rules are derived, reducing the amount of trial-and-error work required in the design and tuning of the drive.

1.5 Publications

Many of the results in this thesis have been presented in the form of one Licentiate Thesis, three conference papers and three accepted journal papers. In chronological order, with references to where the paper appears in this thesis, the publications are:

1. J. Svensson and R. Ottersten. “Shunt active filtering of vector current-controlled VSC at a moderate switching-frequency,” *IEEE Trans. Ind. Applicat.*, vol. 35, no. 5, pp. 1083–1090, Sept./Oct. 1999.

The algorithms for active-power filtering in Chapter 7 were studied. These algorithms have, essentially, remained unchanged throughout this project.

2. R. Ottersten. “Vector control of a double-sided PWM converter and induction machine drive,” Lic. Thesis, Electrical Machines and Power Electronics, Dept. of Electric Power Eng., Chalmers Univ. of Technology, Göteborg, Sweden, 2000.

A control scheme for the back-to-back converter was developed. Parts of this control scheme is greatly improved in Chapters 5–6. The active filter algorithms and a preliminary variant of the deadbeat current control structure in Chapter 7 were presented. A more thorough analysis of deadbeat current control is added in the present thesis.

3. R. Ottersten and J. Svensson. “Active filtering using vector-current controlled VSC—Deadbeat control and saturation strategies,” *Proc. IEEE Nordic Workshop Power and Industrial Electronics*, Aalborg, Denmark, June 2000, vol. 1, pp. 278–282.

The deadbeat current controller in the Licentiate Thesis and Chapter 7 was considered for an active filter application.

4. R. Ottersten and J. Svensson. “Vector current controlled voltage source converter—Deadbeat control and saturation strategies,” *IEEE Trans. Power Electron.*, vol. 17, no. 2, pp. 279–285, Mar. 2002.

The deadbeat current controller in Chapter 7, more thoroughly analyzed in the present thesis, was presented. A similar version of this paper appeared already in 1998 as:

R. Ottersten and J. Svensson. “Vector current controlled voltage source converter—Deadbeat control and saturation strategies,” *Proc. IEEE Nordic Workshop Power and Industrial Electronics*, Espoo, Finland, Aug. 1998, vol. 1, pp. 65–70.

5. R. Ottersten and L. Harnefors. “Design and analysis of inherently sensorless rotor-flux-oriented vector control system,” *Proc. IEEE Nordic Workshop Power and Industrial Electronics*, Stockholm, Sweden, Aug. 2002, CD-ROM.

A preliminary variant of the SCVM in Chapter 3 was considered.

6. L. Harnefors, M. Jansson, R. Ottersten, and K. Pietiläinen. “Unified sensorless vector control of synchronous and induction motors,” *IEEE Trans. Ind. Electron.*, vol. 50, no. 1, pp. 153–160, Feb. 2003.

Chapter 1. Introduction

Parts of this paper considered the SCVM in Chapter 3 for the induction machine at nominal speeds. Moreover, the SCVM was compared to a phase-locked-loop type estimator for sensorless operation of ac machines. This comparison is not included in this thesis, but a similar study is made in Chapter 5 for a PWM rectifier.

Some results are still unpublished, however, since they have been produced at a fairly late stage in this project. The unpublished work includes the final version and the in-depth analysis of the SCVM in Chapter 3, and the analysis of grid-flux estimators in Chapter 5.

Chapter 2

Induction Machine Dynamics and Vector Control

The objective of this chapter is to derive and describe a model for the induction machine, see Appendix C for a list of glossary terms. We also analyze a few well-known flux estimators for vector control, and discuss the limitations of each estimator. The fundamentals of speed-sensorless operation is treated thoroughly, and one speed-sensorless flux estimator is selected for further analysis in the next chapter.

2.1 Induction Machine Model

The dynamic equivalent circuit of the squirrel-cage induction machine, which will be defined in the following, is based on the common simplifications that the magnetomotive force distribution along the airgap of the machine is sinusoidal, and that the hysteresis loss and the eddy-current loss [39] of the machine are negligible.

Space vectors [74] are commonly used to describe the dynamics of the induction machine, and these vectors are rms-value scaled in simulations and experiments in this thesis. The space vector of the stator current, for instance, is therefore

$$\mathbf{i}_s^s = \frac{\sqrt{2}}{3} [\mathbf{a}^0 i_{s1} + \mathbf{a}^1 i_{s2} + \mathbf{a}^2 i_{s3}] \quad (2.1)$$

where $\mathbf{a} = e^{j2\pi/3}$ represents the spatial distribution of the stator winding for a three-phase ac machine, while i_{s1} , i_{s2} and i_{s3} are the phase quantities of the stator current.

2.1.1 Electrical Subsystem Model

The *inverse- Γ model* [102] is used to model the induction machine. The inverse- Γ model is mathematically equivalent, both dynamically and in the steady-state operation, to the perhaps more well-known *T model* [102].

The electrical differential equations of the inverse- Γ model are obtained by applying the loop method to the equivalent circuit in Fig. 2.1. However, the loop method alone is not sufficient to directly derive the differential equations in a convenient form.

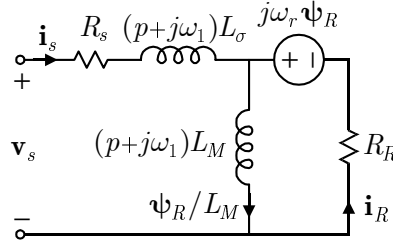


Fig. 2.1. Dynamic inverse- Γ circuit for the induction machine, where $p=d/dt$.

It is, for instance, desirable that the rotor current vanishes from the differential equations. This can be achieved by using the constitutive relations between the flux linkages and the currents of the induction machine:

$$\boldsymbol{\psi}_s = L_\sigma \mathbf{i}_s + \boldsymbol{\psi}_R, \quad \boldsymbol{\psi}_R = L_M(\mathbf{i}_s + \mathbf{i}_R) \quad (2.2)$$

where

L_M, L_σ magnetizing and leakage inductance;
 $\mathbf{i}_R, \mathbf{i}_s$ rotor and stator current;
 $\boldsymbol{\psi}_R, \boldsymbol{\psi}_s$ rotor and stator flux (linkage).

When selecting the stator current and the rotor flux as complex-valued state variables, the two loops in Fig. 2.1 can be written as [102]

$$L_\sigma \frac{d\mathbf{i}_s}{dt} = \mathbf{v}_s - (R_s + j\omega_1 L_\sigma) \mathbf{i}_s - j\omega_1 \boldsymbol{\psi}_R - \frac{d\boldsymbol{\psi}_R}{dt} \quad (2.3)$$

$$\frac{d\boldsymbol{\psi}_R}{dt} = R_R \mathbf{i}_s - \left[\frac{R_R}{L_M} + j(\omega_1 - \omega_r) \right] \boldsymbol{\psi}_R \quad (2.4)$$

where

R_s, R_R stator and rotor resistance;
 ω_1 synchronous (excitation) frequency;
 ω_r electrical rotor speed;
 \mathbf{v}_s stator voltage.

The former equation, (2.3), is related to the stator circuit, while (2.4) concerns the rotor circuit.

Stator-Oriented and Synchronous Reference Frames

The above dynamic model of the induction machine can be given in any two-axis reference frame. Mainly two reference frames are of interest for our purposes, though, namely the *stator-oriented reference frame* and the *synchronous reference frame*.

From the perspective of the stator-oriented reference frame in the steady-state operation, the real and the imaginary parts of a space vector vary sinusoidally in the time domain. This is quite a natural property for an ac machine. However, sinusoidal quantities are not desirable in control applications. For instance, a proportional-plus-integral (PI) controller with a sinusoidal input will not achieve a steady-state control error of

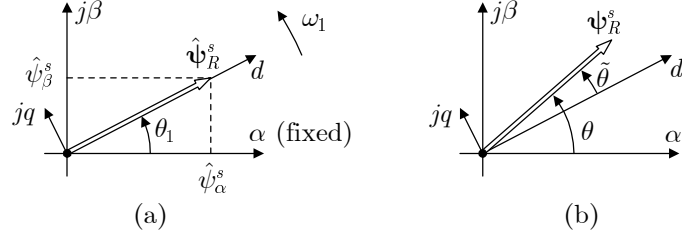


Fig. 2.2. The stator-oriented ($\alpha\beta$) and the synchronous (dq) reference frames. (a) Estimated rotor flux. (b) True rotor flux.

zero. Only step-formed set points, which are dc quantities in the steady-state operation, are adequate for a PI controller. It is, therefore, worthwhile to transform the dynamic model of the induction machine to a reference frame where all quantities become dc in the steady state. The synchronous reference frame is one such “dc” reference frame.

The transformation between the stator-oriented and the synchronous reference frames is known as the *Park transformation*:

$$\mathbf{y} = e^{-j\theta_1} \mathbf{y}^s, \quad \mathbf{y}^s = e^{j\theta_1} \mathbf{y}, \quad \theta_1 = \int \omega_1 dt \quad (2.5)$$

where θ_1 is the transformation angle, and \mathbf{y} is an arbitrary complex-valued variable. The transformation angle is given by the angle of the *estimated rotor flux*, $\hat{\Psi}_R^s = \hat{\psi}_R e^{j\theta_1}$. The estimated flux is, therefore, real-valued in the synchronous reference frame, while the true rotor flux, $\Psi_R^s = \psi_R e^{j\theta}$, is generally not real-valued in the synchronous coordinate system:

$$\Psi_R = \Psi_R^s e^{-j\theta_1} = \psi_R e^{j(\theta - \theta_1)} = \psi_d + j\psi_q. \quad (2.6)$$

For the special case of *perfect field orientation*, meaning $\theta = \theta_1$, the rotor flux is real-valued as well though. Fig. 2.2 depicts the stator-oriented and the synchronous reference frames, as well as the estimated and the true rotor flux.

In (2.3) and (2.4), the Park transformation has already been introduced, so these equations are already given in the synchronous reference frame. As seen, variables in the synchronous reference frame are in this thesis denoted without superscripts, e.g., Ψ_R , \mathbf{i}_s , and \mathbf{v}_s . For stator coordinates, on the other hand, we put $\omega_1 = 0$ in (2.3) and (2.4), and denote the variables with superscript “s.” The differential equations that describe the electrical dynamics of the induction machine then become

$$L_\sigma \frac{d\mathbf{i}_s^s}{dt} = \mathbf{v}_s^s - R_s \mathbf{i}_s^s - \frac{d\Psi_R^s}{dt} \quad (2.7)$$

$$\frac{d\Psi_R^s}{dt} = R_R \mathbf{i}_s^s - \left(\frac{R_R}{L_M} - j\omega_r \right) \Psi_R^s. \quad (2.8)$$

The synchronous frequency $\omega_1 = \dot{\theta}_1$ equals both the estimated rotor flux and the frequency of the applied stator voltage. The latter implies that the synchronous frequency is the *excitation frequency* of the machine, which equals the *stator frequency* in the steady-state operation. Being the excitation frequency, ω_1 can be considered as a control variable that is available for manipulation, as will be shown.

2.1.2 Flux EMF and Back EMF

The study of flux estimators that are based on the rotor-flux induced EMF is one important objective of this thesis. The induced EMF is often referred to as the *back EMF*, but the term *flux EMF* is preferred in this thesis. In order to properly define the flux EMF, and to distinguish it from the back EMF, the following definition is given [48]:

$$\underbrace{\frac{d\psi_R^s}{dt}}_{\text{flux EMF}} = R_R \dot{\mathbf{i}}_s^s + \underbrace{\left(j\omega_r - \frac{R_R}{L_M} \right)}_{\text{back EMF}} \psi_R^s \quad (2.9)$$

which results from (2.8). As seen, the flux EMF and the back EMF differ only by the term $R_R \dot{\mathbf{i}}_s^s$.

2.1.3 Parameter Variations

The model parameters of the equivalent circuit are usually not equal to the “true” parameters of the induction machine. In the following, we briefly discuss the parameter variations that may occur. Model parameters are, henceforth, denoted by a hat, e.g., \hat{L}_M , while “true” parameters are denoted without a hat, e.g., L_M .

The stator resistance varies mainly due to thermal drift; the resistance increases with increasing temperature. The temperature dependency of the stator resistance can be modeled as [77]

$$R_s = \frac{235 + T}{235 + T_0} R_{s0} \quad (2.10)$$

where T is a measure of the winding temperature, and R_{s0} is the stator resistance for a “cold” machine, at $T_0 = 20^\circ\text{C}$. The maximum winding temperature allowed is given by the classification in Table 2.1 [89]. A class H winding is considered for a numerical example, so $T_{\max} = 170^\circ\text{C}$. When the winding temperature rises from T_0 to T_{\max} , the relative increment in R_s becomes

$$\xi = \frac{R_s}{R_{s0}} = \frac{235 + 170}{235 + 20} \approx 1.6. \quad (2.11)$$

“Cold” and “hot” values for R_s may therefore differ by up to 60 %. The variation of the rotor resistance is similar to that of the stator resistance, although the variation for R_R is usually larger, due to the larger thermal resistance of the rotor [77].

The magnetization inductance L_M varies with the modulus of the rotor flux [33], due to magnetic saturation. An example of the variation of the magnetization inductance is shown in Fig. 2.3. The graph has been derived from no-load measurements on a 22-kW induction machine, see Appendix B for further details on this machine.

TABLE 2.1

MAXIMUM WINDING TEMPERATURE FOR MEDIUM POLYPHASE MOTORS				
Motor type (37 W–370 kW)	Class A	Class B	Class F	Class H
Totally enclosed, nonventilated	105°C	125°C	150°C	170°C

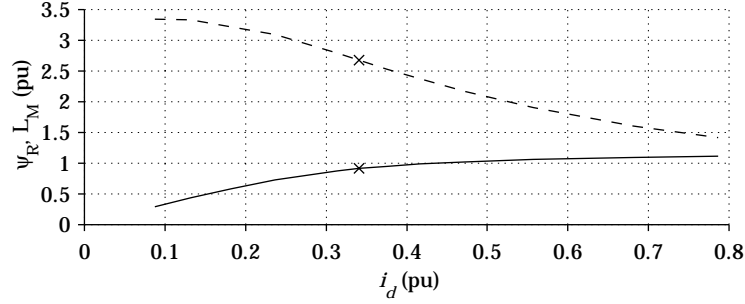


Fig. 2.3. No-load magnetization characteristic (solid) and corresponding L_M variation (dashed) for the 22-kW test machine. Nominal ψ_R and L_M are marked.

According to Fig. 2.3, L_M increases by 15 % when the magnetization current is reduced from its nominal value to half of its nominal value.

The leakage inductance L_σ depends mainly on the current modulus. The leakage inductance can be considered as fairly constant for machines with open rotor slots [33], because a large stator-current modulus (above the nominal value) is then required to magnetically saturate L_σ . The picture is quite different for machines with closed rotor slots, though, where larger variations in L_σ can be expected.

2.1.4 Mechanical Subsystem Model

Provided that the rotor shaft is stiff, the linearized mechanical dynamics of the induction machine are given by

$$\frac{J}{n_p} \frac{d\omega_r}{dt} = T_e - T_l - \frac{b}{n_p} \omega_r \quad (2.12)$$

where

- T_e, T_l electro-mechanical torque and load torque disturbance;
- n_p number of pole pairs;
- J, b moment of inertia and viscous friction constant.

Space vectors are rms-value scaled in this thesis, so the electro-mechanical torque equals [74]

$$T_e = 3n_p \operatorname{Im}\{\boldsymbol{\Psi}_R^* \mathbf{i}_s\} \quad (2.13)$$

which for the special case of perfect field orientation reduces to

$$T_e = 3n_p \operatorname{Im}\{(\psi_R - j0)(i_d + ji_q)\} = 3n_p \psi_R i_q. \quad (2.14)$$

2.2 Time-Scale Separation

For closed-loop current control in the synchronous reference frame [69], a current rise time of 1–5 ms is fully attainable [18]. This is normally much faster than the open-loop dynamics of the rotor flux, which are governed by the rotor time constant L_M/R_R . For a numerical example, parameters of three induction machines are listed in Table 2.2 [109].

TABLE 2.2
PER-UNIT PARAMETERS OF THREE INDUCTION MACHINES

Parameter	4-kW machine	22-kW machine	800-kW machine
R_R	0.040	0.034	0.010
R_s	0.040	0.023	0.010
L_σ	0.16	0.21	0.3
L_M	1.4	2.8	4.2
L_M/R_R	35	82	420
J	300	1000	1300
n_p	2	2	2

The rotor time constants of these machines correspond to rise times between 0.1 s and 1.3 s, which are roughly 20 to 1000 times slower than the closed-loop stator current dynamics. The current dynamics and the rotor flux dynamics are, hence, characterized by two totally different time scales, which is referred to as a *singularly perturbed* system [70]. Consequently, the dynamics of the rotor flux and the stator current can be treated separately for closed-loop current control [45, 58, 114].

Due to the time-scale separation, the stator current will in this thesis be considered as the input signal to the induction machine when studying the dynamics of the rotor flux. The stator voltage is then given by putting $d\mathbf{i}_s/dt = 0$ in (2.3), splitting the real and imaginary parts, and solving for v_d and v_q :

$$v_d = (R_s + R_R)i_d - \omega_1 L_\sigma i_q - \frac{R_R}{L_M}\psi_d - \omega_r \psi_q \quad (2.15)$$

$$v_q = (R_s + R_R)i_q + \omega_1 L_\sigma i_d - \frac{R_R}{L_M}\psi_q + \omega_r \psi_d. \quad (2.16)$$

The 22-kW machine in Table 2.2 will, henceforth, be referred to as the *test machine*, since it is used for theoretical and experimental verifications in this thesis. Appendix B contains a more detailed description of the test machine.

2.2.1 Component and Polar Representation of Flux Dynamics

One major objective of this thesis is to study the resulting dynamics from various flux estimators. For this purpose, the dynamics of the rotor flux in (2.4) will often be considered. Splitting the real and imaginary parts of this equation yields the component representation of the rotor flux dynamics as

$$\dot{\psi}_d = R_R i_d - \frac{R_R}{L_M}\psi_d + (\omega_1 - \omega_r)\psi_q \quad (2.17)$$

$$\dot{\psi}_q = R_R i_q - \frac{R_R}{L_M}\psi_q - (\omega_1 - \omega_r)\psi_d. \quad (2.18)$$

Occasionally, it is also useful to consider the rotor flux in polar form

$$\boldsymbol{\psi}_R = \psi_R e^{j\tilde{\theta}} \quad (2.19)$$

where ψ_R is the modulus of the rotor flux, and $\tilde{\theta}$ is the relative angle between the rotor-flux-oriented and synchronous reference frames:

$$\tilde{\theta} = \theta - \theta_1. \quad (2.20)$$

Substituting $\Psi_R = \psi_R e^{j\tilde{\theta}}$ in (2.4), and evaluating the time derivative of Ψ_R , provides the polar representation of the rotor flux dynamics

$$\begin{aligned} (\dot{\psi}_R + j\dot{\tilde{\theta}}\psi_R)e^{j\tilde{\theta}} &= R_R \mathbf{i}_s - \left[\frac{R_R}{L_M} + j(\omega_1 - \omega_r) \right] \psi_R e^{j\tilde{\theta}} \\ \Rightarrow \dot{\psi}_R + j\dot{\tilde{\theta}}\psi_R &= R_R \mathbf{i}_s e^{-j\tilde{\theta}} - \left[\frac{R_R}{L_M} + j(\omega_1 - \omega_r) \right] \psi_R \end{aligned} \quad (2.21)$$

which can be split into real and imaginary parts

$$\dot{\psi}_R = R_R(i_d \cos \tilde{\theta} + i_q \sin \tilde{\theta}) - \frac{R_R}{L_M} \psi_R \quad (2.22)$$

$$\dot{\tilde{\theta}} = \frac{R_R}{\psi_R} (i_q \cos \tilde{\theta} - i_d \sin \tilde{\theta}) + \omega_r - \omega_1. \quad (2.23)$$

In the following, $\tilde{\theta}$ is used as a measure for field-orientation accuracy, and will for this purpose be referred to as the *error angle* (in the steady-state operation). Observe that the special case $\tilde{\theta} = 0$ corresponds to perfect field orientation.

2.3 Flux Estimation

Vector control of electric machines is based on field orientation [15, 54], which requires that the position of the rotor flux is known. However, induction machines do not allow the rotor flux position to be easily measured, so *flux estimation* must normally be relied upon. Some fundamental principles of field orientation are described in this section, and two common flux estimators, namely the “*current model*” and the “*voltage model*,” are studied.

2.3.1 Direct and Indirect Field Orientation

There are two fundamental principles to implement a flux estimator, which are often referred to as *direct field orientation* (DFO) and *indirect field orientation* (IFO). DFO implies that the flux estimator is implemented in the stator-oriented reference frame, where the flux estimate becomes $\hat{\Psi}_R^s = \hat{\psi}_\alpha^s + j\hat{\psi}_\beta^s$. The transformation factors $e^{j\theta_1}$ and $e^{-j\theta_1}$ are then “directly” obtained from

$$e^{j\theta_1} = \frac{\hat{\Psi}_R^s}{\hat{\psi}_R} = \frac{\hat{\psi}_\alpha^s + j\hat{\psi}_\beta^s}{\sqrt{(\hat{\psi}_\alpha^s)^2 + (\hat{\psi}_\beta^s)^2}}, \quad e^{-j\theta_1} = \frac{(\hat{\Psi}_R^s)^*}{\hat{\psi}_R} = \frac{\hat{\psi}_\alpha^s - j\hat{\psi}_\beta^s}{\sqrt{(\hat{\psi}_\alpha^s)^2 + (\hat{\psi}_\beta^s)^2}}. \quad (2.24)$$

An IFO flux estimator, on the other hand, is implemented in the synchronous reference frame. A so-called *slip relation* provides ω_1 , which is integrated in order to obtain the transformation angle θ_1 :

$$\theta_1 = \int \omega_1 dt. \quad (2.25)$$

The transformation factors $e^{j\theta_1}$ and $e^{-j\theta_1}$ are then obtained “indirectly;”

$$e^{j\theta_1} = \cos \theta_1 + j \sin \theta_1, \quad e^{-j\theta_1} = \cos \theta_1 - j \sin \theta_1. \quad (2.26)$$

An important advantage for IFO is that one additional degree of freedom is present compared to DFO [47], since complex-valued notation is no longer used. As will be shown in the next chapter, the additional freedom for IFO manifests itself as an extra gain parameter, which allows for arbitrarily placement of the resulting closed-loop poles.

IFO requires the calculation of cosine and sine, while DFO demands for the computation of an inverse square root. This difference between IFO and DFO may be important when implementing the flux estimator in hardware, although modern digital signal processors and numerical algorithms tend to make this less important [49].

2.4 “Current Model”

The “current model” (CM) estimates the rotor flux by simulating the differential equation of the rotor flux that results from the rotor circuit. The DFO variant of the CM is derived by substituting the true parameters in (2.8) with their model correspondences:

$$\frac{d\hat{\Psi}_R^s}{dt} = \hat{R}_R \mathbf{i}_s^s - \left(\frac{\hat{R}_R}{\hat{L}_M} - j\omega_r \right) \hat{\Psi}_R^s. \quad (2.27)$$

The CM is the only flux estimator for which stability at low speeds has been proven [42, 115], at least for the realistic case of inaccurate model parameters. This makes the CM a safe choice for demanding low-speed applications.

Speed-sensorless operation can be troublesome when using the CM, since ω_r in (2.27) must then be replaced by a speed estimate $\hat{\omega}_r$. Speed estimation methods that rely on saliency [67] or rotor-slot harmonics [63] have the ability to provide a very accurate $\hat{\omega}_r$, which can be safely substituted in (2.27). However, the former method requires a special machine, while the latter method may fail for induction machines that have skewed rotors [38]. Therefore, speed estimation methods that rely upon the fundamental excitation (based on the flux EMF) often have to be used. Unfortunately, all flux-EMF-based methods share the property that the speed estimate indirectly becomes a function of the estimated flux [46]. Therefore, the flux-dependent speed estimate cannot be substituted in a speed-sensored estimator, such as the CM, without completely altering the system dynamics [46].

In addition to being less suitable for speed-sensorless operation, the CM has also a fairly high parameter sensitivity [75], as will be shown below. The parameter sensitivity results in inaccurate field orientation, which is not necessarily critical for stability [42, 115], but degrades the dynamic properties: a slow flux transient is initiated every time i_q changes. The flux transient affects the torque in particular [75, 79], but occasionally also the rotor speed [57]. Due to the parameter sensitivity, the CM should be used at low speeds only. A seamless transition from the CM to the less parameter sensitive “voltage model” is preferred at nominal speeds [60, 66], even when the rotor speed is measured.

2.4.1 Indirect Field Orientation

The IFO variant of the CM is derived by substituting the true parameters in (2.4) with their model correspondences:

$$\frac{d\hat{\psi}_R}{dt} = \hat{R}_R \mathbf{i}_s - \left[\frac{\hat{R}_R}{\hat{L}_M} + j(\omega_1 - \omega_r) \right] \hat{\psi}_R. \quad (2.28)$$

Observe that the estimated flux is now real-valued, since it is the angle of estimated rotor flux itself that defines the position of the synchronous reference frame. By splitting the imaginary and real parts of (2.28), the slip relation and the flux-modulus estimator of the CM are found to be [41]

$$\omega_1 = \omega_r + \frac{\hat{R}_R i_q}{\hat{\psi}_R} \quad (2.29)$$

$$\frac{d\hat{\psi}_R}{dt} = \hat{R}_R i_d - \frac{\hat{R}_R}{\hat{L}_M} \hat{\psi}_R. \quad (2.30)$$

The dynamic flux estimate is superfluous [99], provided that the setpoint for i_d is selected via the relation $i_d = \psi_{\text{ref}}/\hat{L}_M$, and ψ_{ref} is constant. Then, $\hat{\psi}_R$ converges to ψ_{ref} with the time constant \hat{L}_M/\hat{R}_R , which implies that the static estimate $\hat{\psi}_R = \psi_{\text{ref}}$ can just as well be substituted in (2.29) directly:

$$\omega_1 = \omega_r + \frac{\hat{R}_R i_q}{\psi_{\text{ref}}} \quad (2.31)$$

and (2.30) can be dropped. The selection of ω_1 in (2.31) is referred to as the *standard slip relation*, or the slip relation of the CM. A vector control scheme that uses the standard slip relation is shown in Fig 2.4.

2.4.2 Parameter Sensitivity

This section describes how the error angle of the CM is affected when the true parameters R_R and L_M are inaccurately modeled by \hat{R}_R and \hat{L}_M , respectively. Fairly accurate model parameters are considered, meaning that $\tilde{\theta}$ is small, so $\sin \tilde{\theta} \approx \tilde{\theta}$ and $\cos \tilde{\theta} \approx 1$ can be assumed in the analysis.

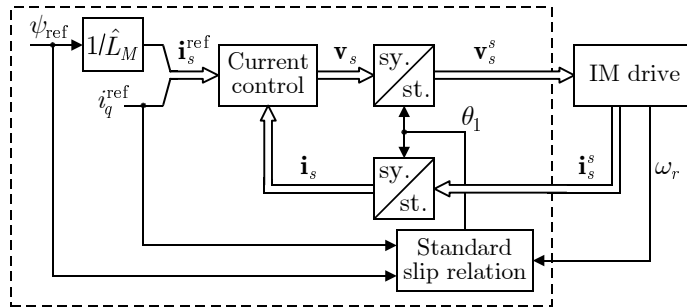


Fig. 2.4. IFO vector control system that uses the standard slip relation.

The closed-loop dynamics resulting from the CM are found by repeating (2.22) and by substituting the standard slip relation in (2.23):

$$\dot{\psi}_R = R_R(i_d + i_q\tilde{\theta}) - \frac{R_R}{L_M}\psi_R \quad (2.32)$$

$$\dot{\tilde{\theta}} = \dot{\theta} - \omega_1 = \frac{R_R}{\psi_R}(i_q - i_d\tilde{\theta}) - \frac{\hat{R}_R i_q}{\psi_{\text{ref}}}. \quad (2.33)$$

Putting $\dot{\psi}_R = 0$ in the above equation, and solving for ψ_R , gives the following steady-state relation between ψ_R and $\tilde{\theta}$:

$$\psi_R = L_M \left(\frac{\psi_{\text{ref}}}{\hat{L}_M} + i_q\tilde{\theta} \right). \quad (2.34)$$

The convergence point for $\tilde{\theta}$ can now be derived by substituting (2.34) in (2.33), putting $\dot{\tilde{\theta}} = 0$, and solving for $\tilde{\theta}$:

$$\begin{aligned} \tilde{\theta}^* &= \frac{(\hat{L}_M R_R - L_M \hat{R}_R) i_q \psi_{\text{ref}}}{R_R \psi_{\text{ref}}^2 + L_M \hat{L}_M \hat{R}_R i_q^2} \approx \frac{(\hat{L}_M R_R - L_M \hat{R}_R) i_q \psi_{\text{ref}}}{R_R (\psi_{\text{ref}}^2 + L_M^2 i_q^2)} \\ &= \left(\frac{\tilde{R}_R}{R_R} - \frac{\tilde{L}_M}{L_M} \right) \frac{L_M \hat{L}_M i_d i_q}{(\hat{L}_M i_d)^2 + (L_M i_q)^2} \approx \left(\frac{\tilde{R}_R}{R_R} - \frac{\tilde{L}_M}{L_M} \right) \frac{i_d i_q}{i_d^2 + i_q^2} \end{aligned} \quad (2.35)$$

where

$$\tilde{R}_R = R_R - \hat{R}_R, \quad \tilde{L}_M = L_M - \hat{L}_M \quad (2.36)$$

are the errors in the model parameters. Based on (2.35), the following conclusions can be drawn:

- Perfect field orientation, $\tilde{\theta} = 0$, results for accurate model parameters ($\tilde{R}_R = \tilde{L}_M = 0$), at no load ($i_q = 0$), or when the model errors cancel ($\tilde{R}_R/R_R = \tilde{L}_M/L_M$). Otherwise, the field orientation is imperfect.
- The relative errors in the model parameters have similar impact on the error angle, but the largest parameter error can be expected for the rotor resistance.
- The maximum error angle, obtained for $i_q = \pm i_d$, becomes

$$\tilde{\theta}_{\text{max}} = \frac{1}{2} \left(\frac{\tilde{R}_R}{R_R} - \frac{\tilde{L}_M}{L_M} \right) \text{sign}(i_q). \quad (2.37)$$

The values $\hat{L}_M = L_M$, $\hat{R}_R = 0.7R_R$ and $i_q > 0$ are considered for a numerical example, which yields the maximum error angle $\tilde{\theta}_{\text{max}} = 0.35 \text{ rad} = 20^\circ$. This is a fairly large error angle, which makes exact torque control impossible.

2.5 Inherently Sensorless Flux Estimation

As discussed in Section 2.4, a flux-EMF-based speed estimate unavoidably becomes a function of the true rotor flux. In order to avoid that the speed estimate alters the closed-loop dynamics, the preferred alternative for speed-sensorless operation is to use a flux

estimator that does not require knowledge of ω_r . Such a flux estimator will, henceforth, be referred to as *inherently sensorless*, and we shall only consider this type of speed-sensorless flux estimation in this thesis. This section investigates the fundamentals of inherently sensorless flux estimation. It is assumed that the stator voltage and the stator current are accurately measured.

An inherently sensorless flux estimator must rely upon the information that is available in the stator circuit loop, in order to estimate the flux angle. By considering (2.7):

$$\mathbf{v}_s^s = R_s \mathbf{i}_s^s + L_\sigma \frac{d\mathbf{i}_s^s}{dt} + \frac{d\boldsymbol{\psi}_R^s}{dt} \quad (2.38)$$

it becomes clear that this equation does not require knowledge of ω_r . Specifically, it is only the flux EMF

$$\mathbf{E}_f^s = \frac{d\boldsymbol{\psi}_R^s}{dt} = \mathbf{v}_s^s - R_s \mathbf{i}_s^s - L_\sigma \frac{d\mathbf{i}_s^s}{dt} \quad (2.39)$$

in (2.38) that contains information regarding the flux angle. Now, let us study how this information is given. For this purpose, the polar representation of the rotor flux is substituted in (2.39):

$$\mathbf{E}_f^s = \frac{d(\psi_R e^{j\theta})}{dt} = (\dot{\psi}_R + j\dot{\theta}\psi_R)e^{j\theta} \quad (2.40)$$

where ψ_R and θ are the true flux modulus and the true flux angle, respectively. With $\mathbf{E}_f^s = \mathbf{E}_f e^{j\theta_1}$, $\mathbf{v}_s^s = \mathbf{v}_s e^{j\theta_1}$ and $\mathbf{i}_s^s = \mathbf{i}_s e^{j\theta_1}$, the flux EMF in the synchronous reference frame becomes

$$\begin{aligned} \mathbf{E}_f e^{j\theta_1} &= (\dot{\psi}_R + j\dot{\theta}\psi_R)e^{j\theta} = \mathbf{v}_s e^{j\theta_1} - R_s \mathbf{i}_s e^{j\theta_1} - L_\sigma \frac{d(\mathbf{i}_s e^{j\theta_1})}{dt} \\ \Rightarrow \mathbf{E}_f &= (\dot{\psi}_R + j\dot{\theta}\psi_R)e^{j\tilde{\theta}} = \mathbf{v}_s - R_s \mathbf{i}_s - j\omega_1 L_\sigma \mathbf{i}_s. \end{aligned} \quad (2.41)$$

The above equation represents the “true” flux EMF in the synchronous reference frame, but a flux estimator must, of course, rely on the estimated flux EMF. This estimate is derived by substituting the true parameters in (2.41) with their model correspondences:

$$\hat{\mathbf{E}}_f = \mathbf{v}_s - \hat{R}_s \mathbf{i}_s - j\omega_1 \hat{L}_\sigma \mathbf{i}_s. \quad (2.42)$$

Provided accurate model parameters, $\hat{R}_s = R_s$ and $\hat{L}_\sigma = L_\sigma$, the estimated flux EMF actually equals the true flux EMF:

$$\hat{\mathbf{E}}_f = \mathbf{E}_f = (\dot{\psi}_R + j\dot{\theta}\psi_R)e^{j\tilde{\theta}} \quad (2.43)$$

which is called the *fundamental relation for sensorless flux estimation* [50], since any inherently sensorless flux estimator must rely on it. Several interesting conclusions can be directly drawn from (2.43):

- In order to maintain accurate field orientation, $\tilde{\theta} = 0$, a flux estimator must be able to extract the information that is related to $\tilde{\theta}$ from the flux EMF. However, this information is given as a nonlinear combination of ψ_R , $\dot{\psi}_R$, $\dot{\theta}$, and $\tilde{\theta}$, so a change in $\tilde{\theta}$ cannot for sure be separated from a change in ψ_R , for instance. This is an indication of speed-sensorless operation being non-trivial, even for the ideal case of accurate model parameters.

- The estimated flux EMF is a function of the true rotor flux, so the flux estimate of an inherently sensorless estimator must become a function of the true flux as well. A nonlinear feedback of the true rotor flux is, therefore, introduced in the closed-loop dynamics, which will now be demonstrated. Consider the angle of the synchronous reference frame $\theta_1(\boldsymbol{\Psi}_R^s)$, which becomes a function of the true rotor flux via a slip relation, $d\theta_1/dt = \omega_1(\boldsymbol{\Psi}_R^s)$. The angle is used in the Park transformation, giving $\mathbf{i}_s^s = e^{j\theta_1(\boldsymbol{\Psi}_R^s)}\mathbf{i}_s$. By substituting this relation in (2.8), the rotor flux dynamics are found to be

$$\frac{d\boldsymbol{\Psi}_R^s}{dt} = R_R e^{j\theta_1(\boldsymbol{\Psi}_R^s)}\mathbf{i}_s - \left(\frac{R_R}{L_M} - j\omega_r \right) \boldsymbol{\Psi}_R^s \quad (2.44)$$

which is nonlinear with respect to $\boldsymbol{\Psi}_R$. Due to the nonlinear feedback, the resulting closed-loop dynamics are heavily dependent on how $\theta_1(\boldsymbol{\Psi}_R^s)$ is derived [47]. An inherently sensorless flux estimator must, thus, be carefully chosen, since a small change in the estimator design may have a large influence on the resulting dynamics.

For an IFO-type estimator, one may just as well argue that the nonlinear feedback of the rotor flux is introduced by $\omega_1(\boldsymbol{\Psi}_R)$. This can be deduced from (2.4):

$$\frac{d\boldsymbol{\Psi}_R}{dt} = R_R \mathbf{i}_s - \left(\frac{R_R}{L_M} + j[\omega_1(\boldsymbol{\Psi}_R) - \omega_r] \right) \boldsymbol{\Psi}_R. \quad (2.45)$$

One additional conclusion can be drawn from (2.45), namely that the nonlinear feedback is present for all excitation frequencies except zero.

- Observe the difference between an inherently sensorless flux estimator and the CM: the resulting dynamics from the CM are linear, since the standard slip relation, $\omega_1 = \omega_r + \hat{R}_R i_q / \psi_{\text{ref}}$, does not introduce feedback of the true rotor flux.
- An inherently sensorless estimator is, by necessity, only sensitive to the model parameters \hat{R}_s and \hat{L}_σ , as seen from (2.42).
- The model parameter \hat{L}_M is also sensitive for some inherently sensorless estimators [93]. This cannot be observed from (2.42), but will be discussed in a following section.
- With respect to the accuracy of the field orientation and stability, it is well known that \hat{R}_R is *never* a sensitive parameter for an inherently sensorless flux estimator [100]. This can be deduced from the equivalent circuit in Fig. 2.1: neither knowledge of ω_r nor R_R is required for an inherently sensorless flux estimator.

The real and imaginary parts of (2.43) are now split:

$$\hat{E}_d = E_d = -\dot{\theta}\psi_R \sin \tilde{\theta} + \dot{\psi}_R \cos \tilde{\theta} \quad (2.46)$$

$$\hat{E}_q = E_q = \dot{\theta}\psi_R \cos \tilde{\theta} + \dot{\psi}_R \sin \tilde{\theta} \quad (2.47)$$

which allow to draw the following additional conclusions on inherently sensorless flux estimation, at nominal speeds and at low frequencies:

- **Nominal speeds.** It can be assumed that $\dot{\theta} \approx \omega_1$ dominates the flux EMF at nominal speeds, so the influence from $\dot{\psi}_R$ in (2.46)–(2.47) is then negligible. This gives

$$\hat{E}_d \approx -\omega_1 \psi_R \sin \tilde{\theta} \approx -\omega_1 \psi_R \tilde{\theta} \quad (2.48)$$

for small $\tilde{\theta}$. A deviation from correct field orientation, $\tilde{\theta} = 0$, is thus immediately seen in \hat{E}_d . For similar reasons, $\hat{E}_q \approx \omega_1 \psi_R \cos \tilde{\theta} \approx \omega_1 \psi_R$ at nominal speeds, so \hat{E}_q provides information about the flux modulus.

It follows that speed-sensorless at nominal speeds should not produce any significant difficulty, since the information regarding $\tilde{\theta}$ is easily seen in \hat{E}_d .

- **Low frequencies.** The influence from $\dot{\psi}_R$ cannot be neglected at low frequencies. A change in ψ_R , giving $\dot{\psi}_R \neq 0$, may then be misinterpreted by the flux estimator as a change in $\tilde{\theta}$. Consider $\dot{\theta} = 0$ in (2.46), then

$$\hat{E}_d = \dot{\psi}_R \cos \tilde{\theta} \approx \dot{\psi}_R \quad (2.49)$$

for small $\tilde{\theta}$, so a deviation from $\tilde{\theta} = 0$ cannot be seen in \hat{E}_d , or at least not be separated from $\dot{\psi}_R$. For similar reasons, $\hat{E}_q = \dot{\psi}_R \sin \tilde{\theta} \approx \dot{\psi}_R \tilde{\theta}$, so neither \hat{E}_q provides useful information regarding $\tilde{\theta}$: a change in $\tilde{\theta}$ cannot be separated from a change in $\dot{\psi}_R$.

It follows that speed-sensorless operation at low frequencies is, most likely, notoriously difficult, and stable operation for $\omega_1 \approx \dot{\theta} = 0$ is even impossible, which can be deduced from (2.46)–(2.47).

As here discussed, instability phenomena for speed-sensorless operation at low frequencies have indeed been reported [32, 46, 94, 100].

2.5.1 Speed Estimation

An inherently sensorless flux estimator does not require knowledge of ω_r , so the choice of speed estimator is not critical for the system stability. A simple and elegant solution for estimating the rotor speed was presented in [116]; the standard slip relation can be used backwards:

$$\hat{\omega}_r = \omega_1 - \frac{\hat{R}_R i_q}{\hat{\psi}_R}. \quad (2.50)$$

The speed estimate is sensitive to \hat{R}_R , but this is unavoidable, since a flux-EMF-based speed estimate cannot be separated from an error in \hat{R}_R [100].

For IFO, ω_1 is an explicit control variable that is readily available for the above speed estimator. For DFO, however, ω_1 needs to be calculated separately. The following relation can be used for this purpose [116]:

$$\omega_1 = \frac{d\theta_1}{dt} = \frac{d}{dt} \left[\text{atan} \left(\frac{\hat{\psi}_\beta}{\hat{\psi}_\alpha} \right) \right] = \frac{\hat{E}_\beta \hat{\psi}_\alpha - \hat{E}_\alpha \hat{\psi}_\beta}{(\hat{\psi}_\alpha)^2 + (\hat{\psi}_\beta)^2}. \quad (2.51)$$

With fast and accurate stator current control, i_q in (2.50) can be substituted with i_q^{ref} in order to reduce the sensitivity to noise. For speed control, the speed estimator must

then be embedded in a low-pass filter [47]:

$$\frac{d\hat{\omega}_r}{dt} = \alpha_f \left(\omega_1 - \frac{\hat{R}_R i_q^{\text{ref}}}{\hat{\psi}_R} - \hat{\omega}_r \right) \quad (2.52)$$

in order to avoid the algebraic loop that would otherwise be created, due to that i_q^{ref} is the output of the speed controller, while $\hat{\omega}_r$ is the input. The above filter gain α_f should be chosen at least a decade larger than the bandwidth of the speed control loop, in order to avoid that $\hat{\omega}_r$ lags ω_r .

2.6 “Voltage Model”

The open-loop simulation of (2.7):

$$\frac{d\hat{\Psi}_R^s}{dt} = \hat{\mathbf{E}}_f^s \quad (2.53)$$

is known as the “*voltage model*” (VM). The VM is the traditional inherently sensorless flux estimator but it has, unfortunately, little practical use in the form of (2.53). The limited usefulness is due to the fact that the resulting closed-loop dynamics have poles on the imaginary axis [47], and the VM is also known to cause problems with integrator drift [22].

In spite of the mentioned problems, the VM is known to provide a very accurate flux estimate at nominal speeds, but good low-speed operation can only be accomplished through good knowledge of the stator resistance [116].

By substituting $\hat{\Psi}_R^s = \hat{\psi}_R e^{j\theta_1}$ and $\mathbf{E}_f^s = \mathbf{E}_f e^{j\theta_1}$ in (2.53), the equivalent IFO representation of the VM becomes

$$\begin{aligned} \hat{\mathbf{E}}_f e^{j\theta_1} &= \frac{d\hat{\psi}_R}{dt} e^{j\theta_1} + j\dot{\theta}_1 \hat{\psi}_R e^{j\theta_1} \\ \Rightarrow \frac{d\hat{\psi}_R}{dt} &= \hat{\mathbf{E}}_f - j\omega_1 \hat{\psi}_R. \end{aligned} \quad (2.54)$$

After splitting the real and imaginary parts of (2.54), and solving the imaginary part for ω_1 , the flux-modulus estimator and the slip relation for the VM are found to be

$$\frac{d\hat{\psi}_R}{dt} = \hat{E}_d \quad (2.55)$$

$$\omega_1 = \frac{\hat{E}_q}{\hat{\psi}_R}. \quad (2.56)$$

An IFO vector control system that uses the VM is shown in Fig. 2.5.

Recall that the static flux estimate $\hat{\psi}_R = \psi_{\text{ref}}$ sufficed when using the CM. This is not applicable for the VM, though: stability is lost when ω_r and i_q have different signs [47] (and $|\omega_r| > R_R |i_q| / \psi_{\text{ref}}$). A dynamic flux estimate is therefore useful for the VM, at least marginal stability is then obtained [47].

Several VM variants have been proposed in order to circumvent the above discussed problems of the traditional VM. The following sections present an overview of some VM variants, and one of these estimators will be selected for further studies.

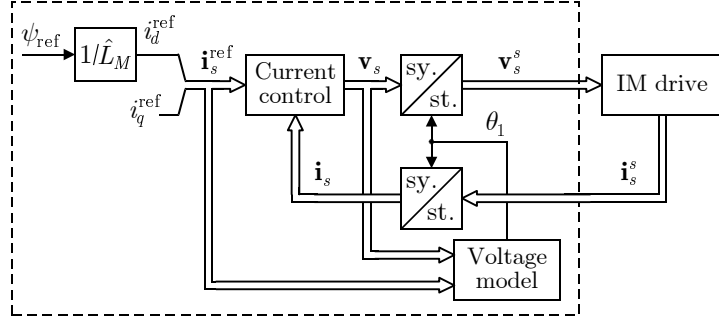


Fig. 2.5. IFO vector control system that uses the VM.

2.6.1 Lowpass Integrator

The damping of the VM can be slightly improved by transforming the direct integration in (2.53) to the following lowpass integrator

$$\hat{\Psi}_R^s = \frac{\hat{\mathbf{E}}_f^s}{p + \alpha_v} \quad (2.57)$$

where $p = d/dt$. The filter bandwidth α_v should increase with increasing stator frequency, in order to obtain a reasonable trade-off between sufficient damping and field orientation accuracy [22]. Henceforth, we select $\alpha_v = \lambda|\omega_1|$, where λ is a gain parameter that is greater than zero.

Unfortunately, the lowpass integrator does not allow for the combination of a well-damped system and accurate field orientation [47, 99]. Consider (2.39) with accurate model parameters in the steady-state operation, then $\hat{\mathbf{E}}_f^s = j\omega_1\boldsymbol{\Psi}_R^s$. Substituting this in (2.57) gives

$$\hat{\Psi}_R^s = \frac{j\omega_1}{j\omega_1 + \lambda|\omega_1|}\boldsymbol{\Psi}_R^s = \frac{1}{1 - j\lambda \text{sign}(\omega_1)}\boldsymbol{\Psi}_R^s \quad (2.58)$$

for which the error angle becomes

$$\tilde{\theta} = \arg\left(\frac{\hat{\Psi}_R^s}{\boldsymbol{\Psi}_R^s}\right) = -\arctan(\lambda) \text{sign}(\omega_1). \quad (2.59)$$

A small λ must clearly be chosen in order to obtain a small error angle. For a numerical example, the selections $\lambda = 0.1$ and $\lambda = 0.2$ yield $\tilde{\theta} = \pm 5.7^\circ$ and $\tilde{\theta} = \pm 11.3^\circ$, respectively, which are fairly small error angles. However, a closed-loop analysis, not to be included here, would reveal that the system becomes poorly damped when selecting such a small λ . The lowpass integrator offers, therefore, only a modest improvement compared to the voltage model.

2.6.2 Modified Voltage Models

Reference [93] presented a modified VM, in which feedback of the quantity $\psi_{ref}e^{j\theta_1} - \hat{\Psi}_R^s$ was introduced in the flux estimator. Although good results were shown, a drawback of this estimator is that sensitivity to \hat{L}_M is introduced, via the selection of $i_d = \psi_{ref}/\hat{L}_M$.

The sensitivity to \widehat{L}_M can be avoided by using other modified schemes, since \widehat{R}_s and \widehat{L}_σ are the only, by necessity, sensitive model parameters for an inherently sensorless flux estimator.

Reference [61] presented three modified variants of the VM. The most interesting modified scheme was referred to as Algorithm 3, which introduced an additional state variable. This estimator is only sensitive to the model parameters \widehat{R}_s and \widehat{L}_σ , but the additional state variable complicates the analysis and the implementation of this estimator.

Reference [101], similar variants have also appeared in [56, 64], presented a compensation method for the lowpass integrator in (2.57):

$$\widehat{\Psi}_R^s = \frac{j\omega_1 + \lambda|\omega_1|}{j\omega_1} \frac{\widehat{\mathbf{E}}_f^s}{p + \lambda|\omega_1|}. \quad (2.60)$$

We shall, henceforth, refer to this flux estimator as the *statically compensated voltage model* (SCVM). The ingenious property of the SCVM is that the “correct” flux estimate of the VM is restored in the steady-state operation. The restoration to the VM can be deduced by substituting $p \rightarrow j\omega_1$ in (2.60), which recovers the open-loop integrator $\widehat{\Psi}_R^s = \widehat{\mathbf{E}}_f^s / j\omega_1$.

2.6.3 Discussion

It appears that the SCVM is the most promising alternative, of the ones here discussed, for inherently sensorless flux estimation. Although the VM variants in [61] and [93] are viable flux estimators, they have drawbacks that can be avoided. The SCVM is, therefore, selected for further analysis and development, which will be the topic of the following chapter.

Chapter 3

Analysis and Development of the SCVM

The previous results of [56, 64, 101] for the SCVM will be extended in this chapter, by analyzing and developing the flux estimator.

The IFO implementation of the SCVM that results directly from DFO will in this chapter be modified, by introducing a new gain parameter. This new parameter enables arbitrarily pole placement for the SCVM, which is impossible for the previously presented SCVM. A thorough stability analysis follows, which provides several enlightening observations and design guidelines for the SCVM. It is shown that the dynamics resulting from the SCVM are asymptotically stable for small machines. For large machines, however, stability at low speeds can only be ensured for lighter loads. Recommendable gain parameters for nominal and low speeds are given.

The parameter sensitivity for the SCVM is analyzed. The existence of a singularity for zero stator frequency is demonstrated, which makes operation at very low frequencies difficult for the SCVM. Recommendations for proper selection of the model parameters are given.

The chapter concludes with a discussion on various implementation issues for the SCVM and experimental evaluation.

3.1 Indirect Field Orientation

The equivalent IFO implementation of the SCVM is derived by substituting $p \rightarrow p + j\omega_1$ in (2.60), removing superscripts “ s ,” and taking $\hat{\psi}_R$ real-valued:

$$\hat{\psi}_R = \frac{j\omega_1 + \lambda|\omega_1|}{j\omega_1} \frac{1}{p + j\omega_1 + \lambda|\omega_1|} \hat{\mathbf{E}}_f = \frac{1 - j\lambda \operatorname{sign}(\omega_1)}{p + j\omega_1 + \lambda|\omega_1|} \hat{\mathbf{E}}_f. \quad (3.1)$$

By splitting (3.1) into real and imaginary parts, and solving for ω_1 in the imaginary part, the slip relation and the flux-modulus estimator are found to be

$$\hat{\psi}_R = \frac{\hat{E}_d + \lambda \operatorname{sign}(\omega_1) \hat{E}_q}{p + \lambda|\omega_1|} \quad (3.2)$$

$$\omega_1 = \frac{\hat{E}_q - \lambda \operatorname{sign}(\omega_1) \hat{E}_d}{\hat{\psi}_R}. \quad (3.3)$$

Eqs. (3.2)–(3.3) are obtained directly from DFO. In the present form, the estimator has therefore one degree of freedom [47], since only the gain parameter λ is available for pole placement. A new coefficient μ is hereby introduced:

$$\hat{\psi}_R = \frac{\mu \hat{E}_d + \lambda \operatorname{sign}(\omega_1) \hat{E}_q}{p + \lambda |\omega_1|} \quad (3.4)$$

$$\omega_1 = \frac{\hat{E}_q - \lambda \operatorname{sign}(\omega_1) \hat{E}_d}{\hat{\psi}_R} \quad (3.5)$$

in order to take advantage of the additional degree of freedom that is present for IFO. We thus had $\mu = 1$ in (3.2). The below presented stability analysis will show that μ enables arbitrarily pole placement for the closed-loop system, which is not possible otherwise. Meanwhile, μ does not affect the accuracy of the field orientation in the steady-state operation.

Let us study the estimated flux modulus in (3.4). Solving this equation for $d\hat{\psi}_R/dt$ yields

$$\frac{d\hat{\psi}_R}{dt} = \mu \hat{E}_d + \lambda \operatorname{sign}(\omega_1) \hat{E}_q - \underbrace{\lambda \operatorname{sign}(\omega_1) \omega_1}_{|\omega_1|} \hat{\psi}_R. \quad (3.6)$$

When substituting (3.5) in this relation, the flux-modulus estimator reduces to

$$\frac{d\hat{\psi}_R}{dt} = \mu \hat{E}_d + \lambda \operatorname{sign}(\omega_1) \hat{E}_q - \lambda \operatorname{sign}(\omega_1) \frac{\hat{E}_q - \lambda \operatorname{sign}(\omega_1) \hat{E}_d}{\hat{\psi}_R} \hat{\psi}_R = (\mu + \lambda^2) \hat{E}_d \quad (3.7)$$

which reveals that $\hat{\psi}_R$ does not depend on \hat{E}_q . An equivalent but slightly simpler variant of the SCVM can therefore be used:

$$\frac{d\hat{\psi}_R}{dt} = \gamma \hat{E}_d \quad (3.8)$$

$$\omega_1 = \frac{\hat{E}_q - \lambda \operatorname{sign}(\omega_1) \hat{E}_d}{\hat{\psi}_R} \quad (3.9)$$

where $\gamma = \mu + \lambda^2$. These equations represent the flux estimator that will, henceforth, be referred to as the SCVM, while the previous variant of the SCVM, resulting from DFO ($\mu=1$), will be referred to as the original SCVM.

Observe that the conventional VM or the original SCVM can easily be recovered from (3.8)–(3.9): $[\lambda, \gamma] = [0, 1]$ and $\gamma = 1 + \lambda^2$ yield the VM and the SCVM variant that results from DFO, respectively.

3.1.1 Slip Relation in Disguise

For analysis purposes, the flux EMF can be expressed in terms of the rotor circuit loop in (2.8):

$$\mathbf{E}_f^s = \frac{d\boldsymbol{\Psi}_R^s}{dt} = R_R \mathbf{i}_s^s - \left(\frac{R_R}{L_M} - j\omega_r \right) \boldsymbol{\Psi}_R^s. \quad (3.10)$$

By substituting $d/dt \rightarrow d/dt + j\omega_1$, and removing superscript “s,” the corresponding expression in the synchronous reference frame becomes

$$\mathbf{E}_f = \frac{d\boldsymbol{\Psi}_R}{dt} + j\omega_1\boldsymbol{\Psi}_R = R_R\mathbf{i}_s - \left(\frac{R_R}{L_M} - j\omega_r \right) \boldsymbol{\Psi}_R \quad (3.11)$$

which has the following real and imaginary parts

$$E_d = \frac{R_R}{L_M}(L_M i_d - \psi_d) - \omega_r \psi_q \quad (3.12)$$

$$E_q = R_R i_q + \omega_r \psi_d - \frac{R_R}{L_M} \psi_q. \quad (3.13)$$

Accurate model parameters are now assumed, meaning that $\hat{\mathbf{E}}_f = \mathbf{E}_f$ and $i_d = \psi_{\text{ref}}/L_M$. By substituting the above expressions for E_d and E_q in (3.9), the relation between the excitation frequency and the true flux components is then found to be

$$\omega_1 = \frac{\omega_r \psi_d + R_R i_q - \frac{R_R}{L_M} \psi_q - \lambda \text{sign}(\omega_1) \left(\frac{R_R}{L_M} (\psi_{\text{ref}} - \psi_d) - \omega_r \psi_q \right)}{\hat{\psi}_R}. \quad (3.14)$$

Provided that the resulting dynamics from the SCVM are stable, ψ_d and $\hat{\psi}_R$ both converge to ψ_{ref} and ψ_q converges to zero. Eq. (3.14) then simplifies to $\omega_1 = \omega_r + R_R i_q / \psi_R$. Even though (3.14) appears complicated at a first glance, it is, hence, simply the standard slip relation in disguise. This is not very surprising: $\omega_1 = \omega_r + R_R i_q / \psi_R$ must hold for any flux estimator during perfect field orientation, which can be deduced from (2.18).

3.2 Stability Analysis

The following stability analysis considers the dynamics that result when substituting the slip relation of the SCVM in (2.4):

$$\frac{d\boldsymbol{\Psi}_R}{dt} = R_R\mathbf{i}_s - \left(\frac{R_R}{L_M} + j[\omega_1(\boldsymbol{\Psi}_R, \hat{\psi}_R) - \omega_r] \right) \boldsymbol{\Psi}_R. \quad (3.15)$$

Together with the flux-modulus estimator in (3.8), these differential equations form the closed-loop system model of the SCVM.

It is necessary to introduce some simplifications before initiating the stability analysis. As discussed in Section 2.2, the stator current dynamics are disregarded, and the rotor speed is assumed to be slowly varying for simplicity reasons. Therefore, ω_r , $i_d = i_d^{\text{ref}}$, and $i_q = i_q^{\text{ref}}$ will be treated as quasi-static parameters in the following analysis. The model parameters are all assumed to be accurate, since the stability analysis becomes far too complex to be tractable otherwise. The case of inaccurate model parameters will eventually be treated separately, by studying the resulting error angle in the steady-state operation.

Due to the assumptions, the below analysis is valid for a somewhat idealized case, but several enlightening conclusions can still be drawn, as will be seen.

3.2.1 Nonlinear Dynamics Resulting from the SCVM

Provided the above assumptions, the dynamics resulting from the SCVM are governed by the following equations:

$$\frac{d\psi_d}{dt} = R_R i_d - \frac{R_R}{L_M} \psi_d + (\omega_1 - \omega_r) \psi_q \quad (3.16)$$

$$\frac{d\psi_q}{dt} = R_R i_q - \frac{R_R}{L_M} \psi_q - (\omega_1 - \omega_r) \psi_d \quad (3.17)$$

$$\frac{d\hat{\psi}_R}{dt} = \gamma E_d = \gamma \left(R_R i_d - \frac{R_R}{L_M} \psi_d - \omega_r \psi_q \right) \quad (3.18)$$

where $i_d = \psi_{\text{ref}}/L_M$, and ω_1 is given by (3.14). Eqs. (3.16)–(3.18) represent a third-order nonlinear system. The nonlinearity is introduced by the synchronous frequency ω_1 , which is a function of the real-valued state variables ψ_d , ψ_q and $\hat{\psi}_R$.

3.2.2 Equilibrium Points

By putting $\dot{\psi}_d = \dot{\psi}_q = \dot{\hat{\psi}}_R = 0$, and solving (3.16)–(3.18) for ψ_d , ψ_q and $\hat{\psi}_R$, the following two equilibrium points are found:

$$\begin{bmatrix} \psi_{d,1}^* \\ \psi_{q,1}^* \\ \hat{\psi}_{R,1}^* \end{bmatrix} = \begin{bmatrix} \psi_{\text{ref}} \\ 0 \\ \psi_{\text{ref}} \end{bmatrix} \quad (3.19)$$

$$\begin{bmatrix} \psi_{d,2}^* \\ \psi_{q,2}^* \\ \hat{\psi}_{R,2}^* \end{bmatrix} = \begin{bmatrix} \frac{R_R(R_R\psi_{\text{ref}} - \omega_r L_M^2 i_q)}{(\omega_r L_M)^2 + R_R^2} \\ \frac{R_R L_M (\omega_r \psi_{\text{ref}} + R_R i_q)}{(\omega_r L_M)^2 + R_R^2} \\ \frac{R_R^2 [\psi_{\text{ref}}^2 + (L_M i_q)^2]}{\psi_{\text{ref}} [(\omega_r L_M)^2 + R_R^2]} \end{bmatrix}. \quad (3.20)$$

These convergence points are henceforth labeled EP1 and EP2, respectively. The field orientation at EP1 is perfect, while the error angle at EP2 is

$$\tan \tilde{\theta} = \frac{\psi_{q,2}^*}{\psi_{d,2}^*} = \frac{R_R (\omega_r \psi_{\text{ref}} + R_R i_q)}{-\omega_r R_R L_M i_q + R_R^2 i_d}. \quad (3.21)$$

EP1 is hence the desirable convergence point, and should ideally be stable (sink) for all speeds and torques, while EP2 should be unstable (source or saddle point). Unfortunately, this is not the case. The following analysis will show that EP1 may become unstable at low speeds, which results in various instability phenomena that concern EP2.

When substituting the expressions for EP2 in (3.14), the resulting excitation frequency is found to become

$$\omega_1(\psi_{d,2}^*, \psi_{q,2}^*, \hat{\psi}_{R,2}^*) = 0. \quad (3.22)$$

Hence, $\omega_1 \approx 0$ for operation about EP2. This is an important observation, which in a following section will help us to understand the instability phenomena of speed-sensorless flux estimation.

Inaccurately Modeled L_M

For simplicity, $\widehat{L}_M = L_M$ has been assumed in the present stability analysis. This does not affect the validity of the analysis, which can be deduced by substituting $i_d = \psi_{\text{ref}}/\widehat{L}_M$ in (3.16)–(3.18), putting $\dot{\psi}_d = \dot{\psi}_q = \dot{\widehat{\psi}}_R = 0$, and solving for ψ_d , ψ_q and $\widehat{\psi}_R$. The following then results

$$\psi_{d,1}^* = \widehat{\psi}_{R,1}^* = \frac{L_M}{\widehat{L}_M} \psi_{\text{ref}}, \quad \psi_{q,1}^* = 0 \quad (3.23)$$

for the equilibrium point that corresponds to the above EP1. The q -axis flux being $\psi_{q,1}^* = 0$ implies perfect field orientation, so \widehat{L}_M affects the flux modulus only. Since \widehat{L}_M and ψ_{ref} have similar effect on the flux modulus, $\widehat{L}_M \neq L_M$ can therefore be modeled in the present analysis by altering the value for ψ_{ref} .

3.2.3 Linearization of Closed-Loop System

Linearization about EP1

The three nonlinear differential equations in (3.16)–(3.18) are linearized about EP1. The resulting state-space system is found to become

$$\frac{d}{dt} \begin{bmatrix} \tilde{\psi}_d \\ \psi_q \\ \tilde{\psi}_R \end{bmatrix} = \begin{bmatrix} -\frac{R_R}{L_M} & \frac{R_R i_q}{\psi_{\text{ref}}} & 0 \\ -\left(\omega_r + \omega_2 + \frac{R_R}{L_M} \lambda_s\right) & -\lambda_s \omega_r & \omega_r + \omega_2 \\ -\frac{R_R}{L_M} \gamma & -\gamma \omega_r & 0 \end{bmatrix} \begin{bmatrix} \tilde{\psi}_d \\ \psi_q \\ \tilde{\psi}_R \end{bmatrix} \quad (3.24)$$

where $\lambda_s = \lambda \text{sign}(\omega_1)$, $\omega_2 = R_R i_q / \psi_{\text{ref}}$, and the error variables

$$\tilde{\psi}_d = \psi_d - \psi_{\text{ref}}, \quad \tilde{\psi}_R = \widehat{\psi}_R - \psi_{\text{ref}} \quad (3.25)$$

are introduced. Apparently, the standard slip relation appears in the matrix A . This is in consequence of that accurate model parameters are assumed and the linearization around the ideal operating point $[\psi_d = \widehat{\psi}_R = \psi_{\text{ref}}, \psi_q = 0]$, which in polar form becomes $[\psi_R = \widehat{\psi}_R = \psi_{\text{ref}}, \tilde{\theta} = 0]$. According to (2.23), the relation $\omega_r + \omega_2 = \dot{\theta} = \omega_1$ then holds, which can, thus, be substituted in (3.24):

$$\frac{d}{dt} \begin{bmatrix} \tilde{\psi}_d \\ \psi_q \\ \tilde{\psi}_R \end{bmatrix} = \underbrace{\begin{bmatrix} -\frac{R_R}{L_M} & \omega_1 - \omega_r & 0 \\ -\left(\omega_1 + \frac{R_R}{L_M} \lambda_s\right) & -\lambda_s \omega_r & \omega_1 \\ -\frac{R_R}{L_M} \gamma & -\gamma \omega_r & 0 \end{bmatrix}}_{A_{\text{EP1}}} \begin{bmatrix} \tilde{\psi}_d \\ \psi_q \\ \tilde{\psi}_R \end{bmatrix}. \quad (3.26)$$

This provides a slightly simpler representation of the system matrix, which alleviates the following analysis.

Analysis of the Linearized Dynamics about EP1

Due to the coupling between $\tilde{\psi}_d$, ψ_q and $\tilde{\psi}_R$, the full complex nature of the dynamics resulting from the SCVM is not easily grasped, not even from the linearization about EP1 in (3.26). The purpose of the following analysis is therefore mainly to point out some essential characteristics of the dynamics that result from the SCVM for operation about EP1.

The d direction in (3.26) is independent of the choice of gain parameters. For small i_q , ψ_d converges to ψ_{ref} with the rotor time constant L_M/R_R , independently of ψ_q :

$$\frac{d\tilde{\psi}_d}{dt} = -\frac{R_R}{L_M}\tilde{\psi}_d + \frac{R_R i_q}{\psi_{\text{ref}}}\psi_q. \quad (3.27)$$

The q direction in (3.26) is, on the other hand, very dependent on the gain parameter λ :

$$\frac{d\psi_q}{dt} = -\left(\omega_1 + \frac{R_R}{L_M}\lambda \text{sign}(\omega_1)\right)\tilde{\psi}_d - \lambda \text{sign}(\omega_1)\omega_r\psi_q + \omega_1\tilde{\psi}_R. \quad (3.28)$$

For $\lambda = 0$, the open-loop integration of the traditional VM is recovered in the closed-loop dynamics, due to the lack of ψ_q in the right-hand side of (3.28). This indicates an oscillating behavior for the traditional VM. Interestingly, the damping of ψ_q is greatly improved for $\lambda \neq 0$: at moderate speeds $\lambda \text{sign}(\omega_1)\omega_r \gg R_R/L_M$ is reasonable to assume, so the dynamics of ψ_q are then much faster than those of ψ_d . Provided that EP1 is stable, this implies that accurate field orientation, $\psi_q = 0$, is retrieved quickly after a disturbance of some kind. However, at low speeds, then $\lambda \neq 0$ appears to be troublesome. Consider the term $-\lambda \text{sign}(\omega_1)\omega_r\psi_q$ in (3.28): $\text{sign}(\omega_1) \neq \text{sign}(\omega_r)$ leads to $\dot{\psi}_q \sim +\lambda\psi_q$, i.e., ψ_q has then positive feedback.

The dynamics of $\tilde{\psi}_R$ appear to be open loop, since there is no $\tilde{\psi}_R$ in the right-hand side of (3.26):

$$\frac{d\tilde{\psi}_R}{dt} = -\gamma\frac{R_R}{L_M}\tilde{\psi}_d - \gamma\omega_r\psi_q. \quad (3.29)$$

This is not the case, though, since ψ_q and $\tilde{\psi}_R$ are coupled: a deviation from $\psi_q = 0$ is easily seen in $\tilde{\psi}_R$ at nominal speeds. This provides negative feedback to ψ_q , via the above equation and (3.28). The picture is quite different for low frequencies, however: the coupling between ψ_q and $\tilde{\psi}_R$ vanishes for $\omega_1 = 0$. Moreover, for $\text{sign}(\omega_1) \neq \text{sign}(\omega_r)$, then $\tilde{\psi}_R$ provides positive feedback to ψ_q .

Based on the above observations, it appears that stability problems at EP1 may arise for the operation mode $\text{sign}(\omega_1) \neq \text{sign}(\omega_r)$. Below, this is confirmed strictly, by analyzing the characteristic polynomial of EP1 at low speeds.

Linearization about EP2

The three nonlinear differential equations in (3.16)–(3.18) have been linearized about EP2. Unfortunately, the resulting state-space system was found to be too complicated to be tractable. In order to simplify the analysis, it is therefore assumed that $\omega_r = 0$. This assumption follows from $\omega_1 \approx 0$ at EP2, which leads to $\omega_r \approx -R_R i_q / \psi_R \approx 0$, on condition that the mechanical dynamics are stable.

Due to the assumption on $\omega_r = 0$, the below analysis about EP2 is valid for a slightly idealized case. Nevertheless, the approximation is fairly accurate for a specific operation mode at EP2 (which will be referred to as “frequency lockup”), so some valuable conclusions can still be drawn, as will be seen.

The linearization about EP2 involves the following steps:

- The assumption $\omega_r = 0$ is substituted in (3.20). EP2 then simplifies to: $\psi_{d,2}^* = \psi_{\text{ref}}$, $\psi_{q,2}^* = L_M i_q$, and $\hat{\psi}_{R,2}^* = \psi_{\text{ref}} + (L_M i_q)^2 / \psi_{\text{ref}}$.
- Error variables are introduced: $\tilde{\psi}_d = \psi_d - \psi_{d,2}^*$, $\tilde{\psi}_q = \psi_q - \psi_{q,2}^*$, and $\tilde{\psi}_R = \hat{\psi}_R - \hat{\psi}_{R,2}^*$, where the equilibrium points are the ones that result from $\omega_r = 0$.
- The assumption $\omega_r = 0$ is substituted in the resulting state-space system.

By performing these steps, the linearized dynamics about EP2 are found to be

$$\frac{d}{dt} \begin{bmatrix} \tilde{\psi}_d \\ \tilde{\psi}_q \\ \tilde{\psi}_R \end{bmatrix} = \underbrace{\begin{bmatrix} -\frac{R_R}{L_M} + \frac{R_R i_q \psi_{\text{ref}} \lambda_s}{\psi_{\text{ref}}^2 + (L_M i_q)^2} & -\frac{R_R i_q \psi_{\text{ref}}}{\psi_{\text{ref}}^2 + (L_M i_q)^2} & 0 \\ -\frac{R_R \psi_{\text{ref}}^2 \lambda_s}{L_M [\psi_{\text{ref}}^2 + (L_M i_q)^2]} & \frac{R_R L_M i_q^2}{\psi_{\text{ref}}^2 + (L_M i_q)^2} & 0 \\ -\gamma \frac{R_R}{L_M} & 0 & 0 \end{bmatrix}}_{A_{\text{EP2}}} \begin{bmatrix} \tilde{\psi}_d \\ \tilde{\psi}_q \\ \tilde{\psi}_R \end{bmatrix} \quad (3.30)$$

where $\lambda_s = \lambda \text{sign}(\omega_1)$. It can be seen from (3.30) that $\hat{\psi}_R$ is decoupled from both ψ_d and ψ_q , since there are only zeros in the third column of A_{EP2} .

Characteristic Polynomial of EP2

The characteristic polynomial of (3.30), belonging to EP2, can be factorized to

$$\det(pI - A_{\text{EP2}}) = p \left(p + \frac{R_R}{L_M} \right) \left(p + \frac{R_R L_M i_q^2}{\psi_{\text{ref}}^2 + (L_M i_q)^2} - \frac{R_R i_q \psi_{\text{ref}} \lambda \text{sign}(\omega_1)}{\psi_{\text{ref}}^2 + (L_M i_q)^2} \right) \quad (3.31)$$

which has the following roots (poles of linearized system about EP2)

$$p_1 = 0, \quad p_2 = -\frac{R_R}{L_M}, \quad p_3 = \frac{R_R i_q \psi_{\text{ref}} \lambda \text{sign}(\omega_1) - R_R L_M i_q^2}{\psi_{\text{ref}}^2 + (L_M i_q)^2}. \quad (3.32)$$

The pole p_1 being at the origin is a reminder of that $\hat{\psi}_R$ is open loop in (3.30). Since $\hat{\psi}_R$ is no longer involved in the “physical” dynamics of $\mathbf{\psi}_R$, this means that p_1 and the dynamics of $\hat{\psi}_R$ can be disregarded when analyzing EP2. Having drawn this observation, the stability for EP2 is thus governed by p_2 and p_3 .

The pole p_2 is stable, while p_3 may be either stable or unstable. By substituting $\psi_{\text{ref}} = L_M i_d$ in p_3 , the following condition results

$$|i_q| > i_d \lambda \text{sign}(\omega_1) \text{sign}(i_q) \quad (3.33)$$

for stable operation about EP2. EP2 is thus bound to be stable for $\text{sign}(i_q) \neq \text{sign}(\omega_1)$. Stable operation is also guaranteed for $|i_q| > |i_d \lambda|$, which requires that i_q is fairly large. This means that the undesirable convergence point EP2 is, unfortunately, not unstable for all speeds and torques. By recalling our previous observation $\omega_1 \approx 0$ about EP2, EP2 may hence be stable for small ω_1 and large i_q .

Characteristic Polynomial of EP1

The characteristic polynomial of (3.26), belonging to EP1, is found to be

$$\det(pI - A_{EP1}) = p^3 + k_2p^2 + k_1p + k_0 \quad (3.34a)$$

where

$$k_2 = \frac{R_R}{L_M} + \lambda \operatorname{sign}(\omega_1)\omega_r \quad (3.34b)$$

$$k_1 = \omega_1 \left(\omega_1 + \frac{R_R}{L_M} \lambda \operatorname{sign}(\omega_1) + (\gamma - 1)\omega_r \right) \quad (3.34c)$$

$$k_0 = \gamma \frac{R_R}{L_M} \omega_1^2. \quad (3.34d)$$

Stable operation about EP1 requires that all coefficients in the characteristic polynomial are positive, and that the elements in the first column of the *Routh array*

$$\begin{array}{c|cc} p^3 & 1 & k_1 \\ p^2 & k_2 & k_0 \\ \hline p^1 & k' = \frac{k_2k_1 - k_0}{k_2} & 0 \\ p^0 & k_0 & 0 \end{array} \quad (3.35)$$

are positive as well, giving the additional constraint $k' > 0$. Since $k_2 > 0$ is required for stability, $k' > 0$ is equivalent to

$$k = k_2k_1 - k_0 > 0. \quad (3.36)$$

Henceforth, k will be analyzed instead of k' , due to its simpler expression. This analysis will be carried out in the following two sections, where the two cases of nominal and low speeds are treated separately.

3.2.4 Stability Analysis for EP1 at Nominal Speeds

The slip is negligible at nominal speeds, meaning that $\omega_1 = \omega_r$ holds approximately. The coefficients in (3.34) then simplify to

$$k_2 = \frac{R_R}{L_M} + \lambda \operatorname{sign}(\omega_r)\omega_r = \frac{R_R}{L_M} + \lambda|\omega_r| \quad (3.37)$$

$$k_1 = \omega_r \left(\omega_r + \frac{R_R}{L_M} \lambda \operatorname{sign}(\omega_r) + (\gamma - 1)\omega_r \right) = \frac{R_R}{L_M} \lambda |\omega_r| + \gamma \omega_r^2 \quad (3.38)$$

$$k_0 = \gamma \frac{R_R}{L_M} \omega_r^2 \quad (3.39)$$

which give the following characteristic polynomial

$$\begin{aligned} \det(pI - A_{EP1}) &\approx p^3 + \left(\frac{R_R}{L_M} + \lambda|\omega_r| \right) p^2 + \left(\gamma \omega_r^2 + \frac{R_R}{L_M} \lambda |\omega_r| \right) p + \frac{R_R}{L_M} \gamma \omega_r^2 \\ &= \left(p + \frac{R_R}{L_M} \right) (p^2 + \lambda|\omega_r|p + \gamma \omega_r^2). \end{aligned} \quad (3.40)$$

The characteristic polynomial at nominal speeds has the following roots (poles of the linearized system):

$$p_1 = -\frac{R_R}{L_M}, \quad p_{2,3} = -(\lambda \pm j\sqrt{4\gamma - \lambda^2})\frac{|\omega_r|}{2}. \quad (3.41)$$

Based on (3.41), the following conclusions can be drawn:

- The system is always asymptotically stable for $\lambda > 0$, since this selection yields poles that are located in the left-hand side of the complex plane.
- The traditional VM is recovered for $\lambda = 0$, $\gamma = 1$. The poles are then located at $p_{2,3} = \pm j\omega_r$, giving a system that is marginally stable.
- For small λ and $\gamma = 1$, the closed-loop poles of the SCVM approximately coincide with the poles of the uncompensated VM with lowpass integrator. With $\lambda = 0.2$ —see Section 2.6.1 for the corresponding error angle—the poles are at $p_{2,3} \approx -(0.1 \pm j)|\omega_r|$. This corresponds to an angle of 84° relative the negative real axis, which is only a modest improvement compared to the damping of the traditional VM.
- The selection $\gamma = 1 + \lambda^2$ recovers the original variant of the SCVM, which results from DFO. The system is then still fairly poorly damped, since the poles $p_{2,3}$ are located at an angle of $\arctan[\sqrt{4/\lambda^2 + 3}]$ relative the negative real axis. Even if a large λ is selected, an angle of less than 60° relative the negative real axis cannot be obtained.
- The additional degree of freedom for IFO ($\mu \neq 1$) enables arbitrarily pole placement. A rule of thumb is that poles at 45° relative the negative real axis yield sufficient damping. Such poles are obtained by selecting γ according to

$$\gamma = \frac{\lambda^2}{2} \Rightarrow p_{2,3} = -\lambda(1 \pm j)\frac{|\omega_r|}{2} = -\frac{\lambda}{\sqrt{2}}|\omega_r|e^{\pm j\pi/4}. \quad (3.42)$$

Henceforth, the specific gain parameters

$$\lambda = \sqrt{2}, \quad \gamma = 1 \quad (3.43)$$

are selected at nominal speeds, giving poles at $p_{2,3} = -|\omega_r|e^{\pm j\pi/4}$. The usefulness of these gain parameters, and particularly $\gamma = 1$, will become apparent in the following analysis at low speeds.

- Interestingly, the above gain parameters reveal a close relationship between the SCVM and the traditional VM. Consider the SCVM in (3.8)–(3.9) with $\gamma = 1$:

$$\frac{d\hat{\psi}_R}{dt} = \hat{E}_d, \quad \omega_1 = \frac{\hat{E}_q - \lambda \operatorname{sign}(\omega_1)\hat{E}_d}{\hat{\psi}_R} \quad (3.44)$$

and compare this to the VM in (2.55)–(2.56):

$$\frac{d\hat{\psi}_R}{dt} = \hat{E}_d, \quad \omega_1 = \frac{\hat{E}_q}{\hat{\psi}_R}. \quad (3.45)$$

The two estimators differ only by the introduction of \hat{E}_d in the slip relation of the SCVM. As discussed in Section 2.5: $\hat{E}_d \approx -\omega_1 \psi_R \tilde{\theta}$ and $\hat{E}_q \approx \omega_1 \psi_R$ for small $\tilde{\theta}$ at nominal speeds. Substituting these relations in the SCVM slip relation results in

$$\omega_1 \approx \frac{\psi_R}{\hat{\psi}_R} (\omega_1 + \lambda |\omega_1| \tilde{\theta}). \quad (3.46)$$

The additional feedback of $\tilde{\theta}$ is, hence, the explanation to the well-damped dynamics resulting from the SCVM at nominal speeds.

3.2.5 Stability Analysis for EP1 at Low Speeds

The above selection $\gamma = 1$ at nominal speeds can also be recommended for low speeds. Consider (3.34c): $\gamma = 1$ clears the dependency on ω_r in k_1 , and this ensures $k_1 \geq 0$. Regarding λ , the following analysis will reveal that $\lambda = \sqrt{2}$ is suitable for nominal speeds only, while a better choice exists for low speeds.

By repeating the expression for k_2 from (3.34b), substituting $\gamma = 1$ in (3.34c)–(3.34d), and evaluating k in (3.36), the following coefficients

$$k_2 = \frac{R_R}{L_M} + \lambda \operatorname{sign}(\omega_1) \omega_r \quad (3.47)$$

$$k_1 = \omega_1 \left(\omega_1 + \frac{R_R}{L_M} \lambda \operatorname{sign}(\omega_1) \right) \quad (3.48)$$

$$k_0 = \frac{R_R}{L_M} \omega_1^2 \quad (3.49)$$

$$\begin{aligned} k &= \omega_1 \left(\frac{R_R}{L_M} + \lambda \operatorname{sign}(\omega_1) \omega_r \right) \left(\omega_1 + \frac{R_R}{L_M} \lambda \operatorname{sign}(\omega_1) \right) - \frac{R_R}{L_M} \omega_1^2 \\ &= \lambda |\omega_1| \left[\left(\frac{R_R}{L_M} \right)^2 + \left(\omega_1 + \frac{R_R}{L_M} \lambda \operatorname{sign}(\omega_1) \right) \omega_r \right] \end{aligned} \quad (3.50)$$

must remain positive for stable operation at low speeds. Based on (3.47)–(3.50), the following conclusions can be drawn:

- Marginal stability is obtained for $\omega_1 = 0$, since the coefficients then become $k_1 = k_0 = k = 0$. As discussed in Section 2.5, it is impossible to extract information regarding $\tilde{\theta}$ from the flux EMF at zero excitation frequency.
- For $\omega_1 \neq 0$ and $\operatorname{sign}(\omega_1) = \operatorname{sign}(\omega_r)$, then $\{k_2, k_1, k_0, k\} > 0$. The dynamics resulting from the SCVM are therefore asymptotically stable when ω_1 and ω_r have equal signs, which is always fulfilled for normal operation at nominal speeds.
- Stability cannot be ensured for $\operatorname{sign}(\omega_1) \neq \operatorname{sign}(\omega_r)$: the coefficients k_1 and k_0 are then still positive, but at least one of the coefficients k_2 or k may become negative. The troublesome operation mode $\operatorname{sign}(\omega_1) \neq \operatorname{sign}(\omega_r)$ was indicated already in Section 3.2.3.
- The following observations can be made for the critical mode $\operatorname{sign}(\omega_1) \neq \operatorname{sign}(\omega_r)$:

1. A speed reversal under load (non-zero slip) is problematic. The critical moment for stability occurs immediately after a reversal of either ω_1 or ω_r , such that the signs of ω_1 and ω_r differ.
2. A speed reversal for an application where the load torque is zero at standstill should be a relatively easy task. The slip for such a load is (almost) zero at zero speed, so ω_1 and ω_r change signs (almost) simultaneously.
3. The selection $\widehat{L}_M < L_M$ is recommended, which can be achieved by performing the usual no-load test at a stator voltage that is slightly above the nominal value. This selection ensures, via the relation $i_d^{\text{ref}} = \psi_{\text{ref}}/\widehat{L}_M$, that the machine is not operating below the nominal rotor flux. Consequently, the slip is slightly reduced, and the region where $\text{sign}(\omega_1) \neq \text{sign}(\omega_r)$ is made smaller.

This recommendation for \widehat{L}_M is the opposite compared to [46], but the flux estimator in this reference used $\widehat{\psi}_R = \psi_{\text{ref}}$ instead of a dynamic $\widehat{\psi}_R$.

Consider a slow speed reversal under non-zero load torque for accurate field orientation. Immediately after a sign change in ω_1 , then $\omega_r = -R_R i_q / \psi_{\text{ref}}$. Substituting this in (3.47) gives the following necessary condition for stability:

$$k_2 = \frac{R_R}{L_M} - \lambda \text{sign}(\omega_1) \frac{R_R i_q}{\psi_{\text{ref}}} = \frac{R_R}{L_M} \left(1 - \lambda \text{sign}(\omega_1) \frac{i_q}{i_d} \right) > 0 \quad (3.51)$$

which is equivalent to

$$i_d > i_q \lambda \text{sign}(\omega_1). \quad (3.52)$$

For stability, i_q can therefore be no larger than

$$\begin{aligned} i_q &< \frac{i_d}{\lambda}, & \omega_1 > 0 \\ i_q &> -\frac{i_d}{\lambda}, & \omega_1 < 0. \end{aligned} \quad (3.53)$$

The following additional conclusions can now be drawn on low-speed operation about EP1:

- Only loads requiring $|i_q| < i_d/\sqrt{2}$ can be safely reversed when $\lambda = \sqrt{2}$. The critical moment for stability is when $\omega_1 \approx 0$, and the sign of ω_1 equals the sign of i_q . This corresponds to that the signs of ω_1 and ω_r differ, and agrees with the above conclusions.
- With respect to the requirement $k_2 > 0$, the gain parameter λ must be lowered in order to allow for $|i_q| > i_d/\sqrt{2}$. This can be accomplished with

$$\lambda = \rho |\omega_1|, \quad \rho > 0 \quad (3.54)$$

for instance. It can be observed that this selection for λ , and $\gamma = 1$, recovers the traditional VM for $\omega_1 = 0$.

The coefficients k_2 and k will now be investigated for the selection $\lambda = \rho|\omega_1|$, since these two coefficients are the ones that may become negative at low speeds. By seeking the minima for the coefficients, it will be shown that the dynamics resulting from the SCVM can be made asymptotically stable for small machines, even for the critical mode $\text{sign}(\omega_1) \neq \text{sign}(\omega_r)$.

Analysis of k_2

Substituting $\lambda = \rho|\omega_1|$ and $\omega_r = \omega_1 - \omega_2$ in (3.47) gives

$$k_2 = \frac{R_R}{L_M} + \rho|\omega_1| \text{sign}(\omega_1)(\omega_1 - \omega_2) = \rho\omega_1^2 - \rho\omega_2\omega_1 + \frac{R_R}{L_M}. \quad (3.55)$$

The second derivative of k_2 with respect to ω_1 is 2ρ , which is positive for $\rho > 0$. Therefore, k_2 has a global minimum when

$$\frac{\partial k_2}{\partial \omega_1} = 2\rho\omega_1 - \rho\omega_2 = 0. \quad (3.56)$$

Solving this equation for ω_1 yields the critical frequency

$$\omega_1 = \frac{\omega_2}{2}. \quad (3.57)$$

Substituting this in (3.55) gives the minimal value for k_2

$$k_{2,\min} = -\frac{\rho\omega_2^2}{4} + \frac{R_R}{L_M}. \quad (3.58)$$

By solving the inequality $k_{2,\min} > 0$ for ρ , and considering $\rho > 0$, the following constraint

$$0 < \rho < \frac{4R_R}{\omega_2^2 L_M} = \left\{ \omega_2 = \frac{R_R i_q}{\psi_{\text{ref}}} \right\} = \frac{L_M}{R_R} \left(\frac{2i_d}{i_q} \right)^2 \quad (3.59)$$

is found to ensure $k_2 > 0$, which can be fulfilled by selecting sufficiently small ρ . Unfortunately, a stricter constraint is imposed on ρ for $k > 0$, as will be shown in the next section.

Analysis of k

The minimum of k coincides with the minimum of

$$\xi = \frac{k}{\lambda|\omega_1|} = \left(\frac{R_R}{L_M} \right)^2 + \left(\omega_1 + \frac{R_R}{L_M} \lambda \text{sign}(\omega_1) \right) \omega_r \quad (3.60)$$

since $\lambda|\omega_1| > 0$ for all $\omega_1 \neq 0$. The case $\omega_1 = 0$ can be neglected in the present analysis, since it unavoidably yields a system that is only marginally stable. Substituting $\lambda = \rho|\omega_1|$ and $\omega_r = \omega_1 - \omega_2$ in ξ gives

$$\begin{aligned} \xi &= \left(\frac{R_R}{L_M} \right)^2 + \left(\omega_1 + \frac{R_R}{L_M} \rho|\omega_1| \text{sign}(\omega_1) \right) (\omega_1 - \omega_2) \\ &= \left(1 + \frac{\rho R_R}{L_M} \right) \omega_1^2 - \left(1 + \frac{\rho R_R}{L_M} \right) \omega_2 \omega_1 + \left(\frac{R_R}{L_M} \right)^2. \end{aligned} \quad (3.61)$$

The second derivative of k_2 with respect to ω_1 is $2(1 + \rho R_R/L_M)$, which is positive for $\rho > -L_M/R_R$. Therefore, k_2 has a global minimum when

$$\frac{\partial \xi}{\partial \omega_1} = \left(1 + \frac{\rho R_R}{L_M}\right) 2\omega_1 - \left(1 + \frac{\rho R_R}{L_M}\right) \omega_2 = 0. \quad (3.62)$$

Solving this equation for ω_1 yields the critical frequency

$$\omega_1 = \frac{\omega_2}{2}. \quad (3.63)$$

Hence, k_2 and k have the same critical frequency. By substituting the critical frequency in (3.61), the minimal value for ξ is found to be

$$\xi_{\min} = - \left(1 + \frac{\rho R_R}{L_M}\right) \frac{\omega_2^2}{4} + \left(\frac{R_R}{L_M}\right)^2. \quad (3.64)$$

For stability, $\xi_{\min} > 0$ is required. By solving this inequality for ρ , and considering $\rho > 0$, the following constraint

$$0 < \rho < \frac{4R_R}{\omega_2^2 L_M} - \frac{L_M}{R_R} = \frac{L_M}{R_R} \left[\left(\frac{2i_d}{i_q}\right)^2 - 1 \right] \quad (3.65)$$

is found is to ensure $k > 0$. Based on (3.65), the following conclusions can be drawn:

- The constraint in (3.65) is stricter than the one that results from $k_2 > 0$. Eq. (3.65) is therefore the ultimate condition for stable operation about EP1.
- The maximum i_q that can be safely reversed, for $\hat{R}_s = R_s$, becomes

$$\left(\frac{2i_d}{i_q}\right)^2 - 1 > 0 \Rightarrow |i_q| < 2i_d. \quad (3.66)$$

However, this requires a very small value for ρ , which provides poor damping. Recall that $\rho \approx 0$ results in $\lambda \approx 0$, which recovers the marginally stable VM. The following ρ is instead recommended:

$$\rho = \frac{\sqrt{2}}{\omega_{1,\min}} \quad (3.67)$$

in order to achieve a reasonable damping at low speeds. By substituting this in (3.54), the following λ is then obtained:

$$\lambda = \frac{\sqrt{2}|\omega_1|}{\omega_{1,\min}}, \quad |\omega_1| \leq \omega_{1,\min} \quad (3.68)$$

for frequencies below $\omega_{1,\min}$. Except reasonable damping, this selection also allows for a smooth transition between nominal speeds ($\lambda = \sqrt{2}$) and low speeds, which is depicted in Fig. 3.1. The parameter $\omega_{1,\min}$ should be selected much smaller than the nominal frequency, i.e., in the range of 0.05–0.1 pu.

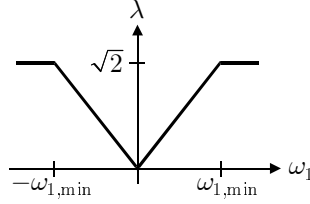


Fig. 3.1. Selection of λ .

Let us study the above gain parameter selection, and see what loads that can be safely reversed. By substituting $\rho = \sqrt{2}/\omega_{1,\min}$ in (3.65), the condition for stability is found to be:

$$\frac{\sqrt{2}}{\omega_{1,\min}} < \frac{L_M}{R_R} \left[\left(\frac{2i_d}{i_q} \right)^2 - 1 \right] \Rightarrow \left(\frac{i_q}{i_d} \right)^2 < \frac{4}{1 + \frac{\sqrt{2}R_R}{\omega_{1,\min}L_M}}. \quad (3.69)$$

The current components are hereby expressed as $i_q = \sqrt{|\mathbf{i}_s|_{\max}^2 - i_d^2}$ and $i_d = \psi_{\text{ref}}/L_M$, which are then substituted in the above inequality:

$$\frac{|\mathbf{i}_s|_{\max}^2 - i_d^2}{i_d^2} = \left(\frac{L_M |\mathbf{i}_s|_{\max}}{\psi_{\text{ref}}} \right)^2 - 1 < \frac{4}{1 + \frac{\sqrt{2}R_R}{\omega_{1,\min}L_M}}. \quad (3.70)$$

This inequality has been solved numerically for L_M , with the values $\psi_{\text{ref}} = 0.9$ pu, $|\mathbf{i}_s|_{\max} = 1$ pu, $R_R = 0.04$ pu and $\omega_{1,\min} = 0.05$ pu. The resulting condition for L_M was found to be

$$L_M < 1.6 \text{ pu}. \quad (3.71)$$

With the exception of $\omega_1 = 0$, this condition implies that *reversal of rotation with rated current is guaranteed to be stable for small machines*, i.e., machines that have small L_M . For larger machines, *reversal of rotation is guaranteed to be stable only for lighter loads*.

Observe that EP1 is *asymptotically stable* for $\{k_2, k\} > 0$, but *global stability* has not been shown. Therefore, even if $k_2 > 0$ and $k > 0$, a large disturbance of some kind may make EP1 unstable.

Fig. 3.2 shows pole loci for a stable rotation reversal with $|\mathbf{i}_s| = 1$ pu. The loci are plotted for a small machine, which has $L_M = 1.4$ pu. As seen, the pole loci for $\omega_1 \leq 0$ and $\omega_1 \geq 0$ are quite different. Poor damping is indicated in Fig. 3.2(b), where the poles for $\omega_1 > 0$ initially slide along the imaginary axis. Two of the poles are at the origin for $\omega_1 = 0$, which confirms marginal stability for zero excitation frequency.

3.3 Instability Phenomena

As already indicated in Section 2.5, and now confirmed analytically, speed-sensorless operation is not necessarily stable at low frequencies. The above stability analysis provided an accurate description of *when* instability phenomena are present, i.e., when EP1 becomes unstable. However, the analysis can only partly explain *how* these phenomena manifest themselves, since also the mechanical dynamics need then to be considered.

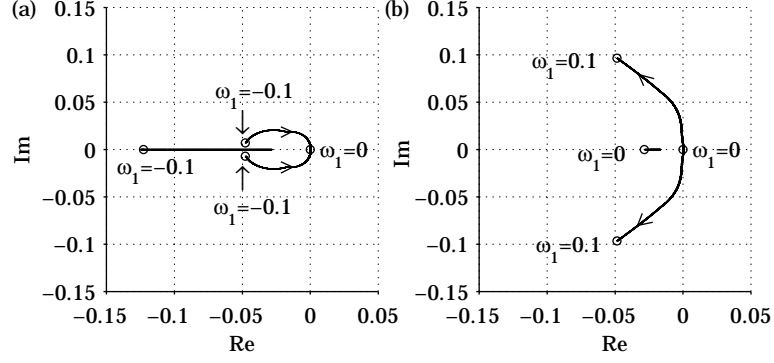


Fig. 3.2. Pole loci for the linearized dynamics resulting from the SCVM. Stable rotation reversal with $\omega_{1,\min}=0.05$ pu, $|\mathbf{i}_s|=1$ pu, $\psi_{\text{ref}} = 0.9$ pu, $L_M=1.4$ pu, $i_q=0.77$ pu. (a) $\omega_1 \leq 0$. (b) $\omega_1 \geq 0$.

Two instability phenomena are present for speed-sensorless flux estimation. These are here referred to *flux collapse* [46] and *frequency lockup*. Frequency lockup has previously been reported in [32], where it was referred to as “speed estimation failure.” We shall now extend the results of [32, 46], by discussing the underlying mechanisms behind these instability phenomena. The resulting conclusions are verified by simulations made on the 22-kW test machine in Table 2.2. The simulation parameters are: $\omega_{1,\min} = 0.05$ pu, $\hat{L}_\sigma = 1.1L_\sigma$, $\hat{L}_M = 1.1L_M$, $\hat{R}_R = 0.9R_R$, $\psi_{\text{ref}} = 0.8$ pu, and the bandwidth of the speed control loop is 0.02 pu. The critical model parameter \hat{R}_s is explicitly stated for each simulation.

3.3.1 Instability and Flux Dynamics

Once EP1 becomes unstable, $[\psi_d, \psi_q, \hat{\psi}_R]$ converge to EP2, where either flux collapse or frequency lockup may occur. In order to gain a better understanding of these instability phenomena, the flux dynamics in (2.22) must be considered:

$$\dot{\psi}_R = R_R(i_d \cos \tilde{\theta} + i_q \sin \tilde{\theta}) - \frac{R_R}{L_M} \psi_R \quad (3.72)$$

which for small $\tilde{\theta}$, such that $\sin \tilde{\theta} \approx \tilde{\theta}$ and $\cos \tilde{\theta} \approx 1$, simplifies to

$$\dot{\psi}_R \approx R_R(i_d + i_q \tilde{\theta}) - \frac{R_R}{L_M} \psi_R. \quad (3.73)$$

This approximation is sufficiently accurate for our discussion purposes. It will now be argued that the above product of i_q and $\tilde{\theta}$, which may be large at EP2, determines the resulting instability phenomenon at EP2.

3.3.2 Flux Collapse

Consider $\text{sign}(\tilde{\theta}) \neq \text{sign}(i_q)$ in (3.73). In consequence of the resulting magnetizing current in the rotor-flux-oriented reference frame:

$$i_d^R = i_d + i_q \tilde{\theta} = i_d - |i_q \tilde{\theta}| \quad (3.74)$$

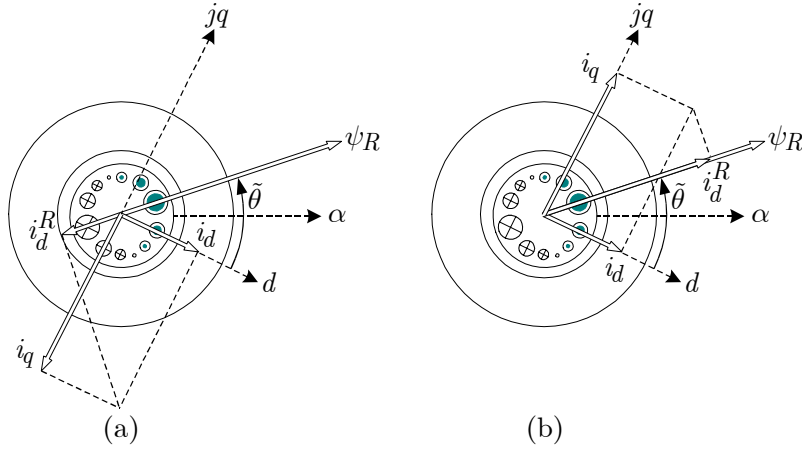


Fig. 3.3. Instability phenomena. (a) Flux collapse: $\tilde{\theta} > 0$ and $i_q < 0$, giving $i_d^R < i_d$ and $\dot{\psi}_R < 0$. (b) Frequency lockup: $\tilde{\theta} > 0$ and $i_q > 0$, giving $i_d^R > i_d$ and $\dot{\psi}_R > 0$.

then being smaller than i_d , or even negative for $|i_q \tilde{\theta}| > i_d$, the flux modulus begins to decrease. Fig. 3.3(a) depicts this process as a space-vector diagram. For a constant i_q , the reduced flux modulus in turn reduces the electro-mechanical torque. Unless the load torque is almost zero at zero rotor speed, the speed is then being accelerated by the load torque. Since $\omega_1 \approx 0$ at EP2, this implies that the slip frequency increases, and the breakdown torque of the machine is eventually exceeded. Provided that the load torque remains constant, the rotor speed may now reach a very high value. By substituting a large value for ω_r in (3.20), this asymptotically leads to

$$\psi_d \approx 0, \quad \psi_q \approx 0. \quad (3.75)$$

The machine is thus being nearly fully demagnetized—the flux *collapses*—and the machine is therefore incapable of developing torque. With respect to the equivalent circuit, the rotor appears as short-circuited seen from the stator terminal, due to the large slip now present, so the current through the magnetizing inductance is close to zero.

A simulation of flux collapse is shown in Fig. 3.4, where $\hat{R}_s = 0.7R_s$. The speed reference in Fig. 3.4(a) is initially stepped through the sequence $-0.2, 0.2, 0, -0.02$ pu, and a constant load torque that requires $i_q = 0.6$ pu is applied after one second. Eventually, the speed reference is slowly positively ramped at $t = 8$ s. For $t < 8$ s, the performance is good, except for some minor deviations from $\tilde{\theta} = 0$, which are seen in Fig. 3.4(c). These deviations occur when the speed reference is stepped from -0.2 pu to 0.2 pu, and for zero rotor speed. Observe that zero rotor speed is not necessarily critical for stability, at least not for non-zero slip. Unfortunately, the slow positive speed ramp against the load torque eventually results in flux collapse at $t = 10$ s. The following additional remarks can be made on flux collapse:

- Flux collapse results in total failure for a speed-sensorless drive, since neither the torque nor the speed can be controlled.
- For a reversal of rotation, the greatest risk for flux collapse occurs when the load torque opposes the speed reversal. Otherwise, the speed reversal may be completed by the load torque, such that stable operation at EP1 once again results. However,

this is not a general rule, since the load torque must be capable of reversing the speed faster than the flux modulus decreases.

- For speed closed-loop control, flux collapse is sensed by the speed controller as a deviation from the speed setpoint. In an attempt to correct this, the speed controller requests for a larger q -axis current, and eventually the maximum i_q allowed is reached. As seen in (3.73), this accelerates the reduction of the flux modulus. Flux collapse is, hence, initially a fairly slow process, essentially governed by the rotor time constant L_M/R_R , but this is speeded up the speed controller. Alternatively, the speed controller may trigger a tendency to flux collapse into complete collapse.
- If the speed reversal is made sufficiently fast, the flux modulus is initially reduced, but there is not sufficient time for the flux collapse to fully develop. After all, the flux modulus cannot change instantaneously. A similar phenomenon was in [46] referred to as *flux excursion*. Consequently, flux collapse can only occur if ω_1 dwells at low excitation frequencies.
- The flux modulus is hardly affected at all if the low-speed region is ridden through quickly or if i_q is small, where the latter implies small load torque for zero speed. The risk for flux collapse is then minimal.

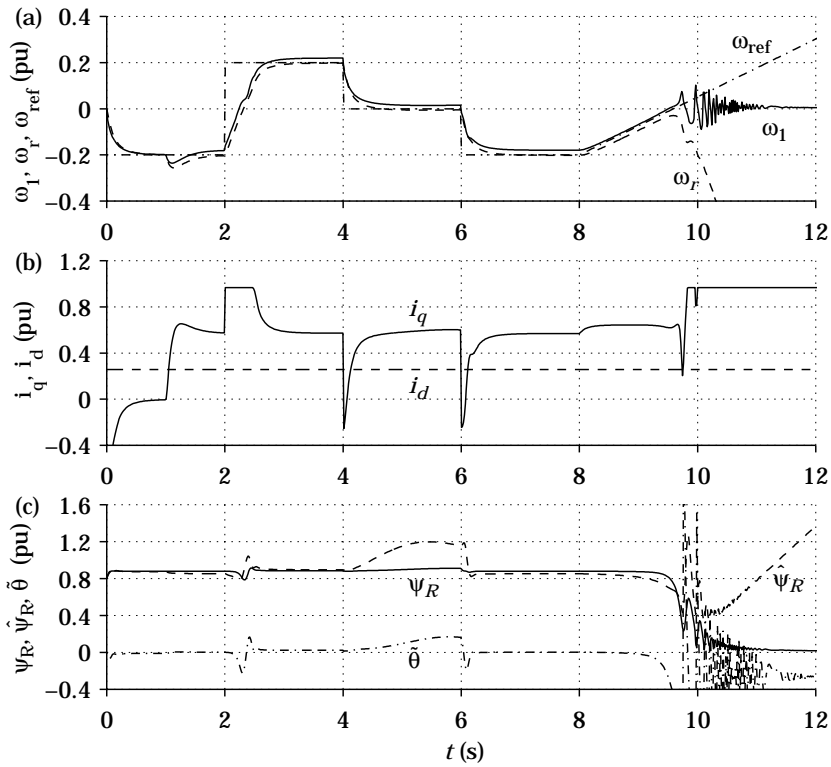


Fig. 3.4. Simulation of flux collapse with $\hat{R}_s=0.7R_s$; a constant load torque is applied at $t=1$ s, resulting in $i_q=0.6$ pu.

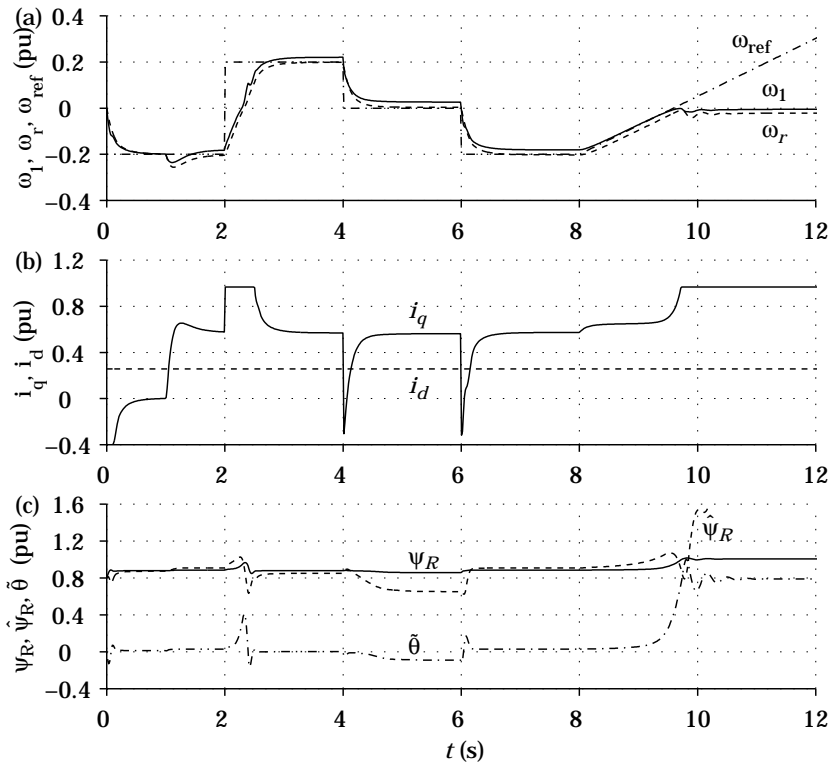


Fig. 3.5. Simulation of frequency lockup with $\hat{R}_s=1.4R_s$; a constant load torque is applied at $t=1$ s, resulting in $i_q=0.6$ pu.

3.3.3 Frequency Lockup

Consider $\text{sign}(\tilde{\theta}) = \text{sign}(i_q)$ in (3.73). This is the opposite case compared to flux collapse, so the flux modulus now begins to increase. Fig. 3.3(b) depicts this process as a space-vector diagram. Practically, the flux modulus can only become slightly larger compared to the nominal rotor flux, due to magnetic saturation, but this operation mode can at least not result in flux collapse. In contrast to flux collapse, the machine is therefore capable of developing torque and the mechanical dynamics are stable. Although frequency lockup is here referred to as an instability phenomena, the lockup hence corresponds to stable flux and speed dynamics about the undesirable equilibrium point EP2. In consequence of the stable mechanical dynamics and $\omega_1 \approx 0$ for operation about EP2, both ω_1 and ω_r lock on to constant values.

Frequency lockup has much in common to an induction machine in the open-loop operation, since the SCVM provides almost no feedback for operation about EP2. According to (3.68), λ is selected small for small ω_1 . Hence, the SCVM provides only minor feedback for operation about EP2, where $\omega_1 \approx 0$. In addition, the SCVM provides no feedback at all for $\omega_1 \equiv 0$, as discussed in Section 2.5.

The final settling point for frequency lockup results when the mechanical subsystem reaches the steady-state operation. Substituting (2.19) in (2.12), putting $\dot{\omega}_r = 0$ and assuming $b = 0$, gives:

$$0 = 3n_p\psi_R(i_q \cos \tilde{\theta} - i_d \sin \tilde{\theta}) - T_l. \quad (3.76)$$

We now consider the above equation for a small load torque, such that $T_l \approx 0$. This is a somewhat doubtful assumption, however, since EP1 is normally stable for zero load torque at low speeds, meaning that frequency lockup is unlikely to occur. Bearing this remark in mind, $T_l = 0$ is substituted in (3.76), which is then solved for $\tilde{\theta}$:

$$\tan \tilde{\theta} = \frac{i_q}{i_d}. \quad (3.77)$$

The above equation can be interpreted as the error angle opposes any attempt to increase the electro-mechanical torque through i_q .

Let us now compare (3.77) with the error angle for EP2 in (3.21), which resulted from the stability analysis of the electrical subsystem. Since $\omega_1 \approx 0$ about EP2, the no-load operation must correspond to $\omega_r \approx 0$. By substituting this in (3.21), the error angle for the no-load operation at EP2 becomes

$$\tan \tilde{\theta} = \frac{i_q}{i_d}. \quad (3.78)$$

This is identical to (3.77), which indicates that frequency lockup indeed corresponds to operation about EP2 for stable mechanical dynamics.

A simulation of frequency lockup is shown in Fig. 3.5. Similar to the above simulation of flux collapse, the slow ramping of the speed reference against the load torque is critical. The flux modulus in 3.5(c) does not collapse, but the field orientation deteriorates, and the synchronous frequency in Fig. 3.5(a) locks on to a value close to zero at $t = 10$ s. The speed controller attempts to complete the speed reversal by increasing

i_q , but this does not increase the torque since the error angle meanwhile increases, as seen in (3.77). It can be observed from Fig. 3.5(a) that the speed estimate is fairly accurate for frequency lockup; the stationary values for the speed and the speed estimate become $\omega_r \approx -R_R i_q / \psi_R$ and $\hat{\omega}_r = \omega_1 - \hat{R}_R i_q / \hat{\psi}_R \approx -\hat{R}_R i_q / \hat{\psi}_R$, respectively. The following additional remarks can be made on frequency lockup:

- For a reversal of rotation, frequency lockup can only occur if the load torque opposes the speed reversal. Otherwise, the load torque completes the speed reversal when T_e reduces, so the equilibrium in (3.76) cannot occur.
- The flux modulus is hardly affected at all if the low-speed region is ridden through quickly, or if i_q is small, i.e., the load torque is almost zero for zero speed. Then, the risk for frequency lockup is minimal.
- Fig. 3.5(c) reveals that $\hat{\psi}_R$ is much larger than ψ_{ref} for frequency lockup. This can be deduced from the equilibrium point in (3.20): $\hat{\psi}_{R,2}^* > \psi_{\text{ref}}$ for small ω_r .

3.4 Parameter Sensitivity

Although the above analysis of the dynamics resulting from the SCVM has provided several enlightening observations and design guidelines, the complete picture is in reality even more complicated. This is partly due to that accurate model parameters have, until now, been assumed.

By subtracting the true flux EMF in (2.41) from the estimated one in (2.42), the parameter sensitivity of the SCVM is revealed:

$$\begin{aligned} \hat{\mathbf{E}}_f &= (R_s + j\omega_1 L_\sigma) \mathbf{i}_s + (\dot{\psi}_R + j\dot{\theta} \psi_R) e^{j\tilde{\theta}} - (\hat{R}_s + j\omega_1 \hat{L}_\sigma) \mathbf{i}_s \\ &= (\tilde{R}_s + j\omega_1 \tilde{L}_\sigma) \mathbf{i}_s + \underbrace{(\dot{\psi}_R + j\dot{\theta} \psi_R) e^{j\tilde{\theta}}}_{\mathbf{E}_f}. \end{aligned} \quad (3.79)$$

where

$$\tilde{R}_s = R_s - \hat{R}_s, \quad \tilde{L}_\sigma = L_\sigma - \hat{L}_\sigma \quad (3.80)$$

are the errors in the model parameters. The steady-state operation is now considered in order to derive the error angle. By substituting the real part of (3.79):

$$\hat{E}_d = \tilde{R}_s i_d - \omega_1 \tilde{L}_\sigma i_q + \dot{\psi}_R \cos \tilde{\theta} - \dot{\theta} \psi_R \sin \tilde{\theta} \quad (3.81)$$

in (3.8), putting $\dot{\psi}_R = \dot{\hat{\psi}}_R = 0$, and solving for $\tilde{\theta}$, the error angle is found to be

$$\tilde{\theta} = \arcsin \left(\frac{\tilde{R}_s i_d}{\dot{\theta} \psi_R} - \frac{\omega_1 \tilde{L}_\sigma i_q}{\dot{\theta} \psi_R} \right) \approx \arcsin \left(\frac{\tilde{R}_s i_d}{\omega_1 \psi_R} - \frac{\tilde{L}_\sigma i_q}{\psi_R} \right) \quad (3.82)$$

where the latter approximation assumes $\dot{\theta}_1 \approx \omega_1$. Eq. (3.82) holds for operation at both EP1 and EP2, since \hat{E}_d , via (3.8), is always forced to zero by the flux-modulus estimator.

At nominal speeds, the resistive part in (3.82) is small and the inductive part dominates:

$$\tilde{\theta} \approx -\arcsin\left(\frac{\tilde{L}_\sigma i_q}{\psi_R}\right). \quad (3.83)$$

The values $\tilde{L}_\sigma = 0.1$ pu, $i_q = 1$ pu and $\psi_R = 0.9$ pu are considered for a numerical example, i.e., a fairly large \tilde{L}_σ and a large current. These values give the error angle $\tilde{\theta} = -0.11$ rad = -6.4° . This is a small error angle, which shows that the field orientation of SCVM is accurate at nominal speeds. In the field-weakening region, where ψ_R must be lowered, slightly less accurate field orientation can be expected.

The picture at low speeds is the opposite to the above; the resistive part of $\tilde{\theta}$ then dominates:

$$\tilde{\theta} = \arcsin\left(\frac{\tilde{R}_s i_d}{\omega_1 \psi_R}\right) \approx \arcsin\left(\frac{\tilde{R}_s}{\omega_1 L_M}\right) \quad (3.84)$$

where the latter approximation assumes $\psi_R \approx L_M i_d$. It can be seen that $\omega_1 = 0$ yields a singularity in (3.84). The singularity is due to that the error $\tilde{R}_s i_d$ in (3.81) is misinterpreted by the flux estimator as a change in $\tilde{\theta}$, which has a devastating effect on the field orientation. If ω_1 dwells at $\omega_1 \approx 0$ for too long, the dynamics of $\tilde{\theta}$ are given sufficient time for the field orientation to fully deteriorate, even for $\tilde{R}_s \approx R_s$. Not surprisingly, this is highly critical for the stability of EP1.

To avoid the singularity for $\omega_1 = 0$, the preferred alternative would be if the sensitivity to \tilde{R}_s were less severe, or if \tilde{R}_s could be accurately estimated. Two approaches are thus possible for making \tilde{R}_s less critical a model parameter:

1. Design the flux estimator such that it does not require knowledge of \tilde{R}_s . Such estimators were studied in [97], which used an MRAS scheme, and [47], which used an estimator that was referred to as the “reactive power model.” Unfortunately, at least the reactive power model was found to be unstable for $\text{sign}(\omega_r) \neq \text{sign}(i_q)$ [47].
2. Estimate R_s “on-line.” Such schemes have been around for a long time, see for instance [16, 45]. However, this approach may very well be equivalent to the above one, i.e., to design a flux estimator that does not require knowledge of \tilde{R}_s .

We consider both methods as interesting, but leave them to future research.

3.4.1 Selection of Model Parameters

Neither flux collapse nor frequency lockup is desirable, but at least flux collapse must be avoided, since it is the most critical instability phenomenon. As discussed in Section 3.3.3, flux collapse cannot occur if $\text{sign}(\tilde{\theta}) = \text{sign}(i_q)$. The following model parameters aim to satisfy this relation, such that frequency lockup results when EP1 becomes unstable. For this purpose, (3.82) is considered for small $\tilde{\theta}$, such that $\sin \tilde{\theta} \approx \tilde{\theta}$:

$$\tilde{\theta} \approx \frac{\tilde{R}_s}{\omega_1 L_M} - \frac{\tilde{L}_\sigma i_q}{\psi_R}. \quad (3.85)$$

Essentially, only the sign of $\tilde{\theta}$ is relevant in following discussion. The assumption on small $\tilde{\theta}$ is therefore valid for $|\tilde{\theta}| < 90^\circ$. Based on (3.85), the following recommendations can be given for \hat{L}_σ and \hat{R}_s in order to achieve $\text{sign}(\tilde{\theta}) = \text{sign}(i_q)$:

\hat{L}_σ : Make sure that $\hat{L}_\sigma > L_\sigma$, such that $\tilde{L}_\sigma = L_\sigma - \hat{L}_\sigma < 0$. The signs of $\tilde{\theta}$ and the inductive part in (3.85) are then related as

$$\text{sign}(\tilde{\theta}) = -\text{sign}\left(\frac{\tilde{L}_\sigma i_q}{\psi_R}\right) = \text{sign}(i_q). \quad (3.86)$$

Interestingly, $\hat{L}_\sigma > L_\sigma$ agrees with the recommended \hat{L}_σ for field-weakening control in [53].

\hat{R}_s : Theoretically, \hat{R}_s should be selected as:

$$\hat{R}_s \leq R_s, \quad \text{sign}(\omega_1) = \text{sign}(i_q) \quad (3.87a)$$

$$\hat{R}_s \geq R_s, \quad \text{sign}(\omega_1) \neq \text{sign}(i_q) \quad (3.87b)$$

such that \tilde{R}_s and the product $\omega_1 i_q$ have equal signs. The signs of $\tilde{\theta}$ and the resistive part in (3.85) are then related as

$$\text{sign}(\tilde{\theta}) = \text{sign}\left(\frac{\omega_1 i_q}{\omega_1 L_M}\right) = \text{sign}(i_q). \quad (3.88)$$

It may be difficult to fulfill the above selection for \hat{R}_s in practice, however, since the true R_s is generally unknown. If R_s is greatly overestimated or greatly underestimated by \hat{R}_s , then frequency lockup may occur at low frequencies even for seemingly “simple” operation. It is hence preferred that R_s is confined to a well-defined and relatively small interval. Such an interval can possibly be found from a thermal model of the machine [112].

Fig. 3.6 shows a simulation where the system is forced to frequency lockup via \hat{R}_s . Notice that the flux modulus remains fairly constant about ψ_{ref} , so the critical flux collapse is safely avoided. The resulting performance is still far from satisfactory, however, since the speed reversal cannot be completed.

3.4.2 Lower Limit for Sustained Low-Frequency Operation

For inaccurately modeled R_s , an approximate value of the lowest stator frequency allowed in the steady-state operation can be calculated from (3.84). Solving this equation for ω_1 , and considering $\tilde{\theta} = 20^\circ = 0.34$ rad as the maximum error angle allowed, gives

$$\omega_{1,\min} = \frac{\tilde{R}_{s,\max}}{L_M \sin(0.34)} \approx 3 \frac{\tilde{R}_{s,\max}}{L_M} \quad (3.89)$$

where $\tilde{R}_{s,\max}$ is the maximum model error for R_s . For a worst-case scenario, a 60 % model error of R_s is considered:

$$\omega_{1,\min} = 3 \frac{0.6 R_{s,\text{cold}}}{L_M} = 1.8 \frac{R_{s,\text{cold}}}{L_M} \quad (3.90)$$

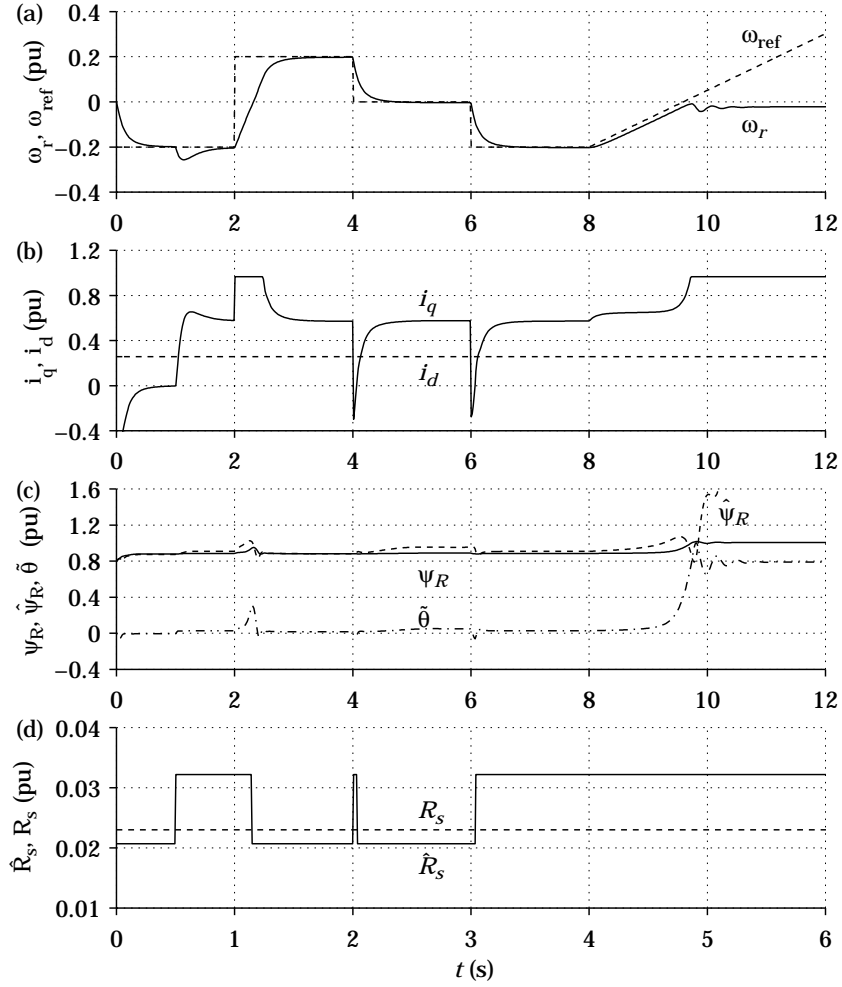


Fig. 3.6. Selection of stator resistance to avoid flux collapse; a constant load torque is applied at $t=1$ s, resulting in $i_q=0.6$ pu. The estimate \hat{R}_s is varied between $0.9R_s$ and $1.4R_s$, in order to avoid flux collapse.

where $R_{s,cold}$ is the resistance of a “cold” machine. Small machines, with relatively large R_s and small L_M , will have the largest $\omega_{1,min}$, so the 4-kW machine in Table 2.2 is considered for a numerical example. With $R_{s,cold} = 0.04$ pu and $L_M = 1.4$ pu, then $\omega_{1,min} = 1.8 \cdot 0.04/1.4 \approx 0.05$ pu. Hence, in order to be prepared for a very incorrect \hat{R}_s , sustained speed-sensorless operation for $|\omega_1| < 0.05$ pu should be avoided.

A method to avoid sustained low-frequency operation was presented in [31], and a similar algorithm also appeared in [76]. The synchronous frequency is with this method controlled by the flux modulus, such that the time spent in the low-frequency region is reduced to a minimum. However, this procedure demands for a large current modulus, since the flux modulus must be lowered quickly by i_d . We find this algorithm interesting; it is already patented and used in practice [34]. However, since a large current modulus is required (the inverter must be designed to allow over-current), the method is henceforth not considered.

3.5 Destabilization of Frequency Lockup

If frequency lockup has resulted from EP1 being unstable, then it may be possible to destabilize this instability phenomenon, such that stable operation about EP1 once again results. Below, two remedies that may accomplish this are discussed. Both methods presume that it is possible to avoid flux collapse by proper selection of \widehat{R}_s , as described in Section 3.4.1.

According to (3.33), frequency lockup (operation about EP2 with stable flux and mechanical dynamics) is stable for

$$|i_q| > i_d \lambda \text{sign}(\omega_1) \text{sign}(i_q). \quad (3.91)$$

This condition must be falsified in order to destabilize frequency lockup. Once EP2 has been made unstable, stable operation about EP1 is hopefully recovered. As seen from the above inequality, there are several alternatives that may destabilize EP2, but only two of these possibilities will be explored here: destabilization of EP2 by means of decreasing i_q , and destabilization by means of increasing λ . Consider (3.91): given that i_q and ω_1 have equal signs, then $\lambda i_d > |i_q|$ destabilizes frequency lockup. Thus, both decreasing i_q and increasing λ have similar destabilizing effects on frequency lockup.

3.5.1 Destabilization through i_q

Fig. 3.7 shows a simulation of making frequency lockup unstable via i_q through speed control. A constant load torque is applied at $t=1$ s, resulting in $i_q=0.6$ pu. The frequency lockup is first detected from ψ_R being much larger than ψ_{ref} . Then, the intended speed reversal is temporarily abandoned by selecting a negative speed reference. In consequence of the negative ω_{ref} , the speed controller demands for a smaller i_q , which has a destabilizing affect on frequency lockup according to (3.91). As seen in Fig. 3.7(c), accurate field orientation is retrieved at $t = 10$ s, and $\widehat{\psi}_R$ approaches ψ_{ref} . Once $\widehat{\psi}_R \approx \psi_{\text{ref}}$, then a faster attempt to reverse ω_r is triggered. This leads to a successful rotation reversal, since there is not sufficient time for frequency lockup to develop this time.

Even though the rotation of reversal is eventually completed, the drawback of the described algorithm is that the true rotor speed must temporarily deviate from ω_{ref} .

3.5.2 Destabilization through λ

As observed in Section 3.3.3, $\widehat{\psi}_R$ is larger than ψ_{ref} for frequency lockup. In order to make frequency lockup unstable by means of increasing λ , this observation is integrated with our previous choice for λ at low frequencies in (3.68):

$$\lambda = \frac{\sqrt{2}|\omega_1|}{\omega_{1,\text{min}}} + \lambda_p(\widehat{\psi}_R - \psi_{\text{ref}}), \quad |\omega_1| \leq \omega_{1,\text{min}} \quad (3.92)$$

where λ_p is a positive gain parameter. As seen, feedback of the quantity $\widehat{\psi}_R - \psi_{\text{ref}}$ is added to λ for $|\omega_1| \leq \omega_{1,\text{min}}$. For stable operation about EP1, then $\widehat{\psi}_R \approx \psi_R$ and the feedback hardly affects λ at all. For frequency lockup, on the other hand, the feedback gains λ , which in turn makes (3.91) false, such that stable operation about EP1 hopefully

results. Given that ω_1 and i_q have equal signs, then the following selection for λ_p falsifies (3.91) for $\hat{\psi}_R > 1.4\psi_{\text{ref}}$:

$$\lambda_p = 3 \frac{|i_q|}{i_d}. \quad (3.93)$$

Fig. 3.8 shows a simulation of the described algorithm. Frequency lockup is about to occur at $t = 9.5$ s, which can be seen from the large $\tilde{\theta}$ in Fig. 3.8(c). The flux estimate in Fig. 3.8(c) increases due to the lockup, which in turn gains λ via the feedback in (3.92). This makes EP2 unstable—accurate field orientation is retrieved—and the large accumulated i_q provides a fast and successful speed reversal, since there is not sufficient time for frequency lockup to once again develop.

Even though the speed reversal in Fig. 3.8 is completed in nearly the intended manner, the success of the method relies on that flux collapse is avoided through proper selection of \hat{R}_s , and stability has not been proven. Nevertheless, the promising result indicates that it may be possible to overcome the large sensitivity to \hat{R}_s for sensorless control. As discussed in Section 3.4, the preferred alternative would be if this could be directly integrated in the flux estimator design.

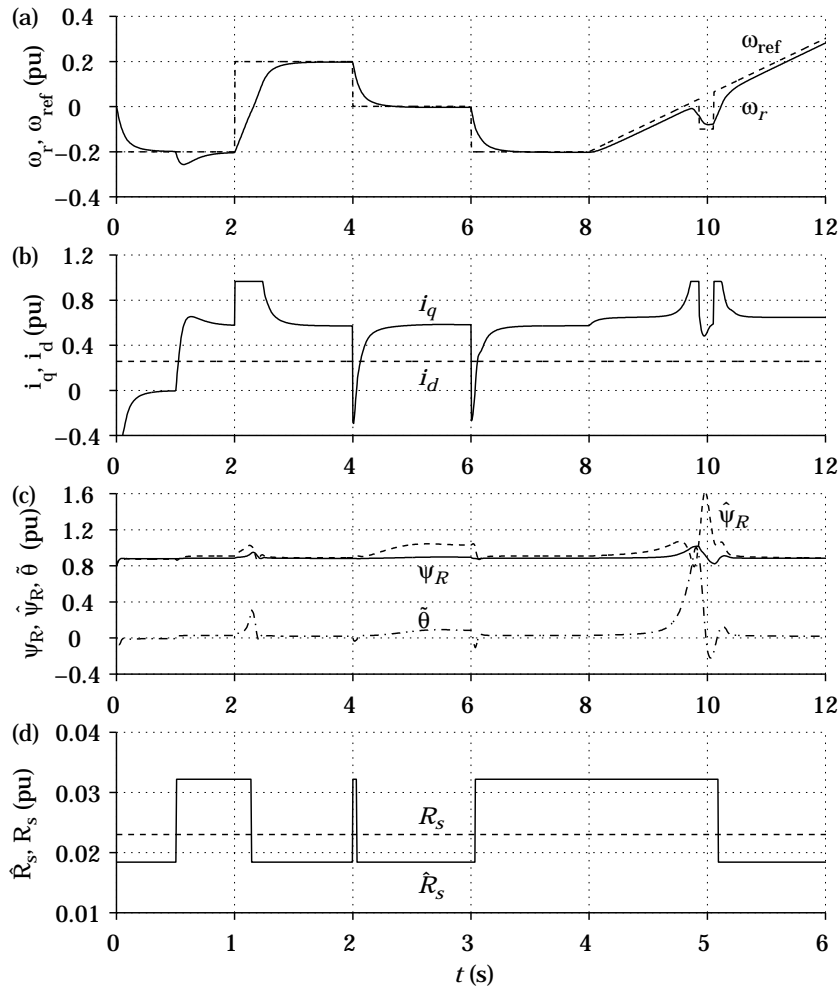


Fig. 3.7. Destabilization of EP2 through i_q ; a constant load torque is applied at $t=1$ s, resulting in $i_q=0.6$ pu.

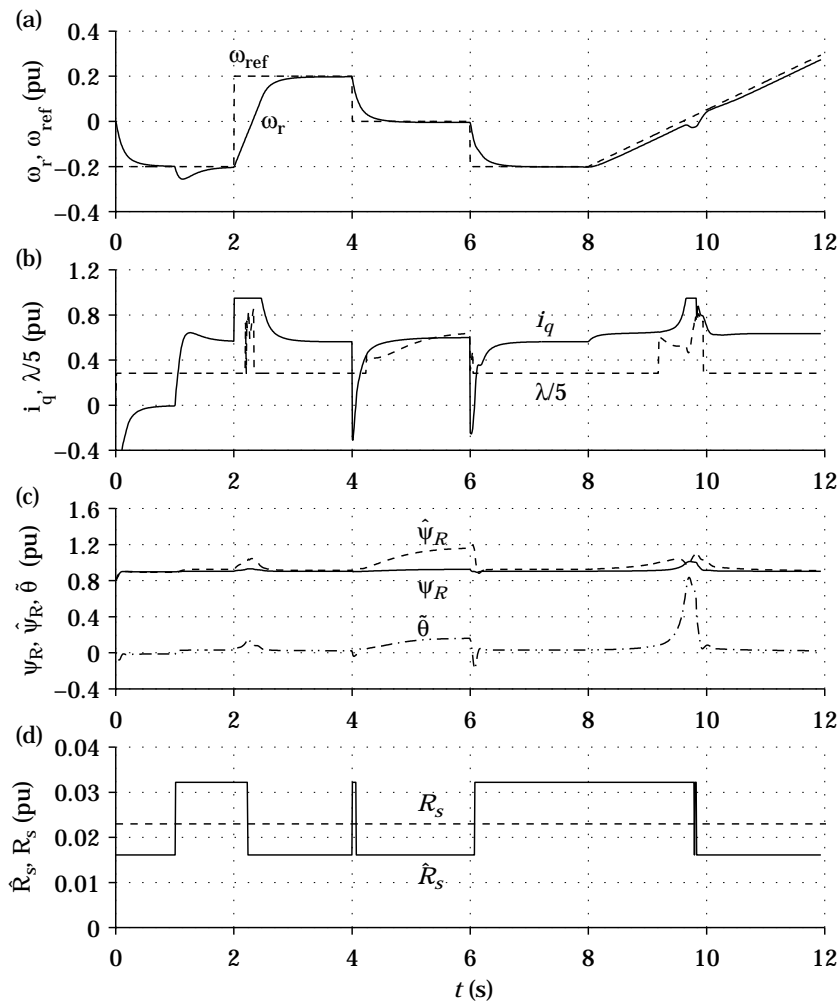


Fig. 3.8. Destabilization of EP2 through λ ; a constant load torque is applied at $t=1$ s, resulting in $i_q=0.6$ pu.

3.6 Implementation Issues

SCVM cannot be directly implemented in the form of (3.8)–(3.9). This is due to that (3.9) has an algebraic loop; both \hat{E}_d and \hat{E}_q are functions of ω_1 . In [50], this algebraic loop was broken up by embedding the selection of ω_1 within a first-order low-pass filter. This is a perfectly viable solution, but it is here preferred to solve (3.9) for ω_1 . Splitting the real and imaginary parts of (2.42) gives

$$\hat{E}_d = v_d - \hat{R}_s i_d + \omega_1 \hat{L}_\sigma i_q, \quad \hat{E}_q = v_q - \hat{R}_s i_d - \omega_1 L_\sigma i_d. \quad (3.94)$$

By substituting these relations in (3.8)–(3.9) and solving (3.9) for ω_1 , the following practical implementation of the SCVM results

$$\omega_1 = \frac{v_q - \hat{R}_s i_q - \lambda \text{sign}(\omega_1)(v_d - \hat{R}_s i_d)}{\hat{\psi}_R + \hat{L}_\sigma [i_d + \lambda \text{sign}(\omega_1) i_q]} \quad (3.95)$$

$$\frac{d\hat{\psi}_R}{dt} = \gamma(v_d - \hat{R}_s i_d + \omega_1 \hat{L}_\sigma i_q) \quad (3.96)$$

where

$$\lambda = \begin{cases} \sqrt{2}, & |\omega_1| > \omega_{1,\min} \\ \frac{\sqrt{2}|\omega_1|}{\omega_{1,\min}}, & |\omega_1| \leq \omega_{1,\min} \end{cases} \quad (3.97)$$

$$\gamma = 1. \quad (3.98)$$

It is recommended to select $\omega_{1,\min}$ equal to the above discussed lower limit for sustained low-frequency operation, which means $\omega_{1,\min} = 0.05$ pu.

With fast and accurate stator current control, i_d and i_q in the above SCVM equations can be replaced with i_d^{ref} and i_q^{ref} . This reduces the sensitivity to noise.

3.6.1 Discrete Implementation

The discrete form of the SCVM, using the forward difference approximation [10], is

$$\omega_{1,k} = \frac{v_{q,k} - \hat{R}_s i_{q,k} - \lambda_k \text{sign}(\omega_{1,k-1})(v_{d,k} - \hat{R}_s i_{d,k})}{\hat{\psi}_{R,k} + \hat{L}_\sigma [i_{d,k} + \lambda_k \text{sign}(\omega_{1,k-1}) i_{q,k}]} \quad (3.99)$$

$$\hat{\psi}_{R,k+1} = \hat{\psi}_{R,k} + \gamma T_s (v_{d,k} - \hat{R}_s i_{d,k} + \omega_{1,k} \hat{L}_\sigma i_{q,k}) \quad (3.100)$$

where T_s is the sampling period. Note that $\text{sign}(\omega_{1,k})$ is approximated with $\text{sign}(\omega_{1,k-1})$ in the right-hand side of (3.99). This approximation is incorrect for one sampling instant only, namely immediately after a sign change in ω_1 .

3.6.2 Summary of Recommended Model Parameters

The following model parameters are recommended:

\hat{R}_s : If R_s is known within a well-defined and relatively small interval, such that $R_{s,\min} < R_s < R_{s,\max}$, the following selection is recommended

$$\hat{R}_s < R_{s,\min}, \quad \text{sign}(\omega_1) = \text{sign}(i_q) \quad (3.101a)$$

$$\hat{R}_s > R_{s,\max}, \quad \text{sign}(\omega_1) \neq \text{sign}(i_q) \quad (3.101b)$$

since this avoids flux collapse, as long as $|\tilde{\theta}| < 90^\circ$. If no well-defined interval for R_s exists, we resign to the recommendation $\hat{R}_s = R_{s,\text{cold}}$.

\hat{L}_σ : Make sure that $\hat{L}_\sigma > L_\sigma$. This can be achieved by performing the usual blocked-rotor test at a stator current that is below the nominal value, and possibly adding some extra margin by hand for machines with closed rotor slots.

\hat{L}_M : Make sure that $\hat{L}_M < L_M$, so that the machine, via the relation $i_d^{\text{ref}} = \psi_{\text{ref}}/\hat{L}_M$, is not running under-fluxed at low speeds. This can be achieved by performing the usual no-load test at a stator voltage that is slightly above the nominal value.

Alternatively, the recommendation for \hat{L}_M can be formulated as: make sure that $\psi_R \approx \psi_{R,\text{nom}}$ at low speeds, or use preferably even a larger ψ_R if possible. This reduces the slip and, consequently, the region where $\text{sign}(\omega_1) \neq \text{sign}(\omega_r)$.

\hat{R}_R : It is recommended to overestimate the “cold” value for R_R by, say, 20 %, giving $\hat{R}_R = 1.2R_{R,\text{cold}}$. This yields an accurate speed estimate, via the relation $\hat{\omega}_r = \omega_1 - \hat{R}_R i_q / \hat{\psi}_R$, even for some heating of the rotor.

3.6.3 Combined “Current Model” and SCVM

Based on the discussion in Section 3.4.2, sustained low-frequency operation using the SCVM is only recommended if one of the following requirements is fulfilled:

- the stator resistance is confined within a relatively small interval;
- the load torque is almost zero for zero rotor speed.

If neither of these two requirements is fulfilled, the SCVM should be used for nominal speeds only, and the speed-sensored CM should be used for low speeds. This combines the low parameter sensitivity of the SCVM with the low-speed stability of the CM. The following allows for a smooth transition between the SCVM and the CM [48]:

$$\omega_1 = [1 - f_{\text{tr}}(\omega_1)] \frac{v_q - \hat{R}_s i_q - \lambda \text{sign}(\omega_1)(v_d - \hat{R}_s i_d)}{\hat{\psi}_R + \hat{L}_\sigma [i_d + \lambda \text{sign}(\omega_1) i_q]} + f_{\text{tr}}(\omega_1) \left(\omega_r + \frac{R_R i_q}{\psi_{\text{ref}}} \right) \quad (3.102)$$

$$\frac{d\hat{\psi}_R}{dt} = \begin{cases} \gamma \hat{E}_d, & |\omega_1| \geq \omega_{\Delta 1} \\ \alpha_f (\psi_{\text{ref}} - \hat{\psi}_R), & |\omega_1| < \omega_{\Delta 1} \end{cases} \quad (3.103)$$

where the filter gain α_f is chosen at least a decade larger than the speed control loop bandwidth, such that $\hat{\psi}_R$ converges quickly to ψ_{ref} for frequencies below $\omega_{\Delta 1}$. The function $f_{\text{tr}}(\cdot)$ makes a linear transition from 0 and 1 between the frequencies $\omega_{\Delta 1}$ and $\omega_{\Delta 2}$

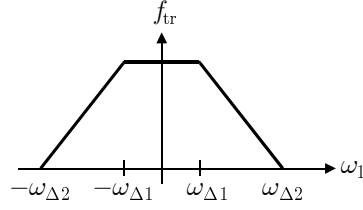


Fig. 3.9. Graph of $f_{\text{tr}}(\omega_1)$.

(recommended choices for these are 0.1 and 0.2 pu, respectively) [48]:

$$f_{\text{tr}}(\omega_1) = \begin{cases} 1, & |\omega_1| < \omega_{\Delta 1} \\ \frac{\omega_{\Delta 2} - |\omega_1|}{\omega_{\Delta 2} - \omega_{\Delta 1}}, & \omega_{\Delta 1} \leq \omega_1 < \omega_{\Delta 2} \\ 0, & |\omega_1| \geq \omega_{\Delta 2}. \end{cases} \quad (3.104)$$

Fig 3.9 depicts $f_{\text{tr}}(\cdot)$. With the above method, the CM is used for frequencies below $\omega_{\Delta 1}$, the SCVM ($\lambda = \sqrt{2}$ and $\gamma = 1$ can be used) for frequencies above $\omega_{\Delta 2}$, and a “compromise” of the two estimators is used in between.

3.7 Experimental Results

This section presents experimental evaluation of the SCVM. Only experiments at low speeds are conducted, since speed-sensorless operation at nominal speeds is unproblematic, as already shown in this chapter.

The experiments are carried out on the 22-kW test machine, which is described in Appendix B. Temperature sensors (PT-100, for monitoring only) are used to ensure that the machine is “cold” before each experiment, such that the “true” stator resistance is accurately represented by $R_s = 0.023$ pu. In addition, the resistance of the feeding power cable and cable interfaces is $R = 0.006$ pu. The cable resistance is added to \hat{R}_s in the experiments, but not included in the following discussion nor in the presented graphs.

The induction machine is loaded by a separately excited dc machine, which acts as a constant load torque. The armature current of the dc machine is controlled by way of a thyristor converter. In contrast to the simulations in this chapter, the load torque that requires $i_q = 0.6$ pu is applied before $t = 0$. This is made for reasons of simplicity, and does not affect the results of the experiments. The model parameters for the experiments are:

$$\hat{L}_\sigma = 1.1L_\sigma, \quad \hat{L}_M = 0.9L_M, \quad \hat{R}_R = 0.9R_R$$

while the critical model parameter \hat{R}_s is explicitly stated for each experiment. The SCVM is implemented as described in Section 3.6, and $\omega_{1,\text{min}} = 0.05$ pu. The command stator voltage vector is used for flux estimation, meaning that the true stator voltage is not measured.

Closed-loop current and speed control according to Chapter 6 is implemented. The bandwidths of the current control loop and the speed control loop are 2.5 pu and

0.02 pu, respectively, which correspond to approximate rise times of 2.8 ms and 0.35 s. The filter bandwidth of the speed estimator in (2.52) is $\alpha_f = 0.2$ pu. The rotor flux reference is set to $\psi_{\text{ref}} = 0.9$ pu, and the maximum allowed stator current modulus is 1 pu.

The PWM inverter is based on a Skippack 342GD120-314CTV, and the dc-link voltage is 400 V. The control computer is an IEA-MIMO [24], which uses a Texas TMS320C30 floating-point processor, and 4.9 kHz sampling and switching frequency is used for the experiments. Fluctuations in the dc-link voltage, as well as the blanking time and on-state voltage drop of the semiconductor valves, are compensated as described in [88]. RMS-value scaling is used between the three-phase system and the stator-oriented reference frame. A resolver is used for speed and position measurement (for monitoring only).

3.7.1 Very Accurately Modeled Stator Resistance

The purpose of this experiment is to investigate the ideal case of a very accurately modeled stator resistance. The speed reference is stepped through the sequence

$$\begin{array}{rccccc} t \text{ (s)} \approx & 0 & 2 & 4 & 6 \\ \omega_{\text{ref}} \text{ (pu)} & -0.2 & 0.2 & 0 & -0.2 \end{array}$$

and then slowly positively ramped at $t = 8$ s, starting from $\omega_{\text{ref}} = -0.2$ pu. The machine is throughout the entire experiment loaded by a constant load torque that requires $i_q = 0.6$, and the stator resistance estimate is $\hat{R}_s = R_s$.

Fig. 3.10 shows the results of the experiment. The performance is generally good, but some “bumps” can be seen in $\hat{\psi}_R$ and i_q for zero-speed operation and for zero-speed crossing. These “bumps” can be due to one, or several, of the following three reasons. Firstly, there is a small poorly damped region about $\omega_1 = 0$, as seen from the pole loci in Fig. 3.2. Secondly, stable low-speed operation with $\hat{R}_s = R_s$ cannot be guaranteed for this machine, since $L_M = 2.8$ pu is larger than the condition for stability in (3.71). Thirdly, it is unlikely that the stator resistance is perfectly modeled.

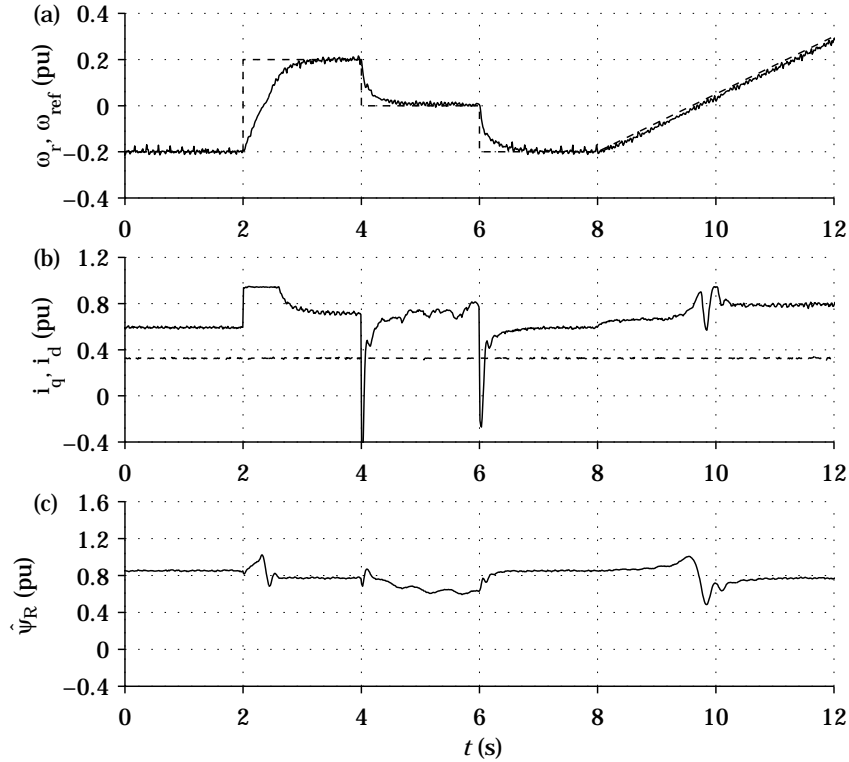


Fig. 3.10. Successful operation for the ideal case $\hat{R}_s = R_s$: experiment.

3.7.2 Flux Collapse

The purpose of this experiment is to verify the instability phenomenon flux collapse, for the SCVM in particular. The speed reference is stepped through the same sequence as above described, and an identical load torque is present, but the stator resistance estimate is now $\hat{R}_s = 0.7R_s$.

Fig. 3.11 shows the results of the experiment. Good agreement to the corresponding simulation in Fig. 3.4 can be observed, albeit the speed step from -0.2 pu to 0.2 pu is more troublesome in the experiment. At $t = 9.5$ s, flux collapse occurs for the slow speed ramping against the load torque, and the experiment is interrupted on purpose at $t = 10.5$ s.

3.7.3 Frequency Lockup

The purpose of this experiment is to verify the instability phenomenon frequency lockup, for the SCVM in particular. The speed setpoint is varied in the same manner as described in the first experiment, and the same load torque is present, but the stator resistance estimate is now $\hat{R}_s = 1.4R_s$.

Fig. 3.12 shows the results of the experiment. Good agreement to the corresponding simulation in Fig. 3.5 can be observed, even though a more oscillatory behavior can be spotted in the experiment for the zero-speed operation, indicating stability problems. The slow positive speed ramp against the load torque is once again critical for stability, and frequency lockup occurs at $t = 10$ s.

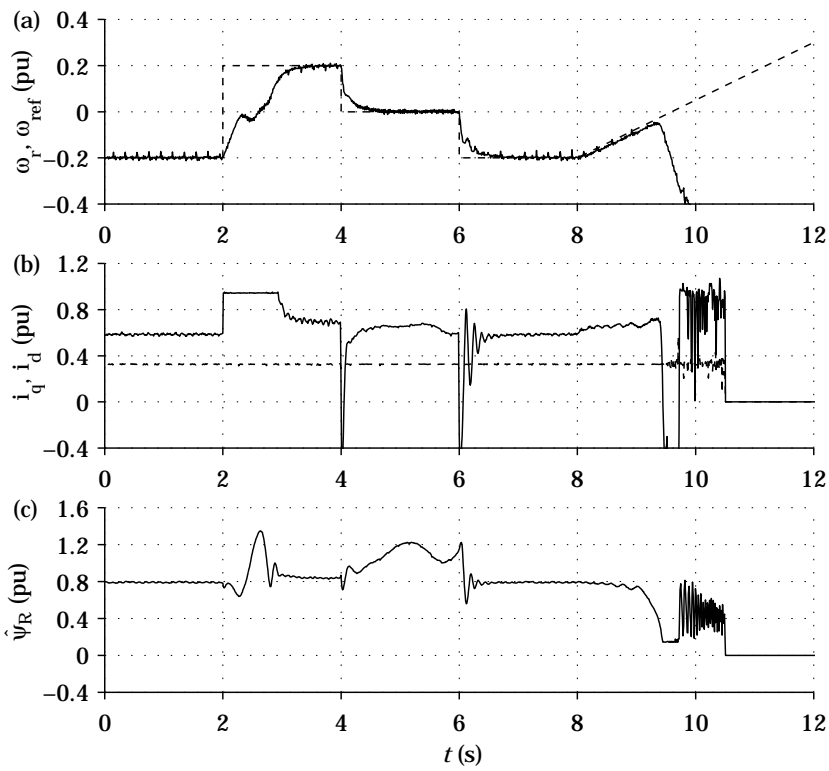


Fig. 3.11. Flux collapse with $\hat{R}_s = 0.7R_s$: experiment.

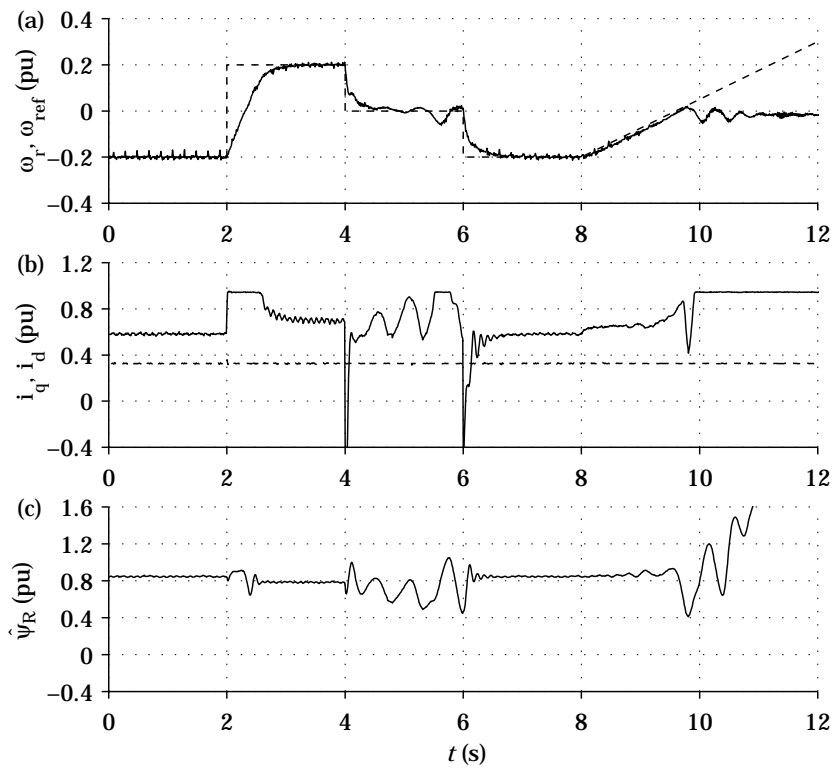


Fig. 3.12. Frequency lockup with $\hat{R}_s = 1.4R_s$: experiment.

3.7.4 Very Slow Speed Ramping

The purpose of this experiment is to investigate the performance of the SCVM for an even slower speed ramping and larger load torque than in the previous experiments. The speed setpoint is slowly ramped from 0.2 to -0.2 pu in ten seconds, and then slowly ramped from -0.2 to 0.2 pu. The load torque is meanwhile constant, corresponding to $i_q = 0.8$ pu. In contrast to the previous experiments, \hat{R}_s is selected as described in Section 3.6.2 in order to avoid flux collapse. The underestimated and the overestimated values are $\hat{R}_s = 0.7R_s$ and $\hat{R}_s = 1.4R_s$, respectively.

Fig. 3.13 shows the results of the experiment. The negative speed ramp is stable, while frequency lockup results at $t = 16$ s for the positive speed ramp against the load torque. It can be seen from Fig. 3.13(c) that λ is close to zero for frequency lockup, so the SCVM provides almost no feedback to the closed-loop dynamics. If λ were not lowered, however, then the resulting dynamics from the SCVM would be fairly unstable at low frequencies even when $\hat{R}_s = R_s$, as shown in Section 3.2.5.

3.7.5 Destabilization of Frequency Lockup through λ

The purpose of this experiment is to verify that frequency lockup, once it has occurred, can be destabilized through the gain parameter λ . The speed setpoint is varied in the same manner as above described for the experiment on very slow speed ramping.

Fig. 3.14 shows the results of the experiment. It can be seen that the speed is now successfully reversed for the positive speed ramping, although tendencies to frequency lockup can be spotted in $\hat{\psi}_R$ and i_q . These tendencies are suppressed by λ increasing, so frequency lockup does not fully develop.

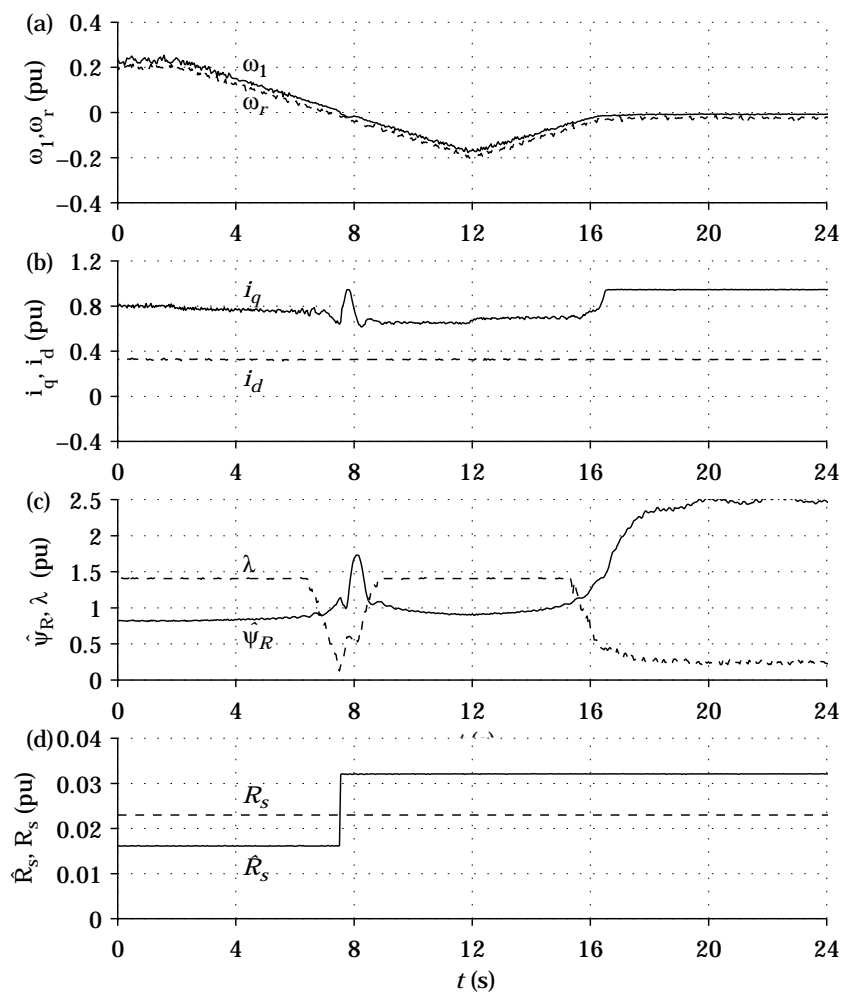


Fig. 3.13. Very slow speed ramping with alternating \hat{R}_s : experiment.

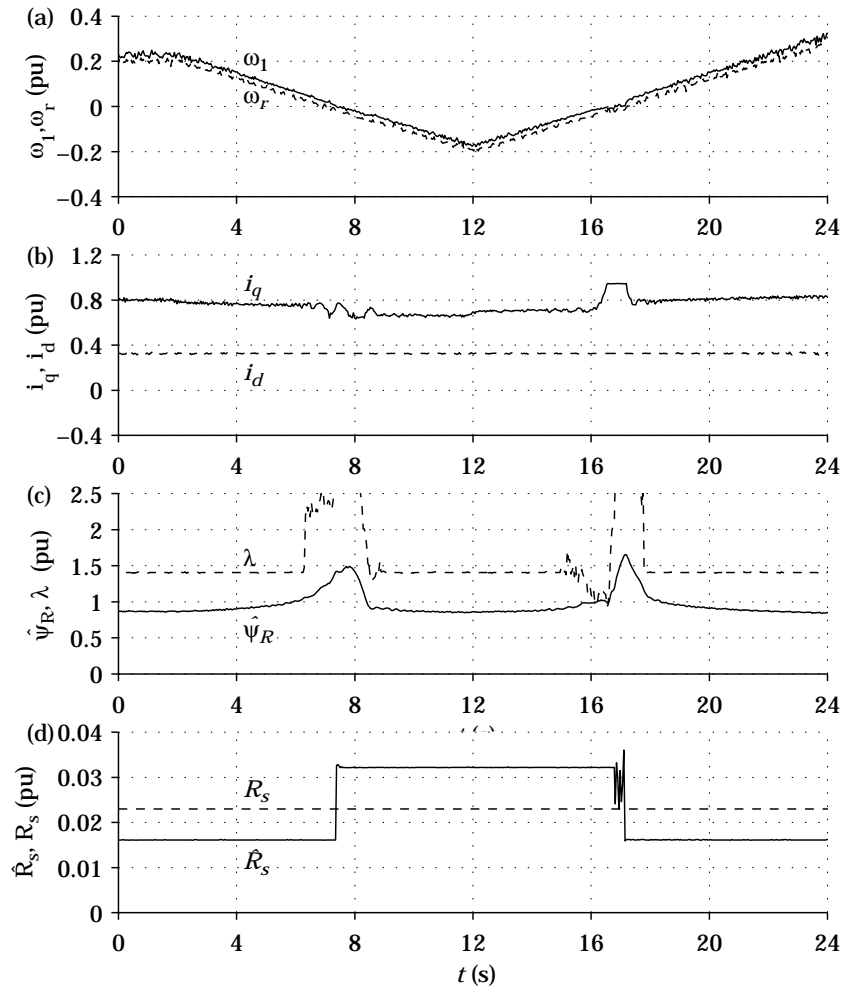


Fig. 3.14. Very slow speed ramping with alternating \hat{R}_s and destabilization through λ : experiment.

Chapter 4

PWM Rectifier Models and Vector Control

The objective of this chapter is to derive and describe models for a PWM rectifier, see Appendix C for a list of glossary terms. Moreover, the concepts of grid flux and grid-flux estimation are described, and some grid voltage disturbances that may occur are discussed.

4.1 PWM Rectifier Models

An ideal lossless representation of the back-to-back converter, depicted in Fig. 4.1 is assumed. Since a single PWM converter has an efficiency of 94–98 % [14], the lossless approximation is reasonable for our modeling purposes. It is also assumed that the PWM rectifier is connected to a stiff utility grid, such that a grid filter constitutes the grid current dynamics.

Motor references are used for both the utility grid and the ac machine. The positive reference directions for the grid power, P_g , and the machine power, P_s , are therefore as indicated in Fig. 4.1. Observe that the true directions for P_g and P_s may change at any instant, due to the four-quadrant capability of the back-to-back converter.

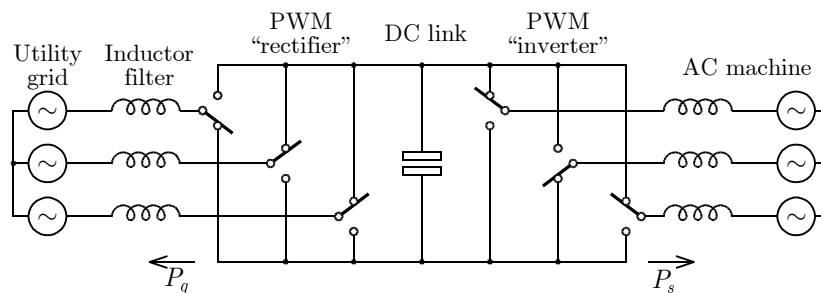


Fig. 4.1. Back-to-back converter model.

4.1.1 Introducing Grid Flux

References [36, 84, 85] all proposed the same idea, namely to introduce a *virtual grid flux*, $\boldsymbol{\psi}_g$, in order to fully acknowledge the similarities between vector control of PWM rectifiers and field orientation of ac machines. The grid flux vector is defined by the following static quantity:

$$\boldsymbol{\psi}_g^s \triangleq \frac{\mathbf{E}_g^s}{j\omega_g} = \psi_g e^{j\theta_g} \quad (4.1)$$

where

\mathbf{E}_g^s grid voltage;
 ω_g angular grid frequency;
 ψ_g, θ_g grid flux modulus and grid flux angle.

The grid frequency is normally almost constant. According to Swedish standard, for instance, the grid frequency remains within 50 ± 0.1 Hz, except for a few hours every year [108]. Consequently, the grid flux is directly related to the grid voltage. Field orientation for a PWM rectifier can therefore be expressed either in terms of grid voltage or grid flux—the latter alternative is preferred in this thesis.

4.1.2 Synchronous and Stator-Oriented Reference Frames

Similar to the induction machine, space vectors given in the stator-oriented reference frame are denoted with superscript “s,” e.g., $\boldsymbol{\psi}_g^s = \psi_g e^{j\theta_g}$, while space vectors given in the synchronous reference frame are denoted without superscript, e.g., $\boldsymbol{\psi}_g = \psi_g e^{j\tilde{\theta}}$. Of course, the synchronous coordinates for a PWM rectifier and an induction machine are two totally different reference systems; the synchronous reference frame is for a PWM rectifier defined by the *estimated grid flux*, i.e., $\hat{\boldsymbol{\psi}}_g^s = \hat{\psi}_g e^{j\theta_1}$. Fig. 4.2 shows the synchronous and the stator-oriented reference systems for a PWM rectifier.

4.1.3 Dynamic Inductor Filter Model

A filter is required to reduce the ripple of the grid current, and thereby comply with standards such as [65]. A variety of filters are available, for instance inductor filters, LCL filters [55, 82], and filters that are tuned for resonance at multiples of the switching frequency [110]. Only inductor filters are henceforth considered, we refer to the mentioned references for details on the other filter topologies.

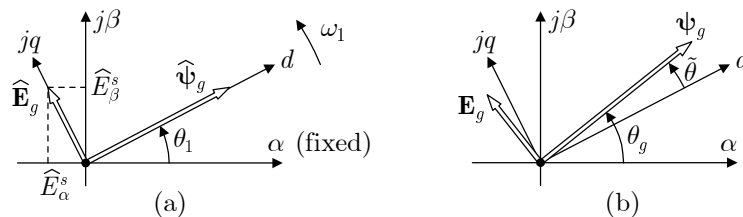


Fig. 4.2. The synchronous (dq) and the stator-oriented ($\alpha\beta$) reference frames. (a) Estimated grid flux and grid voltage. (b) True grid flux and grid voltage.

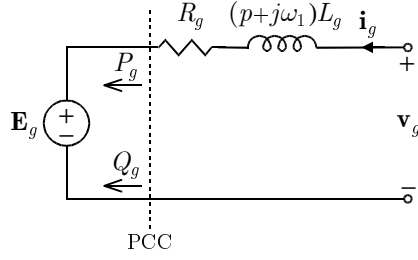


Fig. 4.3. Dynamic model of the inductor filter. The point of common connection (PCC) is indicated.

Fig. 4.3 shows the dynamic equivalent circuit of an inductor filter in the synchronous reference frame, which can be written as

$$L_g \frac{d\mathbf{i}_g}{dt} = \mathbf{v}_g - (R_g + j\omega_1 L_g)\mathbf{i}_g - \mathbf{E}_g \quad (4.2)$$

where

- \mathbf{v}_g terminal voltage of the PWM rectifier;
- \mathbf{E}_g grid voltage;
- \mathbf{i}_g grid current;
- L_g, R_g inductance and resistance of the inductor filter.

The equivalent circuit in the stator-oriented reference frame is obtained by putting $\omega_1 = 0$ in (4.2), and adding superscripts “s” to \mathbf{i}_g , \mathbf{E}_g , \mathbf{v}_g .

In the following, the grid current dynamics in (4.2) will normally be neglected, which is done for similar reasons as described in Section 2.2. By putting $di/dt = 0$, solving for \mathbf{v}_g , and splitting the real and the imaginary parts of \mathbf{v}_g , the components of the terminal voltage are then found to be

$$v_d = R_g i_d - \omega_1 L_g i_q + E_d \quad (4.3)$$

$$v_q = R_g i_q + \omega_1 L_g i_d + E_q. \quad (4.4)$$

The grid current dynamics are only considered in Chapter 6, where current control is studied.

4.1.4 Grid Voltage Disturbances

Various disturbances are present in the grid voltage, so $E_\alpha^s(t)$, for instance, is therefore not a perfect sinusoid. The grid voltage disturbances are often due to *voltage harmonics* or *voltage dips* [37], and these disturbances are here discussed and modeled. Note that there are also other types of types of disturbances, such as swells and unbalances [37], but these will essentially be covered by our resulting grid voltage model.

Voltage Harmonics

The grid voltage harmonics may contain all odd multiples of the fundamental frequency, i.e., $[5\omega_g, 7\omega_g, 11\omega_g, \dots]$, including triplen harmonics, i.e., $[3\omega_g, 9\omega_g, 15\omega_g, \dots]$. The triplens are not critical for a PWM rectifier, as they are zero sequences [37] and, hence, disappear from the phase currents due to the absence of a neutral conductor.

Voltage Dips

A voltage dip is a decrease in the grid voltage magnitude from 1 pu to 0.1–0.9 pu, having a duration of between 0.5 cycles up to one minute [37].

Symmetrical voltage dips are due to three-phase faults, and result in a simultaneous reduction of the voltage modulus in all three phases. Large symmetrical voltage dips are highly critical for a PWM rectifier. In order to maintain a certain active power, the reduced voltage modulus must be compensated by a larger current modulus. This is, however, only possible as long as the grid current modulus remains below the maximum value allowed.

Non-symmetrical voltage dips are due to single-phase and two-phase faults. Generally, the grid voltage during a non-symmetrical voltage dip can be described by a positive sequence, a negative sequence and a zero sequence [37]. The positive and negative sequences both have the same frequency, equal to the fundamental grid frequency, but their space-vector correspondences rotate in the counter-clockwise and clockwise directions, respectively.

A voltage dip is often associated with a so-called “*phase-angle jump*,” which is a sudden change in the grid voltage angle. The “*phase-angle jump*” is essentially due to that the grid impedance changes during the fault [37].

Model of Grid Voltage Disturbances

The grid voltage disturbances are modeled as

$$\mathbf{E}_g^s = jE_1^+ e^{j\theta_g} + jE_1^- e^{-j(\theta_g+\phi_1)} + jE_5 e^{-j(5\theta_g+\phi_5)} + jE_7 e^{j(7\theta_g+\phi_7)} \quad (4.5)$$

where

- E_1^+, E_1^- magnitudes of the positive and negative sequence voltages;
- E_5, E_7 magnitudes of the fifth- and the seventh-order voltage harmonics.

The magnitude of the negative-sequence voltage may be as large as the magnitude of the positive-sequence voltage for a non-symmetrical fault, but is normally small for normal operation [37].

It is for modeling purposes useful to transform the grid voltage to the synchronous reference frame. By substituting $\mathbf{E}_g^s = \mathbf{E}_g e^{j\theta_1}$ in (4.5), the grid voltage vector then transforms to

$$\begin{aligned} \mathbf{E}_g &= jE_1^+ e^{j\tilde{\theta}} + jE_1^- e^{-j(2\theta_g - \tilde{\theta} + \phi_1)} + jE_5 e^{-j(6\theta_g - \tilde{\theta} + \phi_5)} + jE_7 e^{j(6\theta_g + \tilde{\theta} + \phi_7)} \\ &= jE_1^+ e^{j\tilde{\theta}} + \mathbf{E}_g^{2,6} \end{aligned} \quad (4.6)$$

where $\tilde{\theta} = \theta_g - \theta_1$ is the error angle, and $\mathbf{E}_g^{2,6}$ is the “total” grid voltage disturbance. The frequency of the negative sequence, formed by E_1^- , appears as $2\omega_g$ in the synchronous reference frame, while the fifth- and seventh-order harmonics appear as $-6\omega_g$ and $6\omega_g$, respectively.

For the special case of the grid voltage being a pure sinusoid, (4.6) reduces to

$$\mathbf{E}_g = jE_g e^{j\tilde{\theta}} = j\omega_g \psi_g e^{j\tilde{\theta}}. \quad (4.7)$$

Eq. (4.7) will, henceforth, be considered for stability analyses, while (4.6) will be used for designating the disturbance reduction of different flux estimators.

4.1.5 Active and Reactive Power

The *instantaneous active power* and the *instantaneous reactive power* [4] at the point of common connection, see Fig. 4.3, are

$$P_g = 3 \operatorname{Re}\{\mathbf{E}_g \mathbf{i}_g^*\} = 3E_g(i_q \cos \tilde{\theta} - i_d \sin \tilde{\theta}) \quad (4.8)$$

$$Q_g = 3 \operatorname{Im}\{\mathbf{E}_g \mathbf{i}_g^*\} = 3E_g(i_q \sin \tilde{\theta} + i_d \cos \tilde{\theta}). \quad (4.9)$$

respectively. Due to the small losses of the inductor filter, P_g more or less equals the active power at the terminal of a PWM rectifier.

For accurate field orientation, (4.8)–(4.9) simplify to

$$P_g = 3E_g i_q, \quad Q_g = 3E_g i_d \quad (4.10)$$

so the active power and the reactive power can now be controlled independently via i_q and i_d , respectively. Often $i_d = 0$ is selected, which provides unity power factor at the point of common connection and the minimal modulus for \mathbf{i}_g .

4.1.6 DC-Link Model

The dc-link is modeled as a pure capacitor. The dynamic equivalent circuit of the dc-link is shown in Fig. 4.4, where

- C dc-link capacitance;
- v_{dc}, i_C dc-link voltage, capacitor current;
- P_s load power that results from the ac machine, $P_s = 3 \operatorname{Re}\{\mathbf{v}_s \mathbf{i}_s^*\}$.

The electrolytic capacitor bank at the dc-link is an energy storage, where the stored electrical energy is $Cv_{dc}^2/2$. The time derivative of the stored energy must equal the sum of the instantaneous grid power and P_s . For accurate field orientation, the dc voltage dynamics can thus be written as

$$\frac{1}{2}C \frac{d(v_{dc}^2)}{dt} = -P_g - P_s = -3E_g i_q - P_s \quad (4.11)$$

which is nonlinear with respect to v_{dc} . The time derivative of v_{dc}^2 in the above differential equation can be evaluated as

$$Cv_{dc} \frac{dv_{dc}}{dt} = -P_g - P_s \quad (4.12)$$

which yields an alternative expression for the dc voltage dynamics. The equivalent circuit in Fig. 4.4 is based on this alternative expression.

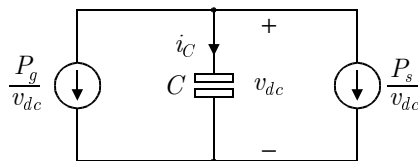


Fig. 4.4. Dynamic equivalent circuit of the dc link.

4.2 Grid-Flux Estimation

Grid-flux estimation for a PWM rectifier has many similarities to inherently sensorless flux estimation for an induction machine, since the grid voltage can be considered as the correspondence to the flux EMF. In contrast to an induction machine, however, the grid flux is hardly affected by a single PWM rectifier. The problem of grid-flux estimation is therefore a matter of synchronizing the vector control system to the grid flux vector (or grid voltage vector). This means that there is no correspondence to the CM for grid-flux estimation, and that the grid flux angle is initially unknown at startup of a PWM rectifier. The former issue is unavoidable, but the latter one can be circumvented by either measuring the grid voltage or, if the grid voltage is not measured, by implementing a special startup procedure [11].

The classical grid flux “estimator” is derived by measuring the grid voltage, giving the following “estimated” grid flux [72, 73]:

$$\widehat{\Psi}_g^s = \frac{\mathbf{E}_g^s}{j\omega_1} = \frac{E_\beta^s - jE_\alpha^s}{\omega_1}. \quad (4.13)$$

This can be considered as a DFO-type estimator, so the transformation factors $e^{j\theta_1}$ and $e^{-j\theta_1}$ are then readily available from

$$e^{j\theta_1} = \frac{\widehat{\Psi}_g^s}{\widehat{\psi}_g} = \frac{E_\beta^s - jE_\alpha^s}{\sqrt{(E_\beta^s)^2 + (E_\alpha^s)^2}} \quad (4.14)$$

$$e^{-j\theta_1} = \frac{(\widehat{\Psi}_g^s)^*}{\widehat{\psi}_g} = \frac{E_\beta^s + jE_\alpha^s}{\sqrt{(E_\beta^s)^2 + (E_\alpha^s)^2}}. \quad (4.15)$$

Unfortunately, disturbances in \mathbf{E}_g are for this method directly transmitted to $e^{j\theta_1}$ and $e^{-j\theta_1}$, and will therefore be reproduced in the grid current [36]. To circumvent this problem, a phase-locked-loop (PLL) type estimator is often applied for grid-flux estimation [11, 28, 36]. The PLL-type estimator improves the rejection of the grid voltage disturbances, as will be shown in the next chapter. Ideally, the grid voltage disturbances should be fully rejected, such that the synchronous reference frame is aligned with the fundamental grid flux only. This is here defined as perfect field orientation for a PWM rectifier, and corresponds to $\tilde{\theta} = 0$ in (4.6).

The flux “estimator” in (4.14)–(4.15) is static, since the field orientation is retrieved instantaneously. For a dynamic flux estimator, such as a PLL-type estimator, field orientation is not retrieved instantaneously. This is unavoidable, since a dynamic estimator should have a fairly low bandwidth in order to reduce grid voltage harmonics [28]. The dynamics of a grid flux estimator are not coupled to the “true” static grid flux though, so the resulting dynamics are not as complex as for flux estimation of an induction machine. It is nonetheless important to properly assess the dynamics, for at least the following two reasons. Firstly, an estimator that rejects grid voltage harmonics poorly, or a poorly damped flux estimator, introduces harmonics in \mathbf{i}_g^s via the Park transformation. Secondly, active and reactive power can only be controlled independently for accurate field orientation, as discussed in Section 4.1.5.

4.2.1 Voltage-Sensorless Flux Estimation

As described in [85], and similar proposals have also appeared in [11, 84, 91], it is not necessary to achieve grid-flux orientation by measuring the grid voltage. We shall refer to this as *voltage-sensorless flux estimation*, and discuss the fundamentals of such estimation in the following.

By solving (4.2) for \mathbf{E}_g , assuming $d\mathbf{i}_g/dt = 0$, the true grid voltage vector is found to be

$$\mathbf{E}_g = \mathbf{v}_g - (R_g + j\omega_1 L_g)\mathbf{i}_g. \quad (4.16)$$

This vector is, however, unknown for a voltage-sensorless flux estimator, which must rely on the estimated grid voltage. The estimated grid voltage is derived by substituting the true parameters in the above expression with their model correspondences:

$$\hat{\mathbf{E}}_g = \mathbf{v}_{\text{ref}} - \hat{R}_g \mathbf{i}_g - j\omega_1 \hat{L}_g \mathbf{i}_g. \quad (4.17)$$

Observe that the estimate does not use the true measured terminal voltage, since not much would have been gained by eliminating the grid voltage sensors otherwise. The estimated grid voltage must instead rely on the command terminal voltage, \mathbf{v}_{ref} , which results from the current control loop.

By subtracting (4.16) from (4.17), assuming $\mathbf{v}_{\text{ref}} = \mathbf{v}_g$, and solving for $\hat{\mathbf{E}}_g$, the parameter sensitivity of voltage-sensorless flux estimation is revealed:

$$\hat{\mathbf{E}}_g = (\tilde{R}_g + j\omega_1 \tilde{L}_g)\mathbf{i}_g + \mathbf{E}_g \quad (4.18)$$

where

$$\tilde{R}_g = R_g - \hat{R}_g, \quad \tilde{L}_g = L_g - \hat{L}_g \quad (4.19)$$

are the errors in the model parameters. As seen, $\hat{\mathbf{E}}_g = \mathbf{E}_g$ for accurate model parameters. Moreover, a good agreement can be expected for inaccurate model parameters as well, since the resistive and inductive parts of the above equation are normally small compared to \mathbf{E}_g . This means that *similar performance can be expected for sensed and voltage-sensorless operation with respect to field orientation*, as previously noticed in [11, 84, 85, 91]. Fig. 4.5 shows a voltage-sensored vector control system for a PWM rectifier, while Fig. 4.6 depicts a voltage-sensorless system.

As for inherently sensorless flux estimation, information regarding the grid flux angle (or grid voltage angle) is mainly seen in \hat{E}_d . Substituting (4.7) in (4.18), assuming accurate model parameters, and splitting the real and the imaginary parts, gives

$$\hat{E}_d = E_d = -\omega_g \psi_g \sin \tilde{\theta}, \quad \hat{E}_q = E_q = \omega_g \psi_g \cos \tilde{\theta} \quad (4.20)$$

which for small $\tilde{\theta}$, such that $\sin \tilde{\theta} \approx \tilde{\theta}$ and $\cos \tilde{\theta} \approx 1$, can be approximated by

$$\hat{E}_d = E_d \approx -\omega_g \psi_g \tilde{\theta}, \quad \hat{E}_q = E_q \approx \omega_g \psi_g. \quad (4.21)$$

Since the grid frequency for normal operation is constant at $\omega_g = 1$ pu, a deviation from accurate field orientation, meaning $\tilde{\theta} = 0$, is hence always seen directly in \hat{E}_d .

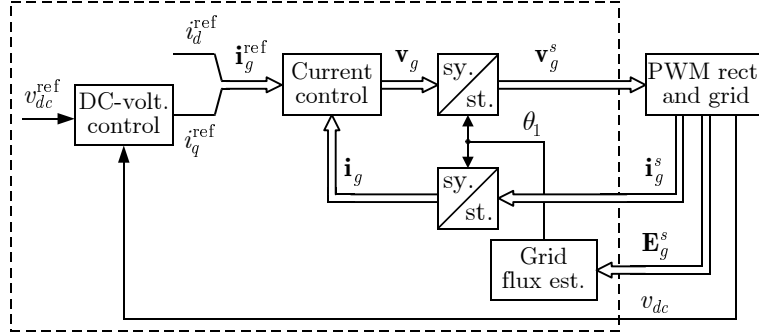


Fig. 4.5. Vector control system for the PWM rectifier that uses the measured grid voltage for field orientation, consisting of a “flux estimator,” a dc voltage controller that yields the setpoint for the q -axis current, and a current controller.

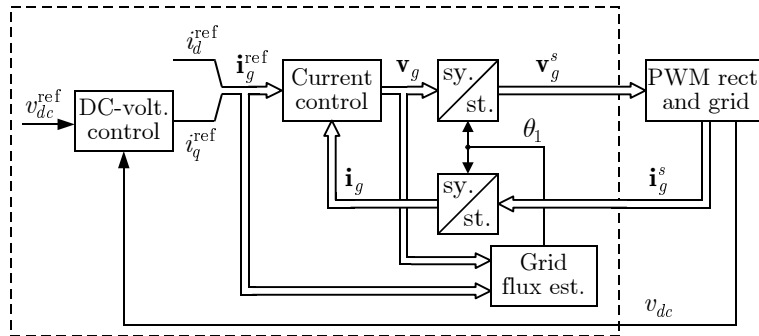


Fig. 4.6. Vector control system for the PWM rectifier that uses an IFO voltage-sensorless flux estimator.

4.2.2 VM for Grid-Flux Estimation

In addition to the PLL-type estimator, also the traditional VM has been proposed for dynamic grid-flux estimation [85]:

$$\frac{d\hat{\Psi}_g^s}{dt} = \mathbf{E}_g^s. \quad (4.22)$$

Observe that the VM is here expressed in terms of the measured grid voltage, but a grid voltage estimate may just as well be used for input. The dynamics of the VM are derived by substituting $\hat{\psi}_g^s = \hat{\psi}_g e^{j\theta_1}$ and $\mathbf{E}_g^s = j\omega_g \psi_g e^{j\theta_g}$ in (4.22):

$$\begin{aligned} (\hat{\dot{\psi}}_g + j\dot{\theta}_1 \hat{\psi}_g) e^{j\theta_1} &= j\omega_g \psi_g e^{j\theta_g} \\ \Rightarrow \hat{\dot{\psi}}_g &= j\omega_g \psi_g e^{j\tilde{\theta}} - j\dot{\theta}_1 \hat{\psi}_g. \end{aligned} \quad (4.23)$$

By splitting the real and imaginary parts of this equation, substituting $\theta_1 = \theta_g - \tilde{\theta}$, and solving the imaginary part for $d\tilde{\theta}/dt$, the resulting nonlinear dynamics of the VM become

$$\frac{d\hat{\psi}_g}{dt} = -\omega_g \psi_g \sin \tilde{\theta} \quad (4.24)$$

$$\frac{d\tilde{\theta}}{dt} = \dot{\theta}_g - \dot{\theta}_1 = \omega_g \left(1 - \frac{\psi_g}{\hat{\psi}_g} \cos \tilde{\theta} \right). \quad (4.25)$$

For $\widehat{\psi}_g \approx \psi_g$, the quotient in the above equation can be approximated by

$$\frac{\psi_g}{\widehat{\psi}_g} = \frac{\psi_g}{\psi_g + \widetilde{\psi}_g} \approx 1 - \frac{\widetilde{\psi}_g}{\psi_g}. \quad (4.26)$$

By substituting this in (4.25), and assuming small $\tilde{\theta}$ in (4.24)–(4.25), such that $\cos \tilde{\theta} \approx 1$ and $\sin \tilde{\theta} \approx \tilde{\theta}$, the following state-space system results for the VM:

$$\frac{d}{dt} \begin{bmatrix} \widetilde{\psi}_g \\ \tilde{\theta} \end{bmatrix} = \begin{bmatrix} 0 & -\omega_g \psi_g \\ \omega_g / \psi_g & 0 \end{bmatrix} \begin{bmatrix} \widetilde{\psi}_g \\ \tilde{\theta} \end{bmatrix}. \quad (4.27)$$

It can be directly seen that the poles resulting from the VM are located at $\pm j\omega_g$, so the dynamics are quite oscillatory. This is a similar conclusion that was drawn for the induction machine in Section 2.6. The damping of the VM can be slightly improved by using various lowpass-filtered variants [22, 36], but a better solution was described in Section 3.1: the SCVM. The analysis of the SCVM for grid-flux estimation is partly the content of the following chapter.

Chapter 5

Analysis and Development of Grid Flux Estimators

Three grid-flux estimators are analyzed in this chapter, both dynamically and for the steady-state operation. These estimators are the commonly used PLL-type estimator, the SCVM, and a simplified variant of the SCVM, which is developed in this chapter. The PLL-type estimator has previously been proposed for grid-flux estimation in [11, 28], albeit our design is closest in spirit with that in [52] for speed-sensorless vector control of ac machines.

The SCVM is found to be applicable not only for flux estimation of synchronous and induction motors [50], but also for vector control of a PWM rectifier. The position for the SCVM as a *universal* flux estimator [50] is strengthened.

The static nature of the grid flux implies that it is unnecessary to use a dynamic estimate for this quantity. A simplified variant of the SCVM is designed for this purpose, which will be referred to as the MCVM.

The steady-state performances of the PLL-type estimator and the MCVM are studied. Provided that both estimators are designed for similar dynamic response times, the analysis shows that the MCVM is more robust against disturbances coming from grid voltage harmonics.

5.1 SCVM

The SCVM is adapted for grid-flux estimation by repeating the expression for (3.8) and putting $\text{sign}(\omega_1) = 1$ in (3.9), since the grid frequency is constant and greater than zero:

$$\frac{d\hat{\psi}_g}{dt} = \gamma \hat{E}_d \quad (5.1)$$

$$\omega_1 = \frac{\hat{E}_q - \lambda \hat{E}_d}{\hat{\psi}_g}. \quad (5.2)$$

Of course, \hat{E}_d and \hat{E}_q now refer to the estimated (or measured) grid voltage, and not to the estimated flux EMF of an ac machine.

5.1.1 Stability Analysis

The system model for the SCVM results from (5.1) and the dynamics of the error angle:

$$\frac{d\tilde{\theta}}{dt} = \omega_g - \omega_1 = \omega_g - \frac{\hat{E}_q - \lambda \hat{E}_d}{\hat{\psi}_g}. \quad (5.3)$$

After substituting (4.20) in these equations, the system model becomes:

$$\frac{d\hat{\psi}_g}{dt} = \gamma E_d = -\gamma \omega_g \psi_g \sin \tilde{\theta} \quad (5.4)$$

$$\frac{d\tilde{\theta}}{dt} = \omega_g - \frac{\hat{E}_q - \lambda \hat{E}_d}{\hat{\psi}_g} = \omega_g \left[1 - \frac{\psi_g}{\hat{\psi}_g} (\cos \tilde{\theta} + \lambda \sin \tilde{\theta}) \right]. \quad (5.5)$$

By putting $d\hat{\psi}_g/dt = d\tilde{\theta}/dt = 0$, and solving for $\hat{\psi}_g$ and $\tilde{\theta}$, the following equilibrium points are obtained

$$\hat{\psi}_{g,1}^* = \psi_g, \quad \tilde{\theta}_1^* = 2n\pi, \quad n = 0, \pm 1, \pm 2, \dots \quad (5.6)$$

$$\hat{\psi}_{g,2}^* = -\psi_g, \quad \tilde{\theta}_2^* = n\pi, \quad n = \pm 1, \pm 3, \pm 5, \dots \quad (5.7)$$

These points are henceforth labeled EP1 and EP2, respectively. In addition to the above convergence points, $\tilde{\theta} = \hat{\psi}_g = 0$ is a form of saddle point, even though $\tilde{\theta}$ is undefined for $\hat{\psi}_g = 0$, which yields a singularity in (5.5).

Once the SCVM has reached steady-state operation, then the periodicity for EP1 and EP2 is irrelevant: the system cannot separate $\tilde{\theta} = 0$ from $\tilde{\theta} = 2n\pi$, for instance. All convergence points related to EP1 and EP2, respectively, are thus equal for practical purposes.

EP1 corresponds to accurate field orientation, and is therefore the desirable equilibrium point. The linearization of (5.4)–(5.5) about EP1 follows the same procedure as in Section 4.2.2, i.e., small $\tilde{\theta}$ and $\hat{\psi}_g \approx \psi_g$ are assumed, such that $\sin \tilde{\theta} \approx \tilde{\theta}$, $\cos \tilde{\theta} \approx 1$ and $\psi_g/\hat{\psi}_g \approx 1 - \tilde{\psi}_g/\psi_g$. By also introducing the scaled flux-modulus estimation error

$$\xi = \omega_g \tilde{\psi}_g / \psi_g \quad (5.8)$$

in order to make a better comparison to the PLL-type estimator in the next section, the linearized dynamics about EP1 become

$$\frac{d}{dt} \begin{bmatrix} \xi \\ \tilde{\theta} \end{bmatrix} = \underbrace{\begin{bmatrix} 0 & -\gamma \omega_g^2 \\ 1 & -\lambda \omega_g \end{bmatrix}}_{A_{\text{SCVM}}} \begin{bmatrix} \xi \\ \tilde{\theta} \end{bmatrix}. \quad (5.9)$$

The characteristic polynomial of A_{SCVM} is

$$\det(pI - A_{\text{SCVM}}) = p^2 + \lambda \omega_g p + \gamma \omega_g^2. \quad (5.10)$$

The SCVM is thus asymptotically stable about EP1, given that λ and γ are both greater than zero.

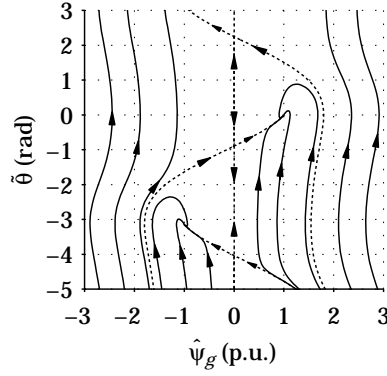


Fig. 5.1. Phase portrait for the SCVM, with $E_g=1$ pu, $\omega_g=1$ pu, and $\rho=0.4$; $\hat{\psi}_g$ and $\tilde{\theta}$ converge to either EP1 or EP2, depending on the initial value for $\hat{\psi}_g$. The dashed lines are the separatrices of the singularity $\hat{\psi}_g = 0$.

The roots of (5.10) (poles of the linearized system) can be arbitrary placed. It is recommended to place both poles on the negative real axis, since grid voltage disturbances may introduce oscillations in θ_1 for a poorly damped estimator. A double pole at $p_{1,2} = -\rho$ implies that $\det(pI - A_{\text{SCVM}}) = (p + \rho)^2$, and solving this equation for λ and γ provides the following gain parameters

$$\lambda = \frac{2\rho}{\omega_g}, \quad \gamma = \frac{\rho^2}{\omega_g^2}. \quad (5.11)$$

Fig. 5.1 shows a phase portrait of the nonlinear dynamics in (5.4)–(5.5). Both equilibrium points are sinks (stable), so operation about EP1 does not necessarily result. Fortunately, convergence to EP1 can be ensured by restricting $\hat{\psi}_g$ to a confined interval $[\psi_{\min}, \psi_{\max}]$, where the lower and the upper boundaries satisfy the condition $0 < \psi_{\min} < E_g/\omega_g < \psi_{\max}$. As seen in Fig. 5.1, both the undefined $\hat{\psi}_g = 0$ and EP2 are avoided when using such an interval for $\hat{\psi}_g$.

5.2 PLL-Type Estimator

The PLL-type estimator that will be studied in this section is given by [50]

$$\dot{\omega}_1 = \gamma_1 \varepsilon \quad (5.12)$$

$$\dot{\theta}_1 = \omega_1 + \gamma_2 \varepsilon \quad (5.13)$$

where γ_1 and γ_2 are gain parameters and ε is the *error signal*. Similar to [28, 50], the error signal $\varepsilon = -\hat{E}_d$ is here selected.

5.2.1 Stability Analysis

According to (4.20), the resulting error signal becomes

$$\varepsilon = -E_d = E_g \sin \tilde{\theta}. \quad (5.14)$$

The dynamics of the PLL-type estimator are derived by substituting this resulting error signal in (5.12)–(5.13). Via the introduction of the error variables

$$\tilde{\omega} = \omega_g - \omega_1, \quad \tilde{\theta} = \theta_g - \theta_1 \quad (5.15)$$

the system model for the PLL-type estimator becomes

$$\frac{d\tilde{\omega}}{dt} = \dot{\omega}_g - \dot{\omega}_1 = -\gamma_1 E_g \sin \tilde{\theta} \quad (5.16)$$

$$\frac{d\tilde{\theta}}{dt} = \omega_g - (\omega_1 - \gamma_2 E_d) = \tilde{\omega} - \gamma_2 E_g \sin \tilde{\theta} \quad (5.17)$$

under the reasonable assumption that the grid frequency is constant, meaning that $\dot{\omega}_g = 0$ is assumed. By putting $d\tilde{\omega}/dt = d\tilde{\theta}/dt = 0$, and solving for $\tilde{\omega}$ and $\tilde{\theta}$, the equilibrium points of (5.16)–(5.17) are found to be

$$\tilde{\omega}_1^* = 0, \quad \tilde{\theta}_1^* = 2n\pi, \quad n = 0, \pm 1, \pm 2, \dots \quad (5.18)$$

$$\tilde{\omega}_2^* = 0, \quad \tilde{\theta}_2^* = n\pi, \quad n = \pm 1, \pm 3, \pm 5, \dots \quad (5.19)$$

These are henceforth labeled EQ1 and EQ2, respectively. Similar to the SCVM, all convergence points related to EQ1 and EQ2 are equal for practical purposes. It can be shown that EQ1 is asymptotically stable, while EQ2 is a saddle point [52].

The PLL is said to be *phase locked* when $\theta_1 \approx \theta$, which corresponds to operation about EQ1. Since $\tilde{\theta}$ is small for phase-locked operation, $\sin \tilde{\theta} \approx \tilde{\theta}$ is reasonable to assume. By substituting this in (5.16)–(5.17), the following linearized system model about EQ1 results:

$$\frac{d}{dt} \begin{bmatrix} \tilde{\omega} \\ \tilde{\theta} \end{bmatrix} = \underbrace{\begin{bmatrix} 0 & -\gamma_1 E_g \\ 1 & -\gamma_2 E_g \end{bmatrix}}_{A_{\text{PLL}}} \begin{bmatrix} \tilde{\omega} \\ \tilde{\theta} \end{bmatrix}. \quad (5.20)$$

The characteristic polynomial of A_{PLL} is

$$\det(pI - A_{\text{PLL}}) = p^2 + \gamma_2 E_g p + \gamma_1 E_g. \quad (5.21)$$

It is recommended to place the poles of the PLL-type estimator on the negative real axis, in order to ensure good damping. A double pole at $p_{1,2} = -\rho$ implies that $\det(pI - A) = (p + \rho)^2$, and solving this equation for γ_1 and γ_2 yields the following gain parameters:

$$\gamma_1 = \frac{\rho^2}{\hat{E}_g}, \quad \gamma_2 = \frac{2\rho}{\hat{E}_g}, \quad \hat{E}_g = \sqrt{\hat{E}_d^2 + \hat{E}_q^2}. \quad (5.22)$$

Note that the gain parameters are selected inversely proportional to the estimated grid voltage modulus \hat{E}_g . Consistent dynamics are thereby ensured for the PLL-type estimator, even when E_g is smaller than the nominal grid voltage. This variant of “gain scheduling” is not required for the SCVM, though, since the estimated flux modulus of the SCVM takes E_g into consideration by default.

Fig. 5.2 shows a typical phase portrait for the PLL-type estimator. As seen, EQ1 is stable (sink), while EQ2 is a saddle point. Interestingly, the phase portrait for the PLL-type estimator is completely different compared to the SCVM in Fig. 5.1, but their linearized dynamics in (5.20) and (5.9), respectively, are essentially identical. This indicates similar dynamics for the PLL-type estimator and the SCVM in the vicinity of EQ1 and EP1, respectively, but different responses to large disturbances.

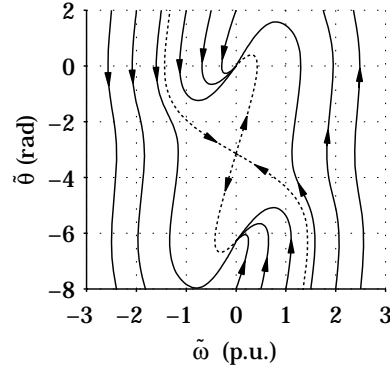


Fig. 5.2. Phase portrait for the PLL-type estimator, with $E_g=1$ pu, $\omega_g=1$ pu, and $\rho=0.4$. The dashed lines represent the separatrices of the saddle point (EQ2).

5.2.2 Rejection of Voltage Harmonics

The distorted grid voltage model in (4.6) is now considered in order to study how the PLL-type estimator rejects grid voltage harmonics. The real part and imaginary parts of this equation are

$$E_d = -E_1^+ \sin \tilde{\theta} + E_d^{2,6}, \quad E_q = E_1^+ \cos \tilde{\theta} + E_q^{2,6}. \quad (5.23)$$

Thus, we had $E_d^{2,6} = 0$ and $E_g = E_1^+$ in (5.14)–(5.17). Of special interest is how harmonics present in $E_d^{2,6}$ affect the error angle $\tilde{\theta}$. Ideally, the PLL-type estimator should synchronize to the fundamental grid flux only, resulting in $\tilde{\theta} = 0$. By repeating the above calculations with consideration taken to the grid voltage disturbances, the linearized state-space system about EQ1 then becomes

$$\frac{d}{dt} \begin{bmatrix} \tilde{\omega} \\ \tilde{\theta} \end{bmatrix} = \underbrace{\begin{bmatrix} 0 & -\gamma_1 E_1^+ \\ 1 & -\gamma_2 E_1^+ \end{bmatrix}}_A \begin{bmatrix} \tilde{\omega} \\ \tilde{\theta} \end{bmatrix} + \underbrace{\begin{bmatrix} \gamma_1 \\ \gamma_2 \end{bmatrix}}_B E_d^{2,6} \quad (5.24)$$

which is fairly similar to (5.20). With $C = [0, 1]$, the transfer function from $E_d^{2,6}$ to $\tilde{\theta}$ is

$$\tilde{\theta} = C(pI - A)^{-1} B E_d^{2,6} = \frac{\gamma_2 p + \gamma_1}{p^2 + \gamma_2 E_1^+ p + \gamma_1 E_1^+} E_d^{2,6}. \quad (5.25)$$

On condition that the grid voltage harmonics are small compared to the fundamental voltage, then $\hat{E}_g \approx E_1^+$ can be assumed. Under this assumption, and by substituting γ_1 and γ_2 with the selections in (5.22), the above transfer function reduces to

$$\tilde{\theta} = \frac{\rho(2p + \rho)}{(p + \rho)^2} \frac{E_d^{2,6}}{E_1^+} = H_{\text{PLL}}(p) \frac{E_d^{2,6}}{E_1^+}. \quad (5.26)$$

The static gain for $H_{\text{PLL}}(p)$ at $n\omega_g$ becomes

$$|H_{\text{PLL}}(jn\omega_g)| = \frac{\rho \sqrt{4(n\omega_g)^2 + \rho^2}}{(n\omega_g)^2 + \rho^2}. \quad (5.27)$$

As seen from (5.27), and not surprisingly, a low bandwidth should be selected for good rejection of grid voltage harmonics. This analytical observation agrees well with the experimental finding in [28].

5.3 Modified Compensated Voltage Model

The SCVM uses a dynamic flux-modulus estimate, which appears to be strange when considering the static nature of the virtual grid flux in (4.1); why should the estimator be different compared to the underlying system? Due to this observation, the following considers the estimator that results when a static flux estimate in (5.2), while (5.1) is, hence, dropped. The obvious static flux estimate results directly from the grid flux definition in (4.1):

$$\hat{\psi}_g = \frac{\hat{E}_g}{\hat{\omega}_g} \quad (5.28)$$

where $\hat{\omega}_g$ is a “model parameter” for the grid frequency; we shall henceforth assume $\omega_g = \hat{\omega}_g = 1$ pu. Substituting the above static estimate in (5.2) gives the following estimator

$$\omega_1 = \frac{\hat{\omega}_g(\hat{E}_q - \lambda\hat{E}_d)}{\hat{E}_g} = \hat{\omega}_g \left(\frac{\hat{E}_q}{\hat{E}_g} - \lambda \frac{\hat{E}_d}{\hat{E}_g} \right). \quad (5.29)$$

The above quotient \hat{E}_q/\hat{E}_g can be approximated by 1, since the error angle is mainly seen in \hat{E}_d , and $\hat{E}_q = \hat{E}_g = E_g$ for accurate field orientation. This gives the final representation of this flux estimator as

$$\omega_1 = \hat{\omega}_g \left(1 - \lambda \frac{\hat{E}_d}{\hat{E}_g} \right) \quad (5.30)$$

which will be referred to as the *modified compensated voltage model* (MCVM).

5.3.1 Stability Analysis

The dynamics of the MCVM are given by the error angle as

$$\frac{d\tilde{\theta}}{dt} = \omega_g - \omega_1 = \omega_g - \hat{\omega}_g \left(1 - \lambda \frac{\hat{E}_d}{\hat{E}_g} \right) = \lambda \omega_g \frac{E_d}{E_g} = -\lambda \omega_g \sin \tilde{\theta}. \quad (5.31)$$

given that the model parameters are accurate and $\omega_g = \hat{\omega}_g$. By putting $d\tilde{\theta}/dt = 0$, and solving for $\tilde{\theta}$, the following equilibrium points result

$$\tilde{\theta}^* = \begin{cases} 2n\pi, & n = 0, \pm 1, \pm 2, \dots \\ n\pi, & n = \pm 1, \pm 3, \pm 5, \dots \end{cases} \quad (5.32)$$

From direct inspection of (5.31), it can be seen that the MCVM is asymptotically stable about $\tilde{\theta} = 2n\pi$, n being an integer. To verify this strictly, though, the stability of the MCVM is below analyzed by means of the direct method of Lyapunov [103].

Consider the Lyapunov function candidate

$$V(\tilde{\theta}) = 1 - \cos \tilde{\theta}. \quad (5.33)$$

The function candidate satisfies $V(\tilde{\theta}) > 0$ for $\tilde{\theta} \neq 2n\pi$, and

$$\dot{V} = \dot{\tilde{\theta}} \sin \tilde{\theta} = -\lambda \omega_g \sin^2 \tilde{\theta} \leq 0 \quad (5.34)$$

is negative semi-definite for $\lambda > 0$. Therefore, $V(\tilde{\theta})$ is indeed a Lyapunov function. Locally, \dot{V} is negative definite ($\dot{V} < 0$) in the region

$$(2n - 1)\pi < \tilde{\theta} < (2n + 1)\pi, \quad n = 0, \pm 1, \pm 2, \dots \quad (5.35)$$

so $\tilde{\theta} = 2n\pi$ is asymptotically stable. The convergence point $\tilde{\theta} = n\pi$, n being an odd integer, is a saddle point.

For small variations about $\tilde{\theta} = 2n\pi$, then $\sin \tilde{\theta} \approx \tilde{\theta}$ can be assumed. Substituting this in (5.31) provides the linearized dynamics of the MCVM as

$$\frac{d\tilde{\theta}}{dt} = -\lambda\omega_g\tilde{\theta}. \quad (5.36)$$

The pole of the linearized system can be placed at $-\rho$, via the selection of

$$\lambda = \rho/\hat{\omega}_g. \quad (5.37)$$

Observe that the MCVM is less suitable for so-called *island operation* [19], where the grid frequency may temporarily deviate from the nominal value. For the less common case $\omega_g \neq \hat{\omega}_g$, corresponding to island operation, then (5.31) becomes

$$\frac{d\tilde{\theta}}{dt} = \omega_g - \hat{\omega}_g - \lambda\hat{\omega}_g \sin \tilde{\theta}. \quad (5.38)$$

Putting $d\tilde{\theta}/dt = 0$, and solving for $\tilde{\theta}$, provides the following error angle

$$\tilde{\theta} = \arcsin\left(\frac{\tilde{\omega}_g}{\lambda\hat{\omega}_g}\right) \quad (5.39)$$

where $\tilde{\omega}_g = \omega_g - \hat{\omega}_g$ is the frequency error. The values $\tilde{\omega}_g = -0.1$ pu, $\lambda = 0.6$ pu and $\hat{\omega}_g = 1$ pu are considered for a numerical example, which result in $\tilde{\theta} = \arcsin(-0.1/0.6) = -0.17$ rad = -10° . This is not particularly a large error angle, but it may still be preferred to use the PLL-type estimator or the SCVM for island operation, since these estimators are insensitive to ω_g in the steady-state operation.

5.3.2 Rejection of Voltage Harmonics

A fair approximation is that the estimated grid voltage is dominated by the fundamental grid voltage, $\hat{E}_g \approx E_1^+$, since the grid voltage harmonics are normally much smaller compared to the fundamental grid voltage. Under this assumption, and by substituting \hat{E}_d and \hat{E}_q with the distorted grid voltage in (5.23), the system model for the MCVM becomes

$$\frac{d\tilde{\theta}}{dt} = \lambda\omega_g \frac{-E_1^+ \sin \tilde{\theta} + E_d^{2,6}}{E_1^+}. \quad (5.40)$$

The grid voltage harmonics are mostly troublesome in the steady-state operation, i.e., when $\tilde{\theta} \approx 0$. For small $\tilde{\theta}$, such that $\sin \tilde{\theta} \approx \tilde{\theta}$, and by substituting $\lambda = \rho/\omega_g$, (5.40) reduces to

$$\frac{d\tilde{\theta}}{dt} \approx \rho \frac{-E_1^+ \tilde{\theta} + E_d^{2,6}}{E_1^+} \Rightarrow \tilde{\theta} = \frac{\rho}{p + \rho} \frac{E_d^{2,6}}{E_1^+} = H_{\text{MCVM}}(p) \frac{E_d^{2,6}}{E_1^+} \quad (5.41)$$

The static gain for $H_{\text{MCVM}}(p)$ at $n\omega_g$ is found to be

$$|H_{\text{MCVM}}(jn\omega_g)| = \frac{\rho}{\sqrt{(n\omega_g)^2 + \rho^2}} \quad (5.42)$$

which can be compared to the static gain for the PLL-type estimator in (5.27):

$$|H_{\text{PLL}}(jn\omega_g)| = \frac{\rho\sqrt{4(n\omega_g)^2 + \rho^2}}{(n\omega_g)^2 + \rho^2}. \quad (5.43)$$

A small bandwidth is required for good rejection of the voltage harmonics. Under the assumption that $n\omega_g \gg \rho$, the above static gains become

$$|H_{\text{MCVM}}(jn\omega_g)| \approx \frac{\rho}{n\omega_g}, \quad |H_{\text{PLL}}(jn\omega_g)| \approx \frac{2\rho}{n\omega_g}. \quad (5.44)$$

As seen, the static gain for the MCVM is only half of the gain for the PLL-type estimator, provided that both estimators have the same bandwidth about $\tilde{\theta} \approx 0$. The MCVM should therefore provide less amplification, and better rejection of voltage harmonics, compared to the PLL-type estimator.

For a specific gain $|H_{\text{MCVM}}|$, the corresponding required bandwidth ρ results from (5.42) as

$$\rho = \frac{n\omega_g |H_{\text{MCVM}}(jn\omega_g)|}{\sqrt{1 - |H_{\text{MCVM}}(jn\omega_g)|^2}}. \quad (5.45)$$

At least $|H_{\text{MCVM}}(j6\omega_g)| = 0.1$ is required for good rejection of the fifth- and the seventh-order harmonics. Therefore, as a rule of thumb, no more than $\rho = 6 \cdot 1 \cdot 0.1 / \sqrt{1 - 0.1^2} \approx 0.6$ pu should be selected for the MCVM.

5.3.3 Modified PLL-Type Estimator

In addition to the SCVM, the PLL-type estimator in (5.12)–(5.13) can also be modified for grid-flux estimation. The modified PLL-type estimator is derived by dropping (5.12) and using only the flux angle estimator of the PLL:

$$\dot{\theta}_1 = \omega_1 = \hat{\omega}_g + \gamma_2 \varepsilon, \quad \varepsilon = -\hat{E}_d. \quad (5.46)$$

By letting the gain parameter equal $\gamma_2 = \lambda \hat{\omega}_g / \hat{E}_g$, the modified PLL-type estimator then becomes

$$\dot{\theta}_1 = \omega_1 = \hat{\omega}_g \left(1 - \lambda \frac{\hat{E}_d}{\hat{E}_g} \right). \quad (5.47)$$

This is the exactly the same expression that was obtained for the MCVM in (5.30). Hence, although derived quite differently, the MCVM and the modified PLL-type estimator are equivalent.

5.3.4 Implementation Issues

The implementation of the MCVM is straightforward for voltage-sensored operation:

$$\omega_1 = \hat{\omega}_g \left(1 - \lambda \frac{E_d}{E_g} \right), \quad E_g = \sqrt{E_d^2 + E_q^2}. \quad (5.48)$$

where λ should be selected smaller than 0.6 pu. The synchronous frequency must be integrated in order to obtain the transformation angle θ_1 :

$$\theta_1 = \int \omega_1 dt \quad (5.49)$$

which can be easily discretized by the forward difference approximation [10]. The transformation factors $e^{j\theta_1}$ and $e^{-j\theta_1}$, required in the Park transformation, are then obtained from:

$$e^{j\theta_1} = \cos \theta_1 + j \sin \theta_1, \quad e^{-j\theta_1} = \cos \theta_1 - j \sin \theta_1. \quad (5.50)$$

An algebraic loop is created for voltage-sensorless operation, however, since both \hat{E}_d and \hat{E}_q are functions of ω_1 . This loop is, on the other hand, easily circumvented via the following remedy:

$$\hat{E}_d = v_d^{\text{ref}} - \hat{R}_g i_d + \hat{\omega}_g \hat{L}_g i_q \quad (5.51)$$

$$\hat{E}_q = v_q^{\text{ref}} - \hat{R}_g i_q - \hat{\omega}_g \hat{L}_g i_d \quad (5.52)$$

$$\hat{E}_g = \sqrt{\hat{E}_d^2 + \hat{E}_q^2} \quad (5.53)$$

$$\omega_1 = \hat{\omega}_g \left(1 - \lambda \frac{\hat{E}_d}{\hat{E}_g} \right). \quad (5.54)$$

As seen, the inductive voltage drop is expressed in terms of $\hat{\omega}_g$ instead of ω_1 , so the algebraic loop is avoided. This approximation is correct in the steady-operation, and fairly correct also for the transient operation, since ω_1 and ω_g approximately equal.

There are several possibilities for simplifying the implementation of the MCVM. The resistive voltage drop in the estimated grid voltage can mostly be neglected, since the filter resistance is small for the purpose of small resistive loss. In addition, the grid voltage modulus can be approximated by $\hat{E}_g = E_g = E_{\text{nom}}$, where E_{nom} is the nominal grid voltage modulus. This makes the computation of the square roots for \hat{E}_g and E_g superfluous but, on the other hand, the dynamics for the MCVM will no longer be consistent, so the settling time for $\tilde{\theta}$ slacken when $E_g < E_{\text{nom}}$.

5.4 Simulations

This section presents simulation results of the studied flux estimators. The simulations are essentially focused on the responses to various grid voltage disturbances. The simulation parameters are: $L_g = 0.07$ pu, $\hat{L}_g = 1.1L_g$, $R_g = 0.007$ pu, $\hat{R}_g = 0.7R_g$ pu, $C = 5$ pu, $E_g = 1$ pu, $\omega_g = 1$ pu and the bandwidth of the dc voltage control loop is

0.8 pu. The dc voltage setpoint is 2 pu, see Appendix A for further details on the per-unit system. The current dynamics are neglected, meaning that $\mathbf{i}_g = \mathbf{i}_g^{\text{ref}}$. A dc voltage controller, which is described Chapter 6, provides the setpoint for i_q , while the d -axis current is held constant at $i_d = 0$.

5.4.1 Rejection of Voltage Harmonics

Fig. 5.3 shows a simulation of the MCVM, where the dc voltage reference is held constant at 2 pu. A load power step that requires $i_q = 0.5$ pu is applied after 0.02 s, and this causes the dc voltage to increase by 0.3 pu. A fifth-order harmonic with the magnitude $E_5 = 0.02$ pu appears at $t = 0.04$ s, which results in a slightly distorted more distorted grid current. The voltage harmonic also introduces fluctuations in the dc voltage. These fluctuations are due to that the distortion \mathbf{E}_g and \mathbf{i}_g cause P_g to fluctuate, and the instantaneous power fluctuations spread to the dc-link, which will be further discussed in the next chapter.

Fig. 5.4 shows the error angle for the MCVM, the PLL-type estimator, and the SCVM, for the last 0.01 s in the above simulation. The bandwidth of all three flux estimators is 0.5 pu in the vicinity of $\tilde{\theta} = 0$. Even though all three estimators reduce the grid voltage harmonic quite satisfactorily, the MCVM has an edge over the PLL-type estimator and the SCVM. The larger angle magnitude of the SCVM is due to that this estimator uses both \hat{E}_d and \hat{E}_q , for which the distortion sum up, while the MCVM and the PLL-type estimation use \hat{E}_d only.

Fig. 5.5 shows a simulation, made under the same conditions as Fig. 5.3, of the classical DFO “flux estimator” in (4.14)–(4.15). It can be seen that the error angle in Fig. 5.5(d) and the grid current in Fig. 5.5(c) are more distorted than for the “dynamic” flux estimators in Fig. 5.4. Observe that the larger current distortion is not seen from i_q in Fig. 5.5(b), since the distortion in the transformation factors $e^{j\theta_1}$ and $e^{-j\theta_1}$ ideally cancel each other for the synchronous reference frame.

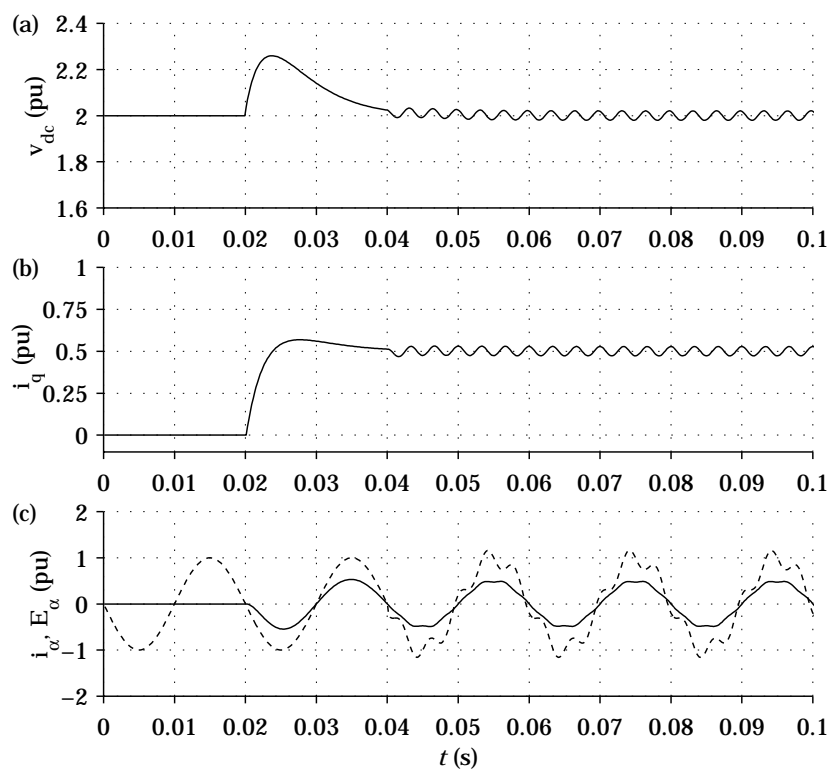


Fig. 5.3. Simulation of the MCVM for a grid voltage disturbance. (a) DC voltage. (b) q -axis current. (c) Grid current and grid voltage in the α direction.

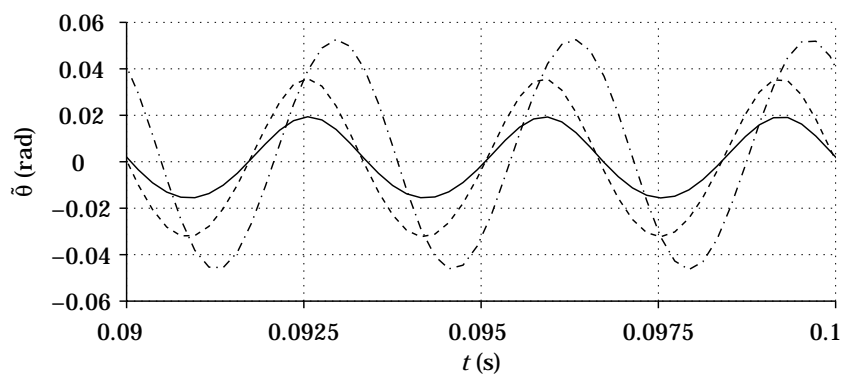


Fig. 5.4. Comparison of rejection to grid voltage disturbances, by means of the resulting error angle. The studied flux estimators are: the MCVM (solid), the PLL-type estimator (dashed), and the SCVM (dash-dotted).

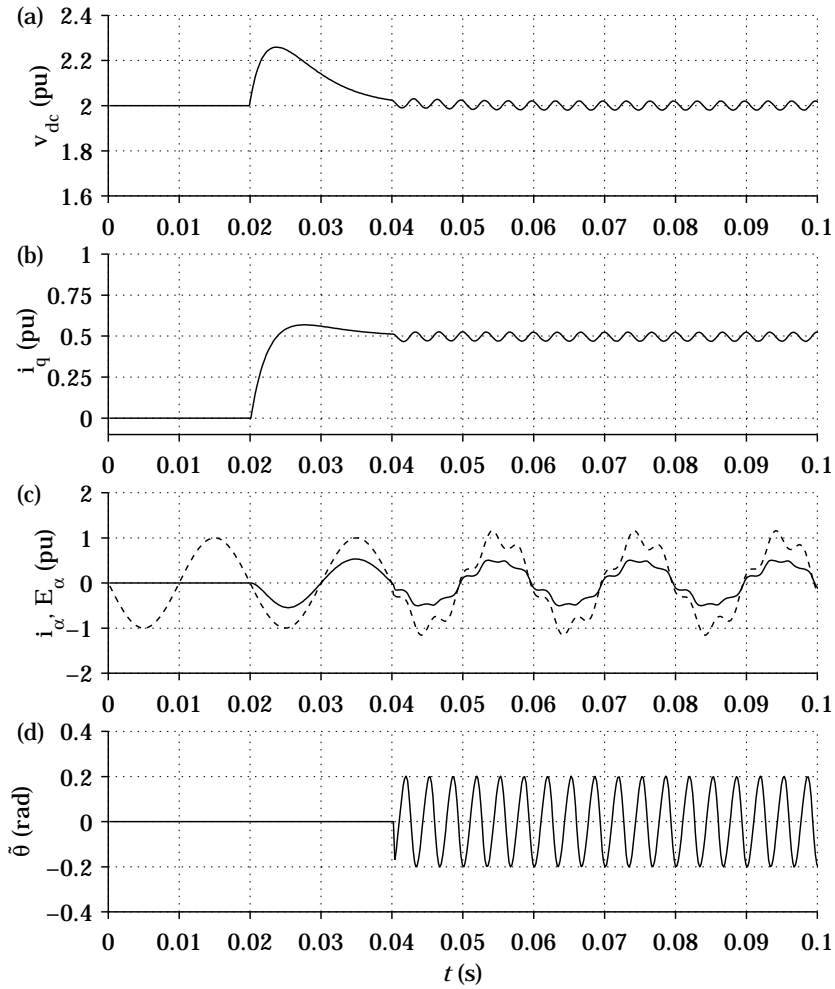


Fig. 5.5. Simulation of the classical DFO grid flux “estimator.” (a) DC voltage. (b) q -axis current. (c) Grid current and grid voltage in the α direction. (d) Error angle.

5.4.2 Response to Phase-Angle Jump

Fig. 5.6 shows the simulated responses to a “phase-angle jump” for the MCVM, the PLL-type estimator and the SCVM. All three estimators are designed for a bandwidth 0.5 pu in the vicinity of $\tilde{\theta} = 0$.

The response to the load power step at $t = 0.02$ s is similar for all three estimators. A symmetrical voltage dip occurs at $t = 0.05$ s, which is associated with a “phase-angle jump” of $\theta = 0.78$ rad = 45° (this is a large “jump” [20]) and the grid voltage modulus reduces by 0.2 pu. All three estimators converge to $\tilde{\theta} \approx 0$ at approximately 0.02 s after the dip appeared. The convergence rate of the SCVM is slow immediately after the voltage dip. The field orientation therefore remains inaccurate, and the instantaneous active power for a given i_q and $i_d = 0$, $P_g = 3E_g i_q \cos \tilde{\theta}$, reduces. This is seen in Figs. 5.6(b)–(c): the SCVM yields the largest deviation in v_{dc} from the dc voltage setpoint, in contrast to having the largest i_q at $t = 0.55$ s.

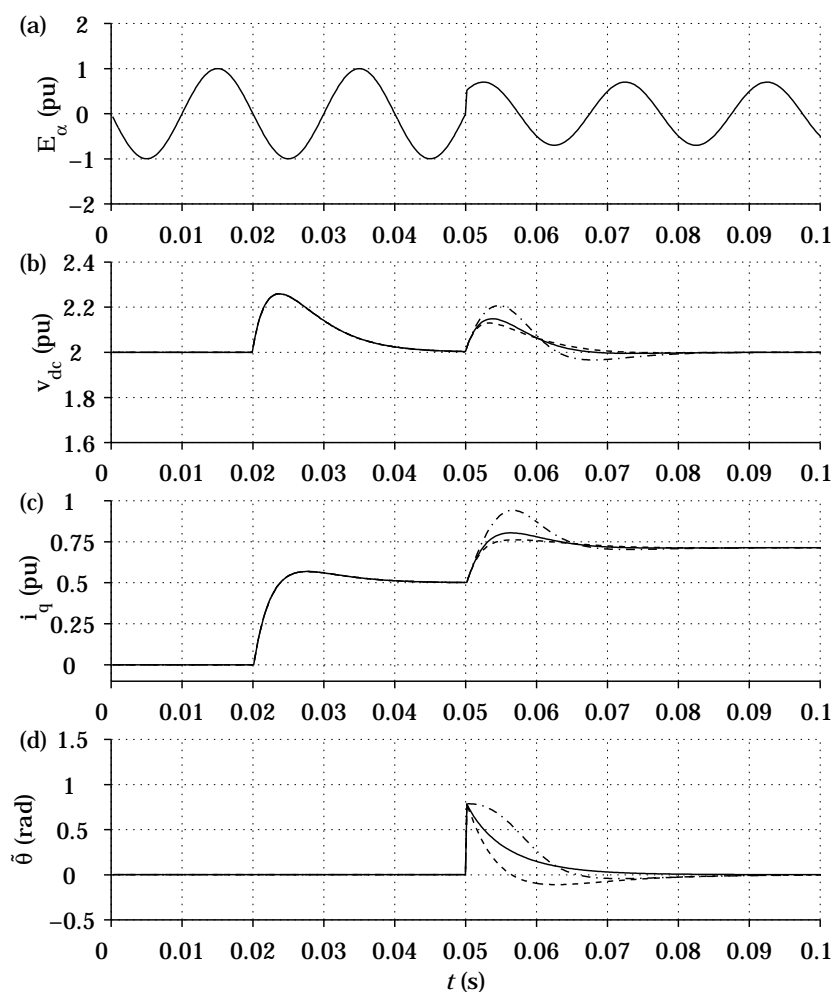


Fig. 5.6. Comparative study of the responses to a 45° “phase-angle jump” for the MCVM (solid), the PLL-type estimator (dashed), and the SCVM (dash-dotted). (a) α -axis grid voltage. (b) DC voltage. (c) q -axis current. (d) Error angle.

5.5 Summary

The emphasis of this chapter was on grid-flux estimation, and three estimators were analyzed. All three estimators were found to be asymptotically stable, and suitable estimator parameters were given in terms of the desired bandwidth and the grid voltage modulus.

A grid flux estimator should be designed for a fairly low bandwidth, since this improves the rejection of grid voltage harmonics. The MCVVM was proven to be very robust against the grid voltage harmonics, albeit less suitable for island operation. For such operation, the PLL-type estimator can instead be recommended. The SCVM is not recommended at all for grid-flux estimation, since simulations indicate that this estimator is associated with fairly poor rejection of grid voltage disturbances. Further analytical studies are, however, required in order to stringently verify this.

Chapter 6

Controller Design

This chapter describes a classical cascaded control system structure for the back-to-back converter. The resulting control design is closely related to previously published work, and this is acknowledged where appropriate. Initially, the fundamentals of the control theory that will be used is presented, and the controller designs then follow.

The principle for feedback current control here chosen is traditional synchronous-frame PI control [69], which is preferably used in combination with carrier-based PWM and regular sampling [59]. We also acknowledge the numerous other variants available for current control, see [69] for a comprehensive survey.

The fairly few contributions of this chapter are related to the control of the PWM rectifier. The design of the fast inner grid current control loop and the design of the outer feedback loop for dc voltage control are described. The reduction of grid voltage disturbances is analyzed, and possible routes to improvements are pointed out. The chapter concludes with a simulation study of the resulting control system structure.

6.1 Internal Model Control

This section provides a brief tutorial on internal model control (IMC) [87] for real- and complex-valued single-loop feedback systems. IMC is a model-based technique for controller design, for which the resulting controller becomes directly parameterized in terms of the plant model parameters and the desired closed-loop bandwidth.

Fig. 6.1 depicts the control system structure of IMC as a block diagram, where

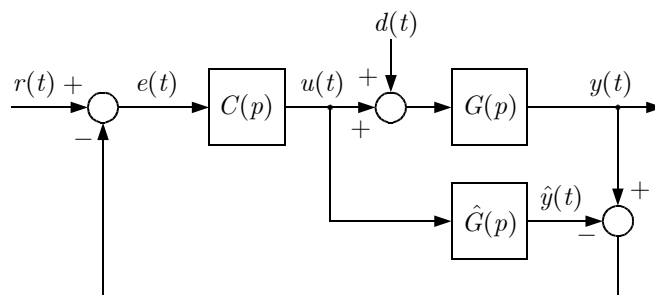


Fig. 6.1. Block diagram of IMC structure.

$G(p), \widehat{G}(p), C(p)$	plant, plant model, IMC controller;
$u(t), y(t), \widehat{y}(t)$	input, output, modeled output;
$r(t), e(t), d(t)$	reference signal, error signal, load disturbance.

Provided that the plant is accurately modeled and that no disturbances are present, i.e., $\widehat{G}(p) = G(p)$ and $d(t) = 0$, then $y(t)$ is canceled by $\widehat{y}(t)$ in the feedback loop. The closed-loop system then equals the open-loop system:

$$G_c(p) = G(p)C(p). \quad (6.1)$$

A not far-fetched idea would be to select the “optimal” IMC controller $C(p) = \widehat{G}^{-1}(p)$, which would cancel all plant dynamics, giving $G_c(p) = 1$ and $y(t) = r(t)$ for all t . This choice for $C(p)$ is not physically realizable, however, for the following reasons:

- $\widehat{G}^{-1}(p)$ is unstable if $\widehat{G}(p)$ has at least one zero in the right-hand side of the complex plane.
- $\widehat{G}^{-1}(p)$ cannot be implemented unless it is *proper*, which means that the degree of the numerator must be equal or lower than the degree of denominator. However, $\widehat{G}^{-1}(p)$ is never proper for a physical process, since the degree of the denominator for a physical $G(p)$ is always higher than the degree of the numerator.
- The choice $C(p) = \widehat{G}^{-1}(p)$ would demand for excessive control action, so $u(t)$ would be large, and the system would be highly sensitive to model errors.

These issues can be resolved by detuning the “optimal” controller with a lowpass filter. With $L(p)$ being the lowpass filter, the detuned $C(p)$ becomes

$$C(p) = L(p)\widehat{G}^{-1}(p) \quad (6.2a)$$

$$L(p) = \left(\frac{\alpha}{p + \alpha} \right)^n. \quad (6.2b)$$

Consequently, the closed-loop system equals $L(p)$ for accurate model parameters:

$$G_c(p) = L(p)\widehat{G}^{-1}(p)G(p) = L(p). \quad (6.2c)$$

Notice that all poles of $L(p)$ have for simplicity been placed in α , but this is no general requirement for IMC. The degree of the filter, though, must be chosen sufficiently large for $C(p)$ to become proper. Hence, n must be larger or, preferably, equal to the denominator degree of $G(p)$.

It is for practical purposes suitable to rearrange the IMC structure in Fig. 6.1 to the “classical” control system structure in Fig. 6.2, where $F(p)$ is a “classical” controller. This controller is given by the transfer function from $e(t)$ to $u(t)$:

$$F(p) = \frac{C(p)}{1 - C(p)\widehat{G}(p)} = \frac{\alpha^n}{(p + \alpha)^n - \alpha^n} \widehat{G}^{-1}(p). \quad (6.3)$$

For the important case that $G(p)$ is a first-order system, then the classical controller reduces to

$$F(p) = \frac{\alpha}{p} \widehat{G}^{-1}(p), \quad n = 1 \quad (6.4)$$

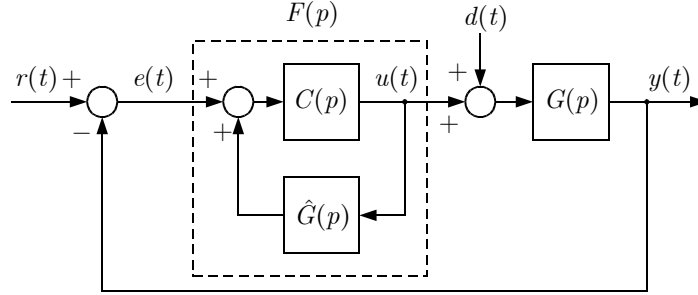


Fig. 6.2. The IMC rearranged as the “classical” control system structure.

while the following controller results for a second-order $G(p)$:

$$F(p) = \frac{\alpha^2}{p^2 + 2\alpha p} \hat{G}^{-1}(p), \quad n = 2. \quad (6.5)$$

For the inner current control loop, the bandwidth α should always be selected smaller than a decade below the sampling frequency [51]. The maximum bandwidth allowed is not always attainable, however, since this choice may demand for excessive control action that frequently saturates the control system [51]. A smaller bandwidth should then be chosen.

The closed-loop bandwidth can occasionally be directly selected from the easily derived formula [48]

$$\alpha = \frac{\ln 9}{t_r} \approx \frac{2.2}{t_r} \quad (6.6)$$

where t_r is the desired rise time (from 10 % to 90 % of the final value) for $y(t)$. This formula holds exactly for real-valued first-order systems, and approximately for first-order complex-valued systems as well, albeit a complex-valued first-order system stringently is a second-order real-valued system [45].

6.1.1 Two-Degrees-of-Freedom IMC

A drawback of IMC is that the resulting control system structure may reject load disturbances poorly. Consider the transfer function from the load disturbance $d(t)$ to the output $y(t)$ in Fig. 6.2:

$$G_{dy}(p) = \frac{G(p)}{1 + F(p)G(p)} = \frac{p}{p + \alpha} G(p). \quad (6.7)$$

If the dynamics of $G(p)$ are fast, or much faster, compared to the dynamics of the closed-loop system, then the load disturbance rejection should be sufficient, or else the rejection can be improved by increasing α . However, the dynamics of $G(p)$ are normally much slower compared to the dynamics of the closed-loop system, so the disturbance reduction is to a great extent determined by the sluggish process.

The principle of *two-degrees-of-freedom IMC* [87] can be implemented in order to speed up the load disturbance rejection for IMC. Such a control system structure is depicted in Fig. 6.3, where the additional degree of freedom is introduced by the feedback controller $F'(p)$ in the inner loop. The controller $F'(p)$ is generally dynamic,

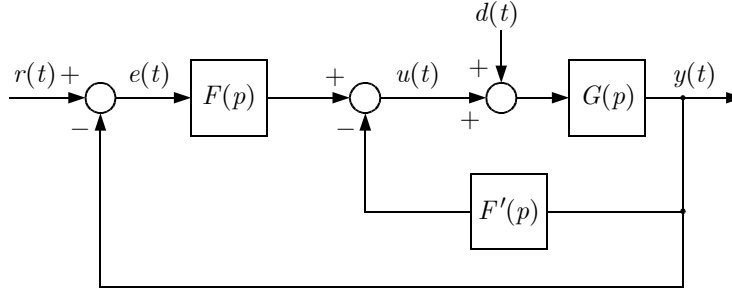


Fig. 6.3. Block diagram of two-degrees-of-freedom IMC. An inner loop provides additional feedback of $y(t)$ through $F'(p)$.

but will for our purposes be static. For a static F' and a first-order $G(p)$, the inner loop solely provides additional damping to $G(p)$, and we shall therefore refer to two-degrees-of-freedom IMC as *active damping*.

6.1.2 Back-Calculation

The input signal $u(t)$ is for practical operation limited to a maximum and a minimal value. Once $u(t)$ becomes limited, the integrator part of a PI controller may introduce the well-known phenomenon *integrator windup* [9]. Integrator windup normally manifests itself as an overshoot in the step response of the output signal.

Back-calculation [9, 51] is a simple and effective technique to circumvent the problem of integrator windup. Consider a conventional PI controller, where $u(t)$ has become limited to $\bar{u}(t)$, due to too large $e(t)$:

$$\frac{dI(t)}{dt} = e(t) \tag{6.8}$$

$$u(t) = k_p e(t) + k_i I(t) \tag{6.9}$$

$$\bar{u}(t) = [u(t)]_{\min}^{\max}. \tag{6.10}$$

In order to avoid integrator windup, the integrator sum $I(t)$ should not be updated with the too large $e(t)$, as in (6.8), but with the modified error $e'(t)$ that would have given $u(t) = \bar{u}(t)$ precisely:

$$\bar{u}(t) = k_p e'(t) + k_i I(t). \tag{6.11}$$

By subtracting (6.9) from (6.11), and solving for $e'(t)$, the modified error is back-calculated as [48]

$$e'(t) = \frac{1}{k_p} [\bar{u}(t) - u(t) + k_p e(t)] = e(t) + \frac{1}{k_p} [\bar{u}(t) - u(t)] \tag{6.12}$$

so the following controller results:

$$\frac{dI(t)}{dt} = e'(t) \tag{6.13}$$

$$u(t) = k_p e(t) + k_i I(t) \tag{6.14}$$

$$\bar{u}(t) = [u(t)]_{\min}^{\max}. \tag{6.15}$$

Observe that the proportional part of the controller still uses the original error $e(t)$.

The upper and the lower boundary for the limited input signal \bar{u} depends on certain physical constraints, which are application-dependent. Take for instance speed control, which is here assumed to be accompanied by a current control loop. Then, the input signal corresponds to the setpoint for the q -axis current, which must be confined within a permissible interval in order to avoid over-current for a PWM converter. The permissible interval is given by the maximum and the minimal q -axis current allowed:

$$i_{q,\max} = \sqrt{|\mathbf{i}|_{\max}^2 - i_d^2}, \quad i_{q,\min} = -\sqrt{|\mathbf{i}|_{\max}^2 - i_d^2} \quad (6.16)$$

where $|\mathbf{i}|_{\max}^2$ is the maximum current modulus allowed. The procedure of confining i_q^{ref} to the interval $[i_{q,\min}, i_{q,\max}]$ is in this chapter denoted by

$$\bar{i}_q^{\text{ref}} = [i_q^{\text{ref}}]_{\min}^{\max} \quad (6.17)$$

where \bar{i}_q^{ref} is the modified q current setpoint. For a current controller, on the other hand, the input signal corresponds to the command voltage vector \mathbf{v} . For large current steps, the current controller may demand for a \mathbf{v} that exceeds the maximum realizable voltage modulus of the PWM converter, which is referred to as voltage saturation. In this chapter, voltage saturation is denoted by:

$$\bar{\mathbf{v}} = \text{PWM}(\mathbf{v}, \theta_1) \quad (6.18)$$

where $\bar{\mathbf{v}}$ is the modified command voltage vector, and PWM stands for *pulsewidth modulation*. Voltage saturation is further treated in Chapter 7.

6.2 Grid Current Control

The basic structure of the following grid current controller follows the guidelines given in [51, 99] and [29], the latter with respect to active damping. Therefore, novelty is not claimed for the basic controller design, but we shall in the following thoroughly analyze the reduction of the grid voltage disturbances for the resulting controller design.

The grid current dynamics in (4.2) are

$$L_g \frac{d\mathbf{i}_g}{dt} = \mathbf{v}_g - (R_g + j\omega_1 L_g)\mathbf{i}_g - \mathbf{E}_g. \quad (6.19)$$

The transfer function from \mathbf{v}_g to \mathbf{i}_g , which represents the process model, is therefore

$$\mathbf{G}(p) = \frac{1}{pL_g + R_g + j\omega_1 L_g}. \quad (6.20)$$

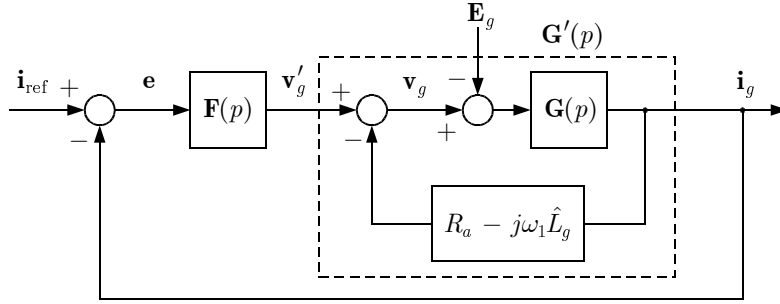


Fig. 6.4. Grid current control with inner feedback loop for current decoupling and active damping.

The inductor resistance R_g is designed to be small, so the grid voltage disturbances will be poorly damped by $\mathbf{G}(p)$ unless active damping is introduced. The first step in the controller design is therefore to introduce the inner feedback loop in Fig. 6.3. The inner loop has two purposes. Firstly, the cross-coupling between i_d and i_q , due to the term $j\omega_1 L_g \mathbf{i}_g$, should be canceled. Provided that L_g is fairly accurately modeled, this is easily accomplished by adding $j\omega_1 \hat{L}_g \mathbf{i}_g$ to F' . Secondly, the disturbance rejection should be speeded up by adding active damping. The active damping and the current decoupling are introduced by selecting \mathbf{v}_g as follows:

$$\mathbf{v}_g = \mathbf{v}'_g - (R_a - j\omega_1 \hat{L}_g) \mathbf{i}_g \quad (6.21)$$

where R_a is the active resistance [29], and \mathbf{v}'_g is the command voltage vector that results from the outer feedback loop in Fig. 6.3. By substituting (6.21) in (6.19), the system model is then

$$L_g \frac{d\mathbf{i}_g}{dt} = \mathbf{v}'_g - (R_a + R_g + j\omega_1 \tilde{L}_g) \mathbf{i}_g - \mathbf{E}_g \quad (6.22)$$

where $\tilde{L}_g = L_g - \hat{L}_g$. Fig. 6.4 depicts the system model as a block diagram. From the perspective of the outer feedback loop, the process model for accurate model parameters is given by the transfer function from \mathbf{v}'_g to \mathbf{i}_g :

$$\mathbf{G}'(p) = \frac{\mathbf{G}(p)}{1 + (R_a - j\omega_1 \hat{L}_g) \mathbf{G}(p)} = \frac{1}{pL_g + R_a + R_g}. \quad (6.23)$$

Following (6.4), since $\mathbf{G}'(p)$ as a first-order system, the current controller becomes

$$\mathbf{F}(p) = \frac{\alpha_c}{p} \mathbf{G}'^{-1}(p) = \alpha_c \hat{L}_g + \frac{\alpha_c}{p} (\hat{R}_g + R_a) \quad (6.24)$$

where α_c is the desired bandwidth for the current control loop. As seen from the above equation, $\mathbf{F}(p)$ becomes an ordinary PI controller. A suitable choice is to make the inner feedback loop as fast as the closed-loop system. Placing the pole of $\mathbf{G}'(p)$ at $-\alpha_c$ provides the active resistance as

$$\frac{R_g + R_a}{L_g} = \alpha_c \Rightarrow R_a = \alpha_c \hat{L}_g - \hat{R}_g. \quad (6.25)$$

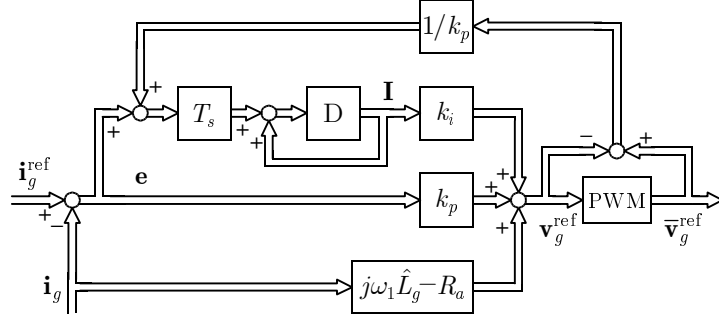


Fig. 6.5. Digitally implemented grid current controller. The integrator part of the controller is discretized by using the forward difference approximation [10]. “D” denotes the unit-delay operator and “ T_s ” is the sampling period.

The following summarizes the resulting current controller:

$$\mathbf{e} = \mathbf{i}_{\text{ref}} - \mathbf{i}_g \quad (6.26)$$

$$\frac{d\mathbf{I}}{dt} = \mathbf{e} + \frac{1}{k_p} (\bar{\mathbf{v}}_{\text{ref}} - \mathbf{v}_{\text{ref}}) \quad (6.27)$$

$$\mathbf{v}_{\text{ref}} = k_p \mathbf{e} + k_i \mathbf{I} + (j\omega_1 \hat{L}_g - R_a) \mathbf{i}_s \quad (6.28)$$

$$\bar{\mathbf{v}}_{\text{ref}} = \text{PWM}(\mathbf{v}_{\text{ref}}, \theta_1) \quad (6.29)$$

where

$$k_p = \alpha_c \hat{L}_g, \quad k_i = \alpha_c (\hat{R}_g + R_a) = \alpha_c^2 \hat{L}_g, \quad R_a = \alpha_c \hat{L}_g - \hat{R}_g \approx \alpha_c \hat{L}_g \quad (6.30)$$

are the proportional gain, the integration gain and the active resistance, respectively, of the grid current controller. Note that back-calculation has been introduced, as described in Section 6.1.2. Fig. 6.5 shows a block diagram of the digital implementation for the current controller.

6.2.1 Assessment of Disturbance Reduction

For accurate model parameters in the above controller design, the transfer function from the grid voltage disturbance \mathbf{E}_g to the error signal \mathbf{e} is found to be

$$\mathbf{G}_{\mathbf{E}\mathbf{e}}(p) = \frac{\mathbf{G}'(p)}{1 + \mathbf{F}(p)\mathbf{G}'(p)} = \frac{p}{p + \alpha_c} \mathbf{G}'(p) = \frac{p}{L_g(p + \alpha_c)^2}. \quad (6.31)$$

The static gain for $\mathbf{G}_{\mathbf{E}\mathbf{e}}(p)$ at the harmonic frequency $n\omega_g$ becomes

$$|\mathbf{G}_{\mathbf{E}\mathbf{e}}(jn\omega_g)| = \frac{n\omega_g}{L_g[(n\omega_g)^2 + \alpha_c^2]}. \quad (6.32)$$

The values $\omega_g = 1$ pu, $L_g = 0.1$ pu and $\alpha_c = 7$ pu, the latter corresponding to a current rise time of approximately 1 ms, are considered for a numerical example. We also recall from Section 4.1.4 that the negative sequence and the fifth-order/seventh-order voltage harmonics can be represented by $n = 2$ and $n = 6$, respectively. For these numerical values, the following static gains result:

$$|\mathbf{G}_{\mathbf{E}\mathbf{e}}(j2\omega_g)| = 2/[0.1 \cdot (2^2 + 7^2)] \approx 0.4, \quad |\mathbf{G}_{\mathbf{E}\mathbf{e}}(j6\omega_g)| \approx 0.7. \quad (6.33)$$

The voltage disturbances are, hence, fairly poorly rejected for the present current controller, in spite of active damping being used. This means that the grid voltage disturbances distort the grid current.

The disturbance reduction can be improved by increasing either the closed-loop bandwidth or the filter inductance L_g , as seen from (6.32). Alternatively, better disturbance reduction can be obtained by complementing the above feedback control with a feedforward design. Such a design has been proposed in [17, 106, 107] and [71], where the latter reference considered only the negative sequence of \mathbf{E}_g . Finally, so-called “dual current control” [105] may possibly be used for improved disturbance rejection. Except for some simulations made below, the topic of disturbance reduction for grid current control is not further considered in this thesis.

6.3 DC Voltage Control

6.3.1 Feedback Linearization

The design of the dc voltage controller is facilitated through use of *feedback linearization* [103]. The feedback linearization transforms the nonlinear dc voltage dynamics in (4.11) to an equivalent linear system representation, on which traditional linear controller techniques can be applied.

The following new state variable is introduced for the purpose of feedback linearization:

$$W = v_{dc}^2. \quad (6.34)$$

Substituting this in (4.11) gives the new system model as

$$\frac{1}{2}C \frac{dW}{dt} = -3E_g i_q - P_s \quad (6.35)$$

which is linear with respect to W . The physical interpretation of the state-variable substitution is that the “energy” is chosen to represent the dc voltage dynamics, instead of the dc voltage itself.

Similar variants for feedback linearization of the dc voltage dynamics have previously appeared in [62, 96]. We shall partly extend the results of these references by introducing active damping for the dc voltage controller, and by thoroughly investigating the load power rejection of the resulting control system structure.

Remark: References [21, 24, 83] proposed a different feedback linearization method compared to the above described one. Consider the alternative expression for the dc voltage dynamics in (4.12):

$$C \frac{dv_{dc}}{dt} = -\frac{3E_g i_q}{v_{dc}} - \frac{P_s}{v_{dc}}. \quad (6.36)$$

This can be linearized, in the sense of feedback linearization, by selecting i_q to

$$\hat{i}_C = -\frac{3E_g i_q}{v_{dc}} - \frac{P_s}{v_{dc}} \quad (6.37)$$

where \hat{i}_C is the *new input* (note that this ideally equals the true capacitor current in Fig. 4.4). By substituting \hat{i}_C in (6.36), the new linear system model then becomes

$$C\dot{v}_{dc} = \hat{i}_C. \quad (6.38)$$

This is the starting-point for the controller designs in [21, 24, 83]. The linearization in (6.37) is slightly more complicated compared to (6.34), however, so the linearized system resulting from the new state variable is preferred in the following controller design.

6.3.2 Controller Design

The transfer function from i_q to W in (6.35) is found to be

$$G(p) = -\frac{6E_g}{pC} \quad (6.39)$$

which has a pole in the origin, so an inner loop for active damping is here highly motivated. The inner loop is introduced by selecting i_q as

$$i_q = i'_q + G_a W \quad (6.40)$$

where G_a is the *active conductance* that provides active damping, and i'_q results from the outer feedback loop in Fig. 6.3. By substituting (6.40) in (6.35), the system model transforms to

$$\frac{1}{2}C \frac{dW}{dt} = -3E_g i'_q - 3E_g G_a W - P_s \quad (6.41)$$

which is depicted as a block diagram in Fig. 6.6. The transfer function from i'_q to W , which describes the resulting process model from the perspective of the controller $F(p)$, becomes

$$G'(p) = -\frac{6E_g}{pC + 6E_g G_a}. \quad (6.42)$$

Following (6.4), since $G'(p)$ is a first-order system, the following dc voltage controller results

$$F(p) = \frac{\alpha_d}{p} G'^{-1}(p) = -\frac{\alpha_d \hat{C}}{6E_{\text{nom}}} - \frac{\alpha_d G_a}{p} \quad (6.43)$$

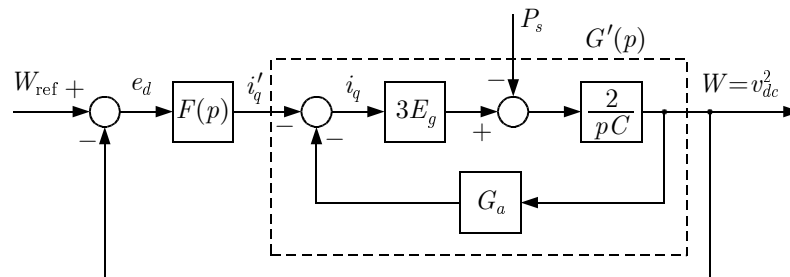


Fig. 6.6. DC voltage closed-loop control with inner feedback loop for active damping.

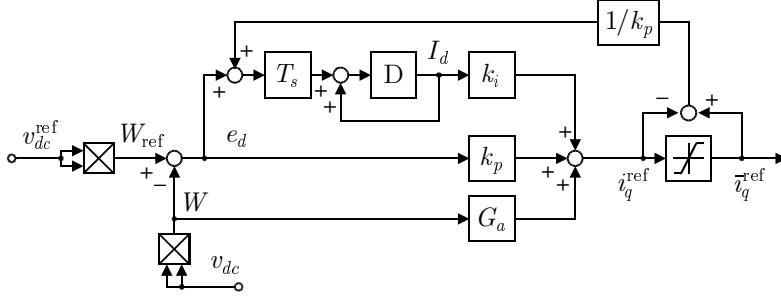


Fig. 6.7. Digitally implemented dc voltage controller. The integrator part of the controller is discretized by using the forward difference approximation [10]. “D” denotes the unit-delay operator and “ T_s ” is the sampling period.

which is an ordinary PI controller. Observe that IMC would have led to a proportional controller unless active damping were used. However, a PI controller is required for zero remaining error after a load power step, and such a controller results directly from IMC when using active damping.

A suitable choice is to make the inner feedback loop as fast as the closed-loop system. Placing the pole of $G'(p)$ at $-\alpha_d$ provides the active conductance as

$$\frac{6E_g G_a}{\hat{C}} = \alpha_d \Rightarrow G_a = \frac{\alpha_d \hat{C}}{6E_{\text{nom}}}. \quad (6.44)$$

The following summarizes the above design for the dc voltage controller:

$$e_d = W_{\text{ref}} - W = (v_{dc}^{\text{ref}})^2 - v_{dc}^2 \quad (6.45)$$

$$\frac{dI_d}{dt} = e_d + \frac{1}{k_p} (\bar{i}_q^{\text{ref}} - i_q^{\text{ref}}) \quad (6.46)$$

$$i_q^{\text{ref}} = k_p e_d + k_i I_d + G_a v_{dc}^2 \quad (6.47)$$

$$\bar{i}_q^{\text{ref}} = [i_q^{\text{ref}}]_{\min}^{\max} \quad (6.48)$$

where

$$k_p = -\frac{\alpha_d \hat{C}}{6E_{\text{nom}}}, \quad k_i = -\frac{\alpha_d^2 \hat{C}}{6E_{\text{nom}}}, \quad G_a = \frac{\alpha_d \hat{C}}{6E_{\text{nom}}} \quad (6.49)$$

are the proportional gain, the integration gain, and the active conductance, respectively, of the dc voltage controller. The bandwidth α_d of the dc voltage control loop must be chosen at least a decade smaller than the bandwidth of the grid current control loop, since the grid current dynamics have been neglected in the present design. Fig. 6.7 shows the digital implementation of the dc voltage controller as a block diagram.

6.3.3 Assessment of Disturbance Reduction

For accurate model parameters in the above controller design, the transfer function from the load power disturbance P_s to the error signal e_d in Fig. 6.6 becomes

$$G_{Pe}(p) = -\frac{1}{3E_g} \frac{G'(p)}{1 + F(p)G'(p)} = -\frac{p}{p + \alpha_d} \frac{G'(p)}{3E_g} = \frac{2p}{C(p + \alpha_d)^2}. \quad (6.50)$$

The load power P_s is capable of changing quickly, since it is roughly proportional to $\omega_r T_e$, and T_e may change as fast as the closed-loop stator current dynamics. Let us therefore study the step response of $e_d(t)$. Provided that the load power changes stepwise from zero to P at $t = 0$, then $e_d(t)$ becomes:

$$e_d = \mathcal{L}^{-1} \left\{ G_{Pe}(p) \frac{P}{p} \right\} = \mathcal{L}^{-1} \left\{ \frac{2P}{C(p + \alpha_d)^2} \right\} = \frac{2P}{C} t e^{-\alpha_d t}. \quad (6.51)$$

The time derivative of $e_d(t)$ is

$$\frac{de_d}{dt} = \frac{2P}{C} (1 - \alpha_d t) e^{-\alpha_d t} \quad (6.52)$$

which has a local maximum for $t = 1/\alpha_d$. By substituting this in (6.51), the maximum error is found to be

$$e_{d,\max} = \frac{2P}{\alpha_d C} e^{-1} \approx \frac{0.7P_s}{\alpha_d C}. \quad (6.53)$$

Given that P is positive, and by considering $v_{dc} = 0.9v_{dc}^{\text{ref}}$ as the minimal dc voltage allowed, then the maximum error for the load power step must remain below

$$e_{d,\max} < (v_{dc}^{\text{ref}})^2 - (0.9v_{dc}^{\text{ref}})^2 \approx 0.2(v_{dc}^{\text{ref}})^2. \quad (6.54)$$

When solving this inequality for α_d , the following constraint results

$$\alpha_d > \frac{0.7P}{0.2C(v_{dc}^{\text{ref}})^2} \approx \frac{4P}{C(v_{dc}^{\text{ref}})^2}. \quad (6.55)$$

The values $C = 20$ pu, $v_{dc}^{\text{ref}} = 2$ pu and $P = 4$ pu are considered for a numerical example (see Appendix A for details on the per-unit system), which give $\alpha_d > 0.2$ pu. This bandwidth corresponds to a dc voltage rise time of $t_r < 35$ ms, which can be considered as fast, but not unattainable for a PWM rectifier.

If only small values for $e_d(t)$ are allowed, or if C is small, it may then be necessary complement the feedback control with a feedforward design, as proposed in [72]. The feedforward compensation should be used with caution, however, since P_s may become highly distorted if the ac machine appears as an unsymmetrical load [83]. The distortion in P_s then spread directly to i_q , via the feedforward compensation, resulting in more a distorted grid current.

The feedforward compensation is introduced by subtracting $P_s/(3E_{\text{nom}})$ from (6.40):

$$i_q = i'_q + G_a W - \frac{P_s}{3E_{\text{nom}}} \quad (6.56)$$

where E_{nom} is the nominal grid voltage modulus, which is preferred over E_g in order to avoid that grid voltage disturbances spread to i_q . By substituting (6.56) in (6.35), the dc voltage dynamics become

$$\frac{1}{2}C \frac{dW}{dt} = -3E_g i'_q - 3E_g G_a W + \left(\frac{E_g}{E_{\text{nom}}} - 1 \right) P_s \quad (6.57)$$

so the load power theoretically cancels in the differential equation for W , provided that $E_{\text{nom}} = E_g$. In practice, however, further design considerations may be required if C is very small, we refer to [24, 62] for details on this topic.

Discussion of Grid Voltage Disturbances and Load Unsymmetrics

The dc voltage dynamics are in practice slightly more complicated than so far discussed, since v_{dc} is also affected by grid voltage disturbances, harmonics in \mathbf{i}_g and by load unsymmetrics [83]. This is not critical with respect to the dc voltage control, but increases the grid current distortion. Consider Fig. 6.6: if either one of E_g , i_q , or P_s (or all three) is distorted, then this distortion appears in v_{dc} , and is also further transmitted to i_q via the dc voltage control loop. The following two methods, at least, can be applied in order to reduce the distortion in \mathbf{i}_g :

Design the dc voltage control loop for a small bandwidth, or use different bandwidths for the transient and the steady-state operation [44, 96]. The dc voltage fluctuations are thereby allowed, given that the harmonic frequencies are at least a decade larger than the bandwidth of the dc voltage control loop. The allowed dc voltage fluctuations are not crucial for the proper operation of the back-to-back converter, since minor variations in v_{dc} are taken into consideration by the pulsewidth modulator [7].

Add zeros to the feedback loop of the dc voltage controller. These zeros should be selected such that the harmonics in the dc voltage are blocked from the feedback path. The dc voltage harmonics are thereby allowed by the controller, as they do not affect the setpoint for i_q .

These methods will not be further investigated, we leave them to future research.

6.4 Induction Machine Controllers

The following briefly describes the controller designs in [52, 99] for the purpose of providing a complete control system structure for the back-to-back converter. The methodology to design these controllers is similar to the procedure described in the present chapter, we refer to the mentioned references for further details. The controllers are here given in their analog form, which can be converted to digital form by using the forward difference method [10], for instance.

The following summarizes the current controller in [52, 99] for an induction machine:

$$\mathbf{e} = \mathbf{i}_{\text{ref}} - \mathbf{i}_s \quad (6.58)$$

$$\frac{d\mathbf{I}}{dt} = \mathbf{e} + \frac{1}{k_p}(\bar{\mathbf{v}}_{\text{ref}} - \mathbf{v}_{\text{ref}}) \quad (6.59)$$

$$\mathbf{v}_{\text{ref}} = k_p \mathbf{e} + k_i \mathbf{I} + (j\omega_1 \hat{L}_\sigma - R_a) \mathbf{i}_s \quad (6.60)$$

$$\bar{\mathbf{v}}_{\text{ref}} = \text{PWM}(\mathbf{v}_{\text{ref}}, \theta_1) \quad (6.61)$$

where

$$k_p = \alpha_c \hat{L}_\sigma, \quad k_i = \alpha_c (\hat{R}_s + R_a) = \alpha_c^2 \hat{L}_\sigma, \quad R_a = \alpha_c \hat{L}_\sigma - \hat{R}_s \quad (6.62)$$

are the proportional gain, the integration gain, and the active resistance, respectively, and α_c is the desired bandwidth for the stator current control loop. As seen, the controller does not differ much from the previously described grid current controller. The essential differences are that the filter inductance is replaced by the leakage inductance, and the filter resistance is substituted with the stator resistance.

The following summarizes the speed controller in [99] for an induction machine:

$$e_s = \omega_{\text{ref}} - \hat{\omega}_r \quad (6.63)$$

$$\frac{dI_s}{dt} = e_s + \frac{1}{k_p} (\hat{i}_q^{\text{ref}} - i_q^{\text{ref}}) \quad (6.64)$$

$$i_q^{\text{ref}} = k_p e_s + k_i I_s + B_a \hat{\omega}_r \quad (6.65)$$

$$\hat{i}_q^{\text{ref}} = [i_q^{\text{ref}}]_{\min}^{\max} \quad (6.66)$$

where

$$k_p = \frac{\alpha_s \hat{J}}{3n_p^2 \psi_{\text{ref}}}, \quad k_i = \frac{\alpha_s^2 \hat{J}}{3n_p^2 \psi_{\text{ref}}}, \quad B_a = \frac{\alpha_s \hat{J} - \hat{b}}{3n_p^2 \psi_{\text{ref}}} \quad (6.67)$$

are the proportional gain, the integration gain, and the active viscous friction, respectively, and α_s is the desired bandwidth of the speed control loop. This speed controller is for constant-inertia loads, a variable-inertia load may require a more sophisticated control system structure [5].

6.5 Simulation of PWM Rectifier

This section presents simulation results of the, in this chapter described, control system structure for the PWM rectifier. The bandwidths of the current control loop is 7 pu, corresponding to a current rise time of 1 ms, while the bandwidth of the dc voltage control loop is explicitly stated for each simulation. Only feedback control is used for both control loops, meaning that no kind of feedforward compensation is implemented.

The MCVN is used for grid flux estimation, having a bandwidth of $\rho = 0.3$ pu in the vicinity of $\tilde{\theta} = 0$. The filter parameters are $L_g = 0.1$ pu, $R_g = 0.01$ pu and the dc link capacitance is $C = 10$ pu. The corresponding model parameters are $\hat{L}_g = 1.1L_g$, $\hat{R}_g = 0.9R_g$ and $\hat{C} = 1.1C$.

The dc voltage setpoint is stepped from 2 pu to 2.5 pu at $t = 0$, and a load power step of 2 pu, corresponding to $i_q = -0.7$ pu, is applied at $t = 0.04$ s. A negative sequence voltage, accompanied by a “phase-angle jump” of -45° and voltage dip of 0.2 pu, occurs at $t = 0.08$ s. The negative sequence vanishes and fundamental voltage recovers at $t = 0.12$ s, which coincides with the occurrence of a fifth-order voltage harmonic. Table 6.1 summarizes the applied test sequence of steps and voltage disturbances.

TABLE 6.1
SIMULATION TEST SEQUENCE

t	(s)	< 0	0	0.04	0.08	0.12
v_{dc}^{ref}	(pu)	2	2.5	2.5	2.5	2.5
P_s	(pu)	0	0	2	2	2
E_1^+	(pu)	1	1	1	0.8	1
E_1^-	(pu)	0	0	0	0.3	0
E_5	(pu)	0	0	0	0	0.1

6.5.1 Fast DC Voltage Control Loop

Fig. 6.8 shows a simulation of the PWM rectifier with a dc voltage control bandwidth of 0.7 pu, corresponding to a rise time of 10 ms for the squared dc voltage. This rise time also approximately agrees with that of v_{dc} , as seen in Fig. 6.8(b).

Harmonics appear in the grid current, due to the fairly poor rejection of grid voltage disturbances for the studied control system structure. It can be seen from Fig. 6.8(a) that i_q is distorted when grid voltage disturbances are present. This distortion results from both the dc voltage and the grid current control loops. The MCVM, on the other hand, provides a good rejection of the voltage disturbances. As seen from Fig. 6.8(a), the maximum oscillation in $\tilde{\theta}$ has a magnitude of only $\tilde{\theta} \approx 0.1 \text{ rad} = 5.7^\circ$. Meanwhile, the “phase-angle jump” at $t = 0.08 \text{ s}$ is quickly tracked by the MCVM.

6.5.2 Slow DC Voltage Control Loop

This simulation is made under similar conditions as above described, but the closed-loop bandwidth for $W = v_{dc}^2$ is now 0.2 pu. This corresponds to a rise time of 35 ms for the squared dc voltage.

Fig. 6.9 shows the results of the simulation. Compared to Fig. 6.8, the smaller dc voltage bandwidth in this simulation reduces the distortion in i_q , as previously noticed in [44, 96]. However, the smaller bandwidth also yields a slower response to load power disturbance at $t = 0.04 \text{ s}$, which leads to a dip in v_{dc} of 0.2 pu. The response can be speeded up by adding feedforward compensation for the load power, as noticed in [72] and also described in Section 6.3.3.

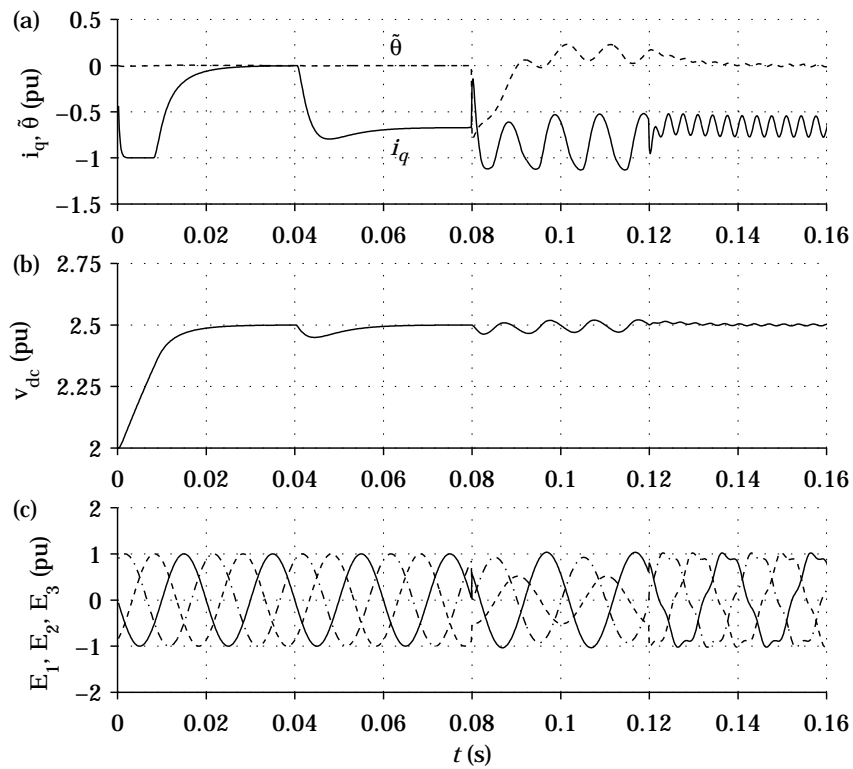


Fig. 6.8. Simulation of PWM rectifier with $\alpha_d = 0.7$ pu.

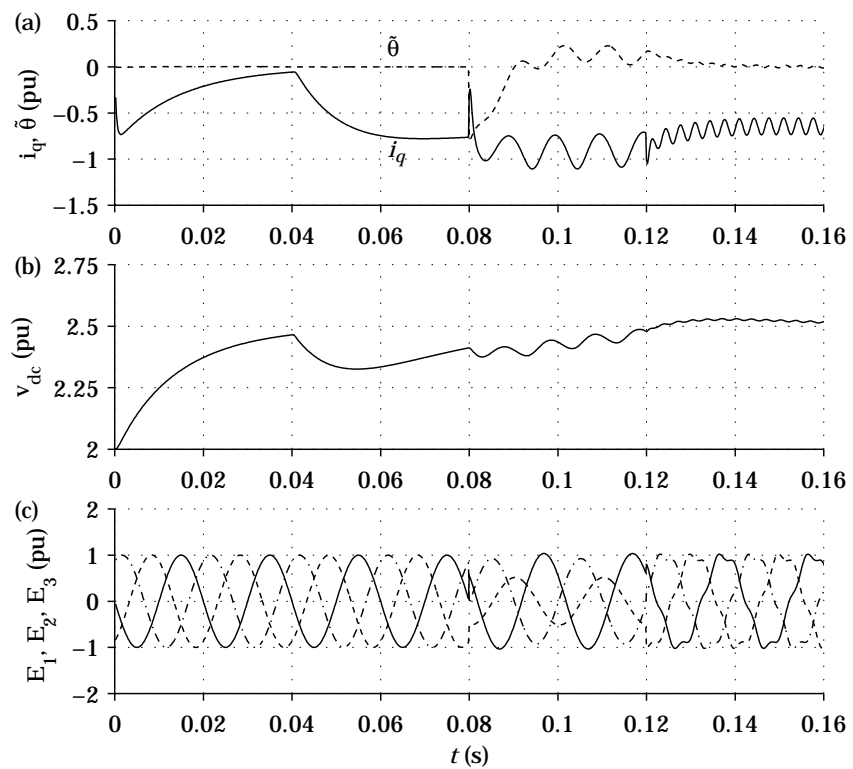


Fig. 6.9. Simulation of PWM rectifier with $\alpha_d = 0.2$ pu.

Chapter 7

Active Power Filtering and Deadbeat Current Control

In this chapter, the fully controlled grid current of a PWM rectifier is exploited for the purpose of shunt active power filtering at a moderate switching frequency. This application put special demands on the control system structure for the PWM rectifier, so the current controller design made in the previous chapter will not be used here. Instead, this chapter deals with current controllers that are tuned for the deadbeat response.

The chapter consists of two main parts. The first part deals with active filtering; some aspects for active filtering are initially described, and the studied system configuration is introduced. Five algorithms for identifying the harmonics to be filtered are then reviewed; these are referred to as harmonic detection algorithms. Experimental evaluation of active filtering follows. The second part of the chapter deals with analysis and development of the deadbeat current control loop. Deadbeat controllers designed to achieve the current command both in one and in two sampling periods are designed. Moreover, various methods to limit a command voltage vector that exceeds the maximum realizable voltage modulus are reviewed.

7.1 Active Filtering

An adjustable-speed drive (ASD) is often fed via a diode or thyristor rectifier. These are simple and cost-effective rectifiers, but produce distorted grid currents. In order to reduce the harmonic distortion of a group of ASDs, an active filter (AF) can be installed in parallel with the ASD [4, 13]. Alternatively, some of the ASDs may use PWM rectifiers that operate both as rectifiers and as AFs. The latter alternative leads to a cost-effective solution, since the size of the PWM rectifier only increases moderately when active filtering functionality is added [2].

Many proposed AFs use a hysteresis current controller with a high switching frequency of about 20 kHz. A classical method for active filtering is the so-called instantaneous reactive power principle [4], accompanied by an analog hysteresis current controller. The switching frequency of a conventional PWM rectifier is, however, usually around 5-to-7-kHz, in order to keep the switching loss of the semiconductor valves at

an acceptable level. The low switching frequency limits the maximum attainable bandwidth for the current control loop, so active filtering becomes more difficult to achieve. In addition, a computational delay is often introduced for a digitally implemented control system structure, which further complicates active filtering.

An AF may be programmed to only remove current harmonics that exceed a certain level, for instance, the level set in [65]. We shall refer to this as *selective filtering*, and study two methods for such type of filtering in the following. An advantage of selective filtering is that the required current modulus for the AF becomes smaller.

7.1.1 System Configuration

The studied system configuration is shown in Fig. 7.1. The system consists of two ASDs, which are fed via a thyristor rectifier and a PWM rectifier, respectively. The PWM rectifier operates as an AF, attempting to filter the harmonic load current of the thyristor rectifier. Unlike the terminology used in the previous chapters, we shall now reserve the term grid current for the sum of the currents that originate from the thyristor and the PWM rectifiers, i.e., the current that is referred to as \mathbf{i}_{grid} in Fig. 7.1.

In the following, the ASD connected to the PWM rectifier is in the no-load operation, so the current of the thyristor rectifier, denoted by \mathbf{i}_L , is the resulting load current of the system. The load current in the three-phase system can therefore be described by the following periodic sequences

$$i_{L,1}(t) = \sum_n i_{L(n)} \cos(n\omega_g t + \phi_{L(n)}) \quad (7.1)$$

$$i_{L,2}(t) = \sum_n i_{L(n)} \cos\left(n\omega_g t + \phi_{L(n)} - n\frac{2\pi}{3}\right) \quad (7.2)$$

$$i_{L,3}(t) = \sum_n i_{L(n)} \cos\left(n\omega_g t + \phi_{L(n)} - n\frac{4\pi}{3}\right) \quad (7.3)$$

where $i_{L(n)}$ is the n th harmonic amplitude of the load current, and $\phi_{L(n)}$ is the n th harmonic phase shift between the load current and the fundamental grid voltage. In the following, current harmonics up to the thirteenth-order are considered, excluding the triplens, since a conventional PWM rectifier is incapable of filtering triplen current harmonics.

The vector-current controller [82, 106] that is used for the PWM rectifier for the purpose of active filtering is depicted in Fig. 7.2. The controller is designed for the deadbeat response, so the current reference $\mathbf{i}_g^{\text{ref}}$ ideally equals the desired value for the true current \mathbf{i}_g at the next sampling instant. However, a current response time of two sampling periods is effectively obtained, since the control computer for the studied system configuration introduces a computational delay of one sampling period.

A special form of delay-time compensation is used by the vector-current controller, in order to tackle the computational delay of the control computer, we refer to [82, 106] for further details on this compensation method.

The AF functionality for the PWM rectifier is essentially introduced by the following three steps. Firstly, the currents originating from the thyristor rectifier, \mathbf{i}_L , are measured by the control system of the PWM rectifier. Secondly, the current harmonics

This delay greatly affects the capability of the AF to cancel current harmonics, especially if the sampling frequency is low: once the true AF current has reached the desired setpoint $\mathbf{i}_{\text{AF}}^{\text{ref}}$, then the load current harmonics no longer remain in the states they were at two sampling periods ago. The true AF current \mathbf{i}_{AF} , hence, appears as phase shifted with respect to the harmonics in \mathbf{i}_L . The sampling frequency 5 kHz and the fundamental frequency 50 Hz are considered for numerical example, which give that the phase shift for the eleventh-order harmonic becomes $\phi_{L(11)} = 11 \cdot 2\pi 50 \cdot 2/5000 \approx 1.4 \text{ rad} \approx 80^\circ$. Evidently, this phase shift reduces for larger sampling frequencies, but is critical for active filtering at a low sampling and switching rate.

Various methods for phase shift compensation have been presented. Reference [40] proposed an adaptive filter, while [81] used a phase leading compensator filter, which was implemented in analog hardware. If the harmonics are stationary, the phase shift can also be compensated by using old load current measurements (half a fundamental grid period minus two samples back) that are stored in RAM [2]. An alternative to this method is to phase compensate each harmonic separately, by using predicted values for the phase shifts of each individual harmonic. This method is only applicable for selective active filtering, though, since it requires that each harmonic is detected separately. We shall investigate the two latter methods for phase shift compensation, i.e., old load current measurements stored in RAM, and individual phase shift compensation.

7.1.3 Selective Active Filtering

Selective active filtering implies that the AF is not attempting to cancel all of the harmonics that are present in \mathbf{i}_L ; only individual harmonic currents, which are selected by the AF control system, are canceled. Since the phase shift for each harmonic can easily be predicted, an effective compensation method for selective active filtering is to add the predicted phase shift to the space vector angle of each detected current harmonic.

In the stator-oriented reference frame, the phase shifts for each harmonic during the delayed current response of two sampling periods are

$$\Delta\phi_L^s = \begin{cases} n\omega_g 2T_s, & n = 7, 13, 19, \dots \\ -n\omega_g 2T_s, & n = 5, 11, 17, \dots \end{cases} \quad (7.4)$$

where n is the harmonic order, ω_g is the angular grid frequency, and $2T_s$ represents the delayed current response of two sampling periods. As seen, negative phase shifts result for $n = 5, 11, 17, \dots$, since these harmonics form negative sequences.

Eq. (7.4) holds only in the stator-oriented reference frame, since also the rotating nature of the coordinate system should be considered for the synchronous reference frame. The total phase shift then equals the sum of the phase shift for each harmonic and the phase shift introduced by the rotation of the synchronous reference system. The predicted phase shifts for the harmonics in the synchronous coordinates thus become

$$\Delta\phi_L = \begin{cases} (n-1)\omega_g 2T_s, & n = 7, 13, 19, \dots \\ -(n+1)\omega_g 2T_s, & n = 5, 11, 17, \dots \end{cases} \quad (7.5)$$

which are, henceforth, referred to as the predicted phase shifts. As seen, the fifth- and the seventh-order harmonics have similar phase shifts, albeit their signs differ, and a

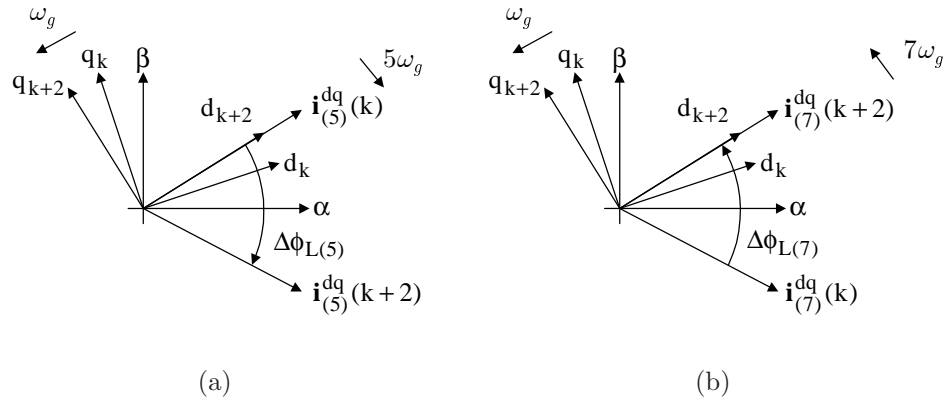


Fig. 7.3. Total phase shift in the synchronous reference frame for the: (a) Fifth-order harmonic. (b) Seventh-order harmonic.

similar observation can be made for the eleventh- and the thirteenth-order harmonics. This is due to that the fifth- and the eleventh-order harmonics form negative sequences, while the seventh- and the thirteenth-order harmonic form positive sequences. Fig. 7.3 illustrates the resulting phase shifts for the fifth- and the seventh-order harmonics.

Selective active filtering can be based on various algorithms. Some of the proposed methods use bandpass filters [92] or Fourier series [2] to extract individual current harmonics, and a recently proposed method uses synchronously rotating coordinate systems for each of the individual current harmonics [68]. We shall in the following consider the latter two methods for selective filtering.

7.1.4 Detection of Current Harmonics

Direct Active Filtering Method

The direct active filtering method (D method) separates the fundamental load current from the load current distortion. Consequently, individual harmonics are not detected. The D method relies on that the fundamental part of \mathbf{i}_L appears as a dc quantity in the synchronous reference frame, which can be separated from the harmonics by implementing lowpass filters in the d and the q directions; one filter is required in each direction. The load current distortion is calculated by subtracting the output signals of the lowpass filters from the non-filtered variants of $i_{L,d}$ and $i_{L,q}$, which is depicted in Fig. 7.4. Observe that the lowpass filter does not phase shift the fundamental, which is a dc signal in the synchronous reference frame. Second-order Butterworth lowpass filters, all having the cut-off frequency 20 kHz, are here used for the D method.

The delayed current response of two sampling periods can for the D method be circumvented by taking advantage of the periodicity of the load current, provided that the load remains in the steady-state operation. In essence, the load current for the previous half period are stored in RAM [2], which are then used to predict the AF reference current two samples ahead. This procedure is henceforth referred to as the direct method using phase shift compensation (DP).

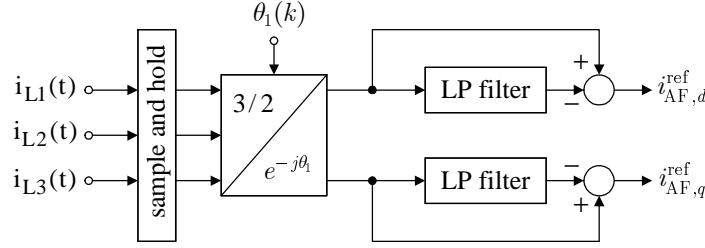


Fig. 7.4. Principle of the D method, which uses lowpass filters to detect the load current distortion.

Fourier Method

The Fourier method, henceforth referred to as the F method, uses a numerical implementation of a moving Fourier series to detect the harmonics of the load current [2]. Due to the assumed three-phase symmetry, it suffices to detect the harmonics in one of the three phases. In the three-phase system, the periodic load phase current can be written in the discrete form as

$$i_L(k) = \sum_{n=1}^{\infty} i_{L(n)} \cos(n\Omega_g kT_s + \phi_{L(n)}) \quad (7.6)$$

where $i_{L(n)}$ is the magnitude of the n th order load current harmonic, and $\Omega_g = 2\pi/N$, N being the number of samples for one fundamental period. Writing the load current as a discrete-time Fourier series yields

$$i_L(k) = \sum_{n=1}^{\infty} a_{(n)} \cos(n\Omega_g kT_s) + b_{(n)} \sin(n\Omega_g kT_s) \quad (7.7)$$

where $a_{(n)}$ and $b_{(n)}$ are the Fourier coefficients. The coefficients $a_{(n)}$ and $b_{(n)}$ can be written recursively as

$$a_{(n)}(k) = a_{(n)}(k-1) + \frac{4}{N} \left[i_L(k) + i_L\left(k - \frac{N}{2}\right) \right] \cdot \cos(n\Omega_g kT_s) \quad (7.8)$$

$$b_{(n)}(k) = b_{(n)}(k-1) + \frac{4}{N} \left[i_L(k) + i_L\left(k - \frac{N}{2}\right) \right] \cdot \sin(n\Omega_g kT_s). \quad (7.9)$$

The magnitudes of the individual harmonics and their corresponding phase angles become

$$i_{L(n)} = \sqrt{a_{(n)}^2 + b_{(n)}^2}, \quad \phi_{L(n)} = \arg(a_{(n)} - jb_{(n)}) \quad (7.10)$$

respectively. Since the phase angle of each harmonic is individually derived, phase shift compensation can be accomplished by adding the predicted phase shift for each harmonic to their corresponding phase angle.

Fig. 7.5 depicts the resulting algorithm for the F method as a block diagram. The phase shifts caused by the delayed current response are added to the phase angles of each harmonic in the block “phase compensation.” The block entitled “reference reduction” controls the amount of compensation for each harmonic, by scaling the amplitudes of the detected harmonics with the scale factors \mathbf{r} . For instance, $r_5=0$ would imply

that the fifth-order harmonic is allowed by the AF. Once the phase shifts have been compensated and the amplitudes have been scaled, the resulting detected harmonics are transformed to the synchronous reference frame. The resulting space vector $\mathbf{i}_{AF}^{\text{ref}}$ becomes the reference current vector for the AF.

Transformation Method

The transformation method (T method) [68] can be considered as the opposite approach compared to the D method. Instead of separating the fundamental from the load current distortion in the synchronous reference frame, the T method separates the individual harmonics from the fundamental load current. This is performed by lowpass filtering the load current in several coordinate systems, where the rotation frequency of each system equals the frequency of a specific current harmonic. For instance, the fifth-order harmonic appears as a dc signal in a reference frame that rotates with $-5\omega_g$, with respect to the stator-oriented system.

Two lowpass filters are required in each rotating reference frame, since the real and the imaginary directions require one filter each. Consequently, totally eight lowpass filters are needed to detect the harmonics of order 5–13. Each lowpass filter has the Butterworth characteristic, and is designed for a cut-off frequency of 20 Hz. The filters are only of the first-order, in order to increase the execution speed of the T method.

Fig. 7.6 depicts the T method as a block diagram. As seen, the phase shift compensation, to circumvent the delayed current response of two sampling periods, is accomplished by adding the predicted phase shifts $\Delta\phi_{L(n)}$ when transforming from the different reference frames of the current harmonics to the synchronous reference frame.

Response Times of the Harmonic Detection Methods

The response time of the F method is 0.5 cycles, i.e., 10 ms for the fundamental frequency 50 Hz, while the response times of the T method and the D method depend on how the lowpass filters are designed. For the present designs, the T method and the D method use first-order and second-order Butterworth filters, respectively, and all filters have the cut-off frequency 20 Hz. Therefore, both the T method and the D method have similar response times, which approximately equal 25 ms. Compared to the D method, the DP method has an additional response time of 0.5 cycles compared to the D method, which is due to that the DP method requires 0.5 cycles to store the previous load current measurements in RAM.

The above presented harmonic detection methods will operate well provided that the load current is periodic, i.e., $\mathbf{i}_L(t) = \mathbf{i}_L(t - T_p)$, T_p being the period time of the fundamental. However, the response times of the detection methods are at least 10 ms, which makes the presented algorithms less suitable if the current harmonics are non-periodic, i.e., $\mathbf{i}_L(t) \neq \mathbf{i}_L(t - T_p)$. More advanced harmonics detection methods are required if the operating mode $\mathbf{i}_L(t) \neq \mathbf{i}_L(t - T_p)$ occurs too frequently. Such advanced algorithms may, for instance, rely on predictive signal processing [113].

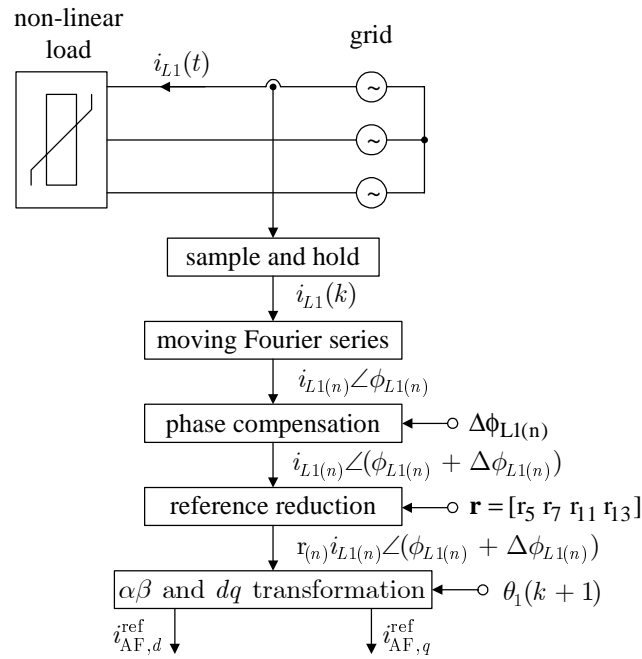


Fig. 7.5. Algorithm of the F method.

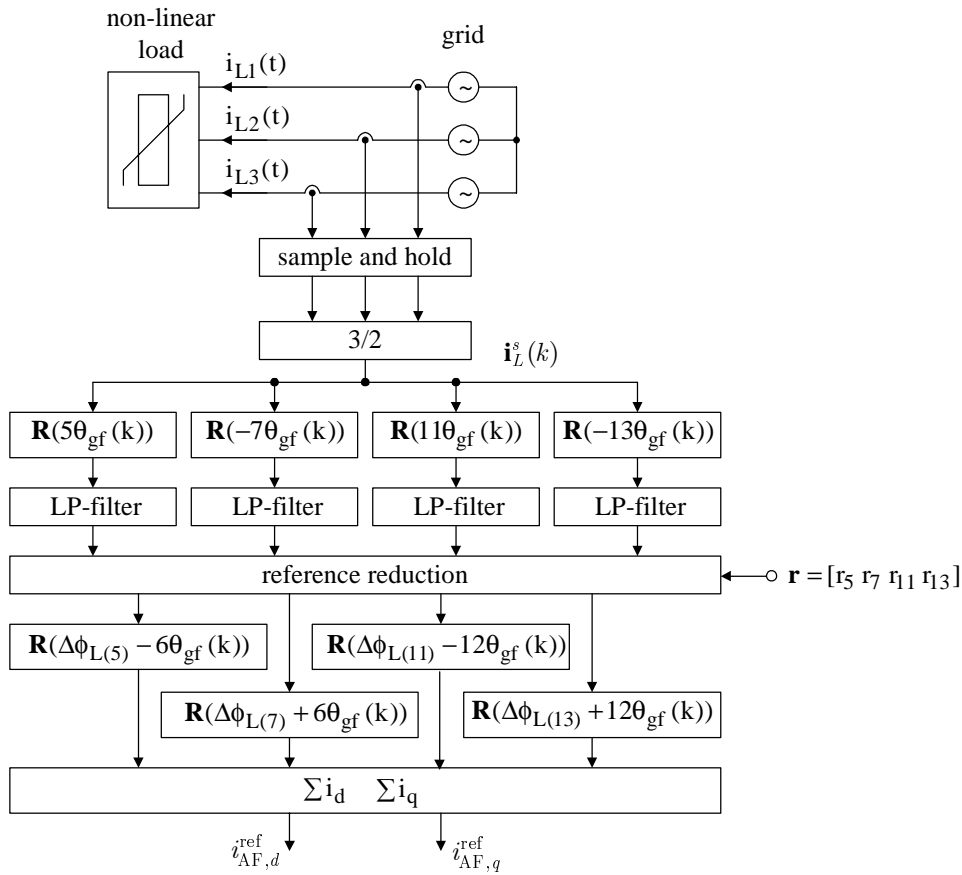


Fig. 7.6. T method algorithm.

7.1.5 Experiments

The experimental AF is a PWM rectifier, equipped with IGBT valves (Toshiba MG400-Q1US41 1200V, 400A) and a TMS320C30 control computer. The base values for the PWM rectifier are 400-V rms phase-to-phase and 35-A rms. Variations in the dc-link voltage, as well as the blanking time and on-state voltage drop of the semiconductor valves, are compensated by the control program. The harmonic load current is produced by a thyristor rectifier, which has a smoothing inductor L_{dc} and a load resistor R_{dc} on the dc-side. Furthermore, a commutation inductor L_{ac} is placed between the grid and the thyristor rectifier in order to reduce commutation notches. The sampling frequency, f_s , equals the switching frequency, f_{sw} , of the PWM rectifier. Table 7.1 summarizes characteristic parameters of the experimental system.

TABLE 7.1
CHARACTERISTIC PARAMETERS OF EXPERIMENTAL SYSTEM

$L_g = 0.071$ pu	$E_g = 1.0$ pu	$\omega_g = 2\pi 50$ rad/s	$f_s = f_{sw} = 6.0$ kHz
$R_g = 0.012$ pu	$v_{dc} = 2.0$ pu	$T_s = 167$ μ s	$R_{dc} = 1.8$ pu
$L_{ac} = 0.021$ pu	$L_{dc} = 1.9$ pu		

TABLE 7.2
EXECUTION TIMES FOR THE HARMONIC DETECTION METHODS

Algorithm	Execution time (μ s)	Algorithm	Execution time (μ s)
D	14	F	17
DP	16	T	34

The controller program is written in the C language, in order to facilitate the development of the control code. The execution speeds for the different harmonic detection methods are listed in Table 7.2. The T method is the most time-demanding algorithm, since it uses eight first-order lowpass filters, while the D method uses only two second-order lowpass filters.

In the following, all currents are normalized to the magnitude of the fundamental load current. The measured load current and its frequency spectrum are shown in Fig. 7.7, where the peak value for the current equals 35 A.

It was necessary to reduce the load current modulus when using the D method and the DP method, since these algorithms provide the total load current distortion. Given the load current in Fig. 7.7, steep current steps appear in $\mathbf{i}_{AF}^{\text{ref}}$, and these steps unavoidably forces the deadbeat current controller into voltage saturation for the D and the DP methods. Unfortunately, the voltage saturation resulted in integrator windup for the here used current controller, which in turn led to poor active filtering performance. The reduced load current alleviated these problems for the here used deadbeat current controller.

Fig. 7.8 shows the performance of active filtering for the D method and the DP method. As seen from the harmonic spectra in Fig. 7.8(b), the grid current is almost as distorted when using the D method as when no AF is used at all (load). This is

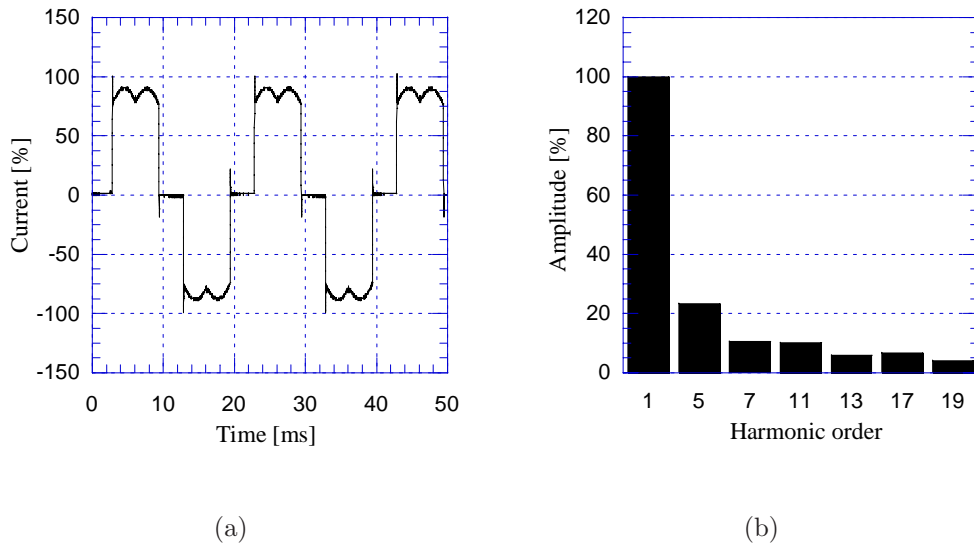


Fig. 7.7. (a) The load current as a function of time. (b) The frequency spectrum of the load current.

due to that the D method does not consider the phase shifts of the current harmonics during the delayed current response. The performance of the DP method is better, since the load current harmonics are reduced by a factor two, at least, in the resulting grid current.

Three experiments were conducted in order to investigate the performance of the selective active filtering methods, i.e., the F method and the T method. In the first experiment, the load current harmonics of the orders 5, 7, 11, and 13 were filtered, while only the fifth-order harmonic was filtered in the second experiment. The third experiment considered active filtering of the seventh-, the eleventh-, and the thirteenth-order harmonics, while the fifth-order harmonic was allowed by the AF. The results of these experiments are shown in Figs. 7.9–7.11. As seen, the current harmonics are successfully canceled by the AF, and the F method has an edge over the T method with respect to filtering capability. This is due that the T method uses only first-order lowpass filters, so the current harmonics cannot be properly separated from the load current fundamental. The T method would have benefitted from higher-order filters, but such filters would also have increased the execution time for the T method.

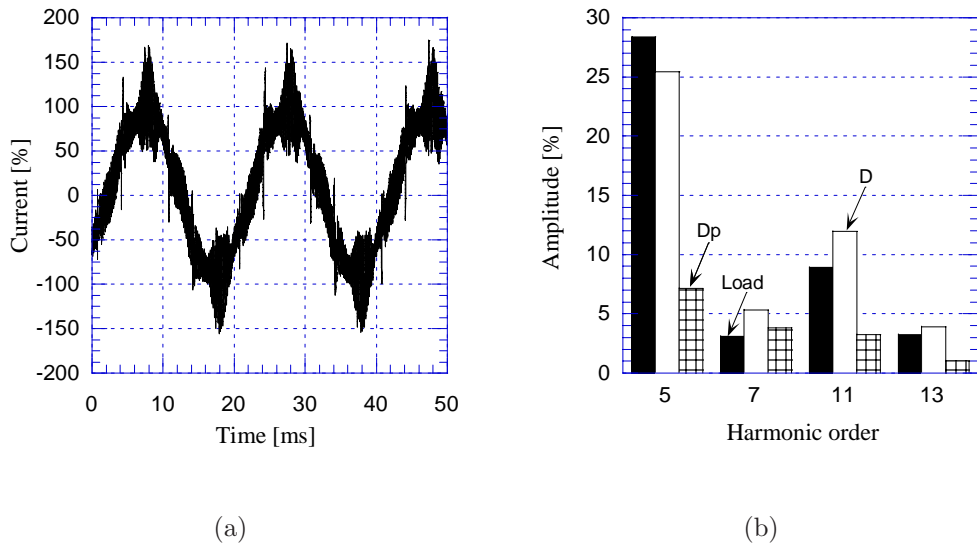


Fig. 7.8. (a) Grid current using DP method. (b) Harmonic spectrum of the grid current for: without AF (load), with AF using the D and DP methods.

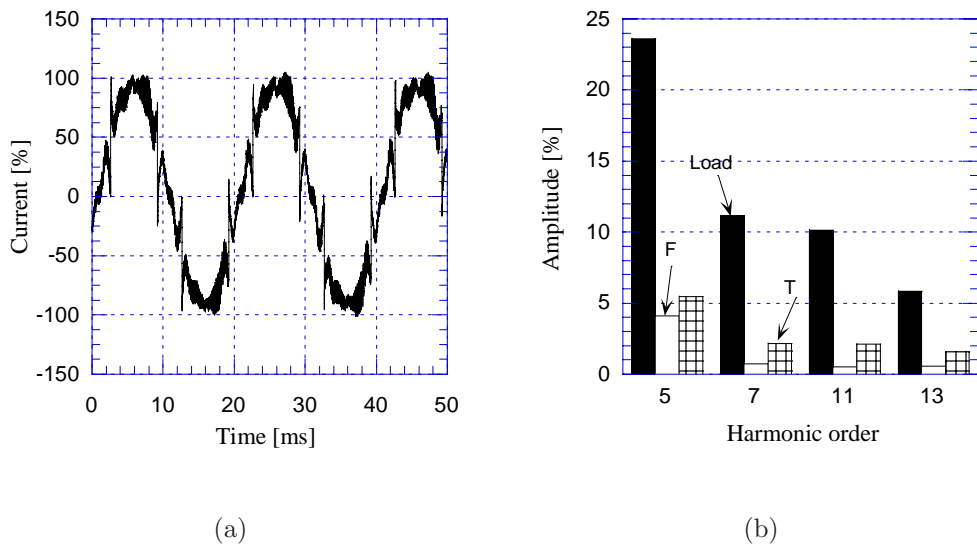


Fig. 7.9. The fifth-, the seventh-, the eleventh-, and the thirteenth-order harmonics of \mathbf{i}_L^s are filtered. (a) Resulting grid current when using the F method. (b) Harmonic spectrum of the grid current for: without AF (load), AF using the F and T methods.

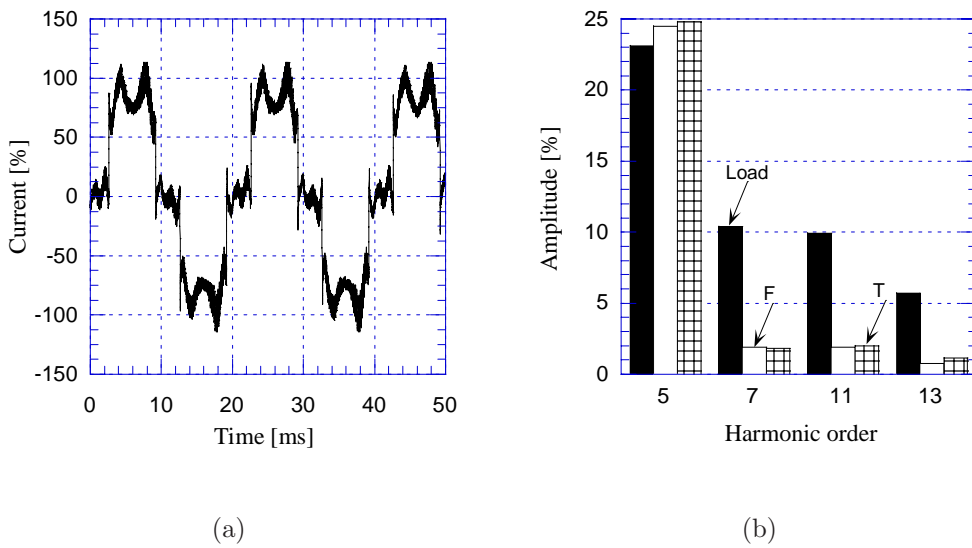


Fig. 7.10. The seventh-, the eleventh-, and the thirteenth-order harmonics of i_L^s are filtered, but the fifth-order harmonic is allowed. (a) Resulting grid current when using the F method. (b) Harmonic spectrum of the grid current for: without AF (load), AF using the F and T methods.

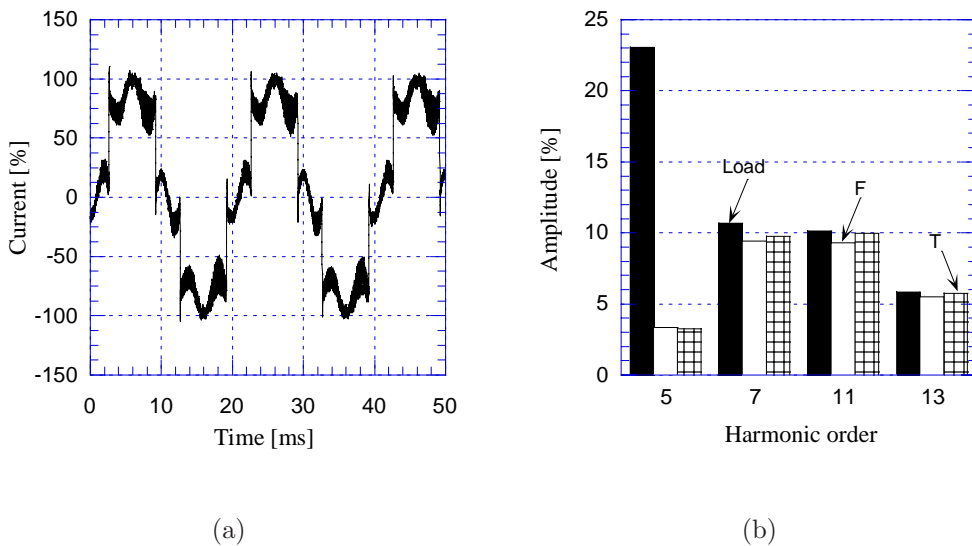


Fig. 7.11. Only the fifth-order harmonic is filtered, the remaining harmonics are allowed by the AF. (a) Resulting grid current when using the F method. (b) Harmonic spectrum of the grid current for: without AF (load), AF using the F and T methods.

7.1.6 Summary

This chapter has so far demonstrated that active filtering can be achieved when using 6 kHz switching and sampling frequencies together with a sub-oscillating PWM and a digitally implemented vector-current controller. All three active filtering methods that use phase shift compensation (i.e., the D method, the F method and the T method) operate satisfactorily. Experimental tests show that individual harmonic cancelations up to the thirteenth order were successful. However, the experiments conveyed that the deadbeat current controller was incapable of handling voltage saturation in a desirable manner. We shall therefore in the remaining part of this chapter investigate the proper design a deadbeat current controller.

7.2 Deadbeat Control and Saturation Strategies

The following sections investigate deadbeat current control for a PWM rectifier. The presence of computational delay in the control system is described, and two current controllers with finite settling times (deadbeat) are designed and analyzed. One of these deadbeat current controllers is designed to achieve the current command in one sampling period (will be referred to as one-sample deadbeat), while the other ideally achieves the current command in two sampling periods (will be referred to as two-samples deadbeat).

Various algorithms to limit a voltage vector that exceeds the maximum realizable voltage modulus of a PWM converter are also described. These limiting algorithms are applicable for any vector current controller, but are particularly valuable for a deadbeat controller: the large proportional gain of a deadbeat controller easily leads to voltage saturation, even for fairly small current steps. Finally, the study concludes with an experimental evaluation of the resulting control system structure.

7.2.1 Computational Delay

The design of a digitally implemented controller depends on whether the computational time of the control computer, which host the control algorithm, is negligible or not compared to the settling time of the feedback control system. Consider Fig. 7.12. The computational time in Fig. 7.12(a) is much smaller than the sampling period. Consequently, a feedback controller can be designed under the assumption on a delay-free control computer. In Fig. 7.12(b), however, the computational time equals the sampling period time. The computational delay is negligible for feedback systems where the

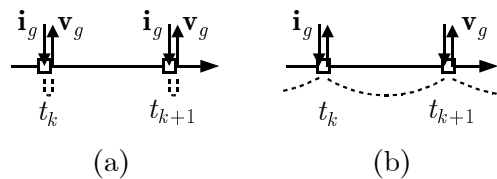


Fig. 7.12. Computational times. (a) Delay-free control computer. (b) One-sample delayed control computer.

closed-loop bandwidth is much smaller than the sampling frequency. Then, the feedback controller can be designed in a similar manner as if a truly delay-free control computer were used. For the one-sample deadbeat controller, however, the computational delay is highly critical: the one-sample settling time then equals the computational delay. It will be below shown that the one-sample deadbeat controller is only marginally stable in the presence of computational delay, while the two-samples deadbeat controller is stable, albeit highly sensitive to the accuracy of the model parameters.

7.2.2 Design of Deadbeat Current Controllers

A deadbeat controller is a special variant of internal model control; both the deadbeat and IMC controller cancel the process dynamics, and then place the closed-loop poles at the desired location. IMC can therefore be used for designing deadbeat controllers, even though the deadbeat response requires that digital control system design is used.

Active damping will not be considered in the following text, since the experiments in this chapter were conducted at an early stage during the development of the present thesis. Instead of active damping, a feedforward design is implemented in order to speed up the response to grid voltage disturbances [107].

References [17, 78] proposed to use the Smith predictor [95, 104] in order to overcome the computational delay of a “slow” control computer for the one-sample deadbeat controller. In the following, it is demonstrated that the resulting control system structure of the Smith predictor is identical to the two-samples deadbeat controller that results from IMC.

Discretization of the Process Model

The first step in the controller design is to cancel to cross-coupling between i_d and i_q in (4.2), and to implement the feedforward design for \mathbf{E}_g . These issues are accomplished by selecting \mathbf{v}_g to [107]

$$\mathbf{v}_g = \mathbf{v}'_g + j\omega_1 \widehat{L}_g \mathbf{i}_g + \mathbf{E}_g. \quad (7.11)$$

where \mathbf{v}'_g results from the feedback control loop. By substituting (7.11) in (4.2), the grid current dynamics become

$$L_g \frac{d\mathbf{i}_g}{dt} = \mathbf{v}'_g - R_g \mathbf{i}_g \quad (7.12)$$

under the assumption that $\widehat{L}_g = L_g$, and that the feedforward compensation cancels \mathbf{E}_g perfectly. Consequently, the transfer function from \mathbf{v}'_g to \mathbf{i}_g becomes

$$\mathbf{G}(p) = \frac{1}{pL_g + R_g}. \quad (7.13)$$

The second step in the deadbeat controller design is to discretize the continuous process model $\mathbf{G}(p)$. However, \mathbf{v}_g is pulsewidth modulated [59] in nature, so $\mathbf{G}(p)$ is hard to meaningfully discretize. It is here assumed that \mathbf{v}'_g can be approximated as piecewise

constant in one sampling period (often referred to as *zero-order hold* [10]), which gives the following discrete model:

$$\mathbf{G}(z) = (1 - z^{-1})\mathcal{Z} \left[\mathcal{L}^{-1} \left\{ \frac{\mathbf{G}(p)}{p} \right\} \right] = \frac{1 - e^{-R_g T_s / L_g}}{R_g (z - e^{-R_g T_s / L_g})} \quad (7.14)$$

where $z = e^{pT_s}$. For small R_g or small T_s , this can be simplified by series expanding $e^{-R_g T_s / L_g}$ about zero:

$$e^{-R_g T_s / L_g} \approx 1 - \frac{R_g T_s}{L_g}. \quad (7.15)$$

The quality factor $q = \omega_g L_g / R_g = 5$ and $T_s = 0.1$ pu, corresponding to a sampling frequency of 3 kHz, are considered in order to verify this assumption numerically. This gives

$$e^{-\omega_g T_s / q} = e^{-1 \cdot 0.1 / 5} = 0.9802, \quad 1 - \frac{\omega_g T_s}{q} = 1 - \frac{1 \cdot 0.1}{5} = 0.9800 \quad (7.16)$$

which are clearly in close agreement, so (7.15) can safely be substituted in (7.14):

$$\mathbf{G}(z) \approx \frac{\frac{R_g T_s}{L_g}}{R_g \left(z - 1 + \frac{R_g T_s}{L_g} \right)} = \frac{1}{\frac{z-1}{T_s} L_g + R_g}. \quad (7.17)$$

This is, not surprisingly, identical to the forward difference approximation [10] of $\mathbf{G}(p)$. We henceforth consider (7.17) as a sufficiently accurate discrete representation of $\mathbf{G}(p)$.

Discretization of the Current Decoupling Term

The current decoupling term $j\omega_1 \tilde{L}_g \mathbf{i}_g$ in (7.11) must be converted to discrete form for a digital implementation. This is, however, not trivial, since a digital decoupling term cannot perfectly cancel the analog nature of the cross-coupling between i_d and i_q in the continuous-time domain. The current decoupling is particularly troublesome to achieve for a deadbeat control system structure, where the low sampling rate in relation to the large closed-loop bandwidth makes it difficult to approximate \mathbf{i}_g digitally.

Reference [8] proposed to approximate \mathbf{i}_g in one sampling period by the following averaged value:

$$\mathbf{i}_{g,k,k+1}^{\text{ave}} \approx \frac{1}{2} (\mathbf{i}_{g,k+1} + \mathbf{i}_{g,k}) = \frac{1}{2} (\mathbf{i}_{g,k}^{\text{ref}} + \mathbf{i}_{g,k}) \quad (7.18)$$

where the latter equality holds for the one-sample deadbeat controller, i.e., $\mathbf{i}_{g,k+1} = \mathbf{i}_{g,k}^{\text{ref}}$ ideally. A similar approximation to the above one can be introduced also for the two-samples deadbeat controller:

$$\mathbf{i}_{g,k,k+2}^{\text{ave}} \approx \frac{1}{2} (\mathbf{i}_{g,k+2} + \mathbf{i}_{g,k}) = \frac{1}{2} (\mathbf{i}_{g,k}^{\text{ref}} + \mathbf{i}_{g,k}). \quad (7.19)$$

The discrete form of (7.11) can hence be approximated by

$$\mathbf{v}_{g,k} = \mathbf{v}'_{g,k} + j\omega_1 \hat{L}_g \frac{\mathbf{i}_{g,k}^{\text{ref}} + \mathbf{i}_{g,k}}{2} + \mathbf{E}_{g,k} \quad (7.20)$$

regardless of whether the current control loop is designed to achieve the current command in one or two sampling periods

One-Sample Deadbeat Controller

The one-sample deadbeat controller will be designed by means of IMC. Since $\mathbf{G}(z)$ is a first-order system, the controller design should rely on the discrete variant of (6.4). By using the forward difference method on (6.4), the controller resulting from IMC becomes

$$\mathbf{F}_1(z) = \frac{\alpha}{z-1} \hat{\mathbf{G}}^{-1}(z). \quad (7.21)$$

The closed-loop system can be evaluated in order to deduce what α that corresponds to the one-sample deadbeat response. For accurate model parameters, the closed-loop system is

$$\mathbf{G}_c(z) = \frac{\mathbf{F}_1(z)\mathbf{G}(z)}{1 + \mathbf{F}_1(z)\mathbf{G}(z)} = \frac{\alpha T_s}{z-1 + \alpha T_s}. \quad (7.22)$$

Hence, $\alpha = 1/T_s$ represents the one-sample deadbeat response for IMC, since this bandwidth yields $\mathbf{G}_c(z) = z^{-1}$. This observation can easily be extended to hold for all deadbeat controllers resulting from IMC, given that the process model is accurately discretized by the forward difference approximation. The closed-loop system must then equal the forward-difference discretized variant of (6.2b):

$$\mathbf{L}(z) = \frac{(\alpha T_s)^n}{(z-1 + \alpha T_s)^n}. \quad (7.23)$$

It can from this equation be concluded that $\alpha = 1/T_s$ *always represents the deadbeat response for IMC*. The resulting current settling time depends on the filter order, however, so the closed-loop deadbeat system for accurate model parameters becomes $\mathbf{G}_c(z) = \mathbf{L}(z) = z^{-n}$.

The sampling frequency and the deadbeat bandwidth are related as

$$\frac{\omega_s}{\alpha} = \frac{2\pi/T_s}{1/T_s} \approx 6.3. \quad (7.24)$$

This is slightly smaller than the recommended selection $\omega_s \geq 10\alpha$ [45, 86], which is required for good correspondence between the true mixed continuous-time-discrete-time system and the digital approximation.

By substituting $\alpha = 1/T_s$ in (7.21), the following one-sample deadbeat controller results:

$$\mathbf{F}_1(z) = \frac{\hat{\mathbf{G}}^{-1}(z)}{z-1} = \frac{\hat{L}_g}{T_s} + \frac{\hat{R}_g}{T_s} \frac{T_s}{z-1} = \frac{\hat{L}_g}{T_s} + \frac{\hat{R}_g}{T_s} \frac{T_s z^{-1}}{1-z^{-1}}. \quad (7.25)$$

The gain parameters in the above equation agree well with the parameters of the one-sample deadbeat controller in [7], albeit the controller in this reference was derived in

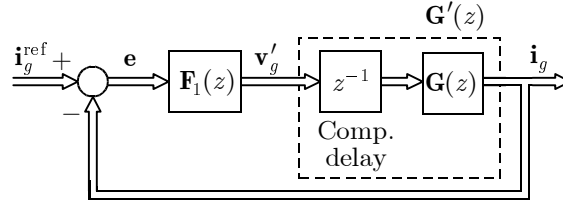


Fig. 7.13. Feedback control system structure for the one-sample deadbeat controller in the presence of computational delay.

a different manner. The deadbeat response essentially originates from the proportional gain being \hat{L}_g/T_s , which was first observed in [107].

As discussed in Section 7.2.1, the one-sample deadbeat controller is only applicable for delay-free control computers. Consider the feedback control system structure in Fig. 7.13, where the computational delay of the control computer is represented by the block “ z^{-1} .” The delay can be combined with $\mathbf{G}(z)$, in order to form the following “delayed” process model:

$$\mathbf{G}'(z) = z^{-1}\mathbf{G}(z) \quad (7.26)$$

for which the closed-loop system becomes

$$\mathbf{G}_c(z) = \frac{\mathbf{F}_1(z)\mathbf{G}'(z)}{1 + \mathbf{F}_1(z)\mathbf{G}'(z)} = \frac{\mathbf{F}_1(z)\mathbf{G}(z)}{z + \mathbf{F}_1(z)\mathbf{G}(z)} = \frac{1}{z^2 - z + 1}. \quad (7.27)$$

under the assumption on accurate model parameters. The denominator of $\mathbf{G}_c(z)$ has the following roots (poles of the closed-loop system)

$$z_{1,2} = \frac{1}{2}(1 \pm j\sqrt{3}) = e^{\pm j\pi/3}. \quad (7.28)$$

Only marginal stability is hence obtained, since $z_{1,2}$ are located at the unit circle. Consequently, the one-sample deadbeat controller can only be used when the computational time of the control computer is negligible compared to the sampling period time.

Two-Samples Deadbeat Controller

The two-samples deadbeat controller will be designed by means of IMC for the “delayed” process model $\mathbf{G}'(z)$. Since $\mathbf{G}'(z)$ is a second-order system, the controller design must now rely on (6.5), instead of the previously used (6.4). By discretizing (6.5) with the forward difference method, the following controller results:

$$\begin{aligned} \mathbf{F}_2(z) &= \frac{\alpha^2}{\left(\frac{z-1}{T_s}\right)^2 + 2\alpha\frac{z-1}{T_s}} \hat{\mathbf{G}}'^{-1}(z) \\ &= \frac{(\alpha T_s)^2}{z^2 + 2(\alpha T_s - 1)z + 1 - 2\alpha T_s} \hat{\mathbf{G}}'^{-1}(z). \end{aligned} \quad (7.29)$$

Substituting the deadbeat bandwidth $\alpha = 1/T_s$ in $\mathbf{F}_2(z)$ provides the two-samples deadbeat controller as

$$\mathbf{F}_2(z) = \frac{\hat{\mathbf{G}}'^{-1}(z)}{z^2 - 1} = \frac{z\hat{\mathbf{G}}^{-1}(z)}{(z+1)(z-1)} = \frac{\hat{\mathbf{G}}^{-1}(z)}{(1+z^{-1})(z-1)}. \quad (7.30)$$

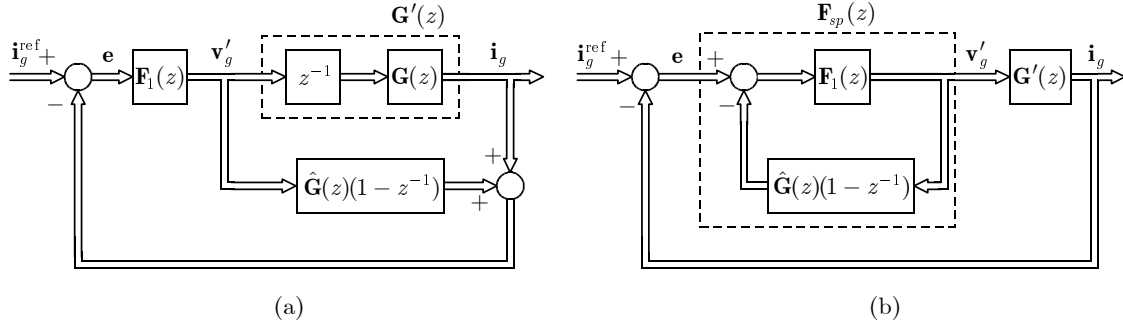


Fig. 7.14. One-sample deadbeat controller with Smith predictor. (a) Block diagram of Smith predictor structure. (b) The Smith predictor rearranged as the “classical” control system structure.

Interestingly, $F_2(z)$ is closely related to the one-sample deadbeat controller in (7.25):

$$\mathbf{F}_2(z) = \frac{\mathbf{F}_1(z)}{1 + z^{-1}} = \frac{1}{1 + z^{-1}} \left(\frac{\hat{L}_g}{T_s} + \frac{\hat{R}_g}{T_s} \frac{T_s z^{-1}}{1 - z^{-1}} \right). \quad (7.31)$$

Both the one-sample and the two-samples deadbeat controller can hence be summarized by the following difference equations:

$$\mathbf{I}_k = \mathbf{I}_{k-1} + T_s (\mathbf{i}_{g,k-1}^{\text{ref}} - \mathbf{i}_{g,k-1}), \quad \mathbf{v}'_{g,k} = \frac{\hat{L}_g}{T_s} (\mathbf{i}_{g,k}^{\text{ref}} - \mathbf{i}_{g,k}) + \frac{\hat{R}_g}{T_s} \mathbf{I}_k - l \mathbf{v}'_{g,k-1} \quad (7.32)$$

where $l = 0$ and $l = 1$ for one-sample and two-samples deadbeat, respectively.

Let us compare (7.31) with the control system structure of the one-sample deadbeat controller implemented on a “slow” control computer, where the one-sample computational delay is circumvented by the Smith predictor [17, 78]. The underlying principle of the Smith predictor can be understood from Fig. 7.14(a): the output of the “delayed” process model should ideally cancel the true process output \mathbf{i}_g , such that only the output of the “non-delayed” process model appears in the feedback path. It can be observed that Fig. 7.14(a) is similar to the IMC structure in Fig. 6.1. In order to further study this similarity, Fig. 7.14(a) is rearranged into the “classical” control structure in Fig. 7.14(b). The “classical” controller $\mathbf{F}_{sp}(z)$ in Fig. 7.14(b) is found to be

$$\mathbf{F}_{sp}(z) = \frac{\mathbf{F}_1(z)}{1 + \mathbf{F}_1(z) \hat{\mathbf{G}}(z)(1 - z^{-1})} = \frac{\mathbf{F}_1(z)}{1 + \frac{1 - z^{-1}}{z - 1}} = \frac{\mathbf{F}_1(z)}{1 + z^{-1}} \quad (7.33)$$

which is identical to the two-samples deadbeat controller in (7.31), resulting from IMC. This implies that the Smith predictor control structure and the IMC structure are completely equivalent, which was first noticed in [23].

The following summarizes the practical implementation of the two-samples dead-

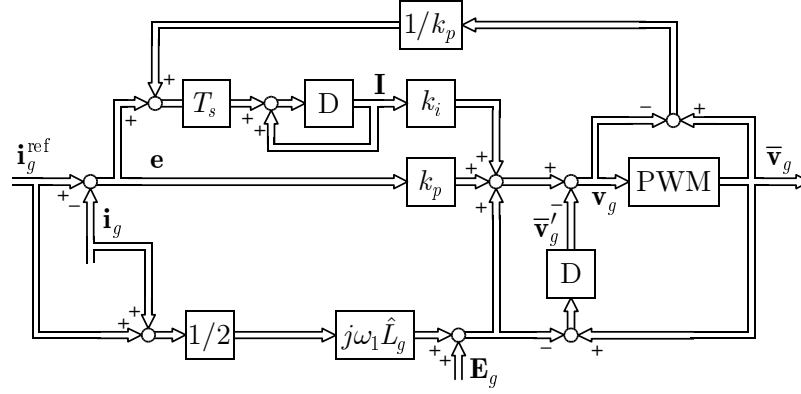


Fig. 7.15. Implementation of the two-samples deadbeat grid current controller, “D” denotes the unit-delay operator.

beat design for grid current control:

$$\mathbf{e}_k = \mathbf{i}_{g,k}^{\text{ref}} - \mathbf{i}_{g,k} \quad (7.34)$$

$$\mathbf{I}_k = \mathbf{I}_{k-1} + T_s \left[\mathbf{e}_{k-1} + \frac{1}{k_p} (\bar{\mathbf{v}}_{g,k-1}^{\text{ref}} - \mathbf{v}_{g,k-1}^{\text{ref}}) \right] \quad (7.35)$$

$$\mathbf{v}_{g,k} = \underbrace{k_p \mathbf{e}_k + k_i \mathbf{I}_k - \bar{\mathbf{v}}'_{g,k-1}}_{\mathbf{v}'_{g,k}} + j\omega_1 \hat{L}_g \frac{\mathbf{i}_{g,k}^{\text{ref}} + \mathbf{i}_{g,k}}{2} + \mathbf{E}_{g,k} \quad (7.36)$$

$$\bar{\mathbf{v}}_{g,k} = \text{PWM}(\mathbf{v}_{g,k}, \theta_1) \quad (7.37)$$

$$\bar{\mathbf{v}}'_{g,k} = \bar{\mathbf{v}}_{g,k}^{\text{ref}} - j\omega_1 \hat{L}_g \frac{\mathbf{i}_{g,k}^{\text{ref}} + \mathbf{i}_{g,k}}{2} - \mathbf{E}_{g,k} \quad (7.38)$$

where

$$k_p = \frac{\hat{L}_g}{T_s}, \quad k_i = \frac{\hat{R}_g}{T_s} \quad (7.39)$$

are the proportional gain and the integration gain, respectively. As seen, back-calculation is implemented for the integrator part (as described in Section 6.1.2), and the decoupling and the feedforward terms in (7.20) are added to $\mathbf{v}'_{g,k}$. Notice that it is required to “back-calculate” $\bar{\mathbf{v}}'_{g,k}$ from the resulting voltage command vector $\bar{\mathbf{v}}_{g,k}$, in order to account for voltage saturation. Fig. 7.15 depicts the two-samples deadbeat controller as a block diagram.

The following trick [6] can be applied in order to slightly improve the transient response of the two-samples deadbeat controller:

$$\bar{\mathbf{v}}_{g,k}^s = e^{j(\theta_{1,k} + 3T_s/2)} \bar{\mathbf{v}}_{g,k}. \quad (7.40)$$

An additional angle of $3T_s/2$ is thus added to $\theta_{1,k}$ when transforming the resulting command vector to the stator-oriented reference frame, where PWM is implemented. This trick accounts for the phase shift in \mathbf{E}_g^s during the computational delay, and centers $\bar{\mathbf{v}}_{g,k}^s$ in the sampling period following the delay.

7.2.3 Stability Analysis of the Two-Samples Deadbeat Controller

The following stability analysis considers the closed-loop dynamics that result from the two-samples deadbeat controller. The analysis is performed for the realistic case of inaccurate model parameters, so it cannot be assumed that the current cross-coupling perfectly cancel in the process model, as in (7.13). The stringent analytic treatment of the current cross-coupling is difficult to achieve, however, since the coupling partly depends on the accuracy of \hat{L}_g , and partly on how well (7.19) approximates \mathbf{i}_g . It is here assumed that (7.19) perfectly corresponds to \mathbf{i}_g in one sampling period, such that the true continuous-time process and the approximate digital process model are

$$\mathbf{G}(p) = \frac{1}{pL_g + j\omega_1(L_g - \hat{L}_g) + R_g}. \quad (7.41)$$

$$\mathbf{G}(z) = \frac{1}{\frac{z-1}{T_s}L_g + j\omega_1(L_g - \hat{L}_g) + R_g}. \quad (7.42)$$

The here studied control system structure is depicted in Fig. 7.16, where $\mathbf{F}_2(z)$ and $\mathbf{G}(z)$ are given by (7.31) and (7.42), respectively. The closed-loop transfer function from $\mathbf{i}_g^{\text{ref}}$ to \mathbf{i}_g is

$$\mathbf{G}_c(z) = \frac{\mathbf{F}_2(z)\mathbf{G}'(z)}{1 + \mathbf{F}_2(z)\mathbf{G}'(z)} \quad (7.43)$$

which has been found to be

$$\mathbf{G}_c(z) = \frac{\left(1 - \frac{\tilde{L}_g}{L_g}\right)z - 1 + \frac{\tilde{L}_g}{L_g} + \frac{R_g T_s}{L_g} - \frac{\tilde{R}_g T_s}{L_g}}{z^3 - \left(1 - \frac{R_g T_s}{L_g} - j\omega_1 T_s \frac{\tilde{L}_g}{L_g}\right)z^2 - \frac{\tilde{L}_g}{L_g}z + \frac{\tilde{L}_g}{L_g} - \frac{\tilde{R}_g T_s}{L_g} - j\omega_1 T_s \frac{\tilde{L}_g}{L_g}} \quad (7.44)$$

where

$$\tilde{L}_g = L_g - \hat{L}_g, \quad \tilde{R}_g = R_g - \hat{R}_g \quad (7.45)$$

are the model parameter errors. For small T_s , such that terms involving T_s in $\mathbf{G}_c(z)$ are negligible, the process model can be approximated by

$$\mathbf{G}_c(z) \approx \frac{\left(1 - \frac{\tilde{L}_g}{L_g}\right)z - 1 + \frac{\tilde{L}_g}{L_g}}{z^3 - z^2 - \frac{\tilde{L}_g}{L_g}z + \frac{\tilde{L}_g}{L_g}} = \frac{(z-1)\left(1 - \frac{\tilde{L}_g}{L_g}\right)}{(z-1)\left(z^2 - \frac{\tilde{L}_g}{L_g}\right)} = \frac{1 - \frac{\tilde{L}_g}{L_g}}{z^2 - \frac{\tilde{L}_g}{L_g}}. \quad (7.46)$$

In consequence of this approximation, the resistive voltage drop and the current cross-coupling are henceforth neglected.

Let us now study (7.46). As expected, $\mathbf{G}_c(z) = z^{-2}$ for $\tilde{L}_g = 0$. Moreover, the denominator of $\mathbf{G}_c(z)$ has the following roots (poles of the closed-loop system)

$$z_1 = \sqrt{\frac{\tilde{L}_g}{L_g}}, \quad z_2 = -\sqrt{\frac{\tilde{L}_g}{L_g}}. \quad (7.47)$$

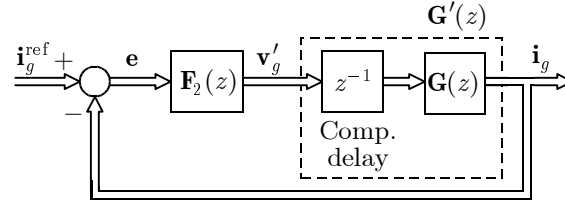


Fig. 7.16. Feedback control system structure for the two-samples deadbeat controller.

It can be directly seen that the poles are at the origin for $\hat{L}_g = L_g$ only, and the closed-loop dynamics are stable for $|\tilde{L}_g| < L_g$, which corresponds to $0 < \hat{L}_g < 2L_g$.

It is, in this case, necessary to assess the transient response in the continuous-time domain in order to further analyze the closed-loop dynamics. For this purpose, $z_2 = -z_1$ is substituted in (7.46), which is then decomposed into partial fractions:

$$\mathbf{G}_c(z) = \frac{1 - \tilde{L}_g/L_g}{(z + z_1)(z - z_1)} = \frac{1}{2z_1} \left(1 - \frac{\tilde{L}_g}{L_g}\right) \left(\frac{1}{z - z_1} - \frac{1}{z + z_1}\right). \quad (7.48)$$

The inverse \mathcal{Z} -transform of $\mathbf{G}_c(z)$ is found to be

$$\begin{aligned} \mathbf{g}_{c,k} &= \frac{1}{2z_1} \left(1 - \frac{\tilde{L}_g}{L_g}\right) [z_1^{k-1} - (-z_1)^{k-1}] \\ &= \frac{z_1^{k-2}}{2} \left(1 - \frac{\tilde{L}_g}{L_g}\right) [1 + (-1)^k], \quad k \geq 1. \end{aligned} \quad (7.49)$$

Since $1 + (-1)^k = 0$ for all odd k , $\mathbf{g}_{c,k}$ can be rewritten as

$$\mathbf{g}_{c,k} = \begin{cases} 0, & k = 1, 3, 5, \dots \\ z_1^{k-2} \left(1 - \frac{\tilde{L}_g}{L_g}\right), & k = 2, 4, 6, \dots \end{cases} \quad (7.50)$$

The following conclusions can now be drawn on the closed-loop dynamics resulting from the two-samples deadbeat controller:

- The poles z_1 and z_2 are complex valued for $\hat{L}_g > L_g$. As expected, the dynamics are then poorly damped, which is due to that z_1^{k-2} in $\mathbf{g}_{c,k}$ changes sign for every other even k .
- Real-valued poles, which are symmetrically placed about the origin, result from $\hat{L}_g < L_g$. In contrast to what could have been expected from the negative real-valued pole, the closed-loop dynamics are then well damped. This slightly surprising finding originates, as above shown, from the oscillatory response of the negative pole, $(-1)^k$, being canceled by the positive pole for all odd k .
- The step response of \mathbf{i}_g is given by the convolution of the unit step and \mathbf{g}_c , which on recursive form becomes

$$\mathbf{i}_{g,k} = \mathbf{i}_{g,k-1} + \mathbf{g}_{c,k}, \quad k \geq 0, \quad \mathbf{i}_{g,0} = 0. \quad (7.51)$$

On condition that $\mathbf{i}_g^{\text{ref}} = j$ for $k \geq 0$, the “initial” response in i_q at $k = 2$ then becomes

$$i_{q,2} = \frac{z_1^{2-2}}{2} \left(1 - \frac{\tilde{L}_g}{L_g} \right) [1 + (-1)^2] = 1 - \frac{\tilde{L}_g}{L_g} \quad (7.52)$$

which can be seen to be directly related to \tilde{L}_g . The two-samples deadbeat response results for $\tilde{L}_g = L_g$, while $\tilde{L}_g = 1.4L_g$, for instance, results in an initial overshoot: $i_{q,2} = 1.4$ pu.

- The true filter inductance should, unless it can be “perfectly” modeled, preferably be underestimated by \tilde{L}_g , since this choice provides well-damped dynamics. Poor damping easily results for $\tilde{L}_g > L_g$, as will be shown in the analysis that now follows.

Correspondence Between Damping in the Continuous-Time and Discrete-Time Domains

Fig. 7.17 shows the pole locus of (7.46) for $-L_g \leq \tilde{L}_g \leq L_g$. As above discussed, the closed-loop dynamics are poorly damped for complex-valued poles only, while real-valued poles provide good damping. The shaded region in the figure corresponds to poles within 45° relative the negative real axis in the continuous-time domain. As seen, complex-valued $z_{1,2}$ are easily located outside this well-damped region; there is “little room” for parameters errors. This graphical observation will now be verified analytically.

Consider poles at 45° relative the negative real axis in the continuous-time domain:

$$p_{1,2} = -\sigma(1 \pm j), \quad \sigma > 0. \quad (7.53)$$

which are related to the digital poles as $z_{1,2} = e^{p_{1,2}T_s}$. Solving the imaginary part and the real part of this relation for σ and \tilde{L}_g , respectively, gives

$$\sigma = \frac{1}{T_s} \left(\frac{\pi}{2} + n\pi \right), \quad n = 0, 1, 2, \dots \quad (7.54)$$

$$\tilde{L}_g = -e^{-(1+2n)\pi} L_g. \quad (7.55)$$

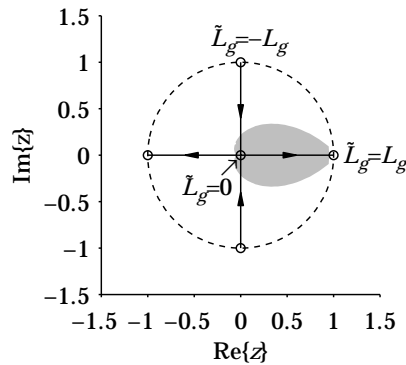


Fig. 7.17. Pole locus for $-L_g \leq \tilde{L}_g \leq L_g$. The shaded region represents poles within 45° relative the negative real axis in the continuous-time domain, the dashed line is the unit circle.

Multiple solutions appear for \tilde{L}_g , but we are interested in the maximum $|\tilde{L}_g|$ that results for $n = 0$:

$$\tilde{L}_g = -e^{-\pi} L_g \approx -0.04 L_g. \quad (7.56)$$

The parameter L_g should hence not be overestimated by no more than 4 % for poles within 45° relative the negative real axis. According to (7.50), this corresponds to an initial overshoot of 4 % in the current step response.

The parameter sensitivity of the deadbeat controller is not critical when the grid is stiff, such that the grid filter constitute the open-loop current dynamics. Then, the grid inductance can be neglected, and L_g equals the easily measurable filter inductance. Problems may arise, however, for operation towards a weak grid, where the grid inductance is not negligible and not easily modeled.

Simulation Results

This section presents simulation results of the two-samples deadbeat controller for grid current control. Particularly, the simulated step response in the continuous-time domain is compared to the discrete-time step response, which is described by (7.51).

The simulation parameters are $T_s = 0.1$ pu, $\hat{R}_g = 0.9 R_g$ and, except where explicitly stated, $v_{dc} = \sqrt{3}(1 + 1.4) = 4.2$ pu. The fairly large dc voltage, see Appendix A for details on the per-unit system, avoids voltage saturation for the continuous step response. The influence from voltage saturation is instead studied in one separate simulation.

Fig. 7.18 shows the simulated step responses for discrete-time and continuous-time models. It can be seen that the models agree well. The step response for $\hat{L}_g = 0.6 L_g$ in Fig. 7.18(a) is, as predicted, well damped, while the overestimated filter inductance in Fig. 7.18(b) provides an oscillatory response.

Fig. 7.19(a) shows the simulated step response for $\hat{L}_g \approx L_g$, which yields the ideal two-samples deadbeat behavior.

The simulations in Fig. 7.19(b) are made under similar conditions as in Fig. 7.18(b), but the dc voltage is now chosen to a smaller value. The smaller dc voltage results in voltage saturation for the continuous-time model, while the discrete-time model here studied does not consider saturation. For voltage saturation, a PWM rectifier can no longer deliver the large voltage modulus that is required to attain the initial oscillatory transients that would have been present in the unsaturated step response. Consequently, large current steps that force the PWM rectifier into voltage saturation tend to be better damped for the two-samples deadbeat controller than expected, as seen in Fig. 7.19(b).

7.2.4 Overmodulation and Saturation

Fig. 7.20 shows the eight realizable voltage vectors for a three-phase PWM converter. The PWM converter is capable of delivering voltage vectors within a voltage hexagon that is spanned by the six active voltage vectors. Linear modulation is possible up to the radius of the maximum circle that can be fitted within the hexagon. Control in the

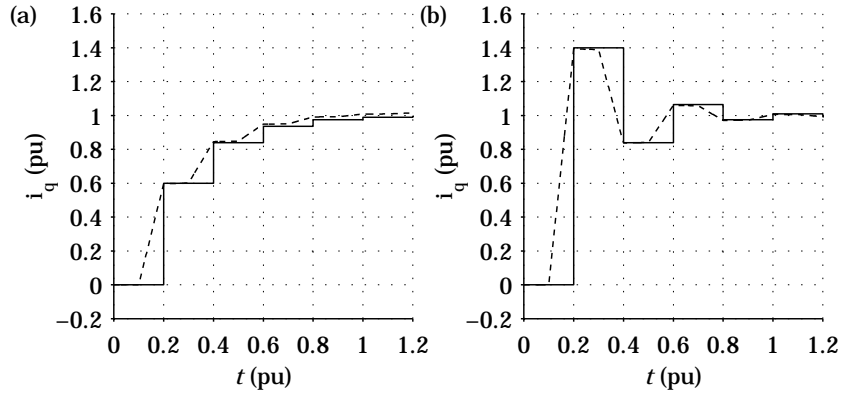


Fig. 7.18. Comparison of discrete-time (solid) and continuous-time (dashed) step responses; i_q^{ref} is stepped from 0 to 1 pu at $t=0$. (a) $\hat{L}_g = 0.6L_g$, $v_{dc} = 4.2$ pu. (b) $\hat{L}_g = 1.4L_g$, $v_{dc} = 4.2$ pu.

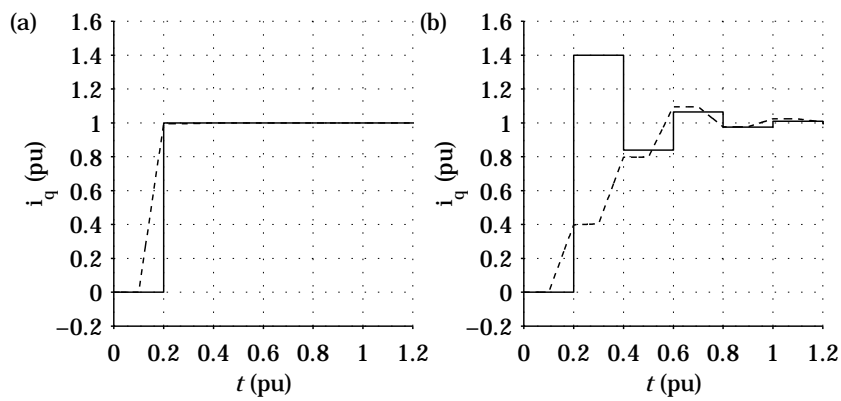


Fig. 7.19. Comparison of discrete-time (solid) and continuous-time (dashed) step responses; i_q^{ref} is stepped from 0 to 1 pu at $t=0$. (a) $\hat{L}_g = L_g$, $v_{dc} = 4.2$ pu. (b) $\hat{L}_g = 1.4L_g$, $v_{dc} = 2.4$ pu.

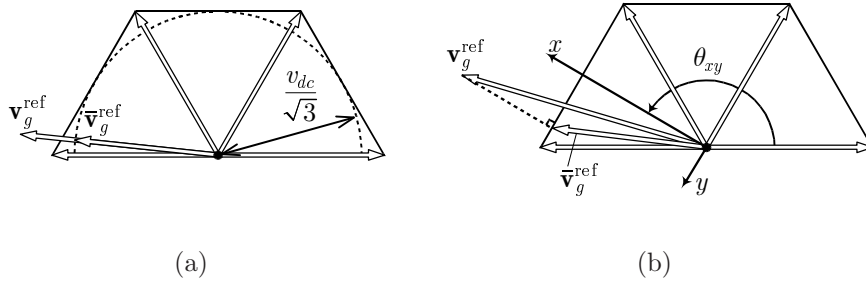


Fig. 7.21. (a) Principle of the CL. (b) Principle of the MVAE.

and n is the sector where $\mathbf{v}_g^{s,\text{ref}}$ is located. The real axis of the xy -coordinate system is always located in between two active voltage vectors in each sector. The maximum realizable voltage vector is, therefore, readily defined by $v_x^{\text{max}} = v_{dc}/\sqrt{3}$ and $v_y^{\text{max}} = v_{dc}/3$ from the perspective of the xy -system. This can be deduced from Fig. 7.20, where the xy -coordinate system happens to be located in the third sector. A command voltage vector outside the hexagon, i.e., voltage saturation, is detected from

$$v_x^{xy,\text{ref}} > \frac{v_{dc}}{\sqrt{3}}. \quad (7.59)$$

Once voltage saturation has been detected, the command voltage vector $\mathbf{v}_g^{\text{ref}}$ should be modified, such that it is precisely located on the boundary of the voltage hexagon.

Circular Limit Method

The circular limit (CL) method chooses the largest voltage vector on the maximum circle within the hexagon that is oriented in the same direction as the original command voltage vector, as shown in Fig. 7.21(a). Thus, sinusoidal voltages are ensured at all times. The CL method is activated if the following condition is true:

$$|\mathbf{v}_g^{\text{ref}}| > \frac{v_{dc}}{\sqrt{3}} \quad (7.60)$$

and the modified voltage vector is given by

$$\bar{\mathbf{v}}_g^{\text{ref}} = \frac{v_{dc}\mathbf{v}_g^{\text{ref}}}{\sqrt{3}|\mathbf{v}_g^{\text{ref}}|}. \quad (7.61)$$

Unfortunately, the transient behavior of the CL method will be rather sluggish, since it does not make use of the available voltage in the overmodulation region.

Minimum Voltage Amplitude Error Method

The minimum voltage amplitude error (MVAE) limit method chooses the voltage vector on the hexagon boundary that is located nearest the original command voltage vector, such that the voltage amplitude error is maintained at a minimum, as shown in Fig. 7.21(b). In the xy -coordinate system, the components of the modified command

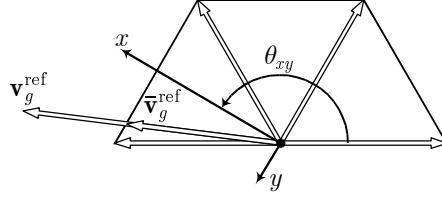


Fig. 7.22. Principle of the MVPE.

voltage vector become

$$\bar{v}_x^{\text{ref}} = \frac{v_{dc}}{\sqrt{3}} \quad (7.62)$$

$$\bar{v}_y^{\text{ref}} = \begin{cases} v_y^{\text{ref}}, & |v_y^{\text{ref}}| < \frac{v_{dc}}{3} \\ \frac{v_{dc}}{3} \text{sign}(v_y^{\text{ref}}), & |v_y^{\text{ref}}| \geq \frac{v_{dc}}{3}. \end{cases} \quad (7.63)$$

The modified command voltage vector,

$$\bar{\mathbf{v}}_g^{xy,\text{ref}} = \bar{v}_x^{\text{ref}} + j\bar{v}_y^{\text{ref}} \quad (7.64)$$

is then transformed to the synchronous reference frame:

$$\bar{\mathbf{v}}_g^{\text{ref}} = e^{j(\theta_{xy} - \theta_1)} \bar{\mathbf{v}}_g^{xy,\text{ref}}. \quad (7.65)$$

Minimum Voltage Phase Error Method

The minimum voltage phase error (MVPE) limit method chooses the voltage vector on the hexagon boundary that is oriented in the same direction as the original command voltage vector, as shown in Fig. 7.22. The modified voltage vector components can be determined by using simple geometry as

$$\bar{v}_x^{\text{ref}} = \frac{v_{dc}}{\sqrt{3}}, \quad \bar{v}_y^{\text{ref}} = \frac{\bar{v}_x^{\text{ref}}}{v_x^{\text{ref}}} v_y^{\text{ref}}. \quad (7.66)$$

The modified command voltage vector is then transformed to the synchronous reference frame, in a similar manner as for the MVAE method.

Minimum Current Phase Error Method

The minimum current phase error (MCPE) method was first presented in [25]. Fig. 7.23 shows the principle of the MCPE method. When a command voltage vector outside the hexagon has been detected, the MCPE considers the current dynamics and the hexagon boundary, and attempts to force the current vector to move in the same direction as intended by the vector-current controller. Consequently, the minimum current phase error results, which minimizes the cross-coupling between the d - and the q -axis currents, as will be shown.

In Fig. 7.23, \mathbf{E}_e is the voltage vector demanded by the current controller excluding the proportional term and $\bar{\mathbf{v}}_g'$, given by

$$\mathbf{E}_{e,k} = k_i \mathbf{I}_k + j\omega_1 \hat{L}_g \frac{\mathbf{i}_{g,k}^{\text{ref}} + \mathbf{i}_{g,k}}{2} + \mathbf{E}_{g,k} \quad (7.67)$$

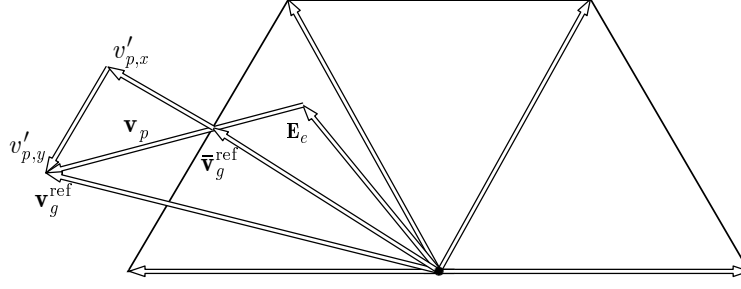


Fig. 7.23. Principle of the MCPE.

which is dominated by $\mathbf{E}_{g,k}$, and \mathbf{v}_p is

$$\mathbf{v}_{p,k}^{xy} = e^{j(\theta_{1,k} - \theta_{xy,k})} (k_p \mathbf{e}_k - \bar{\mathbf{v}}_{g,k-1}'). \quad (7.68)$$

The MCPE chooses the components of the modified command voltage vector by using simple geometry in Fig. 7.23

$$v_{p,x}' = v_x^{\text{ref}} - \frac{v_{dc}}{\sqrt{3}}, \quad v_{p,y}' = \frac{v_{p,y}}{v_{p,x}} v_{p,x}' \quad (7.69)$$

$$\bar{v}_x^{\text{ref}} = \frac{v_{dc}}{\sqrt{3}}, \quad \bar{v}_y^{\text{ref}} = v_y^{\text{ref}} - v_{p,y}' \quad (7.70)$$

where all expressions are given in the xy -reference frame.

***dq*-Axis Cross-Coupling Method**

The dq -axis cross-coupling (DQCC) method was presented in [27] as a simplified version of the “minimum time current control,” presented in [26]. The DQCC is not a command voltage vector limiting method, but a method to enhance the response to q current steps.

The dynamics of the q -axis current in the synchronous reference frame are

$$\frac{di_q}{dt} = \frac{1}{L_g} (v_q - E_q) - \frac{R_g}{L_g} i_q - \omega_1 i_d. \quad (7.71)$$

Normally, a reference step of the q -axis current is handled by the q -axis voltage v_q . According to (7.71), though, the response of the q -axis current can be slightly enhanced by utilizing the cross-coupling of the d -axis current. It was proposed by [27] that the d -axis reference current would be modified to

$$i_d^{\text{ref}} = i_q - i_q^{\text{ref}} + i_d^{\text{ref}}. \quad (7.72)$$

Furthermore, the resulting d current should be limited to

$$\max\{i_d^{\text{ref}}\} = \sqrt{|\mathbf{i}_g|_{\text{max}}^2 - i_q^2} \quad (7.73)$$

where $|\mathbf{i}_g|_{\text{max}}$ maximum grid current modulus allowed.

7.2.6 Experimental Results

This section will demonstrate experimental results of the redesigned deadbeat vector-current controller. The system parameters are shown in Table 7.3, the voltage and the current base values are $U_b = 400$ V and $I_b = 35$ A, respectively, and the impedance of the utility grid is negligible, i.e., the grid is stiff.

The positive reference current steps are triggered when $\mathbf{E}_g^s = E_g + j0$. The measurements have been performed for a step in the reference d current with constant reference q current, and vice versa. The current reference is stepped from -0.5 pu to 0.5 pu at $t = 0$, and from 0.5 pu to -0.5 pu at $t = 10$ ms. The signal “sat” indicates voltage saturation in the following graphs.

TABLE 7.3
PARAMETERS OF THE SYSTEM

E_g	ω_g	$f_s = f_{sw}$	$L_g = \hat{L}_g$	$R_g = \hat{R}_g$	v_{dc}
1.0 pu	$2\pi 50$ rad/s	6.0 kHz	0.071 pu	0.012 pu	2.0 pu

Steps in Reference q Current

The experimental results in Figs. 7.24–7.28 show the reference q current step responses of the investigated vector-current controller, for various voltage limiting methods.

Fig. 7.24 shows the response of the vector-current controller using the CL method. The transient behavior for the q current is rather sluggish for the positive step, since the available voltage in the overmodulation region is not used.

Fig. 7.25 shows the response of the vector-current controller using the MVAE method. The current response is faster compared to the CL method, but there is a dip in the d current.

Fig. 7.26 shows the response of the vector-current controller using the MVPE. The response is approximately as fast as when using the MVAE method, and the d current is almost constant during the step.

Fig. 7.27 shows the response using the vector-current controller and the MCPE method. The result is almost identical to the MVPE.

Fig. 7.28 shows the response using the vector-current controller and the DQCC. The response is slightly faster compared to the MVAE, the MVPE method, and the MCPE method, but at the expense of a huge dip in the d current. This dip is intended, though, since it speeds up the step response slightly.

For comparison, Fig. 7.29 shows the response of the original deadbeat vector-current controller that was used for the previous experiments on active power filtering. The response is rather sluggish, there is a dip in the d current, and the q current overshoots due to integrator windup.

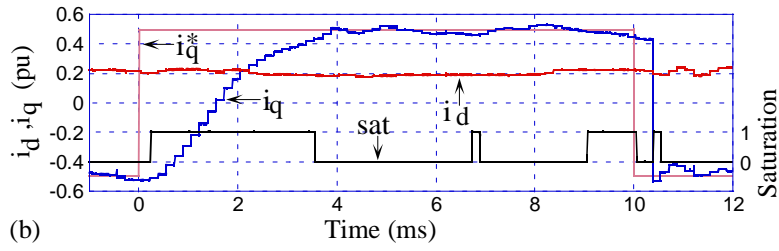


Fig. 7.24. The vector-current controller and the CL, with $i_q^* = i_q^{\text{ref}}$; steps in i_q .

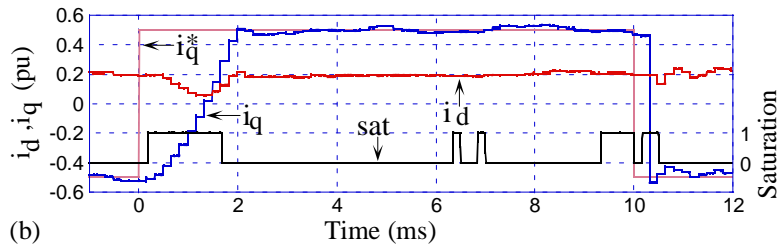


Fig. 7.25. Vector-current controller and the MVAE; steps in i_q .

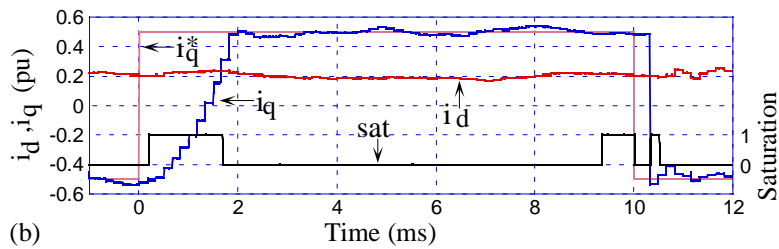


Fig. 7.26. Vector-current controller and the MVPE; steps in i_q .

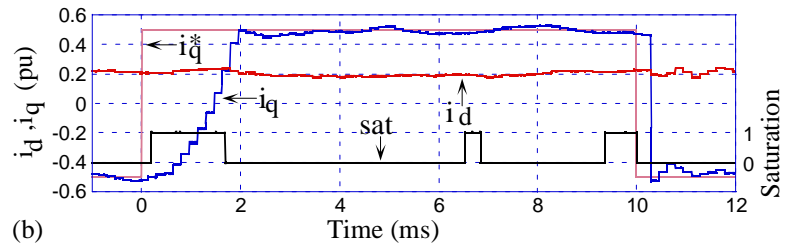


Fig. 7.27. Vector-current controller and the MCPE; steps in i_q .

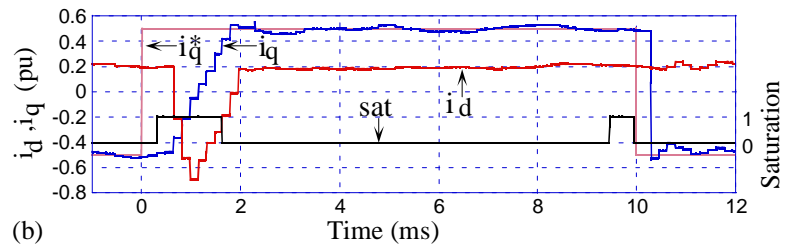


Fig. 7.28. Vector-current controller and the DQCC; steps in i_q .

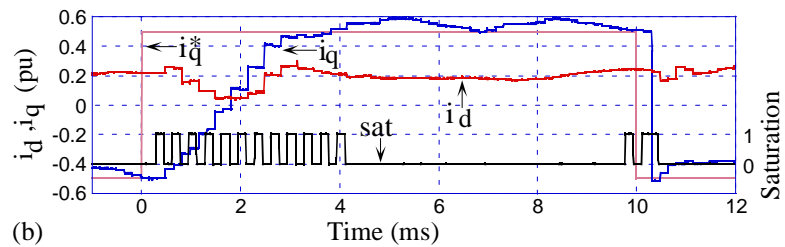


Fig. 7.29. Original deadbeat vector-current controller and the MVAE; steps in i_q .

Steps in Reference d -Current

The experimental results in Figs. 7.30–7.32 show the reference d current step responses using the MVAE, the MVPE and the MCPE methods. There is more “available” voltage in the d direction, due to that the grid voltage vector is aligned with the q axis. Consequently, voltage saturation is less severe for the d current steps. The current cross-coupling differs between the different limiting methods. The MCPE method has the lowest cross-coupling, i.e., the minimum current phase error for the d current step.

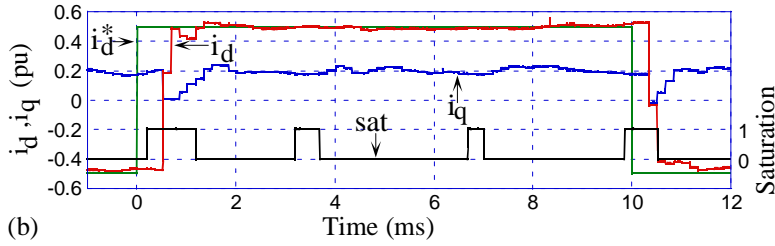


Fig. 7.30. Vector-current controller and the MVAE, with $i_d^* = i_d^{\text{ref}}$; steps in i_d .

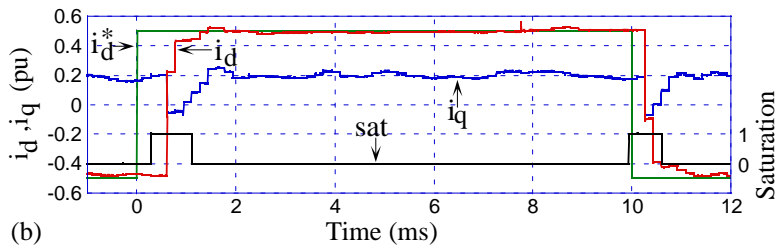


Fig. 7.31. Vector-current controller and the MVPE; steps in i_d .

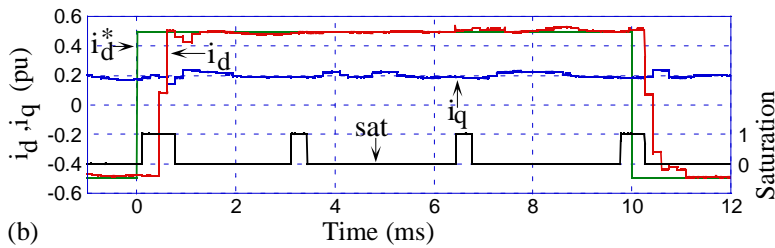


Fig. 7.32. Vector-current controller and the MCPE; steps in i_d .

7.2.7 Summary

This section has investigated a deadbeat vector-current controller that is designed to handle voltage saturation. It was shown the two-samples deadbeat controller is equivalent to previously presented Smith predictor structures. A significant improvement is obtained compared to the deadbeat current controller that was used for active filtering.

Various methods for limiting the command voltage vector were investigated. Only the MCPE yields a constant q -axis current during the reference step in the d -axis current, which makes the MCPE suitable for an active power filter. There are only minor differences between the different limiting methods for the positive q current steps,

with the exception of the sluggish response of the CL method. Many applications will therefore perform well, regardless of the voltage limiting method used. Unless d current steps occur frequently, the MVPE method can be recommended, since it allows for a simple implementation.

Chapter 8

Conclusion

8.1 Summary

In this thesis, control of the back-to-back converter sensorless induction machine drive was studied. Particularly, sensorless control of the induction machine, meaning vector control without a mechanical shaft sensor, and vector control of the PWM rectifier were considered. It can be concluded that the converter topology is very well suited for high-performance applications, particularly for those that benefit from four-quadrant operation. It is also fully possible to exploit the fully controlled grid current of the PWM rectifier to improve local power quality.

The following summarizes the most important conclusions from Chapter 3 regarding sensorless control of the induction machine:

- The SCVM was redesigned, such that arbitrarily placement of the closed-loop poles was enabled.
- The resulting dynamics from the SCVM were thoroughly analyzed. For accurate model parameters, stability at nominal speeds were shown, while only small machines were found to be stable at low speeds. For inaccurate model parameters, the stability at very low frequencies was found to be greatly dependent on the accuracy of the modeled stator resistance. The presence of a singularity for zero stator frequency makes it impossible to guarantee stable low-frequency operation for the SCVM, except for the case of zero external load torque or if the stator resistance is perfectly known.
- The underlying mechanisms behind instability for sensorless control were revealed, of which flux collapse was the most critical instability phenomena, resulting in total failure for a speed-sensorless induction machine.
- Recommendable choices for model parameters selections were given. These recommendations cannot avoid instability, only avoid the critical flux collapse.
- Simple parameter selection rules were derived for the SCVM, such that trial-and-error tuning of the estimator is eliminated.

The following summarizes the most important conclusions from Chapters 5–7 regarding the PWM rectifier:

- In Chapter 5, three grid-flux estimators were analyzed, of which two estimators were designed in this chapter. The MCVN was proven to be very robust against the grid voltage harmonics, albeit less suitable for island operation. For such operation, the PLL-type estimator can instead be recommended.
- In Chapter 6, a control system structure for the PWM rectifier was designed, consisting of an inner vector current control loop and an outer loop for dc voltage control. Analyses and simulations showed that the designed control system structure is well suited for normal operation, but large grid voltage disturbances are fairly poorly rejected.
- In Chapter 7, deadbeat current control for active power filtering at a low switching frequency was studied. The stability and the parameter sensitivity for the two-samples deadbeat controller were assessed, and the controller was found to be equivalent to previously proposed Smith predictor control structures.

For all three mentioned chapters concerning the PWM rectifier, simple controller and estimator parameter selection rules were derived.

8.2 Future Research

The following topics are considered suitable for future research:

- Find a speed-sensorless flux estimator that is less sensitive to R_s . Can the reactive power model in [47] be merged with the SCVM to form a stable sensorless flux estimator that does not require knowledge of the stator resistance? Control algorithms for minimizing the time spent in the low-frequency region, as in [31, 76], are also of interest.
- Verify the conclusions for the PWM rectifier in Chapters 5–6 experimentally.
- Analyze the impact from grid voltage disturbances and load unsymmetries on the grid current of the PWM rectifier.
- Improve the rejection of grid voltage disturbances for the PWM rectifier.
- Study the PWM rectifier connected to a weak grid, using a more advanced grid filter topology than considered in this thesis.

Appendix A

Per-Unit System

Table A.1 defines base values of the per-unit system that is used in the present thesis. This system is for a machine with rated phase-to-phase voltage $\sqrt{3}V_n$, rated current I_n , rated electric angular frequency ω_n , and n_p pole pairs.

The nominal stator flux linkage is 1 pu, but the nominal rotor flux is slightly smaller.

TABLE A.1
BASE VALUES OF THE PER-UNIT SYSTEM

Quantity	Base value
Base voltage, U_b	V_n
Base dc voltage, $U_{dc,b}$	$\sqrt{2}V_n$
Base current, I_b	I_n
Base angular frequency, ω_b	ω_n
Base flux linkage, ψ_b	$\frac{V_n}{\omega_n}$
Base power, P_b, Q_b, S_b	$V_n I_n$
Base torque, T_b	$\frac{V_n I_n}{\omega_n}$
Base impedance, Z_b	$\frac{V_n}{I_n}$
Base dc conductance, $G_{dc,b}$	$\frac{I_n}{2V_n}$
Base inertia, J_b	$\frac{V_n I_n}{\omega_n^3}$
Base viscous friction, b_b	$\frac{V_n I_n}{\omega_n^2}$
Base time, t_b	$\frac{1}{\omega_n}$

Appendix A. Per-Unit System

The parameters of the test machine are considered for the following no-load calculation:

$$\psi_{R,n} = \frac{L_M}{L_M + L_\sigma} \psi_n = \frac{2.8}{2.8 + 0.2} \cdot 1 \approx 0.93 \text{ pu} \quad (\text{A.1})$$

which demonstrates that the nominal rotor flux is less than 1 pu.

It is believed that the definitions of the base power and the base torque in Table A.1 are not commonly used. The motivation for using these definitions is that they allow to use the same formulas for torque and power, i.e., $T_e = 3n_p \text{Im}\{\boldsymbol{\psi}_R^* \mathbf{i}_s\}$ and $P_s = 3 \text{Re}\{\mathbf{u}_s \mathbf{i}_s^*\}$, for both the SI system and the per-unit system. However, nominal torque and nominal power will not, by far, correspond to 1 pu. Instead, the nominal torque and the nominal power correspond to approximately $2.6n_p$ pu and 2.6 pu, respectively, using this per-unit system. For instance, with $\psi_R = 0.9$ pu and $L_M = 2.8$ pu (giving $i_d \approx 0.3$ pu), the nominal torque becomes

$$T_{e,n} = 3n_p \psi_R \sqrt{1 - i_d^2} = 3n_p \cdot 0.9 \cdot \sqrt{1 - 0.3^2} \approx 2.6n_p \text{ pu}. \quad (\text{A.2})$$

The definitions for J_b and b_b have little physical relevance, as they are merely quantities that are obtained when normalizing the equation of motion

$$\frac{J}{n_p} \frac{d\omega_r}{dt} = T_e - T_l - \frac{b}{n_p} \omega_r \quad (\text{A.3})$$

with the base torque and the base frequency, giving

$$\frac{J}{n_p} \frac{\omega_b^2}{V_n I_n} \frac{d\left(\frac{\omega_r}{\omega_b}\right)}{d(\omega_b t)} = \frac{T_e - T_l}{V_n I_n} - \frac{b}{n_p} \frac{\omega_b}{V_n I_n} \frac{\omega_r}{\omega_b} \quad (\text{A.4})$$

which can be considered as the per-unit equation of motion:

$$\frac{J_{\text{pu}}}{n_p} \frac{d\omega_{r,\text{pu}}}{dt_{\text{pu}}} = T_{e,\text{pu}} - T_{l,\text{pu}} - \frac{b_{\text{pu}}}{n_p} \omega_{r,\text{pu}}. \quad (\text{A.5})$$

From (A.4) and (A.5), the inertia and the viscous friction base values become

$$J_b \triangleq \frac{V_n I_n}{\omega_b^3}, \quad b_b \triangleq \frac{V_n I_n}{\omega_b^2}. \quad (\text{A.6})$$

All angles, such as the rotor position θ_r , are the same in the per-unit and in the SI system:

$$\omega_r = \frac{d\theta_r}{dt} \Leftrightarrow \frac{\omega_r}{\omega_b} = \frac{d\theta_r}{d(\omega_b t)} \Leftrightarrow \omega_{r,\text{pu}} = \frac{d\theta_r}{dt_{\text{pu}}}. \quad (\text{A.7})$$

The dc voltage of the back-to-back converter must at least be $v_{dc,\text{min}} = \sqrt{3} \approx 1.7$ pu, in order to deliver a phase voltage of 1 pu. This minimal dc voltage equals $v_{dc,\text{min}} = \sqrt{3}U_{dc,b} = \sqrt{6}V_n$ in the SI system, which is identical to the peak value of the phase-to-phase voltage.

The definition of the base value for the dc conductance, G_b , results when normalizing the dc voltage dynamics (4.11):

$$\frac{1}{2}C\omega_b 2V_n^2 \frac{d\left(\frac{v_{dc}^2}{2V_n^2}\right)}{d(\omega_b t)} = -\left(\frac{P_g}{V_n I_n} + \frac{P_s}{V_n I_n}\right) V_n I_n \quad (\text{A.8})$$

$$\Rightarrow \frac{1}{2}C_{\text{pu}} \frac{d(v_{dc,\text{pu}}^2)}{dt_{\text{pu}}} = -P_{g,\text{pu}} - P_{s,\text{pu}} \quad (\text{A.9})$$

where

$$G_{dc,b} \triangleq \frac{I_n}{2V_n}, \quad C_{\text{pu}} = \frac{\omega_b C}{G_{dc,b}}. \quad (\text{A.10})$$

Appendix B

Induction Machine Data

The induction machine that is used in the simulation and experimental parts of this thesis (the “test machine”) is a wound-rotor induction machine of type ASEA MAG 180L 55-4. This machine is operated as an ordinary vector controlled squirrel-cage induction machine, which means that the PWM inverter is connected to the stator terminal, the rotor terminal is short-circuited, and the measurable rotor currents are not used in the control algorithms.

The rated values of the machine are given in Table B.1, where the machine parameters are given as defined by the inverse- Γ model [102]. The stator resistance is determined from a conventional dc test on a “cold” machine.

The induction machine is loaded by a separately excited dc machine. The inertia of the dc machine has been estimated to 0.6 kg·m², so the total inertia of the two machines becomes 0.93 kg·m², or 2800 pu.

TABLE B.1
RATED VALUES OF THE INDUCTION MACHINE

Connection	Y		
Voltage, $\sqrt{3}V_n$	400	V	
Current, I_n	44	A	
Angular frequency, ω_n	$2\pi 50$	rad/s	
Power	22	kW	
Power factor	0.89		
Rotor speed (mechanical)	1440	r/min	
Torque	150	N·m	
<i>Machine parameters (cold machine at 50 Hz):</i>			
Rotor resistance, R_R	0.18	Ω ,	0.034 pu
Stator resistance, R_s	0.12	Ω ,	0.023 pu
Leakage inductance, L_σ	3.5	mH,	0.21 pu
Magnetizing inductance, L_M	47	mH,	2.8 pu
Rotor inertia, J	0.33	kg·m ² ,	1000 pu

Appendix C

Glossary of Symbols, Subscripts, Superscripts and Abbreviations

Symbols:

A	system matrix
b	viscous friction constant
B	input matrix
C	dc-link capacitance or (less common) output matrix
D	unit-delay operator
e, \mathbf{e}	real-valued and complex-valued control error
E_f, \mathbf{E}_f	flux EMF modulus and space vector
E_g, \mathbf{E}_g	grid voltage modulus and space vector
f_s, f_{sw}	sampling and switching frequency
F, \mathbf{F}	real-valued and complex-valued controller
G, \mathbf{G}	real-valued and complex-valued process
G_c, \mathbf{G}_c	real-valued and complex-valued closed-loop transfer function
G_a	active conductance
H	transfer function
i_g, \mathbf{i}_g	grid current modulus and space vector
i_s, \mathbf{i}_s	stator current modulus and space vector
I	identity matrix
j	$\sqrt{-1}$
J	inertia
k	coefficient or (less common) sampling instant at $t = kT_s$
k_p	proportional gain
k_i	integration gain
L	inductance
\mathcal{L}	Laplace transform
n_p	number of pole pairs
p	d/dt
P	instantaneous active power
Q	instantaneous reactive power
R	resistance

Appendix C. Glossary of Symbols, Subscripts, Superscripts and Abbreviations

R_a	active resistance
t	time
t_r	time constant
S	instantaneous apparent power
T, T_0	temperature
T_s	sampling period
T_e	instantaneous electro-mechanical torque
T_l	load torque disturbance
T_p	period time
v_g, \mathbf{v}_g	terminal voltage of the PWM rectifier: modulus and space vector
v_s, \mathbf{v}_s	stator voltage modulus and space vector
v_{dc}	dc-link voltage
W	v_{dc}^2
z	e^{pT_s}
\mathcal{Z}	z transform
α	bandwidth
ε	error signal for phase-locked loop
ψ_g, Ψ_g	grid flux modulus and space vector
ψ_R, Ψ_R	rotor flux modulus and space vector
$\lambda, \mu, \gamma, \rho$	gain parameters of flux estimators, normally the SCVM
θ	true rotor flux angle
θ_g	true grid flux angle
θ_1	angle of the synchronous reference frame
$\tilde{\theta}$	error angle, $\tilde{\theta} = \theta - \theta_1$ or $\tilde{\theta} = \theta_g - \theta_1$
ω_1	synchronous (excitation) frequency
ω_g	grid frequency
ω_r	electrical rotor speed
Ω	discrete-time frequency
ξ	denotes a relative quantity
ϕ	phase shift
$\hat{\sim}$	estimated
\sim	error
$-$	modified, resulting

Subscripts:

a	active damping
b	base value
c	current
d	real part in the synchronous reference frame
e	electro-mechanical
g	grid
k	sampling instant at $t = kT_s$
L	load
M	mutual, inverse- Γ model
n	nominal

Appendix C. Glossary of Symbols, Subscripts, Superscripts and Abbreviations

(n)	harmonic order
q	imaginary part in the synchronous reference frame
r	rotor
R	rotor, inverse- Γ model
s	stator or (less common) speed
α	real part in the stator-orientated reference frame
β	imaginary part in the stator-orientated reference frame
σ	leakage, inverse- Γ model

Superscripts:

R	rotor-flux-oriented reference frame
s	stator-oriented reference frame
*	complex conjugate
*	equilibrium point
+, -	positive and negative sequence

Space vectors without superscripts are given in the synchronous reference frame.

Abbreviations:

ac	alternating current
AF	active filter
ASD	adjustable speed drive
CM	current model
D	direct method
DP	direct method with phase shift compensation
dc	direct current
det	determinant
DFO	direct field orientation
EMF	electromotive force
F	Fourier method
IFO	indirect field orientation
Im	imaginary
IM	induction machine
max	maximum
MCVM	modified compensated voltage model
min	minimal
nom	nominal
PCC	point of common connection
PI	proportional plus integral
PLL	phase-locked loop
pu	per unit
PWM	pulsewidth modulation, pulsewidth modulated
Re	real
ref	reference
sat	voltage saturation

Appendix C. Glossary of Symbols, Subscripts, Superscripts and Abbreviations

SCVM	statically compensated voltage model
T	transformation method
VM	voltage model

References

- [1] “Electrical braking,” Technical guide no. 8, ABB Drives Oy, 2002.
- [2] F. Abrahamsen and A. David, “Adjustable speed drive with active filtering capability for harmonic current compensation,” in *Proc. IEEE PESC’95*, vol. 2, Atlanta, GA, June 1995, pp. 1137–1143.
- [3] T. Ackermann and L. Söder, “An overview of wind energy status 2002,” *Renewable and Sustainable Energy Reviews*, vol. 6, no. 1-2, pp. 67–127, Feb./Apr. 2002.
- [4] H. Akagi, Y. Kanazawa, and A. Nabae, “Instantaneous reactive power compensators comprising switching devices without energy storage components,” *IEEE Trans. Ind. Applicat.*, vol. 20, no. 3, pp. 625–630, May/June 1984.
- [5] H. Z. Akpolat, G. M. Asher, and J. C. Clare, “A practical approach to the design of robust speed controllers for machine drives,” *IEEE Trans. Ind. Electron.*, vol. 47, no. 2, pp. 315–324, Apr. 2000.
- [6] M. Alakiüla, “Rotororienterad reglering av synkronmaskiner,” Lic. Thesis, Electrical Machines and Power Electronics, Dept. of Electric Power Eng., Chalmers Univ. of Technology, Göteborg, Sweden, 1989.
- [7] —, *Power Electronic Control*. Lund, Sweden: Dept. of Industrial Electrical Eng. and Automation, Lund Univ., 2002.
- [8] M. Alakiüla and A. Carlsson, “An induction machine servo with one current controller and an improved flux observer,” in *Proc. IEEE IECON’93*, vol. 3, Maui, HI, Nov. 1993, pp. 1991–1996.
- [9] K. J. Åström and T. Hägglund, *PID Controllers: Theory, Design and Tuning*, 2nd ed. Research Triangle Park, NC: Instrument Society of America, 1995.
- [10] K. J. Åström and B. Wittenmark, *Computer-Controlled Systems: Theory and Design*, 3rd ed. Upper Saddle River, NJ: Prentice Hall, 1997.
- [11] P. Barrass and M. Cade, “PWM rectifier using indirect voltage sensing,” *Proc. IEE—Elect. Power Applicat.*, vol. 146, no. 5, pp. 539–544, Sept. 1999.
- [12] F. J. Bartos, “Today’s sensorless ac drives have more to offer—Testing some competitors,” *Control Eng.*, no. 3, Mar. 2001. [Online]. Available: <http://www.manufacturing.net/CTL/index.asp?layout=articleWebzine&articleId=CA18868>

References

- [13] S. Bhattacharya, T. M. Frank, D. M. Divan, and B. Banerjee, "Parallel active filter system implementation and design issues for utility interface of adjustable speed drive systems," in *Conf. Rec. IEEE-IAS Annu. Meeting*, vol. 2, San Diego, CA, Oct. 1996, pp. 1032–1039.
- [14] F. Blaabjerg, U. Jaeger, S. Munk-Nielsen, and J. K. Pedersen, "Power losses in PWM-VSI inverter using NPT or PT IGBT devices," *IEEE Trans. Power Electron.*, vol. 10, no. 3, pp. 358–366, May 1995.
- [15] F. Blaschke, "The principle of field orientation as applied to the new TRANSVEKTOR closed-loop control system for rotating-field machines," *Siemens Review*, vol. 34, no. 1, pp. 217–223, May 1972.
- [16] R. Blasco-Giménez, G. M. Asher, M. Summer, and K. J. Bradley, "Dynamic performance limitations for MRAS based sensorless induction motor drives. Part 2: Online parameter tuning and dynamic performance studies," *Proc. IEE—Elect. Power Applicat.*, vol. 143, no. 2, pp. 123–134, Mar. 1996.
- [17] M. Bojrup, "Advanced control of active filters in a battery charger application," Lic. Thesis, Dept. of Industrial Electrical Eng. and Automation, Lund Univ., Lund, Sweden, 1999.
- [18] I. Boldea and S. A. Nasar, *Electric Drives*. Boca Raton, FL: CRC Press, 1999.
- [19] M. H. J. Bollen, *Understanding Power Quality Problems: Voltage Sags and Interruptions*. New York, NY: IEEE Press, 2000.
- [20] M. H. J. Bollen, A. Sannino, J. Svensson, and E. Styvaktakis, "Testing of three-phase converters for voltage disturbances in the power systems," in *Proc. Nordic and Baltic Workshop Power Systems*, Tampere, Finland, Feb. 2002, CD-ROM.
- [21] G. Bon-gwan and N. Kwanghee, "A dc link capacitor minimization method through direct capacitor current control," in *Conf. Rec. IEEE-IAS Annu. Meeting*, vol. 2, Pittsburgh, PA, Oct. 2002, pp. 811–817.
- [22] B. K. Bose and N. R. Patel, "A programmable cascaded low-pass filter-based flux synthesis for a stator flux-oriented vector-controlled induction motor drive," *IEEE Trans. Ind. Electron.*, vol. 44, pp. 140–143, Feb. 1997.
- [23] C. B. Brosilow, "The structure and design of Smith predictors from the viewpoint of inferential control," in *Proc. Joint Automatic Control Conf.*, vol. 1, Denver, CO, June 1979, p. 288.
- [24] A. Carlsson, "The back-to-back converter—Control and design," Lic. Thesis, Dept. of Industrial Electrical Eng. and Automation, Lund Univ., Lund, Sweden, 1998.
- [25] J.-W. Choi and S.-K. Sul, "A new overmodulation strategy for induction motor drive using space vector PWM," in *Proc. IEEE APEC'95*, vol. 1, Dallas, TX, Mar. 1995, pp. 211–216.

- [26] —, “New control concept—Minimum time current control in the three-phase PWM converter,” *IEEE Trans. Power Electron.*, vol. 12, no. 2, pp. 124–131, Jan. 1997.
- [27] —, “Fast current controller in three phase ac/dc boost converter using d-q axis crosscoupling,” *IEEE Trans. Power Electron.*, vol. 13, no. 1, pp. 179–185, Jan. 1998.
- [28] S.-K. Chung, “Phase-locked loop for grid-connected three-phase power conversion systems,” *Proc. IEE—Elect. Power Applicat.*, vol. 147, no. 3, pp. 213–219, May 2000.
- [29] F. B. del Blanco, M. W. Degner, and R. D. Lorenz, “Dynamic analysis of current regulators for ac motors using complex vectors,” *IEEE Trans. Ind. Applicat.*, vol. 35, no. 6, pp. 1424–1432, Nov./Dec. 1999.
- [30] M. Depenbrock, “Direct self-control (DSC) of inverter-fed induction machine,” *IEEE Trans. Power Electron.*, vol. 3, no. 4, pp. 420–429, Oct. 1988.
- [31] M. Depenbrock, C. Foerth, and S. Koch, “Speed sensorless control of induction machines at very low stator frequencies,” in *Proc. EPE Conf.*, Geneva, Switzerland, Sept. 1999, CD-ROM.
- [32] M. Depenbrock, F. Hoffman, and S. Koch, “Speed sensorless high performance control for traction drives,” in *Proc. EPE Conf.*, vol. 1, Trondheim, Norway, Sept. 1997, pp. 418–423.
- [33] M. Depenbrock and N. R. Klaes, “Determination of the induction machine parameters and their dependencies on saturation,” in *Conf. Rec. IEEE-IAS Annu. Meeting*, San Diego, CA, Oct. 1989, pp. 17–22.
- [34] M. Depenbrock and A. Steimel, “Discussion of ‘regenerating-mode low-speed operation of sensorless induction motor drive with adaptive observer’,” *IEEE Trans. Ind. Applicat.*, vol. 39, no. 1, p. 19, Jan./Feb. 2003.
- [35] B. Drury, Ed., *The Control Techniques Drives and Controls Handbook*. London, U.K.: IEE, 2001.
- [36] J. L. Duarte, A. Van Zwam, C. Wijnands, and A. Vandenput, “Reference frames fit for controlling PWM rectifiers,” *IEEE Trans. Ind. Electron.*, vol. 46, no. 3, pp. 628–630, June 1999.
- [37] R. C. Dugan, M. F. McGranaghan, S. Santoso, and H. W. Beaty, *Electrical Power Systems Quality*, 2nd ed. New York, NY: McGraw-Hill, 2002.
- [38] A. Ferrah, P. J. Hogben-Laing, K. J. Bradley, G. M. Asher, and M. S. Woolfson, “Effect of rotor design on sensorless speed estimation using rotor slot harmonics identified by adaptive digital filtering using the maximum likelihood approach,” in *Conf. Rec. IEEE-IAS Annu. Meeting*, vol. 1, New Orleans, LA, Oct. 1997, pp. 128–135.

References

- [39] A. E. Fitzgerald, C. Kingsley, Jr., and S. D. Umans, *Electric Machinery*, 5th ed. London, U.K.: McGraw-Hill, 1992.
- [40] S. Fukuda and S. Sugawa, "Adaptive signal processing based control of active power filters," in *Conf. Rec. IEEE-IAS Annu. Meeting*, vol. 2, San Diego, CA, Oct. 1996, pp. 886–890.
- [41] R. Gabriel, W. Leonhard, and C. J. Nordby, "Field-oriented control of a standard ac motor using microprocessors," *IEEE Trans. Ind. Applicat.*, vol. 16, no. 2, pp. 186–192, Mar./Apr. 1980.
- [42] L. U. Gökdere, M. A. Simaan, and C. W. Brice, "Global asymptotic stability of indirect field-oriented speed control of current-fed induction motors," *Automatica*, vol. 34, no. 1, pp. 133–135, Jan. 1998.
- [43] R. Grünbaum, "Enhancing of power quality and availability in distribution systems by means of voltage source converters," in *Proc. Int. Conf. Electricity Distribution (CIRED)*, vol. 2, Amsterdam, The Netherlands, June 2001.
- [44] T. G. Habetler, "A space vector-based rectifier regulator for ac/dc/ac converters," *IEEE Trans. Power Electron.*, vol. 8, no. 1, pp. 30–36, Jan. 1993.
- [45] L. Harnefors, "On analysis, control and estimation of variable-speed drives," Ph.D. dissertation, Electrical Machines and Power Electronics, Dept. of Electrical Eng., Royal Inst. of Technology, Stockholm, Sweden, 1997.
- [46] —, "Instability phenomena and remedies in sensorless indirect field oriented control," *IEEE Trans. Power Electron.*, vol. 15, no. 4, pp. 733–743, July 2000.
- [47] —, "Design and analysis of general rotor-flux-oriented vector control systems," *IEEE Trans. Ind. Electron.*, vol. 48, no. 2, pp. 383–390, Apr. 2001.
- [48] —, *Control of Variable-Speed Drives*. Västerås, Sweden: Applied Signal Processing and Control, Dept. of Electronics, Mälardalen Univ., 2002.
- [49] L. Harnefors, M. Jansson, and J. Holmberg, "Generalized indirect field orientation with analysis of computational requirements," in *Proc. IEEE Nordic Workshop Power and Industrial Electronics*, vol. 1, Aalborg, Denmark, June 2000, pp. 151–154.
- [50] L. Harnefors, M. Jansson, R. Ottersten, and K. Pietiläinen, "Unified sensorless vector control of synchronous and induction motors," *IEEE Trans. Ind. Electron.*, vol. 50, no. 1, pp. 153–160, Feb. 2003.
- [51] L. Harnefors and H.-P. Nee, "Model-based current control of ac machines using the internal model control method," *IEEE Trans. Ind. Applicat.*, vol. 34, no. 1, pp. 133–141, Jan./Feb. 1998.
- [52] —, "A general algorithm for speed and position estimation of ac motors," *IEEE Trans. Ind. Electron.*, vol. 47, no. 1, pp. 77–84, Feb. 2000.

- [53] L. Harnefors, K. Pietiläinen, and L. Gertmar, “Torque-maximizing field-weakening control: design, analysis, and parameter selection,” *IEEE Trans. Ind. Electron.*, vol. 48, no. 1, pp. 161–168, Feb. 2001.
- [54] K. Hasse, “Drehzahlregelverfahren für schnelle Umrichterantriebe mit stromrichtergespeisten Asynchron-Kurzschlußläufermotoren,” *Regelungstechnik*, vol. 20, no. 2, pp. 60–66, Feb. 1972.
- [55] A. M. Hava, T. A. Lipo, and W. L. Erdman, “Utility interface issues for line connected PWM voltage source converters: A comparative study,” in *Proc. IEEE APEC’95*, vol. 1, Dallas, TX, Mar. 1995, pp. 125–132.
- [56] M. Hinkkanen and J. Luomi, “Modified integrator for voltage model flux estimation of induction motors,” in *Proc. IEEE IECON’01*, vol. 2, Denver, CO, Nov. 2001, pp. 1339–1343.
- [57] —, “Parameter sensitivity of full-order flux observers for induction motors,” in *Conf. Rec. IEEE-IAS Annu. Meeting*, vol. 2, Pittsburgh, PA, Oct. 2002, pp. 851–855.
- [58] H. Hofmann and S. R. Sanders, “Speed-sensorless vector torque control of induction machines using a two-time-scale approach,” *IEEE Trans. Ind. Applicat.*, vol. 34, no. 1, pp. 169–177, Jan./Feb. 1988.
- [59] J. Holtz, *Power Electronics and Variable Frequency Drives: Technology and Applications*. New York, NY: IEEE Press, 1997, ch. 4, pp. 138–208.
- [60] Y. Hori and T. Umeno, “Implementation of robust flux observer based field orientation (FOFO) controller for induction machines,” in *Conf. Rec. IEEE-IAS Annu. Meeting*, vol. 1, New Orleans, LA, Oct. 1989, pp. 523–528.
- [61] J. Hu and B. Wu, “New integration algorithms for estimating motor flux over a wide speed range,” *IEEE Trans. Power Electron.*, vol. 13, pp. 969–977, Sept. 1998.
- [62] N. Hur, J. Jung, and K. Nam, “A fast dynamic dc-link power-balancing scheme for a PWM converter–inverter system,” *IEEE Trans. Ind. Electron.*, vol. 48, no. 4, pp. 794–803, Aug. 2001.
- [63] K. D. Hurst and T. G. Habetler, “Sensorless speed measurement using current harmonics spectral estimation in induction machine drives,” *IEEE Trans. Power Electron.*, vol. 11, no. 1, pp. 66–73, Jan. 1996.
- [64] N. R. N. Idris and A. H. M. Yatim, “An improved stator flux estimation in state-state operation for direct torque control of induction machines,” *IEEE Trans. Ind. Applicat.*, vol. 38, no. 1, pp. 110–116, Jan./Feb. 2002.
- [65] *Electromagnetic Compatibility: Limits*, IEC Std. 61 000-3-4 (1998-10), 1998.

References

- [66] P. L. Jansen and R. D. Lorentz, "A physically insightful approach to the design and accuracy assessment of flux observers for field oriented induction machine drives," *IEEE Trans. Ind. Applicat.*, vol. 30, no. 1, pp. 101–110, Jan./Feb. 1994.
- [67] ———, "Transducerless position and velocity estimation in induction and salient ac machines," *IEEE Trans. Ind. Applicat.*, vol. 31, no. 2, pp. 240–247, Mar./Apr. 1995.
- [68] S.-G. Jeong and M.-H. Woo, "DSP-based active power filter with predictive current control," *IEEE Trans. Ind. Electron.*, vol. 44, no. 3, pp. 329–336, June 1997.
- [69] M. P. Kazmierkowski and L. Malesani, "Current control techniques for three-phase voltage-source PWM converters: A survey," *IEEE Trans. Ind. Electron.*, vol. 45, no. 5, pp. 691–703, Oct. 1998.
- [70] H. K. Khalil, *Nonlinear Systems*. New York, NY: Macmillan, 1992.
- [71] H. S. Kim, H. S. Mok, G. H. Choe, D. S. Hyun, and S. Y. Choe, "Design of current controller for 3-phase PWM converter with unbalanced input voltage," in *Proc. IEEE PESC'98*, vol. 1, Fukuoka, Japan, May 1998, pp. 503–509.
- [72] H. Kohlmeier, O. Niermeyer, and D. F. Schröder, "Highly dynamic four-quadrant ac motor drive with improved power factor and on-line optimized pulse pattern with PROMC," *IEEE Trans. Ind. Applicat.*, vol. 23, no. 6, pp. 1001–1009, Nov./Dec. 1987.
- [73] J. W. Kolar, H. Ertl, K. Edelmoser, and F. C. Zach, "Analysis of the control behavior of a bidirectional three-phase PWM rectifier system," in *Proc. EPE Conf.*, vol. 2, Florence, Italy, 1991, pp. 95–100.
- [74] P. K. Kovács, *Transient Phenomena in Electrical Machines*. Amsterdam, The Netherlands: Elsevier, 1984.
- [75] R. Krishnan and F.-C. Doran, "Study of parameter sensitivity in high-performance inverter-fed induction motor drive systems," *IEEE Trans. Ind. Applicat.*, vol. 23, no. 4, pp. 623–635, July/Aug. 1987.
- [76] H. Kubota, I. Sato, Y. Tamura, K. Matsuse, H. Ohta, and Y. Hori, "Regenerating-mode low-speed operation of sensorless induction motor drive with adaptive observer," *IEEE Trans. Ind. Applicat.*, vol. 38, no. 4, pp. 1081–1086, Sept./Oct. 2002.
- [77] G. Kylander, "Modellering och mätning av temperatur och förluster i mindre asynkronmaskiner," Lic. Thesis, Electrical Machines and Power Electronics, Dept. of Electric Power Eng., Chalmers Univ. of Technology, Göteborg, Sweden, 1993.
- [78] J.-W. Lee, "An intelligent current controller using delay time compensation for PWM converter," in *Proc. EPE Conf.*, vol. 1, Trondheim, Norway, Sept. 1997, pp. 342–347.

- [79] W. Leonhard, *Control of Electric Drives*, 2nd ed. Berlin, Germany: Springer-Verlag, 1996.
- [80] V. F. Lescale, "Modern HVDC: State of the art and development trends," in *Proc. Int. Conf. Power System Technology*, vol. 1, Beijing, China, Aug. 1998, pp. 446–450.
- [81] C. E. Lin, M. T. Tsai, Y. S. Shiao, and C. L. Huang, "An active filter for reactive and harmonic compensation using voltage source inverter," in *Proc. Int. Conf. Advances Power System Control, Operation and Management*, vol. 1, Hong Kong, Nov. 1991, pp. 588–593.
- [82] M. Lindgren, "Modeling and control of voltage source converters connected to the grid," Ph.D. dissertation, Electrical Machines and Power Electronics, Dept. of Electric Power Eng., Chalmers Univ. of Technology, Göteborg, Sweden, 1998.
- [83] L. Malesani, L. Rossetto, P. Tenti, and P. Tomasin, "AC/DC/AC PWM converter with reduced energy storage in the dc link," *IEEE Trans. Ind. Applicat.*, vol. 31, no. 2, pp. 287–292, Mar./Apr. 1995.
- [84] M. Malinowski, M. P. Kazmierkowski, S. Hansen, F. Blaabjerg, and G. D. Marques, "Virtual-flux-based direct power control of three-phase PWM rectifiers," *IEEE Trans. Ind. Applicat.*, vol. 37, no. 4, pp. 1019–1027, July/Aug. 2001.
- [85] V. Manninen, "Application of direct torque control modulation technology to a line converter," in *Proc. EPE Conf.*, vol. 1, Sevilla, Spain, Sept. 1995, pp. 292–296.
- [86] R. H. Middleton and G. C. Goodwin, *Digital Control and Estimation: A Unified Approach*. Englewood Cliffs, NJ: Prentice Hall, 1990.
- [87] M. Morari and M. Zafiriou, *Robust Process Control*. Englewood Cliffs, NJ: Prentice Hall, 1989.
- [88] F. Moynihan, "Fundamentals of DSP-based control for ac machines," presented at the PCIM Conf. Tutorial Course Notes, Nuremberg, Germany, May 1998.
- [89] *Motors and Generators*, NEMA Std. MG-1, 1998.
- [90] The NFO Control website. [Online]. Available: <http://www.nfo.se/>
- [91] T. Noguchi, H. Tomiki, and I. Takahashi, "Direct power control of PWM converter without power-source voltage sensors," *IEEE Trans. Ind. Applicat.*, vol. 34, no. 3, pp. 473–479, May/June 1998.
- [92] M. Nowak, R. Barlik, and P. Grochal, "Three phase line converter with optimising influence on power system," in *Proc. EPE Conf.*, vol. 2, Seville, Spain, Sept. 1995, pp. 534–539.
- [93] T. Ohtani, N. Takada, and K. Tanaka, "Vector control of induction motor without shaft encoder," *IEEE Trans. Ind. Applicat.*, vol. 28, no. 1, pp. 157–164, Jan./Feb. 1992.

References

- [94] K. Ohyama, G. M. Asher, and M. Sumner, "Comparison of the practical performance and operating limits of sensorless induction motor drive using a closed loop flux observer and a full order flux observer," in *Proc. EPE Conf.*, Geneva, Switzerland, Sept. 1999, CD-ROM.
- [95] Z. J. Palmor, *The Control Handbook*. Boca Raton, FL: CRC Press, 1996, sec. 10.8-10.10, pp. 224–237.
- [96] R. Peña, R. Cardenas, R. Blasco, G. Asher, and J. Clare, "A cage induction generator using back-to-back PWM converters for variable speed grid connected wind energy system," in *Proc. IEEE IECON'01*, vol. 2, Denver, CO, Nov. 2001, pp. 1376–1381.
- [97] F.-Z. Peng and T. Fukao, "Robust speed identification for speed-sensorless vector control of induction motors," *IEEE Trans. Ind. Applicat.*, vol. 30, no. 5, pp. 1234–1240, Sept./Oct. 1994.
- [98] A. Peterson, "Analysis, modeling and control of doubly-fed induction generators for wind turbines," Lic. Thesis, Electrical Machines and Power Electronics, Dept. of Electric Power Eng., Chalmers Univ. of Technology, Göteborg, Sweden, 2003.
- [99] K. Pietiläinen, "Voltage sag ride-through control of induction motor drives," Lic. Thesis, Electrical Machines and Power Electronics, Dept. of Electrical Eng., Royal Inst. of Technology, Stockholm, Sweden, 2001.
- [100] C. Schauder, "Adaptive speed identification for vector control of induction motors without rotational transducers," *IEEE Trans. Ind. Applicat.*, vol. 28, no. 5, pp. 1054–1061, Sept./Oct. 1992.
- [101] M.-H. Shin, D.-S. Hyun, S.-B. Cho, and S.-Y. Choe, "An improved stator flux estimation for speed sensorless stator flux orientation control of induction motors," *IEEE Trans. Power Electron.*, vol. 15, no. 2, pp. 312–318, Mar. 2000.
- [102] G. R. Slemon, "Modelling of induction machines for electric drives," *IEEE Trans. Ind. Applicat.*, vol. 25, no. 6, pp. 1126–1131, Nov./Dec. 1989.
- [103] J.-J. E. Slotine and W. Li, *Applied Nonlinear Control*. Upper Saddle River, NJ: Prentice Hall, 1991.
- [104] O. J. M. Smith, "A controller to overcome deadtime," *ISA Journal*, vol. 6, no. 2, pp. 28–33, Feb. 1959.
- [105] H.-S. Song and K. Nam, "Dual current control scheme for PWM converter under unbalanced input voltage conditions," *IEEE Trans. Ind. Electron.*, vol. 46, no. 5, pp. 953–959, Oct. 1999.
- [106] J. Svensson, "Grid-connected voltage source converter—Control principles and wind energy applications," Ph.D. dissertation, Electrical Machines and Power Electronics, Dept. of Electric Power Eng., Chalmers Univ. of Technology, Göteborg, Sweden, 1998.

- [107] T. Svensson, “On modulation and control of electronic power convertors,” Ph.D. dissertation, Electrical Machines and Power Electronics, Dept. of Electric Power Eng., Chalmers Univ. of Technology, Göteborg, Sweden, 1988.
- [108] *EMC Levels in Low Voltage Distribution Systems*, Swedish Standards Institute Std. SS 421 18 11, 1989.
- [109] T. Thiringer and J. Luomi, “Comparison of reduced-order dynamic models of induction machines,” *IEEE Trans. Power Syst.*, vol. 16, no. 1, pp. 119–126, Feb. 2001.
- [110] K. Thorborg, *Power Electronics—In Theory and Practice*. Lund, Sweden: Studentlitteratur, 1993.
- [111] P. Tiitinen, P. Pohjalainen, and J. Lalu, “The next generation motor control method: Direct torque control (DTC),” *EPE Journal*, vol. 5, no. 1, pp. 14–18, Mar. 1995.
- [112] M. A. Valenzuela, P. V. Verbakel, and J. Rooks, “Thermal evaluation for applying TEFC induction motors on short-time and intermittent duty cycles,” *IEEE Trans. Ind. Applicat.*, vol. 39, no. 1, pp. 45–52, Jan./Feb. 2003.
- [113] S. Väiliviita, “Predictive filtering methods for motor drive instrumentation,” Ph.D. dissertation, Intelligent Power Electronics, Dept. of Electrical and Communications Eng., Helsinki Univ. of Technology, Espoo, Finland, 1998.
- [114] M. Velez-Reyes and G. C. Verghese, “Developing reduced order electrical machine models using participation factors,” in *Proc. IMACS World Congress Scientific Computation*, Paris, France, July 1988.
- [115] P. A. S. de Wit, R. Ortega, and I. Mareels, “Indirect field-oriented control of induction motors is robustly globally stable,” *Automatica*, vol. 32, no. 10, pp. 1393–1402, Oct. 1996.
- [116] X. Xu and D. W. Novotny, “Implementation of direct stator flux orientation on a versatile DSP based system,” *IEEE Trans. Ind. Applicat.*, vol. 27, no. 4, pp. 694–700, July/Aug. 1991.
- [117] A. van Zyl, R. Spée, A. Faveluke, and S. Bhowmik, “Voltage sag ride-through for adjustable-speed drives with active rectifiers,” *IEEE Trans. Ind. Applicat.*, vol. 34, no. 6, pp. 179–186, Nov./Dec. 1998.

CHALMERS

Errata

to

“On Control of Back-to-Back Converters and Sensorless Induction Machine Drives”

by Rolf Ottersten

- **Chapter 1 (Page 1)**

The first line of the page reads “...are nowadays used various kinds of kinds industrial...,” however, it should read “...are nowadays used in various kinds of industrial...”

- **Chapter 3 (Page 35)**

The first two lines on page 35 read “...derivative of k_2 with respect to ω_1 is $2(1 + \rho R_R/L_M)$, which is positive for $\rho > -L_M/R_R$. Therefore, k_2 has a global minimum when.” They should read “...derivative of ξ with respect to ω_1 is $2(1 + \rho R_R/L_M)$, which is positive for $\rho > -L_M/R_R$. Therefore, ξ has a global minimum when.”

- **Chapter 3 (Page 23)**

The eighth line (from the top) reads “...dynamics resulting from the SCVM are asymptotically stable for small machines.” It should read “...dynamics resulting from the SCVM are asymptotically stable for small machines, given accurate model parameters.”

- **Chapter 3 (Page 38)**

In Fig. 3.3(a), the direction of the rotor MMF and q -axis stator current in the rotor-flux-oriented reference frame coincide. For correctness, the rotor MMF should oppose the q -axis current, even though this not affect the discussion of the instability phenomenon.

- **Chapter 4 (Page 60)**

The third line (from the bottom) reads “...and filters that are tuned for resonance at multiples of the switching frequency [110].” It should read “...and damped LC filters [110].”

- **Chapter 4 (Page 66)**

The line that precedes (4.23) reads “...by substituting $\hat{\psi}_g^s = \hat{\psi}_g e^{j\theta_1} \dots$,” however, it should read “...by substituting $\hat{\Psi}_g^s = \hat{\psi}_g e^{j\theta_1} \dots$ ”

- **Chapter 6 (Page 95)**

Eq. (6.65) reads

$$i_q^{\text{ref}} = k_p e_s + k_i I_s + B_a \hat{\omega}_r.$$

It should read

$$i_q^{\text{ref}} = k_p e_s + k_i I_s - B_a \hat{\omega}_r.$$

- **Chapter 7 (Page 117)**

Eq. (7.38) reads

$$\bar{\mathbf{v}}'_{g,k} = \bar{\mathbf{v}}_{g,k}^{\text{ref}} - j\omega_1 \hat{L}_g \frac{\mathbf{i}_{g,k}^{\text{ref}} + \mathbf{i}_{g,k}}{2} - \mathbf{E}_{g,k}.$$

It should read

$$\bar{\mathbf{v}}'_{g,k} = \bar{\mathbf{v}}_{g,k} - j\omega_1 \hat{L}_g \frac{\mathbf{i}_{g,k}^{\text{ref}} + \mathbf{i}_{g,k}}{2} - \mathbf{E}_{g,k}.$$

- **Appendix B (Page 139)**

It reads on line 7 (from the top) “...are given in Table B.1 on the next page, where the machine...” This line should read “...are given in Table B.1, where the machine...”

- **Appendix C (Page 143)**

The following two abbreviations should be included in the list:

ave	average
IMC	internal model control